

รายงานวิจัยฉบับสมบูรณ์

โครงการ ความเข้าใจในระดับโมเลกุลของการยับยั้งโดยยาทามิฟลูและสารประกอบไพโรริดีน

A-315675 ในเอนไซม์นิวรามินิเดสกลายพันธุ์ของไข้หวัดนกชนิด H5N1

(Molecular insight into inhibitory activity of oseltamivir and A-315675 against

drug-resistant in influenza neuraminidase subtype N1)

โดย หางสาวธัญญดา รุ่งโรจห์มงคล และคณะ

รายงานวิจัยฉบับสมบูรณ์

โครงการ ความเข้าใจในระดับโมเลกุลของการยับยั้งโดยยาทามิฟลูและสารประกอบไพโรริดีน

A-315675 ในเอนไซม์นิวรามินิเดสกลายพันธุ์ของไข้หวัดนกชนิด H5N1

(Molecular insight into inhibitory activity of oseltamivir and A-315675 against

drug-resistant in influenza neuraminidase subtype N1)

นางสาวธัญญดา รุ่งโรจน์มงคล ศูนย์นวตกรรมนาโนเทคโนโลยี จุฬาลงกรณ์มหาวิทยาลัย

สหับสนุนโดยสำนักงานกองทุนสหับสนุนการวิจัย

(ความเห็นในรายงานนี้เป็นของผู้วิจัย สกว. ไม่จำเป็นต้องเห็นด้วยเสมอไป)

CONTENTS

	Page
Abstract in Thai	1
Abstract in English	2
Executive summary	3
Objectives	7
Methodologies	7
Results and Discussion	10
Suggestion for future work	18
References	19
Appendices	21
Biography	106

Project: TRG5280035

Project Title: โครงการ ความเข้าใจในระดับโมเลกุลของการยับยั้งโดยยาทามิฟลูและสารประกอบไพโรริ ดีน A-315675 ในเอนไซม์นิวรามินิเคสกลายพันธ์ของไข้หวัดนกชนิด H5N1

Molecular insight into inhibitory activity of oseltamivir and A-315675 against drug-resistant in influenza neuraminidase subtype N1

Investigator: Dr. Thanyada Rungrotmongkol, Center of Innovative Nanotechnology, Chulalongkorn University

E-mail Address: t.rungrotmongkol@gmail.com

Project Period: 2 years

บทคัดย่อ

จากการแพร่ระบาดของเชื้อไวรัสไข้หวัดนก H5N1 ในหลายประเทศ และการแพร่ระบาดใหญ่ของ ใช้หวัดใหญ่สายพันธุ์ 2009 ไปทั่วโลกในเดือนเมษายน พ.ศ. 2552 ทำให้เกิดความตื่นตัวในการศึกษา ค้นหา และพัฒนายาตัวใหม่อย่างกว้างขวางทั้งในประเทศและต่างประเทศ เพื่อหายาที่มีประสิทธิภาพที่สามารถ ออกฤทธิ์ ได้ดีกับทั้ง ไวรัส ใช้หวัดสายพันธุ์ปกติและสายพันธุ์กลายพันธุ์ งานวิจัยนี้ ได้สร้างแบบจำลอง โครงสร้างสามมิติของสารประกอบเชิงซ้อนระหว่างยาทามิฟลูและเอนไซม์นิวรามินิเคสของเชื้อไวรัสนก และเชื้อไข้หวัดใหญ่สายพันธ์ใหม่ 2009 ทั้งสายพันธ์ปกติและสายพันธ์กลายพันธ์ที่ตำแหน่งต่าง ๆ โดยใช้ ระเบียบวิธีการคำนวณเชิงโมเลคิวร์ลาไคนามิกซิมเลชั้น จากผลการศึกษาพบว่ายาทามิฟลสามารถใช้รักษา ใช้หวัดใหญ่สายพันธุ์ใหม่ชนิดนี้ได้ดี เนื่องจากยาสามารถเข้าจับในบริเวณ binding site ของเอนไซม์นิวรา มินิเคส N1 ได้อย่างเหมาะสมและจับได้ดีกว่าเอนไซม์นิวรามินิเคส N1 ของไข้หวัดนก H5N1 เล็กน้อย นอกจากนี้การกลายพันธุ์ที่ตำแหน่ง H274Y ของเอนไซม์นิวรามินิเคสจะส่งผลให้ขนาดของ binding site ของยาทามิฟลูลดลงอย่างมาก จึงเป็นสาเหตุสำคัญของการดื้อยา ขณะที่ในการกลายพันธุ์ที่ตำแหน่ง N294S นั้น พบว่าการดื้อยาทามิฟลูไม่รุนแรงนัก เนื่องจากขนาดของ binding site ของยาทามิฟลูมีขนาดค่อนข้างเท่า เดิม จากการศึกษาทำนายประสิทธิภาพของยาทามิฟลูในการยับยั้งไข้หวัดใหญ่ 2009 ที่กาดว่าจะพบการคื้อ ยาในอนาคต เนื่องจากการกลายพันธุ์ที่ตำแหน่งอื่น ๆ เช่น E119V และ R292K จากการศึกษาพบว่า ประสิทธิภาพของยาทามิฟลูจะลดลงอย่างมากถ้าเกิดการกลายพันธุ์ที่ตำแหน่ง R292K คณะผู้วิจัยหวังเป็น อย่างยิ่งว่าข้อมูลที่ได้จากงานวิจัยนี้จะเพิ่มความรู้ความเข้าใจมากยิ่งขึ้นเกี่ยวกับกระบวนการหรือกลไกการ ยับยั้งการแพร่พันธุ์ของเชื้อไวรัสไข้หวัดนกและใช้หวัดใหญ่สายพันธุ์ใหม่ 2009 ตลอดจนใช้เป็นข้อมูลใน การติดตามการกลายพันธุ์หรือการอุบัติขึ้นของไข้หวัดสายพันธุ์ใหม่ในปีต่อๆ ไปอีกด้วย

คำหลัก เชื้อไวรัสไข้หวัดนก H5N1 เชื้อไวรัสไข้หวัดใหญ่สายพันธุ์ใหม่ H1N1 เอนไซม์นิวรามินิเคส ยาทามิ ฟลู โมเลคิวลาร์ไดนามิกส์ซิมุเลชัน

Abstract

Recently, the outbreak of avian influenza virus subtype H5N1 has caused illness in several animals including human infections, while the subsequent appearance of the novel pandemic in 2009 caused by the new strain of influenza virus subtype H1N1, called swine flu or H1N1-2009 virus, has become the first pandemic of the 21st century. Before an effective vaccination against influenza virus had been completed, the antiviral agents such as oseltamivir (commercial name as tamiflu) are the only ways to treat the viruses. Unfortunately, drug resistance to the commercial agents in influenza virus isolated from the treated patients has been detected with high resistance rates. The emergence of oseltamivirresistant H1N1 pandemic viruses with H274Y substitution in neuraminidase (NA) genes has been reported to the World Health Organization (WHO) from many countries. The known H274Y and N294S mutations were found to resistant with oseltamivir in H5N1 NA subtype N1. In this work, the oseltamivir binding to wild-type and mutant neuraminidase strains of the influenza A H5N1 and H1N1-2009 viruses were studied by molecular dynamics simulations. The H1N1 virus was predicted to be susceptible to oseltamivir, with all important interactions with the binding residues being well conserved. In the H274Y mutant, the mutated residue moves towards the -OCHEt2 group leading to a reduction in hydrophobicity and pocket size, whilst in the N294S mutant it acts as the hydrogen network center bridging with R224 and the mutated residue S294. Relative to those of the wild type (WT), loss of drug-target interaction energies, especially in terms of electrostatic contributions and hydrogen bonds were dominantly established in the E119V and R292K mutated systems. The inhibitory potencies of oseltamivir towards the WT and mutants were predicted according to the ordering of binding-free energies: WT (-12.3 kcal·mol⁻¹) > N294S $(-10.4 \text{ kcal·mol}^{-1}) > \text{H274Y} (-9.8 \text{ kcal·mol}^{-1}) > \text{E119V} (-9.3 \text{ kcal·mol}^{-1}) > \text{R292K} (-7.7)$ kcal·mol⁻¹), suggesting that the H1N1-2009 influenza with R292K substitution, perhaps, conferred a high level of oseltamivir resistance, while the other mutants revealed moderate resistance levels. A better understanding of molecular inhibition and source of drug resistance is greatly useful as a rotational guide for synthetic and medicinal chemists to develop a new generation of anti-influenza drugs.

Keywords: Influenza A virus, H5N1, H1N1-2009, Neraminidase, Oseltamivir, Molecular dynamics simulations

Executive summary

The avian influenza A subtype H5N1 is a virulent disease with results in significant outbreaks throughout the world, causing numerous human and animal deaths. In February 2009, the pandemic influenza A/H1N1 virus (pH1N1) emerged from swines in Maxico and rapidly spread out worldwide had raised a global human health concern. The new A (H1N1) virus contains the combination of gene segments of swine, avian and human influenza viruses. Based on genetic characterization, the hemagglutinin (HA) gene is similar to that of the swine influenza virus currently circulating amongst USA pigs, whilst the neuraminidase (NA) and matrix protein (M) genes are similar to those of swine influenza viruses isolated from Europe. This unique genetic combination has not previously been detected elsewhere, and none of the patients have had direct contact with pigs leading to the possibility of increased human-to-human transmission of this new influenza virus. Due to antigenic differences amongst influenza A strains, the current seasonal influenza vaccines cannot provide protection against this new strain of A (H1N1) influenza virus. The A (H1N1) viruses isolated from patients in USA and Mexico are sensitive to NA inhibitors but show resistance to adamantine derivatives.

Influenza A viruses in the family of *Orthomyxoviridae* are composed of eight segments of single-stranded negative sense RNA molecule encoding eleven known proteins (PB2, PB1, PB1-F2, PA, HA, NP, NA, M1 and M2, and NS1A and NS2, Fig. 1). A lipid envelop of the viral particle contains two spike glycoproteins, hemagglutinin (HA) and neuraminidase (NA), and the transmembrane protein M2. HA is responsible for the viral entry into target cells while NA plays a critical role in the release of newly synthesized viral particles. The integral membrane protein M2 has a multifunction including proton selective and ion channel. There are 16 antigenically distinct HA (H1-H16) and 9 NA (N1-N9)

subtypes. A combination of these HA and NA subtypes is used to identify different strains of influenza virus such as H1N1, H2N2, and H5N1.

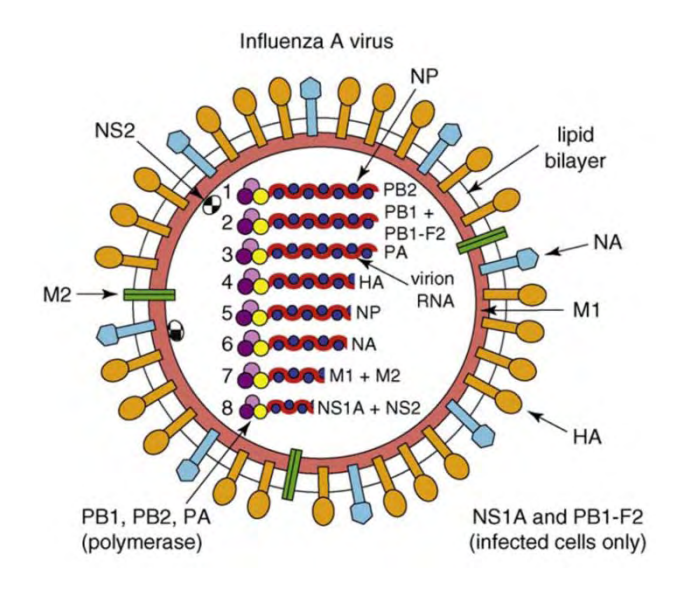


Figure 1. Schematic representation of influenza A virus particle [1]

Neuraminidase (NA), one of two glycoproteins on the surface of influenza virus, is responsible for cleaving the terminal sialic acid from the host receptors in the viral replication cycle. By blocking the NA activity, the new infectious virions cannot be released from the host cell, therefore, NA is an important target for anti-influenza agents in the treatment and prophylaxis of influenza infections. NA predominantly existed as a tetramer of high molecular weight, 240 kDa, as shown in Fig. 2. Based on its phylogenetic tree, the nine subtypes of NA, named N1-N9, are classified into two groups, group-1 (N1, N4, N5 and N8) and group-2 (N2, N3, N6, N7 and N9). The main discrepancy in the structural feature between the two NA groups was revealed by Russell *et al.* in 2006 [2]. The 150-cavity, formed by open conformation of the 150-loop (residues 147-152), was found adjacent to the sialic acid binding pocket in the group-1 NA (Fig. 2). However, the viral influenza pandemic H1N1 NA recently crystallized lacks this cavity [3]. The highly conserved active site in all

subtypes consists of the catalytic residues (R118, D151, D152, R224, E276, R292, R371 and Y406) and the framework residues (E119, R156, W178, S179, D198, I222, E227, H274, E277, N294, and E425).

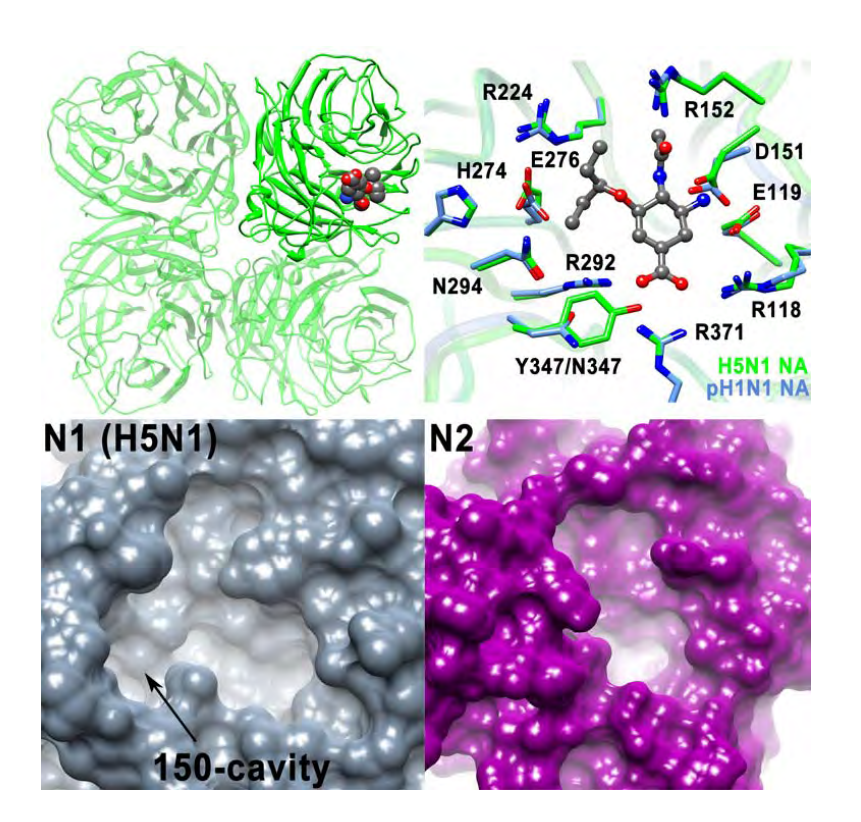


Figure 2. Tetrameric neuraminidase with drug bound. Close up of oseltamivir and its surrounding residues in NA subtype N1 of the influenza A/H5N1 and A/pH1N1 viruses. The active site cavity of NA subtypes N1 and N2.

Up to date, the four anti-influenza drugs (zanamivir, oseltamvir, peramivir and laninamivir in Fig. 3) targeting NA are available to combat the influenza virus. Zanamivir (trade name Relenza® marketed by GlaxoSmithKline) used by oral inhalation is the first NA agent developed through rotational drug design. Oseltamivir (Tamiflu® tablet from Roche) is the most common used for influenza treatment. Peramivir (Rapiacta, brand name in Japan) developed by BioCryst Pharmaceuticals was issued by the Food and Drug Administration as emergency use to treat patients infected by pandemic H1N1 in October 2009. Laninamivir

(Inavir made by Daiichi Sankyo Co. Ltd.) recently approved and released in Japan in September 2010 shows the long-acting inhibitory activity against the influenza virus.

Figure 3. Chemical structures of the four available anti-influenza drugs (OTV, ZNV, PRV and laninamivir) and the new potent inhibitors against influenza NA target

To date, oseltamivir resistances of the H274Y and N294S mutations in H5N1 were experimentally reported as a 300–1700 and 20–80-fold reduction in the sensitivity, respectively, compared to the wild-type. Locations of these two mutated framework residues are adjacent to E276, a residue interacting with the most hydrophobic part (–OCHEt2) of the inhibitor (Fig. 2). In addition, the oseltamivir resistance due to H274Y mutation in neraminidase was also found in H1N1-2009. In the N2 and N9 subtypes, mutations on the binding residues (E119V and R292K) of oseltamivir were detected after treatment in infected patients with high oseltamivir resistance. The probable mutation in the neuraminidase (NA) genes could cause resistance to the available drugs, especially oseltamivir. A new drug-

resistant strain probably leads to a large scale outbreak of influenza virus and an increase the national and global public health concerns.

To provide information at the molecular level to aid the control and prevention of emerging potential pandemic strains of the 2009-H1N1 influenza, multi-molecular dynamics (MD) simulations in conjunction with the linear interaction energy (LIE) method have been performed on complexes of oseltamivir bound to wild-type and mutant neuraminidase strains of H5N1 and H1N1-2009 viruses. The structural property, drug—target interaction and the binding affinity of oseltamivir against the mutated models are extensively discussed and compared with those for the wild-type strain.

Objective

The main goals of this research work are

- 2.1 To understand how oseltamivir inhibits the neuraminidase function of the influenza A virus subtypes H5N1 and H1N1-2009
- 2.2 To compare the oseltamivir binding efficiency among the four different mutated NA strains of H5N1 and H1N1-2009 influenza viruse
- 3.3 To investigate the source of oseltamivir resistance due to neraminidase mutations

Methodologies

Initial structure and system preparation

For H1N1 virus, the X-ray structures of the wild-type, and the two mutant strains (H274Y and N294S), complexed with oseltamivir were obtained from the Protein Data Bank (PDB), entry codes: 2HU4, 3CL0 and 3CL2, respectively, and served as the starting coordinates for the three bound OTV-N1 systems: (1) H5N1 WT, (2) H5N1 H274Y and (3)

H5N1 N294S, respectively. In contrast, the homology model of oseltamivir bound to the wild-type NA of the 2009-H1N1 virus (pH1N1 WT) was used as the initial structure for the modeling of the four single mutations: N294S, H274Y, E119V and R292K. To prepare each mutant, the specific residue was changed using the LEaP module of the AMBER 10 program package, keeping the backbone and identical side chain atoms.

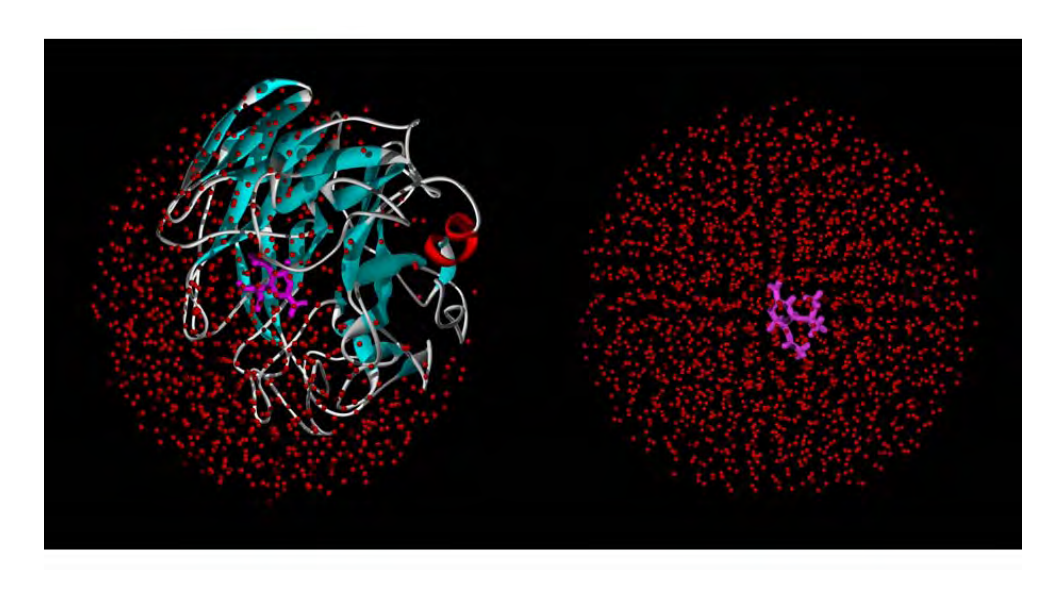


Figure 4. Initial structure of (left) the neuraminidase N1 complexed with oseltamivir and (right) the oseltamivir in free state

All calculations were performed using the Q-program package, version 5. Each system of the drug-protein bound state (left, Fig. 4) was capped by a 25 Å sphere of TIP3P water molecules centered on the C2 atom of oseltamivir and only water molecules where the oxygen was not within a 2.4 Å distance of any heavy atoms of the inhibitor and enzyme were retained. Within a 22 Å sphere of the centered C2 atom, the ionization state of each amino acid with an electrically charged side chain was assigned using the PROPKA program. The ionizable residues lying at 22–25 Å distances were neutralized, except for the pairs of charged residues which probably interact via hydrogen bonds. All ionizable residues positioned further than a 25 Å sphere from the center were treated as a neutral charge. After

solvation, the net charge of the final system of the drug-protein bound state was +2 which was then neutralized by two Cl⁻ ions. For the system with oseltamivir in the free state (right, Fig. 4), the ligand was solvated by a 25 Å sphere of TIP3P water molecules centered on its C2 atom and counterions were added.

Molecular dynamics simulations

Spherical boundary molecular dynamics simulations for all drug-protein systems were carried out under the surface constrained all atom solvent (SCAAS) model. Harmonic constraints were treated to restrain all atoms further than 25 Å from the C2 center. Longrange electrostatic interactions were performed by the local reaction field (LRF) approximation, with a cut-off radius of 10 Å for the non-bonded interactions. To prevent the diffusion of ligand and counterions toward the edge of the simulation sphere, the position of the C2 atom of oseltamivir in the free state system was restrained with a 100 kcal $\text{mol}^{-1} \text{ Å}^{-2}$ harmonic potential, whilst a 75 kcal mol⁻¹ Å⁻² flat-bottom harmonic potential, scaled from a maximum at 20.5 Å to zero at 21.5 Å from the center, was used to treat the counterions. MD simulations of each system were set up as follows. Firstly, the positions of the water molecules were simulated, keeping all other atoms fixed to their initial positions, with the two periods of MD simulations at 5 K. Then, the whole structure was relaxed by four periods of MD simulations at 5 K and the system was heated from 5 K to 298 K in six 50 ps intervals with an increasing temperature of 50 K, and followed by equilibration phase at 298 K. Finally, four different starting structures obtained from the equilibration period were separately performed by 5-ns simulations at 298 K. The NVT ensemble was employed and the SHAKE algorithm was used to constrain all bonds involving hydrogen with a simulation time step of 2 fs. Only the snapshots and energies taken from the production phase were used for the analysis.

Results and Discussion

Susceptibility of oseltamivir against H5N1 and pH1N1 influenza A viruses

To examine the efficiency of oseltamivir binding to the new A (H1N1) influenza NA protein, the percentage and number of hydrogen bond (H-bond) interactions between oseltamivir and the NA binding residues were determined using the following criteria: (i) the distance between proton donor (D) and acceptor (A) atoms ≤ 3.5 Å and (ii) the D–H. . . A angle $\geq 120^{\circ}$. The results are shown in Fig. 5 in comparison to the H5N1 influenza.

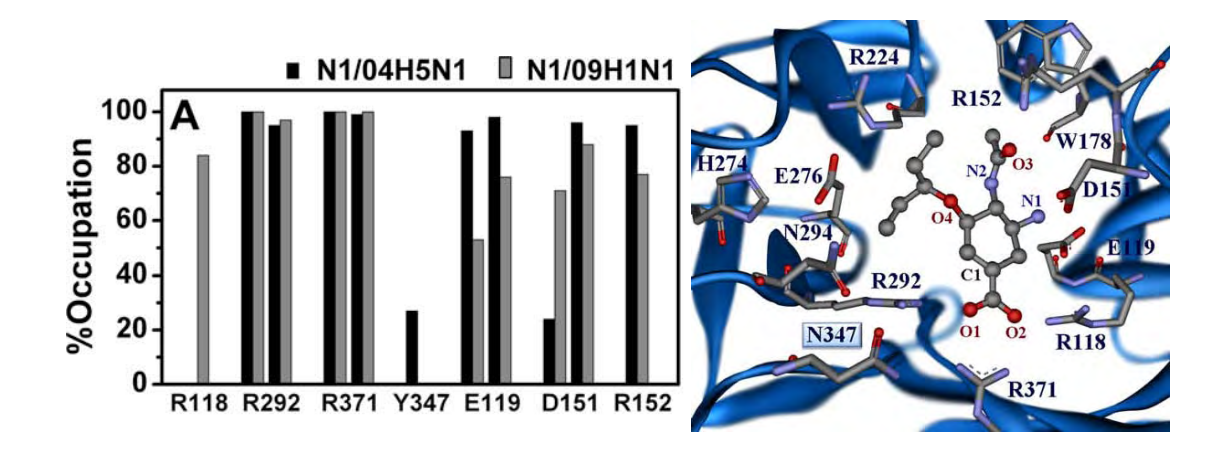


Figure 5. Percentage occupation of hydrogen bonding of oseltamivir and its binding residues

In comparison between the two complexes (Fig. 5), dramatic changes were found at the –COO⁻ group of oseltamivir where a strong H-bond with R118 in the N1/09H1N1 system with 84% occupation. The loss of the H-bond with N347 in the N1/09H1N1 is due to its smaller side chain relative to that of Y347 for the N1/04H5N1. Note that the significance of Y347 was reported in a previous study on oseltamivir-resistance in the N1/04H5N1 isolate as being due to the N294S mutation, which was found to increase the O1(OTV)-OH(374) H-bond distance by 0.5 Å, *i.e.*, the occupation percentage of this H-bond was relatively

decreased. Interestingly, the residues within a spherical radius of 5 Å around the oseltamivir of the new strain are completely identical to those of group-2 NA subtype N9. In addition, oseltamivir was designed to fit to the cavity of this NA group.

To estimate the binding free energies (ΔG_{bind}) of oseltamivir and its four sidechains against the 2009 A (H1N1) influenza NA, 20 ns of MD simulations of OTV-N1/09H1N1 modeled system were carried out using the LIE method with Essex coefficients). Note that the energy of each functional group was evaluated from the fitted LIE equation without the addition of the c constant. The results are summarized in Table 1, where the corresponding values for avian H5N1 influenza NA complexed with oseltamivir, and the experimental energies converted from the IC₅₀ and K_I values [4-7], are also given for comparison. The observed binding affinity of oseltamivir to the N1/09H1N1, at -12.8 kcal·mol⁻¹, is considerably higher than that of its binding to N1/04H5N1, by 1.4 kcal·mol⁻¹, and falls within the range of experimental energies determined for the other N1 strains (-11.8 to -13.1 kcal·mol⁻¹). The contribution from each side chain of oseltamivir to the absolute binding free energy is in the following order: -COO⁻ > -OCHEt₂ > -NHAc > -NH₃ with the corresponding values of -5.2, -4.6, -2.9 and -2.6 kcal·mol⁻¹, respectively (Table 1). These predicted energies were not notably different from those of the avian N1 system, except for the -COO group of N1/09H1N1 which shows an increase in the energetic contribution of 1.1 kcal·mol⁻¹. The calculated binding affinities lead us to conclude that the new A (H1N1) influenza virus is slightly more sensitive to oseltamivir than the avian H5N1 influenza.

How does oseltamivir lose its activity against virulent H5N1 influenza mutants?

The predicted energies of the oseltamivir bound to the H5N1 wildtype and two mutants, H274Y and N294S, evaluated from the LIE with Essex' coefficients are summarized in Table 1. The experimental determined energies for the N1 inhibitory potencies by

oseltamivir converted from the most recently observed K_I and IC_{50} values [4,5], are also given for comparison. In Table 1, the H274Y and N294S mutants were found to reduce the sensitivity to oseltamivir by 1.9 kcal·mol⁻¹ (from -11.4 to -9.5 kcal·mol⁻¹) and 0.5 kcal·mol⁻¹ (from -11.4 to -10.9 kcal·mol⁻¹), respectively. This is in good agreement with the ordering of the experimental binding energies of oseltamivir: wild-type (-13.1 or -12.1 kcal·mol⁻¹) > N294S (-10.5 or -9.3 kcal·mol⁻¹) > H274Y (-9.8 or -8.5 kcal·mol⁻¹).

Table 1. The experimental and predicted binding free energies (ΔG_{bind}) of oseltamivir to the wild-type (OTV-WT) and to the two mutants, OTV-H274Y and OTV-N294S, of H5N1 virus calculated using a MD/LIE approach

System	Resistance	$\Delta G_{\rm bind}$ [kcal mol ⁻¹]		
	fold ^a	Experiments ^b	Essex $\alpha = 0.472$ $\beta = 0.122$, $\gamma = 2.603$ [24]	
OTV-WT	-	-13.1 (-12.1)	-11.4 ± 0.4	
OTV-H274Y	300-1700	-9.8(-8.5)	-9.5 ± 0.6	
OTV-N294S	20-100	-10.5(-9.3)	-10.9 ± 0.7	
rms ^c	-	-	0.8 (1.1)	

The means and standard derivations are derived from four separated 5 ns simulations.

To provide detailed information on the conformational changes of the binding pocket due to the mutations, the distributions of the torsional angle of the side chains of the two mutated residues (τ_{H274Y} and τ_{N294S}) and their neighborhoods (τ_{E276} and τ_{R224}), as well as the bulky –OCHEt₂ moiety of oseltamivir (τ_W , τ_X , τ_Y and τ_Z , see Fig. 6B for definition), were plotted (Fig. 7). The torsional angles were defined by a set of four atoms. To monitor the interaction changes between the two N1 residues, E276 and R224, as a result of the side chain

^b Experimental binding energies were calculated from the K_I inhibitory constants [4] and IC_{50} values [7] (the latter shown in parenthesis).

^c The rms derivations were evaluated from the calculated ΔG_{bind} energies with respect to the experimental ΔG_{bind} energies derived from the K_I and IC_{50} values (the latter shown in parenthesis).

rotations, hydrogen bond distances from the carboxylate group of E276 to the guanidinium group of R224 (which is known to determine the hydrophobic-pocket formation) and to the side chain of N294S were measured and the results are thus summarized and shown in Figs. 8 and 9.

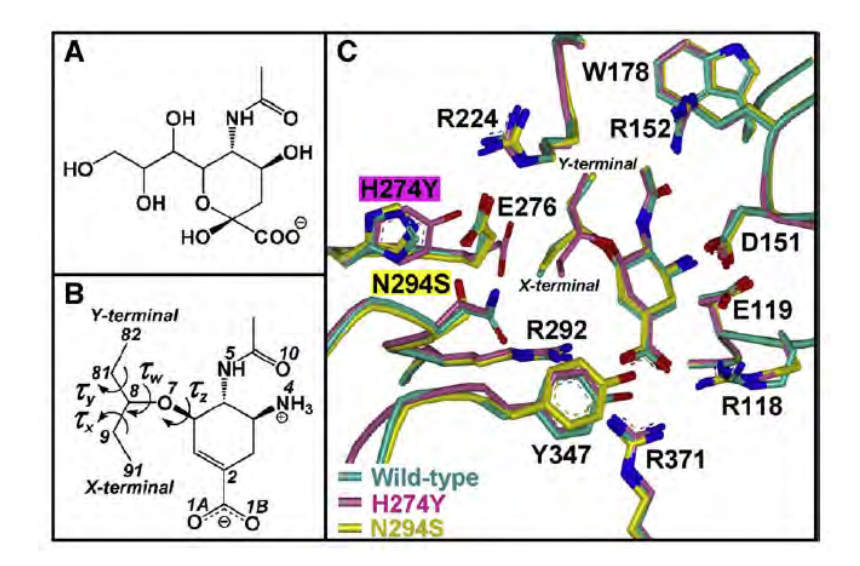


Figure 6. Chemical structures of (A) sialic acid, and (B) oseltamivir's substituent functional groups: $-COO^-$, $-NH_3^+$, -NHAc and $-OCHEt_2$, showing the atomic numbering referred in the text. (C) The crystal structures of oseltamivir bound to the active site of native N1 (cyan), H274Y (pink) and N294S (yellow) mutants

In Fig. 7, the H274Y mutation cannot prevent the E276-R224 hydrogen bonding interactions or the hydrophobic-pocket formation, in contrast to the proposed mechanism of oseltamivir resistance caused by the H274Y mutation [4,8-10]. The primary source of resistance is more likely to be due to the reduction of the hydrophobicity and size of the hydrophobic pocket around the $-OCHEt_2$ side chain. Detailed information on the torsional angle changes is summarized as follows. The H274Y mutation confers a significant change in the sidechain torsional angle of the mutated residue 274, τ_{H274Y} , from a tilted peak dominantly found at -106° in the wild-type to a very sharp peak at -86° in the mutant (Fig. 7A). This rotation, as well as an increase in the bulkiness of the tyrosine's phenol ring, leads to a large

conformational rearrangement of the nearby residue E276 (see Fig. 6C for the initial structure and Fig. 8A for the last MD snapshots).

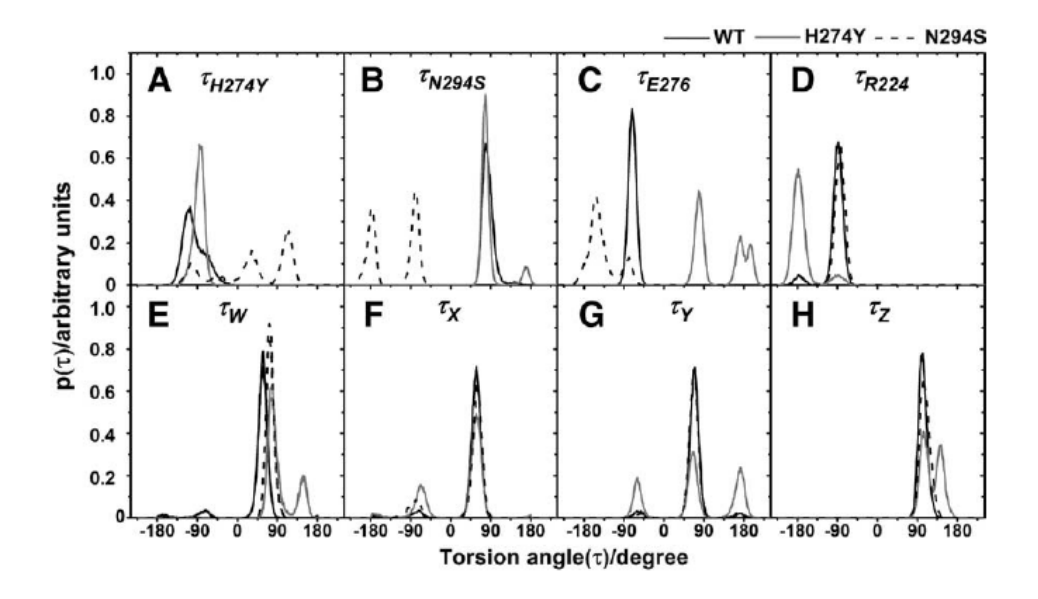


Figure 7. Distribution plots of the torsional angle of the bulky –OCHEt2 group of oseltamivir, and the side chains of two mutated residues (H274Y and N294S) and two neighboring residues (E276 and R224).

The τ_{E276} observed in the H274Y system was noticeably split and shifted from a narrowand sharp peak at -80° for the wild-type, into two peaks at 70° and 180° (Fig. 7C). This accordingly causes the rearrangement of the R224 side-chain orientation, where τ_{R224} was found to consequently rotate by 90° (Fig. 75D) to maintain its hydrogen bonding interactions with the E276 carboxylate group, i.e., the two strongly formed hydrogen bonds indicated by a sharp peak of NE(R224)-OE1(E276) and NH1(R224)-OE2(E276) at ca. 2.8 Å distance. These hydrogen bonds comparable with those found in the wild-type are in contrast to their crystal structures in which only one carboxylate oxygen (OE1) of E276 interacts with the guanidinium group of R224. As mentioned above, the rotations of τ_{E276} and τ_{R224} towards the inhibitor drastically reduce the hydrophobicity and size of the pocket which accommodates the bulky group of oseltamivir. This is the main reason why the oseltamivir's bulkymoiety

cannot fit well into the hydrophobic pocket of the H274Y mutant, a notion which is also supported by the high flexibility of the four torsional angles of the particular moiety (τ_{W-Z} , Fig. 7E–H). The results are in good agreement with the previous study on the H274Y N1 mutant [11] where the Y274 phenol ring was found to push the E276 carboxylate group toward the bulky group of inhibitor; however, the hydrogen bonds between E276 and R224 were not observed.

The remarkable changes in the OTV-N294S complex were originated by the side chain rotation of the mutated residue 294 (τ_{N294S}) shifting from 78° in the wild-type to form the two preferential conformations at -80° and -180°. This leads accordingly to the primary source of oseltamivir resistance in the N294S mutated N1 strain, in contrast to that observed for the oseltamivir-resistant H274Y mutant. The N294S rotation induces the E276 side chain (τ_{E276}) to turn around in the opposite way (-78° an d-152°, Fig. 7C), in comparison to that of the H274Y mutant (78° and ~180°), forming a strong hydrogen bond between the OE2carboxylate oxygen of E276 and the OG hydroxyl oxygen of the mutated residue S294 which is not detected in either the N1 wild-type or the H274Y mutant. Thus, the E276-S294 hydrogen bond formation largely prevents the side chain rotation of E276 and the strong interaction with R224 which is normally stabilized by the presence of two strong hydrogen bonds. In other words, only the remaining carboxylate oxygen of E276 (OE1) in the N294S system is able to form the interactions with the NE- and NH1-guanidinium nitrogens of R224 agreeing well with the crystallographic structure. This is different from the simulations of the N294S N1 mutant [11] where the two hydrogen bonds formed between E276 and R224 were not changed (from wild-type) by the N294S mutation. Although the H274 side chain seemed to be able to rotate freely leading to the three preferential conformations at -104°, 32° and 110° (Fig. 7A), it did not interfere with the hydrophobic pocket which was constantly constructed by the hydrogen bond network around the center residue E276. Instead, the Y347

phenyl ring sometimes partially occupied the pocket and was also found in the crystal structure (Fig. 6C). Again, in contradiction with that observed for the high-level oseltamivir-resistant H274Y strain, the N294S mutation does not influence the conformations of the R224 side chain and $-OCHEt_2$ group. This statement was supported by the insignificant changes in their torsional angles (τ_{R224} , τ_{W-Z} in Fig. 7C and E–H), in comparison to those of wild-type. These results lead us to conclude that the hydrophobicity and size of the hydrophobic pocket were not disturbed by the N294S mutation.

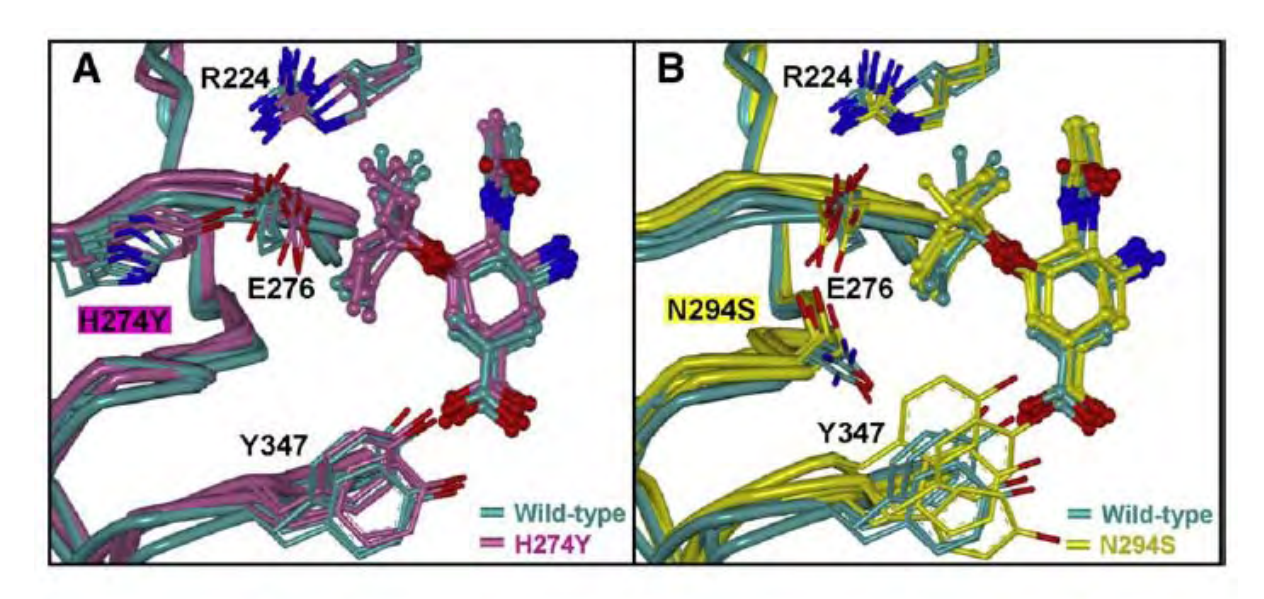


Figure 8. Structural alignment between the four last snapshots of the 5-ns MD simulations of (A) OTV-WT and OTV-H274Y, and (B) OTV-WT and OTV-N294S. Closed view of oseltamivir, the two residues E276 and R224 mainly forming the hydrophobic pocket around the bulky –OCHEt₂ group of oseltamivir, the mutated residues (H274Y and N294S) and Y347, are displayed.

Molecular prediction of oseltamivir efficiency against probable pH1N1 mutants

Multi-MD simulations in conjunction with the LIE method was performed on oseltamivir–NAbound complexes for the four probable NA mutants of influenza A (H1N1-2009): two mutations on the framework residues (N294S and H274Y) and the two others on

the direct-binding residues (E119V and R292K) of oseltamivir (Fig. 9). Reduction in the oseltamivir–enzyme interaction energies, particularly in the electrostatic term, and in the hydrogen bonding were both observed in the two mutated systems with substitution on the direct-binding residues, E119V and R292K.

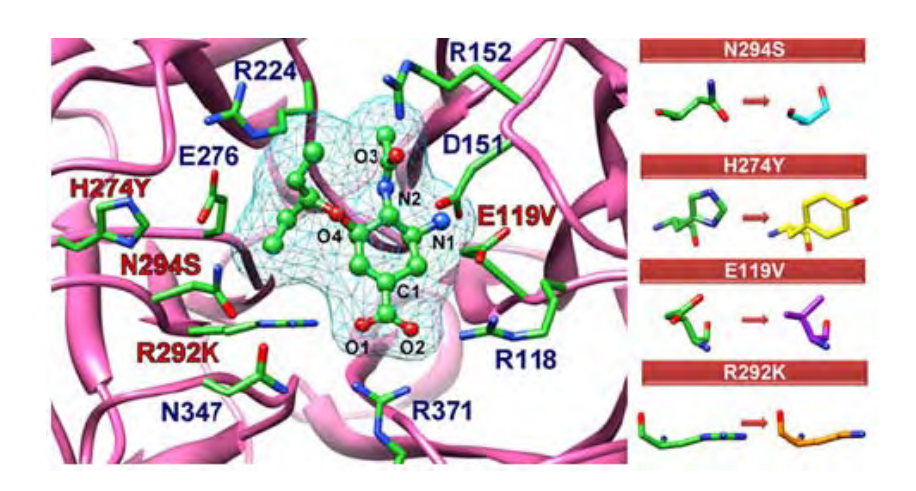


Figure 9. Modeled structure of oseltamivir bound to the wild-type strain of 2009-H1N1 influenza neuraminidase. Among the labeled residues, four residues colored in red are singly mutated for investigation in this work: there are N294S, H274Y, E119V and R292K mutations.

Based on the MD/LIE approach, the binding affinities of oseltamivir towards different mutant models of the 2009-H1N1 influenza [A/California/04/2009(H1N1)] were predicted and are summarized in Table 2. As expected, oseltamivir's binding-free energy against the WT is the most favorable one at -12.8 kcal mol⁻¹. Only moderate binding-free energy values were found for the N294S, H274Y and E119V mutated strains, in which the corresponding ΔG_{bind} of -10.4, -9.8 and -9.3 kcal mol⁻¹, respectively. The lowest favorable binding of oseltamivir is found in the R292K mutant with a predicted ΔG_{bind} of -7.7 kcal mol⁻¹. All the calculated binding-free energies were found to fall within the ranges of those experimentally

determined for various WT and mutant strains of the other influenza N1 and N2 subtypes (Table 2). Taking all the above data into consideration, it seems likely that oseltamivir will be significantly less potent an inhibitor for all the modeled mutants of the 2009-H1N1 strains, with the ranked order of: R292K < E119V < H274Y < N294S.

Table 2 MD/LIE binding-free energies (DGbind) of oseltamivir towards the 2009-H1N1 influenza neuraminidases [A/California/04/2009(H1N1)] for the wild type (WT) and the probable single mutations: N294S, H274Y, E119V and R292K

NA strain	ΔG_{bind} (kcal mol ⁻¹)					
	WT	N294S	H274Y	E119V	R292K	
Predictive						
A/California/04/2009(H1N1)	-12.8 ± 0.9	-10.4 ± 0.9	-9.8 ± 1.0	-9.3 ± 0.8	-7.7 ± 0.7	
Experimental ^a						
A/WSN/33 (H1N1) ^b	-12.1	-9.3	-8.5	-	-	
A/Puerto Rico/8/34 (H1N1) ^c	-11.4	-8.8	-8.1	_	-	
A/Vietnam/1203/04 (H1N1) ^c	-13.0	-11.2	-8.6	-	-	
A/Vietnam/1203/04 (H5N1) ^d	-13.1	-10.5	-9.8	-	-	
A/Sydney/5/97 (H3N2) ^b	-12.8	-8.3	_	-8.6	-7.3	
A/Wuhan/359/95 (H3N2)e	-12.4	-	-	-9.1	-6.2	

Means and standard deviations are derived from four separate 5-ns simulations

The experimental ΔG_{bind} for different strains of N1 and N2, converted from the K_I inhibitory and IC_{50} values, are also given for comparison

Suggestions for future works

- A) Extend MD simulations for longer time period to see whether dynamical behaviors of drug binding at neuraminidase active site are significantly different from that reported in this work
- B) To find new potent drugs, the detailed mechanism of the neuraminidase functions on cleaving the terminal sialic acid from the host receptors in the viral replication cycle should be revealed.

 $^{^{}a}$ $\Delta G_{experiment}$ was calculated from the experimental data using the following references: (b) ref. 5, (c) ref. 12, (d) ref. 4 and (e) ref. 13

C) Surveillance of any mutations in the influenza A (H1N1-2009) needs to be closely watched, and prompt action taken for preparation for the next pandemic of potentially higher oseltamivir-resistant H1N1 influenza strains. This calls for the urgent development of new potent anti-influenza agents against both native and mutants forms of H1N1-2009.

References

- 1. Krug RM, Aramini JM. Emerging antiviral targets for influenza A virus. *Trends Pharmacol Sci* 2009; 30: 269-77.
- 2. Russell RJ, Haire LF, Stevens DJ, et al. The structure of H5N1 avian influenza neuraminidase suggests new opportunities for drug design. *Nature* 2006; 443: 45-9.
- 3. Li Q, Qi J, Zhang W, et al. The 2009 pandemic H1N1 neuraminidase N1 lacks the 150-cavity in its active site. *Nat Struct Mol Biol* 2010; 17: 1266-8.
- 4. P.J. Collins, L.F. Haire, Y.P. Lin, J. Liu, R.J. Russell, P.A. Walker, J.J. Skehel, S.R. Martin, A.J. Hay, S.J. Gamblin, Crystal structures of oseltamivir-resistant influenza virus neuraminidase mutants, *Nature* 2008; 453: 1258–1261.
- 5. Y. Abed, B. Nehm, M. Baz, G. Boivin, Activity of the neuraminidase inhibitor A-315675 against oseltamivir-resistant influenza neuraminidases of N1 and N2, *Antiviral Res.* 2008; 77: 163–166.
- 6. G. Boivin, N. Goyette, Susceptibility of recent Canadian influenza A and B virus isolates to different neuraminidase inhibitors, *Antiviral Res.* 2002; 54: 143–147.
- 7. V.P. Mishin, F.G. Hayden, L.V. Gubareva, Susceptibilities of antiviral-resistant influenza viruses to novel neuraminidase inhibitors, *Antimicrob. Agents Chemother*. 2005; 49: 4515–4520.

- 8. Yen H.L., Ilyushina N.A., Salomon R., Hoffmann E., Webster R.G., Govorkova E.A., Neuraminidase inhibitor-resistant recombinant A/Vietnam/1203/04 (H5N1) influenza viruses retain their replication efficiency and pathogenicity in vitro and in vivo, *J. Virol.* 2007; 81: 12418–12426.
- 9. McKimm-Breschkin J.L., Sahasrabudhe A., Blick T.J., McDonald M., Mechanisms of resistance of influenza virus to neuraminidase inhibitors, *Int. Congr. Ser.* 2001; 1219: 855–861.
- Moscona A., Oseltamivir resistance-disabling our influenza defenses, N. Engl. J. Med.
 2005; 353: 2633–2636.
- 11. Wang N.X., Zheng J.J., Computational studies of H5N1 influenza virus resistance to oseltamivir. *Protein Sci.* 2009; 18:707–715.
- 12. Yen HL, Ilyushina NA, Salomon R, Hoffmann E, Webster RG, Govorkova EA, Neuraminidase inhibitor-resistant recombinant A/Vietnam/1203/04 (H5N1) influenza viruses retain their replication efficiency and pathogenicity in vitro and in vivo. *J Virol* 2007; 81:12418–12426
- 13. Yen HL, Herlocher LM, Hoffmann E, Matrosovich MN, Monto AS, Webster RG, Govorkova EA, Neuraminidase inhibitorresistant influenza viruses may differ substantially in fitness and transmissibility. *Antimicrob Agents Chemother* 2005; 49: 4075–4084

Appendices

สรุป Output จากโครงการวิจัยที่ได้รับทุนจาก สกว

1. ผลงานตีพิมพ์ในวารสารวิชาการนานาชาติ 4 ฉบับ

- 1.1 **T. Rungrotmongkol**, P. Intharathep, M. Malaisree, N. Nunthaboot, N. Kaiyawet, P. Sompornpisut, S. Payungporn, Y. Poovorawan, and S. Hannongbua*, Susceptibility of antiviral drugs against 2009 influenza A (H1N1) virus. *Biochemical and Biophysical Research Communications* 2009; 385(3):390-4. (IF2010 = 2.595)
- 1.2 **T. Rungrotmongkol**, T. Udommaneethanakit, M. Malaisree, N. Nunthaboot, P. Intharathep, P. Sompornpisut and S. Hannongbua*, How does each substituent functional group of oseltamivir lose its activity against virulent H5N1 influenza mutants? *Biophysical Chemistry* 2009; 145(1):29–36. (IF2010 = 2.108)
- 1.3 **T. Rungrotmongkol**, M. Malaisree, N. Nunthaboot, P. Sompornpisut, and S. Hannongbua*, Molecular prediction of oseltamivir efficiency against probable influenza A (H1N1-2009) mutants: Molecular modelling approach, *Amino Acids* 2010; 39(2):393-398. (IF2010 = 4.106)
- 1.4 **T. Rungrotmongkol**, P. Yotmanee, N. Nunthaboot and S. Hannongbua*, Computational studies of influenza A virus at three important targets: hemagglutinin, neuraminidase and M2 protein, *Current Pharmaceutical Design* 2011;17:1720-1739. (IF2010 = 4.774)

2. การนำผลงานวิจัยไปใช้ประโยชน์

เนื่องจากงานวิจัยนี้เป็นงานวิจัยทางด้านทฤษฎี ดังนั้นผลสำเร็จที่ได้จะเป็นการได้มาซึ่งองค์ ความรู้ที่ประกอบด้วยข้อมูลพื้นฐานเชิงโมเลกุลที่สำคัญในการเข้าใจถึงพฤติกรรมและกลไกการออกฤทธิ์ ยับยั้ง รวมถึงสาเหตุของการดื้อยาของยาที่ใช้รักษาโรคไข้หวัดในปัจจุบัน ต่อการทำงานของเอนไซม์ นิวรามินินเดสชนิด N1 และความเข้าใจเชิงลึกนี้จะเป็นพื้นฐานสำคัญต่อการออกแบบและพัฒนายาที่

สามารถออกฤทธิ์ต่อเอนไซม์นิวรามินิเดสของไข้หวัดนกและไข้หวัดใหญ่สายพันธุ์ใหม่ 2009 ทั้งสาย พันธุ์ตั้งเดิมและสายพันธุ์ที่กลายพันธุ์แล้วที่พบว่าดื้อยาทามิฟลูที่พบแล้วในปัจจุบัน และสายพันธุ์ที่คาด ว่าจะเกิดการดื้อยาขึ้นในอนาคต อีกทั้งยังเป็นการผลิตนักวิจัยและงานวิจัยของประเทศไทยให้เป็นที่ ยอมรับของต่างประเทศอีกด้วย

3. มีการนำงานวิจัยนี้ไปเสนอผลงานแบบบรรยาย ในงานประชุมวิชาการ ดังนี้

- 3.1 **T. Rungrotmongkol**, T. Udommaneethanakit, M. Malaisree, N. Nunthaboot, P. Intharathep, and S. Hannongbua. How does oseltamivir lose its activity against virulent H5N1 mutants? Sokendai Asian Winter School, Okazaki, Japan, December 9-12, 2008.
- 3.2 **T. Rungrotmongkol**, M. Malaisree, P. Intharathep, P. Decha, N. Nunthaboot, C. Laohpongspaisan, O. Aruksakunwong, T. Udommaneethanakit, S. Sompornpisut and S. Hannongbua, Concerns, recent outbreak and molecular insight into H5N1 and pandemic H1N1-2009 influenza A viruses ในงานประชุมวิชาการนานาชาติทางวิทยาการและวิศวกรรมทาง คอมพิวเตอร์ประจำปี ครั้งที่ 14 (ANSCSE14) ระหว่างวันที่ 23-26 มีนาคม 2553 ณ มหาวิทยาลัยแม่ ฟ้าหลวง จังหวัดเชียงราย
- 3.3 **T. Rungrotmongkol**, M. Malaisree, S. Hannongbua, S. Phongphanphanee, N. Yoshida, F. Hirata, Neuraminidase and M2-channel of influenza A viruses H5N1 and pandemic H1N1: molecular modelling and 3D-RISM, The Inaugural CU-IMS Joint Symposium, Chulalongkorn University, Bangkok, Thailand, October 19-21, 2010.
- 3.4 **T. Rungrotmongkol**, Computational Studies on Influenza A Virus Subtypes H5N1 and Pandemic H1N1, EXODASS General Meeting & Mini-Symposium, Institute for Molecular Science, Okazaki, Japan, May 26, 2011

4. ผลงานวิจัยอื่นๆ ที่ได้รับการตีพิมพ์ในวารสารระดับนานาชาติในช่วงที่ได้รับการสนับสนุนจากแหล่งทุน

ตีพิมพ์ในวารสารวิชาการนานาชาติ 6 ฉบับ

- 4.1 **T. Rungrotmongkol**, N. Nunthaboot, M. Malaisree, N. Kaiyawet, P. Intharathep, A. Meepraset and S. Hannongbua, Molecular Insight into the Specific Binding of ADP-ribose to the nsP3 Macro Domains of Chikungunya and Venezuelan Equine Encephalitis Viruses: Molecular Dynamics Simulations and Free Energy Calculations, *Journal of molecular graphics and modelling* **2010**;29:347–353.
- 4.2 N. Nunthaboot, **T. Rungrotmongkol**, M. Malaisree, P. Decha, N. Kaiyawet, P. Intharathep, P. Sompornpisut, Y. Poovorawan and S. Hannongbua, Molecular insights into human receptor binding to 2009 H1N1 influenza A hemagglutinin, *Monatshefte fur Chemie Chemical Monthly* **2010**; 141(7):801-807.
- 4.3 N. Nunthaboot, **T. Rungrotmongkol**, M. Malaisree, N. Kaiyawet, P. Decha, P. Sompornpisut, and S. Hannongbua, Evolution of the human-receptor binding affinity of influenza A (H1N1) 2009 pandemic hemagglutinin from 1918- and 1930-H1N1 influenza viruses, *Journal of Chemical Information and Modeling* **2010**;50:1410-1417.
- 4.4 U. Arsawang, O. Saengsawang, **T. Rungrotmongkol**, P. Sornmee, T. Remsungnen and S. Hannongbua, How do carbon nanotubes serve as carriers for gemcitabine transport in drug delivery system? *Journal of molecular graphics and modelling* **2011**;29:591–596.
- 4.5 P. Sornmee, **T. Rungrotmongkol**, O. Saengsawang, U. Arsawang, T. Remsungnen and S. Hannongbua, Understanding of molecular properties of the doxorubicin anticancer drug filling inside and wrapping outside the single-walled carbon nanotube Journal of Computational and Theoretical Nanosciencs **2011**; in press.
- 4.6 **T. Rungrotmongkol**, U. Arsawang, C. Iamsamai, A. Vongachariya, S. Dubas, U. Ruktanonchai, A. Soottitantawat and S. Hannongbua, Increase in dispersion and solubility of carbon nanotubes

noncovalently modified by chitosan-polysaccharide biopolymer: MD simulations, *Chemical Physics Letter* **2011**;507:134–137.



Contents lists available at ScienceDirect

Biochemical and Biophysical Research Communications

journal homepage: www.elsevier.com/locate/ybbrc



Susceptibility of antiviral drugs against 2009 influenza A (H1N1) virus

Thanyada Rungrotmongkol ^{a,b}, Pathumwadee Intharathep ^a, Maturos Malaisree ^a, Nadtanet Nunthaboot ^c, Nopphorn Kaiyawet ^a, Pornthep Sompornpisut ^a, Sanchai Payungporn ^d, Yong Poovorawan ^d, Supot Hannongbua ^{a,*}

- ^a Department of Chemistry, Faculty of Science, Chulalongkorn University, Phayathai Road, Patumwan, Bangkok 10330, Thailand
- ^b Center of Innovative Nanotechnology, Chulalongkorn University, Bangkok 10330, Thailand
- ^c Department of Chemistry, Faculty of Science, Mahasarakham University, Mahasarakham 44150, Thailand
- ^d Center of Excellence in Clinical Virology, Faculty of Medicine, Chulalongkorn University, Bangkok 10330, Thailand

ARTICLE INFO

Article history: Received 13 May 2009 Available online 20 May 2009

Keywords:
2009 H1N1 influenza A virus
Neuraminidase
M2-channel
Oseltamivir
Amantadine
Rimantadine
Molecular dynamics simulations

ABSTRACT

The recent outbreak of the novel strain of influenza A (H1N1) virus has raised a global concern of the future risk of a pandemic. To understand at the molecular level how this new H1N1 virus can be inhibited by the current anti-influenza drugs and which of these drugs it is likely to already be resistant to, homology modeling and MD simulations have been applied on the H1N1 neuraminidase complexed with oseltamivir, and the M2-channel with adamantanes bound. The H1N1 virus was predicted to be susceptible to oseltamivir, with all important interactions with the binding residues being well conserved. In contrast, adamantanes are not predicted to be able to inhibit the M2 function and have completely lost their binding with the M2 residues. This is mainly due to the fact that the M2 transmembrane of the new H1N1 strain contains the S31N mutation which is known to confer resistance to adamantanes.

© 2009 Elsevier Inc. All rights reserved.

Introduction

Since March 2009, the outbreak of a new strain of influenza A (H1N1) virus infection in humans has raised increasing concerns of the risk of a global flu epidemic. Many countries around the world, especially The United States of America and Mexico, have formally reported symptomatic human infections of this new A (H1N1) virus [1]. The most effective antiviral agent, oseltamivir (OTV), is recommended by The World Health Organization (WHO) and the Centers for Disease Control and Prevention (CDC) for treatment of the infected patients, whilst the new A (H1N1) strain confers resistance to amantadine (AMT) and rimantadine (RMT). To overcome this or any other future pandemic, this urgent event needs a detailed understanding at the molecular level of any inhibitory machinery of such commercially available and well stocked front line drugs.

The new A (H1N1) virus contains the combination of gene segments of swine, avian and human influenza viruses. Based on genetic characterization, the hemagglutinin (HA) gene is similar to that of the swine influenza virus currently circulating amongst USA pigs, whilst the neuraminidase (NA) and matrix protein (M)

genes are similar to those of swine influenza viruses isolated from Europe. This unique genetic combination has not previously been detected elsewhere, and none of the patients have had direct contact with pigs leading to the possibility of increased human-to-human transmission of this new influenza virus [2]. In late April 2009, WHO has raised the pandemic alert for influenza A (H1N1) to phase 5, which is when the spread of disease between humans is occurring in more than one country [3].

Due to antigenic differences amongst influenza A strains, the current seasonal influenza vaccines cannot provide protection against this new strain of A (H1N1) influenza virus. Up to date, there are two classes of anti-influenza agents: (i) NA inhibitors, oseltamivir and zanamivir, protecting the release and spread of progeny virions; (ii) adamantane derivatives, amantadine and rimantadine, preventing the proton transfer in the M2 ion-channel [4]. The A (H1N1) viruses isolated from patients in USA and Mexico are sensitive to NA inhibitors but show resistance to adamantane derivatives [5].

To gain the fundamental knowledge on the structure and the drug-target interactions of the new strain of influenza A (H1N1) virus, homology modeling and molecular dynamics (MD) simulations were carried out on the three inhibitor–enzyme complexes: OTV-NA, AMT-M2 and RMT-M2. The present study is an extension from, and is compared to, our previous works on avian influenza H5N1 virus which were focused to understand the structural

^{*} Corresponding author. Fax: +66 22 187603. E-mail address: supot.h@chula.ac.th (S. Hannongbua).

properties, intermolecular interactions and predictive inhibitory potencies of both wild- and mutant-type viruses at the NA and M2 targets [6–10].

Materials and methods

Models of the 2009 H1N1 influenza neuraminidase and M2-channel. The initial structures of the new strain of A (H1N1) influenza NA (N1/09H1N1) and M2-channel (M2/09H1N1) were modeled based on the available 3D structures and the genomic sequence data of virions recently isolated from infected patients in southern California, A/California/04/2009 (H1N1). Here, the crystal structure of avian influenza N1 (N1/04H5N1) with oseltamivir bound, (PDB entry code: 2HU4) [11], and the solid state NMR structure of the transmembrane segment of a homotetrameric M2 channel (2H95.PDB) [12], were used as the templates. The sequence alignment was performed using the homology modeling module implemented in the Discovery Studio 2.0 software. Relative to the amino acid sequences of the templates, the N1/09H1N1 and M2/09H1N1 proteins had 92% and 84% identity, respectively. To prepare the OTV-N1/09H1N1 complex, superimposition of OTV-N1/04H5N1 with N1/09H1N1 was performed and the N1/04H5N1 atomic coordinates were then deleted. For the AMT-M2/09H1N1 and RMT-M2/ 09H1N1 structures, the inhibitor was docked into the tetrameric M2 channel using the Autodock 3.0 program [13]. All built models were further refined by energy minimization and consequently MD simulations were performed for 20 ns on the NA complex, and for 8 ns on the M2 systems. All calculations were set up according to our previous studies on avian influenza NA [14] and M2-channel [9,10] (see detailed methodology in Supplementary material).

Linear interaction energy method. The linear interaction energy (LIE) method was used to calculate the binding free energies ($\Delta G_{\rm bind}$) of the oseltamivir bound to the NA enzyme. This method is a linear response semiempirical technique used to evaluate the free energy changes from the simulations of two states: (i) the solvated ligand (free state), and (ii) the ligand bound to the solvated protein (bound state). Based on the LIE method, the total binding free energy was contributed from van der Waals ($U^{\rm vdW}$) and electrostatic interaction energies ($U^{\rm elec}$) using the equation given below:

$$\Delta G_{\text{bind}} = \alpha (< U^{\text{vdW}} >_{\text{bound}} - < U^{\text{vdW}} >_{\text{free}}) + \beta (< U^{\text{elec}} >_{\text{bound}} - < U^{\text{elec}} >_{\text{free}}) + \gamma$$
(1)

where α and β are empirical scaling coefficients for the van der Waals and electrostatic interaction energies, respectively, and γ is

Table 1

Binding free energies ($\Delta G_{\rm bind}$) of oseltamivir and its functional groups to the 2009 H1N1 influenza neuraminidase (N1/09H1N1) based on the MD/LIE approach. Means and standard deviations are derived from four separate 5 ns simulations. The $\Delta G_{\rm bind}$ for the OTV-N1/04H5N1 complex and the experimental values are also given for comparison.

System	ΔG_{bind} [kcal·mol ⁻¹]				
	Oseltamivir	-COO-	-NH ₃ +	-NHAc	-OCHEt ₂
N1/09H1N1 N1/04H5N1 Experimental	-12.8 ± 0.9 -11.4 ± 0.4 (-11.8)-(-13.1)	-4.1 ± 0.3	-2.6 ± 0.5 -2.8 ± 0.1		-4.6 ± 0.9 -4.5 ± 0.4 -

a constant. Here, Essex's coefficients (α = 0.472, β = 0.122 and γ = 2.603), efficiently derived from a statistical analysis of the inhibitor sets binding to the NA enzyme [15], were used to fit the LIE equation. This set of coefficients has previously been found to be the most predictive model for the NA system amongst the many developed models, with or without the addition of the hydration term.

Results and discussion

All calculations are modeled and discussed in comparison to our previous studies on the avian H5N1 influenza NA (N1/04H5N1) [6–8,14] and M2-channel (M2/04H5N1) [9,10]. Relative to N1/04H5N1, all residues in the N1/09H1N1 binding pocket are conserved except for one, the tyrosine (Y374) being replaced by asparagine (N374) (Fig. 1A). This is not the case for the M2-channel in which amongst the 19 key residues three were changed, that is the I28 and N31 at the extracellular site and T43 close to the gating tryptophan (W41) of M2/09H1N1, were changed from V28, S31 and L43 of the M2/04H5N1, respectively (Fig. 1B).

Efficiency of oseltamivir against influenza A (H1N1) neuraminidase

To estimate the binding free energies ($\Delta G_{\rm bind}$) of oseltamivir and its four sidechains against the 2009 A (H1N1) influenza NA, 20 ns of MD simulations of OTV-N1/09H1N1 modeled system were carried out using the LIE method with Essex coefficients (Eq. (1)). Note that the energy of each functional group was evaluated from the fitted LIE equation without the addition of the γ constant. The results are summarized in Table 1, where the corresponding values for avian H5N1 influenza NA complexed with oseltamivir [14], and the experimental energies converted from the IC₅₀ and K_I values [16–19], are also given for comparison.

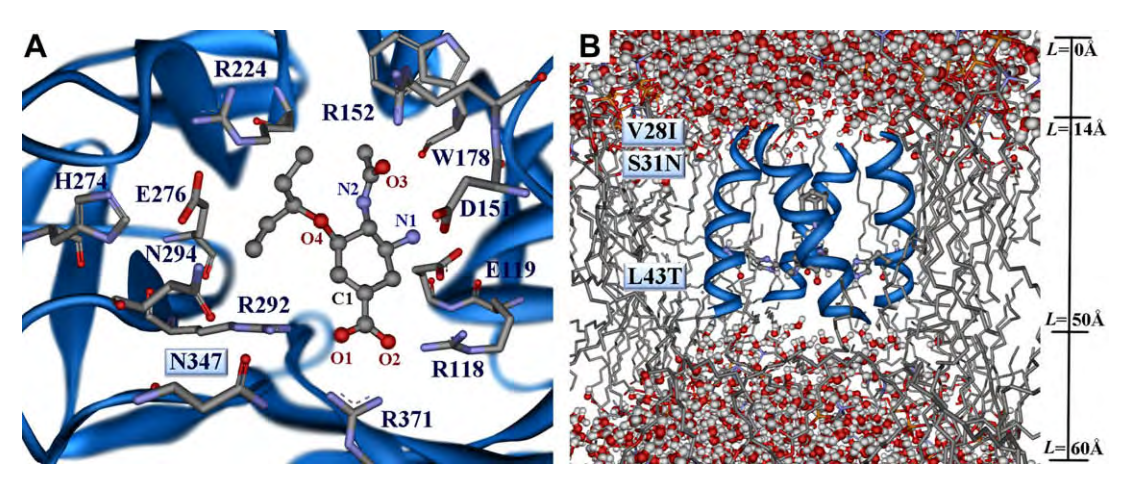


Fig. 1. Modeled structures of 2009 H1N1 influenza A virus: (A) oseltamivir bound to the binding site of neuraminidase, and (B) the adamantane inhibitor docked into the M2-channel. The residues which differ from those of avian H5N1 influenza are highlighted and some atoms are labeled for simplicity in the investigations and discussions.

The observed binding affinity of oseltamivir to the N1/09H1N1, at $-12.8 \text{ kcal} \cdot \text{mol}^{-1}$, is considerably higher than that of its binding to N1/04H5N1, by $1.4 \text{ kcal} \cdot \text{mol}^{-1}$, and falls within the range of experimental energies determined for the other N1 strains ($-11.8 \text{ to} -13.1 \text{ kcal} \cdot \text{mol}^{-1}$) [16-19]. The contribution from each side chain of oseltamivir to the absolute binding free energy is in the following order: $-\text{COO}^- > -\text{OCHEt}_2 > -\text{NHAc} \sim -\text{NH}_3^+$ with the corresponding values of -5.2, -4.6, -2.9 and $-2.6 \text{ kcal} \cdot \text{mol}^{-1}$, respectively (Table 1). These predicted energies were not notably different from those of the avian N1 system, except for the $-\text{COO}^-$ group of N1/09H1N1 which shows an increase in the energetic contribution of $1.1 \text{ kcal} \cdot \text{mol}^{-1}$. The calculated binding affinities lead us to conclude that the new A (H1N1) influenza virus is more sensitive to oseltamivir than the avian H5N1 influenza.

To examine the efficiency of oseltamivir binding to the new A (H1N1) influenza NA protein, the percentage and number of hydrogen bond (H-bond) interactions between oseltamivir and the NA binding residues were determined using the following criteria: (i) the distance between proton donor (D) and acceptor (A) atoms $\leq \! 3.5$ Å and (ii) the D–H. . . A angle $\geq \! 120^\circ$. The results are shown in Fig. 2A (where description is given in Table S1, Supplementary materials) in comparison to the H5N1 influenza [14]. Distributions of the H-bond distance for the 118 and 347 residues are plotted in Fig. 2B.

In comparison between the two complexes, dramatic changes were found at the -COO- group of oseltamivir where a strong Hbond with R118 in the N1/09H1N1 system with 84% occupation (Fig. 2A), and the preferential O2-NH2 (R118) distance of 2.9 Å, was newly formed (Fig. 2B, grey line). This is different for the N1/04H5N1 in which this distance takes place at \sim 4.2 Å (Fig. 2B, black line). The loss of the H-bond with N347 in the N1/09H1N1 is due to its smaller side chain relative to that of Y347 for the N1/04H5N1 (Fig. 2A). This notion is supported by the distribution plots of the H-bond distances (Fig. 2C), in which the maxima of the two peaks were found at 2.8 and 5.3 Å for N1/09H1N1 and N1/04H5N1, respectively. Note that the significance of Y347 was reported in a previous study on oseltamivir-resistance in the N1/ 04H5N1 isolate as being due to the N294S mutation, which was found to increase the O1(OTV)-OH(374) H-bond distance by \sim 0.5 Å, i.e., the occupation percentage of this H-bond was relatively decreased [14].

Interestingly, the residues within a spherical radius of 5 Å around the oseltamivir of the new strain are completely identical to those of group-2 NA subtype N9 as shown in Fig. 3. In addition, oseltamivir was designed to fit to the cavity of this NA group. Superimposition of the snapshots of both the OTV-N1/04H5N1 and the OTV-N1/09H1N1 systems with the crystal structure of oseltamivir bound to N9 (2QWK.PDB) are consistent with the above statement. The guanidinium group of R118 in the N1/09H1N1 and N9 structures approaches significantly closer to stabi-

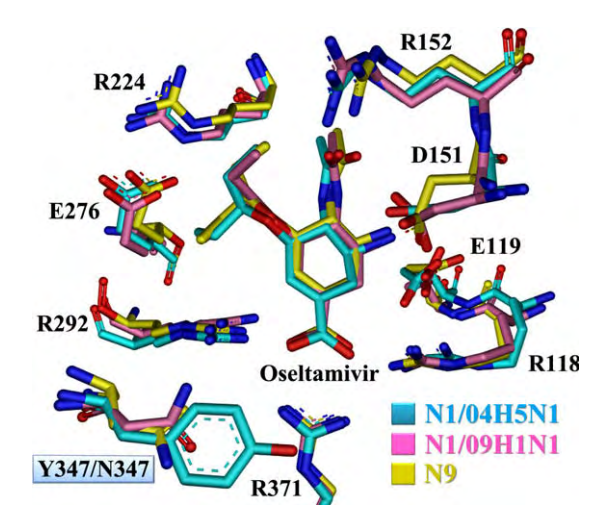


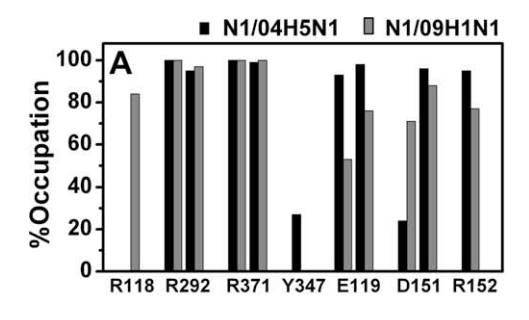
Fig. 3. Superimposition between the MD snapshots of OTV-N1/04H5N1 (cyan) and OTV-N1/09H1N1 (pink), and the crystal structure of OTV-N9 (yellow), where the closed view of oseltamivir in the binding pocket was shown. (For interpretation of the references to colour in this figure legend, the reader is referred to the web version of this article.)

lize the -COO⁻ group of oseltamivir than that observed in the N1/04H5N1 complex. In contrast, the Y347 side chain of the N1/04H5N1 was, as expected, shown to locate much closer to oseltamivir than the other two systems.

2009 H1N1 influenza M2-protein resistance to adamantane derivatives

The susceptibility of the M2-channel of the 2009 H1N1 influenza (M2/09H1N1) to both amantadine and rimantadine is displayed in terms of water density along the channel (Fig. 1B). The results for both closed (OH) and open (3H) states, in comparison to those of the avian influenza H5N1 strain (M2/04H5N1) [9], are given in Fig. 4. To monitor how deep the amantadine and rimantadine molecules can penetrate into the M2-channel, the inhibitor distributions were also plotted in Fig. 4, in which the C^{α} positions of the four A30 and H37 residues were averaged and depicted as the reference. Note that in changing from the M2 channel of avian H5N1 to the new A (H1N1) influenza, three residues (V28, S31 and L43) were, respectively, replaced by I28, N31 and T43 (Fig. 1B). Amongst those changes, S31N is the most common mutation in the M2 protein which is known to confer adamantane-resistance [20-22] and, thus, the M2/09H1N1 resistance to both amantadine and rimantadine would be expected.

Considering all the inhibitor distributions (filled area), amantadine (dark grey) was found to locate deeper into the channel than



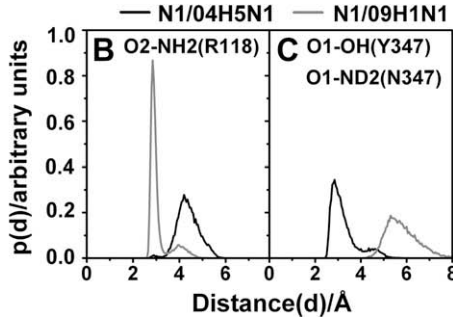


Fig. 2. (A) Percentage occupation of hydrogen bonding of oseltamivir and its binding residues (see Fig. 1A for labels). The distribution plots of the H-bond distances for the NA residues: (B) R118 and (C) Y347/N347.

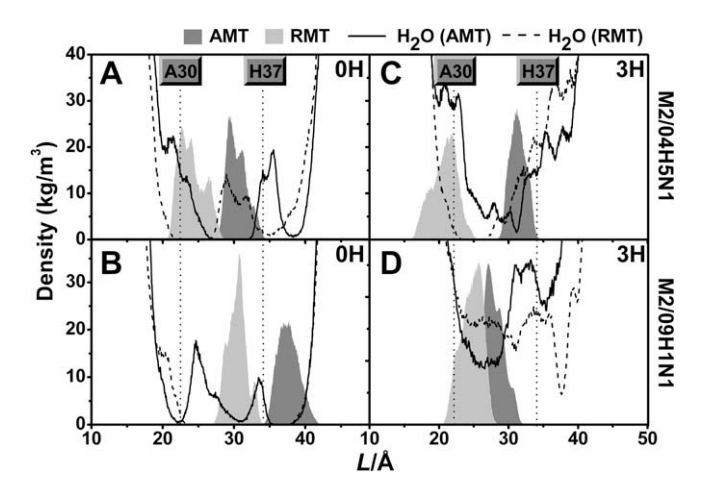


Fig. 4. Water density along the channel as a function of distance L starting from the extracellular site (see Fig. 1B for definition) for the new A (H1N1) M2 strain complexed with two inhibitors (amantadine (AMT) and rimantadine (RMT)) in the closed (0H) and open (3H) states. AMT and RMT distributions (filled area) were shaded by dark and light grey, whereas the vertical dashed lines represent the average C^{α} positions of the four A30 and H37 residues.

rimantadine (light grey). In the closed state (0H), zero-water density was observed for both M2 strains with the inhibitor bound (Fig. 4A and B), indicating that water cannot transport throughout the 0H channel. In addition, zero water density is not detected before the filled area in all the examined systems. This, as expected, reveals that in the M2 channel, water cannot move across inhibitor in the closed state.

Dramatic changes were found for the open state (3H), where only rimantadine can inhibit water transportation through the M2/04H5N1 (Fig. 4C, dashed line). For the AMT-M2/04H5N1 complex, an almost zero-water density was slightly observed at $L \sim 32$ Å, which is in contrast to what is observed in the new A (H1N1) M2 strain where both inhibitors totally lose their functions (Fig. 4D). In addition, the detected density along the M2/09H1N1 channel is greater than those of the singlet S31N and A30T mutations for the AMT-M2/04H5N1, in which the experimental resistance degree for these two mutations are 267- and 3300-fold, respectively [10]. Therefore, the only conclusion based on this data is that the M2/09H1N1 resistance to amantadine is likely to be higher than what was previously observed.

As the inhibitory potency depends on the drug-target interaction, the H-bond between the ammonium group of the inhibitor and the viral M2 residues was measured, and the data are summarized in Table 2. As can be seen, there are two binding regions of inhibitors to the channel: (i) the extracellular site at residues L26, A30 and S31; and (ii) the H37 selective filter. Due to the bulky hydrophobic unit, the two adamantanes were found to interact weakly with the M2/04H5N1 channel in both states, whilst they completely lost their binding in the 3H state of the new M2 strain. Disappearance of H-bonding of the inhibitor to the M2 channel is consistent with the observed loss of adamantane susceptibility in blocking the M2/09H1N1 channel that contains the S31N-drug resistance as well as the replacement of the other two residues at the positions 28 and 43.

In conclusion, the evidence above suggests that both adamantanes will have lost their inhibitory activities towards the M2-channel of the 2009 influenza A (H1N1) virus, mainly due to this virus containing the S31N mutation which is found, in general, to be the main source of adamantane drug resistance against all influenza subtypes [20–22]. This mutation was proposed to indirectly increase the M2-protein mobility [23], and thus the drugs were unable to bind the M2 channel and to block the proton transport in this new A (H1N1) influenza.

Table 2

H-bond occupation between the residues of the M2-channel and the two drugs, amantadine and rimantadine, where I-IV refers to the M2 homotetrameric bundles. The results are given for both closed (0H) and open (3H) states of the M2-channel of the A (H5N1) and the new A (H1N1) influenza viruses.

System	% H-bond	% H-bond				
	AMT-M2/ 04H5N1	RMT-M2/ 04H5N1	AMT-M2/ 09H1N1	RMT-M2/ 09H1N1		
(i) OH state						
A30-III H37-I H37-II H37-III H37-IV (ii) 3H state	- - - 56 29	12 - - -	- 13 - -	- 22 21 -		
L26-II S31-II S31-IV	- 20 -	9 - 10	- - -	- - -		

Conclusions

In the present study, homology modeling and MD simulations were applied on the commercially available drugs bound to the NA and M2-channel of the new influenza A (H1N1) virus. Based on the MD/LIE method, the predicted binding affinity of oseltamivir towards the new A (H1N1) influenza isolate was considerably higher than the avian H5N1 strain. Except for the absence of a weak H-bond with residue 347, all interactions of OTV-N1/ 09H1N1 complex were considerably conserved. Interestingly, oseltamivir was well oriented in the binding pocket and its -COOgroup interacted strongly with the arginine triad, similar to that found in the crystal structure of N9. For M2/09H1N1 channels with two adamantanes bound, water transport explicitly passed throughout the channel of the 3H state, representing the activated channel at a low pH. Either amantadine or rimantadine have totally lost the H-bond interactions with the M2 residues in this state, which results from the M2 transmembrane domain containing the S31N mutation as well as other two residues. I28 at the extracellular site and T43 close to the W41 gating residue, which differs from the avian H5N1. Overall, the simulated results have clearly explained at a molecular level how anti-influenza drugs can either potently inhibit (oseltamivir) or not (amantadine and rimantadine) the new A (H1N1) influenza virus.

Acknowledgments

This work was supported by the Thailand Research Fund. T.R. and P.I. thank the Post-Doctoral Program from the Commission on Higher Education. T.R. also thank TRF Grant for New Research from the Thailand Research Fund. We thank the Computational Chemistry Unit Cell, Chulalongkorn University, for computing facilities and The National Nanotechnology Center (NANOTEC; NSTDA) for the use of the Discovery Studio.

Appendix A. Supplementary data

Supplementary data associated with this article can be found, in the online version, at doi:10.1016/j.bbrc.2009.05.066.

References

- [1] WHO, Epidemic and Pandemic Alert and Response (EPR). Available from: http://www.who.int/csr/don/2009_05_13/en/index.html, (accessed May 2009).
- [2] Emedicine. Available from: http://emedicine.medscape.com/article/1673658-overview, (accessed May 2009).

- [3] WHO, Media centre. Influenza A(H1N1). Available from: http://www.who.int/mediacentre/news/statements/2009/h1n1_20090429/en/index.html, (accessed May 2009).
- [4] E. De Clercq, Antiviral agents active against influenza A virus, Nat. Rev. Drug Discov. 5 (2006) 1015–1025.
- [5] CDC, Antiviral Drugs and H1N1 Flu (Swine Flu). Available from: http://www.cdc.gov/h1n1flu/antiviral.htm, (accessed May 2009).
- [6] O. Aruksakunwong, M. Malaisree, P. Decha, P. Sompornpisut, V. Parasuk, S. Pianwanit, S. Hannongbua, On the lower susceptibility of oseltamivir to influenza neuraminidase subtype N1 than those in N2 and N9, Biophys. J. 92 (2007) 798–807.
- [7] M. Malaisree, T. Rungrotmongkol, P. Decha, P. Intharathep, O. Aruksakunwong, S. Hannongbua, Understanding of known drug-target interactions in the catalytic pocket of neuraminidase subtype N1, Proteins 71 (2008) 1908–1918.
- [8] M. Malaisree, T. Rungrotmongkol, N. Nunthaboot, O. Aruksakunwong, P. Intharathep, P. Decha, P. Sompornpisut, S. Hannongbua, Source of oseltamivir resistance in avian influenza H5N1 virus with the H274Y mutation, Amino Acids (2009), doi:10.1007/s00726-008-0201-z.
- [9] P. Intharathep, C. Laohpongspaisan, T. Rungrotmongkol, A. Loisruangsin, M. Malaisree, P. Decha, O. Aruksakunwong, K. Chuenpennit, N. Kaiyawet, P. Sompornpisut, S. Pianwanit, S. Hannongbua, How amantadine and rimantadine inhibit proton transport in the M2 protein channel, J. Mol. Graph. Model. 27 (2008) 342–348.
- [10] C. Laohpongspaisan, T. Rungrotmongkol, P. Intharathep, M. Malaisree, P. Decha, O. Aruksakunwong, P. Sompornpisut, S. Hannongbua, Why amantadine loses its function in influenza M2 mutants: MD simulations, J. Chem. Inf. Model. 49 (2009) 847–852.
- [11] R.J. Russell, L.F. Haire, D. Stevens, P.J. Collins, Y.P. Lin, G.M. Blackburn, A.J. Hay, S.J. Gamblin, J.J. Skehel, The structure of H5N1 avian influenza neuraminidase suggests new opportunities for drug design, Nature 443 (2006) 45–49
- [12] J. Hu, T. Asbury, S. Achuthan, C. Li, R. Bertram, J.R. Quine, R. Fu, T.A. Cross, Backbone structure of the amantadine-blocked trans-membrane domain M2 proton channel from influenza A virus, Biophys. J. 92 (2007) 4335– 4343

- [13] G.M. Morris, D.S. Goodsell, R.S. Halliday, R. Huey, W.E. Hart, R.K. Belew, A.J. Olson, Automated docking using a lamarckian genetic algorithm and an empirical binding free energy function, J. Comp. Chem. 19 (1998) 1639–1662.
- [14] T. Rungrotmongkol, T. Udommaneethanakit, M. Malaisree, N. Nunthaboot, P. Intharathep, P. Sompornpisut, S. Hannongbua, How does each substituent functional group of oseltamivir lose its activity against virulent H5N1 influenza mutants? (2009), Submitted for publication.
- [15] I.D. Wall, A.R. Leach, D.W. Salt, M.G. Ford, J.W. Essex, Binding constants of neuraminidase inhibitors: an investigation of the linear interaction energy method, J. Med. Chem. 42 (1999) 5142–5152.
- [16] P.J. Collins, L.F. Haire, Y.P. Lin, J. Liu, R.J. Russell, P.A. Walker, J.J. Skehel, S.R. Martin, A.J. Hay, S.J. Gamblin, Crystal structures of oseltamivir-resistant influenza virus neuraminidase mutants, Nature 453 (2008) 1258–1261.
- [17] Y. Abed, B. Nehmé, M. Baz, G. Boivin, Activity of the neuraminidase inhibitor A-315675 against oseltamivir-resistant influenza neuraminidases of N1 and N2, Antiviral Res. 77 (2008) 163–166.
- [18] G. Boivin, N. Goyette, Susceptibility of recent Canadian influenza A and B virus isolates to different neuraminidase inhibitors, Antiviral Res. 54 (2002) 143–147
- [19] V.P. Mishin, F.G. Hayden, L.V. Gubareva, Susceptibilities of antiviral-resistant influenza viruses to novel neuraminidase inhibitors, Antimicrob. Agents Chemother. 49 (2005) 4515–4520.
- [20] J.W. Tang, K.L.K. Ngai, J.C.L. Wong, W.Y. Lam, P.K.S. Chan, Emergence of adamantane-resistant influenza A (H3N2) viruses in Hong Kong between 1997 and 2006, J. Med. Virol. 80 (2008) 895–901.
- [21] R.A. Bright, D.K. Shay, B. Shu, N.J. Cox, A.I. Klimov, Adamantane resistance among influenza A viruses isolated early during the 2005–2006 influenza season in the United States, JAMA 295 (2006) 891–894.
- [22] L. Simonsen, C. Viboud, B.T. Grenfell, J. Dushoff, L. Jennings, M. Smit, C. Macken, M. Hata, J. Gog, M.A. Miller, E.C. Holmes, The genesis and spread of reassortment human influenza A/H3N2 viruses conferring adamantane resistance, Mol. Biol. Evol. 24 (2007) 1811–1820.
- [23] R.M. Pielak, J.R. Schnell, J.J. Chou, Mechanism of drug inhibition and drug resistance of influenza A M2 channel, Proc. Natl. Acad. Sci. USA 106 (2009) 7379–7844.

Author's personal copy

Biophysical Chemistry 145 (2009) 29-36



Contents lists available at ScienceDirect

Biophysical Chemistry

journal homepage: http://www.elsevier.com/locate/biophyschem



How does each substituent functional group of oseltamivir lose its activity against virulent H5N1 influenza mutants?

Thanyada Rungrotmongkol ^{a,b}, Thanyarat Udommaneethanakit ^c, Maturos Malaisree ^a, Nadtanet Nunthaboot ^d, Pathumwadee Intharathep ^a, Pornthep Sompornpisut ^a, Supot Hannongbua ^{a,e,*}

- ^a Computational Chemistry Unit Cell, Department of Chemistry, Faculty of Science, Chulalongkorn University, Bangkok 10330, Thailand
- ^b Center of Innovative Nanotechnology, Chulalongkorn University, Bangkok 10330, Thailand
- ^c Nanoscience and Technology Program, Graduate School, Chulalongkorn University, Bangkok 10330, Thailand
- ^d Department of Chemistry, Faculty of Science, Mahasarakham University, Mahasarakham 44150, Thailand
- ^e Center of Excellence for Petroleum, Petrochemicals, and Advanced Materials, Chulalongkorn University, Bangkok 10330, Thailand

ARTICLE INFO

Article history: Received 15 June 2009 Received in revised form 13 August 2009 Accepted 16 August 2009 Available online 22 August 2009

Keywords:
Oseltamivir resistance
H274Y
N294S
H5N1
Molecular dynamics simulations

ABSTRACT

To reveal the source of oseltamivir-resistance in influenza (A/H5N1) mutants, the drug-target interactions at each functional group were investigated using MD/LIE simulations. Oseltamivir in the H274Y mutation primarily loses the electrostatic and the vdW interaction energies at the $-NH_3^+$ and $-OCHEt_2$ moieties corresponding to the weakened hydrogen-bonds and changed distances to N1 residues. Differentially, the N294S mutation showed small changes of binding energies and intermolecular interactions. Interestingly, the presence of different conformations of E276 positioned between the $-OCHEt_2$ group and the mutated residue is likely to play an important role in oseltamivir-resistant identification. In the H274Y mutant, it moves towards the $-OCHEt_2$ group leading to a reduction in hydrophobicity and pocket size, whilst in the N294S mutant it acts as the hydrogen network center bridging with R224 and the mutated residue S294. The molecular details have answered a question of how the H274Y and N294S mutations confer the high- and medium-level of oseltamivir-resistance to H5N1.

© 2009 Elsevier B.V. All rights reserved.

1. Introduction

Resistance to the current influenza virus neuraminidase (NA) inhibitors is the major concern in the current treatment of patients infected with H5N1 viruses [1,2]. To date, several studies have been reported on the emergence of oseltamivir resistance, as reduced drug sensitivity, that have been associated with either the H274Y or the N294S mutations in NA subtype N1 [3–9]. Here, this study aims to understand how such mutations confer resistance to oseltamivir and is focused upon the binding affinity changes of its substituent functional groups relative to those of the wild-type strain.

Oseltamivir is the first orally active NA drug and was designed upon the transition state analog of the natural sialic acid substrate so as to inhibit the function of NA [10]. The hydroxyl and polar glycerol substitutions on the 6-membered ring of sialic acid (Fig. 1A) are replaced by amino and 3-pentyl ether groups, respectively, where the cyclohexene ring serves as oseltamivir's scaffold (Fig. 1B) [1,11].

E-mail address: supot.h@chula.ac.th (S. Hannongbua).

Currently, oseltamivir is widely stockpiled in many countries for a future treatment of any influenza pandemic [2,12]. The crystal structure of oseltamivir bound to the active site residues of the native N1 is shown in Fig. 1C (cyan) [13]. Its binding residues are composed of four zones: (i) the arginine triad (R118, R292 and R371) and Y347, (ii) R152, (iii) E119 and D151, and (iv) R224 and E276 interacting with the -COO⁻, -NHAc, -NH₃⁺, and -OCHEt₂ groups of oseltamivir, respectively. The hydrophobic pocket around the bulky -OCHEt₂ moiety of oseltamivir is formed by the rotation of the E276's carboxylate group to bind with the guanidinium group of R224.

Oseltamivir resistances of the H274Y and N294S mutations in H5N1 were experimentally reported as a 300–1700 [3–9] and 20–80-fold [2,9] reduction in the sensitivity, respectively, compared to the wild-type. Locations of these two mutated framework residues are adjacent to E276, a residue interacting with the most hydrophobic part (–OCHEt₂) of the inhibitor (Fig. 1C). On the basis of the crystallographic structure data, the H274Y and N294S mutations were proposed to prevent the movement of the side chain of E276 towards the guanidinium group of R224 [2,9] and so preventing the formation of the hydrophobic pocket for accommodating oseltamivir's bulky moiety. In contrast, our results obtained from molecular dynamics (MD) simulations of oseltamivir-resistant H274Y in H5N1 [14]

^{*} Corresponding author. Computational Chemistry Unit Cell, Department of Chemistry, Faculty of Science, Chulalongkorn University, Bangkok 10330, Thailand. Tel.: +66 22 187602; fax: +66 22 187603.

T. Rungrotmongkol et al. / Biophysical Chemistry 145 (2009) 29-36

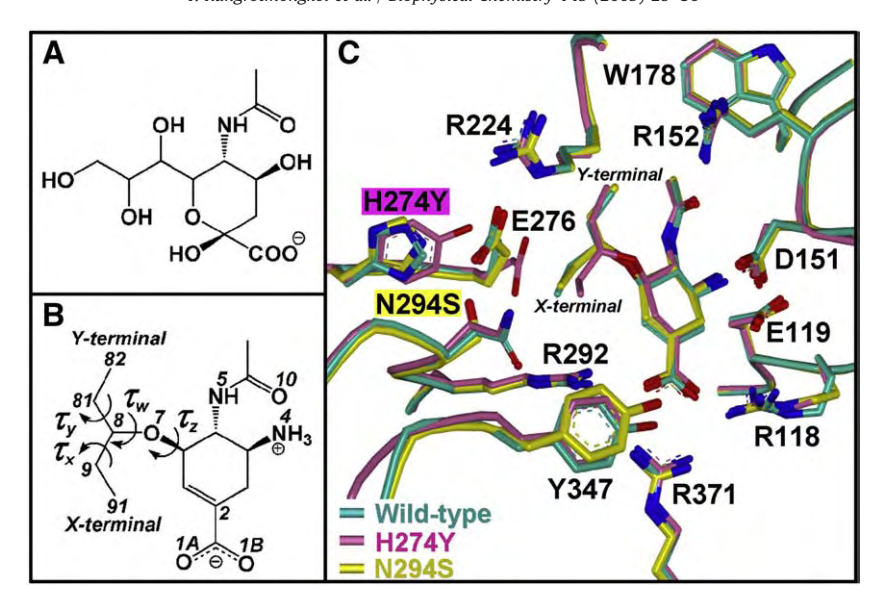


Fig. 1. Chemical structures of (A) sialic acid, and (B) oseltamivir's substituent functional groups: -COO⁻, -NH₃⁺, -NHAc and -OCHEt₂, showing the atomic numbering referred in the text. (C) The crystal structures of oseltamivir bound to the active site of native N1 (cyan), H274Y (pink) and N294S (yellow) mutants [2,13]. (For interpretation of the references to colour in this figure legend, the reader is referred to the web version of this article.)

suggest this mutation does not prevent the rotation of the E276 side chain. Instead, the source of the reduction of the hydrophobicity is due to the displacement of the E276's side chain towards the binding pocket, a notion which is well supported by the recent crystal structure of oseltamivir complexed with the H274Y mutant of H5N1 (pink in Fig. 1C) [2].

The present study has focused upon trying to understand the binding affinities of the four substituent functional groups ($-COO^-$, $-NH_3^+$, -NHAc and $-OCHEt_2$) of oseltamivir in the H274Y and N294S mutants relative to those in the wild-type. The crystallographic structures of oseltamivir complexed with the two mutants and the wild-type were examined using MD simulations in conjunction with the linear interaction energy method (LIE). Drug–target interactions were also extensively analyzed in terms of intermolecular hydrogen bonds and other specific protein-ligand distances.

2. Methods

2.1. Initial structure and system preparation

The X-ray structures of the wild-type, and the two mutant strains (H274Y and N294S), complexed with oseltamivir (OTV-N1) were obtained from the Protein Data Bank (PDB), entry codes: 2HU4 [13], 3CL0 and 3CL2 [2], respectively, and served as the starting coordinates for the three bound OTV-N1 systems: (1) OTV-WT, (2) OTV-H274Y and (3) OTV-N294S, respectively. Since crystal water molecules and Ca²⁺ ion are not present in the OTV-WT and OTV-N294S structures, they are, then, embedded into the simulated systems by superimposition with the apo-enzyme (2HTY) [13] where all water molecules which have their oxygen atoms lying within a 2.4–3.0 Å distance from the OTV-N1 heavy atoms were taken into account. Note, that the Ca²⁺ ion situated ~10 Å from the binding site is needed for the activity and stability of NA.

All calculations were performed using the Q-program package [15], version 5. The AMBER force field [16] was applied for proteins whilst the partial atomic charges and force field parameters of oseltamivir were taken from our previous calculations [17]. Each system of the OTV-N1 bound state was capped by a 25 Å sphere of TIP3P [18] water molecules centered on the C2 atom of oseltamivir (see Fig. 1B for atomic labels), and only water molecules where the oxygen was not within a 2.4 Å distance of any heavy atoms of the inhibitor and enzyme were retained. Within a 22 Å sphere of the

centered C2 atom, the ionization state of each amino acid with an electrically charged side chain was assigned using the PROPKA program [19]. The ionizable residues lying at 22–25 Å distances were neutralized, except for the pairs of charged residues which probably interact via hydrogen bonds. All ionizable residues positioned further than a 25 Å sphere from the center were treated as a neutral charge. After solvation, the net charge of the final system of the OTV-N1 bound state was +2 which was then neutralized by two Cl $^-$ ions. For the system with oseltamivir in the free state (OTV-SOL), the ligand was solvated by a 25 Å sphere of TIP3P water molecules centered on its C2 atom and counterions were added.

2.2. Molecular dynamics simulations

Spherical boundary molecular dynamics simulations of the four systems (OTV-WT, OTV-N274Y, OTV-N294S and OTV-SOL) were carried out under the surface constrained all atom solvent (SCAAS) model [20]. Harmonic constraints were treated to restrain all atoms further than 25 Å from the C2 center. Long-range electrostatic interactions were performed by the local reaction field (LRF) approximation, with a cut-off radius of 10 Å for the non-bonded interactions. To prevent the diffusion of ligand and counterions toward the edge of the simulation sphere, the position of the C2 atom of oseltamivir in the OTV-SOL system was restrained with a 100 kcal mol $^{-1}$ Å $^{-2}$ harmonic potential, whilst a 75 kcal mol $^{-1}$ Å $^{-2}$ flat-bottom harmonic potential, scaled from a maximum at 20.5 Å to zero at 21.5 Å from the center, was used to treat the counterions.

MD simulations of each system were set up as follows. Firstly, the positions of the water molecules were simulated, keeping all other atoms fixed to their initial positions, with the two periods of MD simulations at 5 K. Then, the whole structure was relaxed by four periods of MD simulations at 5 K and the system was heated from 5 K to 298 K in six 50 ps intervals with an increasing temperature of 50 K, and followed by equilibration phase at 298 K. Finally, four different starting structures obtained from the equilibration period were separately performed by 5-ns simulations at 298 K. The NVT ensemble was employed and the SHAKE algorithm [21] was used to constrain all bonds involving hydrogen with a simulation time step of 2 fs. Only the snapshots and energies taken from the production phase were used for the analysis.

2.3. Linear interaction energy (LIE) method

The linear interaction energy (LIE) method developed by Åqvist and co-workers [22,23] was used to calculate the binding free energies ($\Delta G_{\rm bind}$) of the oseltamivir bound to the NA wild-type and to the two mutant strains. This method is a linear response semi-empirical technique used to evaluate the free energy changes from the simulations of two states: (i) the solvated ligand (free state), and (ii) the ligand bound to the solvated protein (bound state). Based on the LIE method, the total binding free energy was contributed from van der Waals ($U^{\rm vdW}$) and electrostatic interaction energies ($U^{\rm elec}$) using the equation given below:

$$\Delta G_{bind} = \alpha \Big(< U^{vdW} >_{bound} - < U^{vdW} >_{free} \Big) + \beta \Big(< U^{elec} >_{bound} - < U^{elec} >_{free} \Big) + \gamma (1)$$

where α and β are empirical scaling coefficients for van der Waals and electrostatic interaction energies, respectively, and γ is a constant. LIE is critically susceptible to α and β coefficients not being transferrable between different systems and therefore the optimized values of these coefficients derived over the series of inhibitors targeting to the NA enzyme [24] were used to fit the LIE equation in the present study. This set of coefficients has previously been found to be the most predictive model for the NA system amongst the many developed models, with or without the addition of the hydration term.

3. Results and discussion

3.1. Predicted free energy of oseltamivir binding

The predicted energies of the oseltamivir bound to the H5N1 wild-type and two mutants, H274Y and N294S, evaluated from the LIE Eq. (1) with Essex' coefficients [24] are summarized in Table 1. The experimental determined energies for the N1 inhibitory potencies by oseltamivir converted from the most recently observed K_1 and IC_{50} values [2,25], are also given for comparison. In Table 1, the H274Y and N294S mutants were found to reduce the sensitivity to oseltamivir by 1.9 kcal mol $^{-1}$ (from -11.4 to -9.5 kcal mol $^{-1}$) and 0.5 kcal mol $^{-1}$ (from -11.4 to -10.9 kcal mol $^{-1}$), respectively. This is in good agreement with the ordering of the experimental binding energies of oseltamivir: wild-type (-13.1 or -12.1 kcal mol $^{-1}$) > N294S (-10.5 or -9.3 kcal mol $^{-1}$) > H274Y (-9.8 or -8.5 kcal mol $^{-1}$).

3.2. Binding free energy of each moiety of oseltamivir

To clarify how oseltamivir loses its binding affinity to the two virulent mutants relative to that of the wild-type H5N1 influenza, the

Table 1The experimental and predicted binding free energies (ΔG_{bind}) of oseltamivir to the wild-type (OTV-WT) and to the two mutants, OTV-H274Y and OTV-N294S, calculated using a MD/LIE approach with the coefficients proposed by Essex et al. [24].

System	Resistance	ΔG _{bind} [ka	$\Delta G_{\rm bind}$ [kcal mol ⁻¹]		
fold ^a	Experiments ^b	Essex $\alpha = 0.472$, $\beta = 0.122$, $\gamma = 2.603$ [24]			
OTV-WT	-	-13.1 (-12.1)	-11.4 ± 0.4		
OTV-H274Y	300-1700	-9.8(-8.5)	-9.5 ± 0.6		
OTV-N294S	20-100	-10.5(-9.3)	-10.9 ± 0.7		
rms ^c	-	_	0.8 (1.1)		

The means and standard derivations are derived from four separated 5 ns simulations.

binding free energies ($\Delta G_{\rm bind}$) contributed from the substituent functional groups ($-{\rm COO}^-$, $-{\rm NH}_3^+$, $-{\rm NHAc}$ and $-{\rm OCHEt}_2$) were computed using the LIE equation (Eq. (1)) with the two coefficients ($\alpha = 0.472$ and $\beta = 0.122$) taken from Essex's model [24]. The free energy differences ($\Delta \Delta G_{\rm bind}$) between the mutant and wild-type strains are simply defined by:

$$\Delta\Delta G_{bind} = \Delta G_{bind}[mutant] - \Delta G_{bind}[wild-type] \tag{2}$$

where $\Delta G_{\rm bind}[{\rm mutant}]$ and $\Delta G_{\rm bind}[{\rm wild-type}]$ denote the binding free energies of each moiety against the mutant and the wild-type, respectively. Therefore, positive and negative values of $\Delta \Delta G_{\rm bind}$ indicate that the selected moiety decreases and increases its binding affinity, respectively, to the mutation, relative to that of the wild-type. In addition, the changes of the average energy components, electrostatic and van der Waals interactions, in the bound states according to Eqs. (3a) and (3b) were evaluated, and are summarized in Table 3.

$$<\Delta\Delta U^{\text{elec}}>_{\text{bound}} = < U^{\text{elec}}>_{\text{bound}} [\text{mutant}] - < U^{\text{elec}}>_{\text{bound}} [\text{wild-type}]$$
(3a)

$$<\Delta\Delta U^{\text{vdW}}>_{\text{bound}} = < U^{\text{vdW}}>_{\text{bound}} [\text{mutant}] - < U^{\text{vdW}}>_{\text{bound}} [\text{wild-type}].$$
(3b)

In Table 2, the contributions of individual functional group of oseltamivir to the absolute binding free energy of the wild-type complex are in the following order: -OCHEt₂~-COO⁻>-NH₃⁺~-NHAc with corresponding values of -4.5, -4.1, -2.8 and -2.6 kcal mol⁻¹, respectively. The high-level resistance to oseltamivir seen in the H274Y mutant (OTV-H274Y), is correlated with the decreases in the electrostatic (9.1 kcal mol⁻¹ in Table 3A) and van der Waals (1.6 kcal mol⁻¹ in Table 3B) interactions. It is particularly noticeable that the -NH₃⁺ and -OCHEt₂ moieties provided a much lower contribution to the intermolecular interactions between oseltamivir and the N1 enzyme, with a reduction of the binding free energies ($\Delta\Delta G_{\text{bind}}$ in Table 2) of 1.1 and 0.8 kcal mol⁻¹ towards the H274Y mutant. As expected, the main contribution to the loss of the -NH₃⁺ binding is due to the 5.5 kcal mol⁻¹ reduced electrostatic interaction energy (Table 3A), whilst the loss of binding for the -OCHEt2 moiety is due to the 1.6 kcal mol⁻¹ lowered van der Waals interaction energy (Table 3B). By contrast, the -COO⁻ and -NHAc groups of oseltamivir were shown to have only a small effect on the H274Y mutation, with slightly changed binding affinities to this strain ($\Delta\Delta G_{\text{bind}}$ in Table 2).

The oseltamivir-resistant N294S mutation shows a small change in the binding affinities of all four assayed functional groups of oseltamivir, 0.1–0.3 kcal mol $^{-1}$ ($\Delta\Delta G_{\text{bind}}$ in Table 2), relative to those of wild-type. This is different from what was observed in the H274Y mutation, where a decrease in the electrostatic contribution of

Table 2 Binding free energies ($\Delta G_{\rm bind}$) of the four substituent functional groups of oseltamivir (see Fig. 1B for defined partition) based on the LIE equation with Essex' coefficients (α =0.472 and β =0.122) [24], where $\Delta \Delta G_{\rm bind}$ was defined in Eq. (2).

System	$\Delta G_{\rm bind}$ [kcal mol ⁻¹]			
	-COO-	-NH ₃ +	-NHAc	-OCHEt ₂
OTV-WT OTV-H274Y OTV-N294S	-4.1 ± 0.3 -4.0 ± 0.5 -4.0 ± 0.4	-2.8 ± 0.1 -1.7 ± 0.2 -2.6 ± 0.3	-2.6 ± 0.1 -2.8 ± 0.3 -2.7 ± 0.3	-4.5 ± 0.4 -3.7 ± 0.7 -4.2 ± 0.7
		$\Delta\Delta G_{\rm bind}$ [k	cal mol ⁻¹]	
OTV-H274Y OTV-N294S	0.1 ± 0.8 0.1 ± 0.7	1.1 ± 0.3 0.2 ± 0.4	-0.2 ± 0.4 -0.1 ± 0.4	0.8 ± 1.1 0.3 ± 1.1

Means and standard deviation values were derived from four separated 5 ns simulations.

^a Values taken from references [2–9,25].

^b Experimental binding energies were calculated from the K_1 inhibitory constants [2] and IC_{50} values [25] (the latter shown in parenthesis).

^c The *rms* derivations were evaluated from the calculated $\Delta G_{\rm bind}$ energies with respect to the experimental $\Delta G_{\rm bind}$ energies derived from the $K_{\rm l}$ and $IC_{\rm 50}$ values (the latter shown in parenthesis).

Table 3Electrostatic and van der Waals interaction energy differences for oseltamivir and its moieties in the bound states of mutant and wild-type strains, as defined in Eqs. (3a) and (3b).

System	$<\Delta\Delta U^{\rm elec}>_{\rm bound}$ [kcal mol ⁻¹]							
	Oseltamivir	-coo-	-NH ₃ +	-NHAc	-OCHEt ₂			
(A) Electrostatic interactions								
OTV-H274Y	9.1 ± 0.3	1.9 ± 0.8	5.5 ± 0.5	1.0 ± 0.4	0.7 ± 0.8			
OTV-N294S	4.6 ± 0.7	3.4 ± 0.4	0.7 ± 0.6	-0.1 ± 0.4	0.5 ± 0.7			
System		$<\Delta\Delta U^{\text{vdW}}>_{\text{bound}} [\text{kcal mol}^{-1}]$						
	Oseltamivir	-C00 ⁻	$-NH_3^+$	-NHAc	-OCHEt ₂			
(B) Van der Waals interactions								
OTV-H274Y	1.6 ± 0.4	-0.3 ± 0.1	1.0 ± 0.2	-0.7 ± 0.2	1.6 ± 0.4			
OTV-N294S	-0.2 ± 0.4	-0.8 ± 0.1	0.3 ± 0.2	-0.1 ± 0.2	0.4 ± 0.4			

Means and standard deviation values were derived from four separated 5 ns simulations.

4.6 kcal mol⁻¹ (Table 3A) was found to potentially play a role in the loss of oseltamivir binding to the N294S mutation.

3.3. Loss of ligand-protein interactions

3.3.1. Around the hydrophilic side chains of oseltamivir

To monitor electrostatic intermolecular attractions, in terms of hydrogen bonds between oseltamivir and NA residues, the following two criteria were applied: (i) the distance between proton donor (D) and acceptor (A) atoms was less than or equal to 3.5 Å and (ii) the D–H..A angle was greater than or equal to 120°. The distribution plots of the D..A distance of the three simulated systems, OTV-WT, OTV-H274Y and OTV-N294S, where hydrogen bonds lay within the above criteria, are compared and shown in Fig. 2.

The intermolecular distances between the -COO⁻ group of oseltamivir (O1A and O1B, Fig. 1B), and the N1 binding residues, are shown in Fig. 2A–E. The strong hydrogen bonding interactions with the guanidinium group of the two conserved arginines (R292 and R371) are detected in all complexes and exhibit a sharp and narrow peak centered at ~2.8 Å (Fig. 2A–D). In addition, a moderate hydrogen bond with the –OH moiety of Y347, O1A...OH(Y347), was also shown in the three simulated systems by a lower and broader peak (Fig. 2E) compared to those in Fig. 2A–D. Interestingly, the peak position for the OTV-N294S was shifted by ~0.5 Å (dashed line in Fig. 2E), indicating a weakened interaction of O1A...OH(Y347) in the N294S mutation.

These results are well supported by the 3.4 kcal mol⁻¹ loss of electrostatic stabilization at the -COO⁻ group in OTV-N294S, whilst in OTV-H274Y a reduced energy of only 1.9 kcal mol⁻¹ has been reported (Table 3A). Similar to our previous studies [14,17] in all N1 strains, the -COO⁻ group of oseltamivir totally loses its interactions with the R118 residue of the arginine triad, yet this interaction is strongly detected in neuraminidase subtypes N2 and N9 [11,26,27].

A plot of the hydrogen bond distances with N4-nitrogen on the -NH₃⁺ group of oseltamivir (defined in Fig. 1B) is shown in Fig. 2F-I. In the OTV-WT and OTV-N294S, this positively charged group was well stabilized by the two -COO⁻ groups of E119 and D151 via the strong (a sharp peak at ~3 Å in Fig. 2F and G) and moderate (the first peak at ~2.8 Å in Fig. 2H and I) hydrogen bonding interactions. This is different from OTV-H274Y where the N4...OE1(E119) and N4...OD2 (D151) distances (Fig. 2F and I) were significantly changed, i.e., the former distance was lengthened by 0.7 Å while the latter one was split into two peaks. The weakened hydrogen bonding interactions from E119 and D151 to the -NH₃⁺ moiety of oseltamivir in OTV-H274Y, with respect to the wild-type strain, contributed a dramatic decrease in the electrostatic interaction energy of 5.5 kcal mol^{-1} (Table 3A). The other hydrogen bond detected was between the -NHAc group of oseltamivir and the guanidinium group of R152, O10...NH2(R152), as shown in Fig. 2J. Similar to the observation on the -NH₃ group, OTV-WT and OTV-N294S exhibit a very sharp peak at 2.8 Å indicating a stable and strong hydrogen bond, whilst this bond is slightly weakened in OTV-H274Y with the presence of another preferential distance at \sim 4.9 Å. This possibly leads to a 1.0 kcal mol $^{-1}$ reduction of the NHAc electrostatic interaction energy in OTV-H274Y (Table 3A). With the intermolecular distances between the N1 binding residues and these two groups of oseltamivir being maintained in the N294S system, the electrostatic interaction energies were considerably similar to those obtained from the wild-type.

3.3.2. Around the hydrophobic side chain of oseltamivir

Besides hydrogen bonds, hydrophobic interactions that are likely to be responsible for accommodating the bulky –OCHEt₂ moiety of oseltamivir (Fig. 1C) were also considered. To investigate how the mutations at positions 274 (H274Y) and 294 (N294S) positioned next to E276 may affect the binding of oseltamivir, the interatomic distances between the –OCHEt₂ group and its surrounding residues, E276 and R224, and the additional residue Y347, were measured and plotted (Fig. 3), where their structural alignment of the four last snapshots taken from the 5-ns MD simulations is shown in Fig. 4.

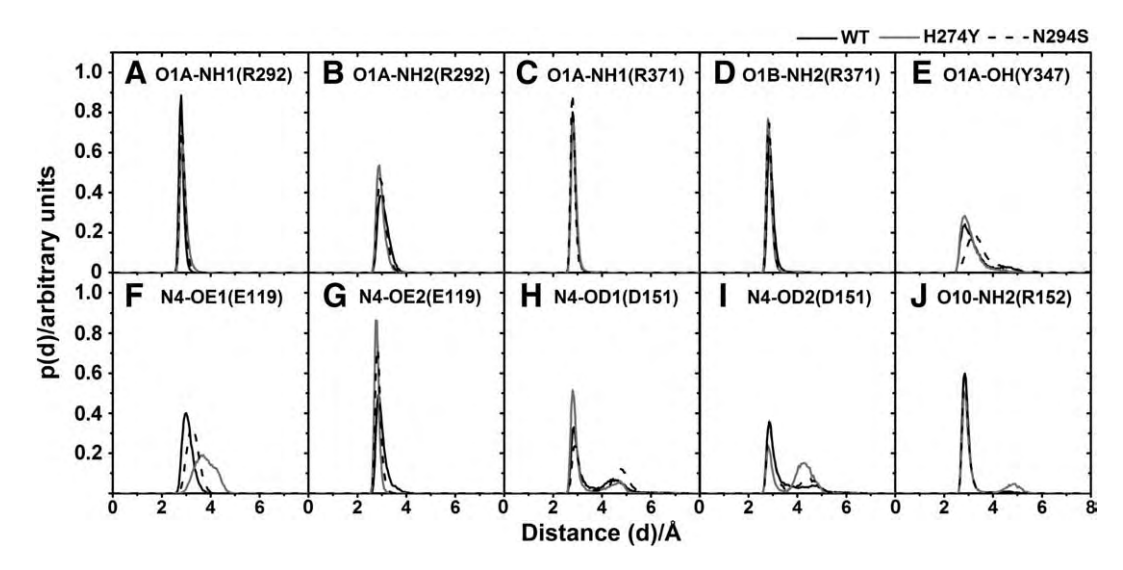


Fig. 2. The probability distributions of hydrogen bond distance between two heavy atoms of oseltamivir and its binding residues (see Fig. 1B and C for labels).

T. Rungrotmongkol et al. / Biophysical Chemistry 145 (2009) 29-36

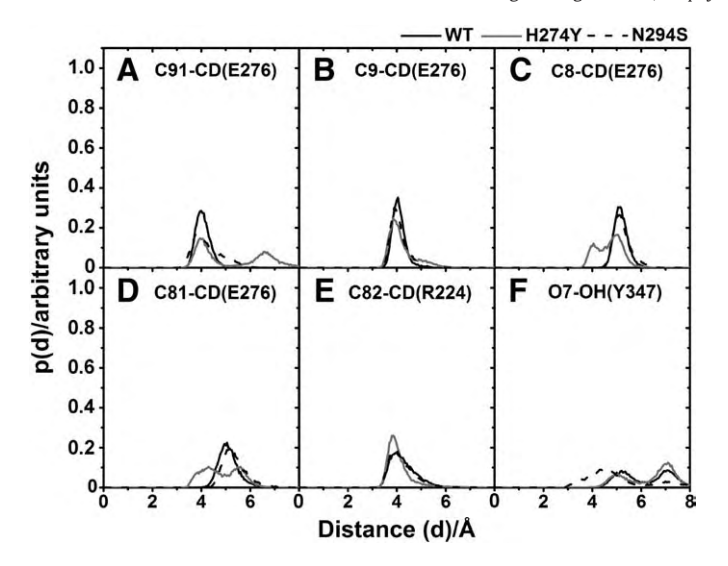


Fig. 3. The probability distributions of the distance between two specific atoms of the X- and Y-terminal of oseltamivir and the binding residues at the hydrophobic pocket (see Fig. 1B and C for labels).

The characteristics of the hydrophobic interactions between the oseltamivir's bulky group and its surrounding residues, where the peak maxima appear to be not shorter than 3 Å, were clearly displayed by the distribution plots of intermolecular distances (Fig. 3). All distance distributions involving E276 and R224 (Fig. 3A-E) in the wild-type complex show only one preferential peak. Two dramatic structural changes in the OTV-H274Y mutation complex, compared to the wild-type, were found as follows. (i) The phenol ring of Y274 repels the -COO⁻ group of E276 towards one end (X-terminal) of the diethyl moiety of oseltamivir (see Figs. 1C and 4, and details in the next section), resulting in a remarkable flexibility of the -OCHEt2 group which can be seen by the splitting of the C91-CD(E276) distance to form another peak at ~6.5 Å (Fig. 3A), and the broadening of the C9-CD(E276) peak to establish a long tail peak (Fig. 3B). (ii) A rearranged side chain of the E276 residue was observed to be more proximal to another diethyl moiety, the Y-terminal (see Figs. 1C and 4), with respect to that seen in the wild-type complex, as witnessed by the formation of the first peak of the C8-CD(E276) and C81-CD(E276) distances centered at ~4 Å (Fig. 3C and D). Consequently, such close contact possibly induces the rigidity of the probability plot of the distance between the Y-terminal and R224, leading to a sharper and narrower peak in the OTV-H274Y than in the other systems (Fig. 3F). The combined information, (i) and (ii), implied that the size of the hydrophobic pocket for the bulky group of oseltamivir was markedly reduced in the OTV-H274Y complex, which is in good agreement with the 1.6 kcal mol⁻¹ lowered van der Waal interaction energy of the –OCHEt₂ group (Table 3B).

For the OTV-N294S complex, the smaller residue substitution on N294 by serine directly leads to an enlargement of the hydrophobic pocket around the X-terminal (Fig. 1C), and thus allows the Y347 phenyl ring to move freely and approach closer to the bulky oseltamivir group. This can be clearly seen by the high flexibility of the Y347 phenyl ring which moves to partially occupy the enlarged hydrophobic pocket (Fig. 4B), and by the significant decrease of the distance between the O7-ester oxygen of the inhibitor and the OH-hydroxyl oxygen of the Y347 phenyl ring in the OTV-N294S complex (Fig. 3F), compared to that of wild-type. A slightly reduced hydrophobic interaction (van der Waals interaction energy) with the – OCHEt₂ group (0.4 kcal mol⁻¹ given in Table 3B) is, therefore, a consequence of the N294S mutation.

In summary, the loss of the ligand–protein binding energies and intermolecular interactions in the NA subtype N1 H274Y and N294S mutations, is in good agreement with the observed high- and moderate-level of resistance to oseltamivir, respectively [2–9,25].

3.4. Conformational changes of the binding pocket due to mutations

To provide detailed information on the conformational changes of the binding pocket due to the mutations, the distributions of the torsional angle of the side chains of the two mutated residues ($\tau_{\rm H274Y}$ and $\tau_{\rm N294S}$) and their neighborhoods ($\tau_{\rm E276}$ and $\tau_{\rm R224}$), as well as the bulky –OCHEt₂ moiety of oseltamivir (τ_W , τ_X , τ_Y and τ_Z , see Fig. 1B for definition), were plotted (Fig. 5). The torsional angles were defined by a set of four atoms. To monitor the interaction changes between the two N1 residues, E276 and R224, as a result of the side chain rotations, hydrogen bond distances from the carboxylate group of E276 to the guanidinium group of R224 (which is known to determine the hydrophobic-pocket formation) and to the side chain of N294S were measured and the results are thus summarized and shown in Figs. 6 and 7.

In Fig. 5, the H274Y mutation cannot prevent the E276-R224 hydrogen bonding interactions or the hydrophobic-pocket formation, in contrast to the proposed mechanism of oseltamivir resistance caused by the H274Y mutation [2,9,28,29]. The primary source of resistance is more likely to be due to the reduction of the hydrophobicity and size of the hydrophobic pocket around the –OCHEt2 side chain. Detailed information on the torsional angle changes (Fig. 5), is summarized as follows. The H274Y mutation confers a significant change in the side-chain torsional angle of the mutated residue 274, $\tau_{\rm H274Y}$, from a tilted peak dominantly found at -106° in the wild-type to a very sharp peak at -86° in the mutant (Fig. 5A). This rotation, as well as an increase in

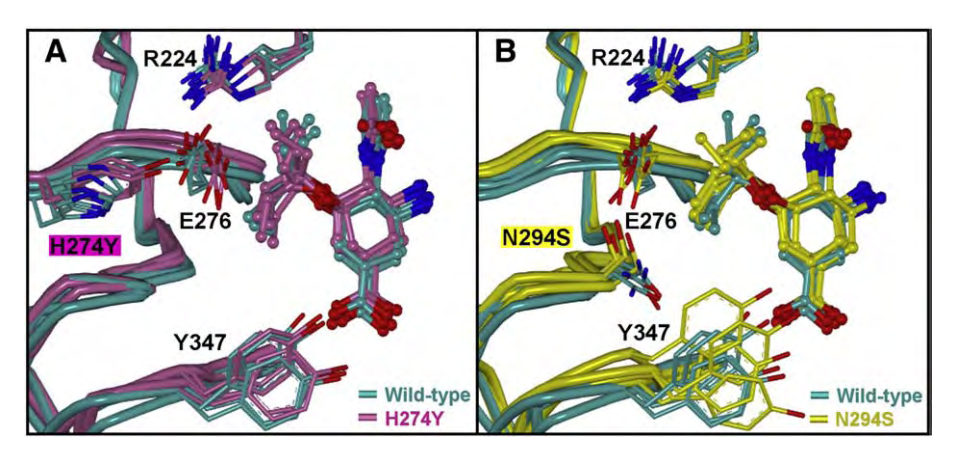


Fig. 4. Structural alignment between the four last snapshots of the 5-ns MD simulations of (A) OTV-WT and OTV-H274Y, and (B) OTV-WT and OTV-N294S. Closed view of oseltamivir, the two residues, E276 and R224, which mainly form the hydrophobic pocket around the bulky –OCHEt₂ group of oseltamivir, the mutated residues (H274Y and N294S) and Y347, are displayed.

T. Rungrotmongkol et al. / Biophysical Chemistry 145 (2009) 29-36

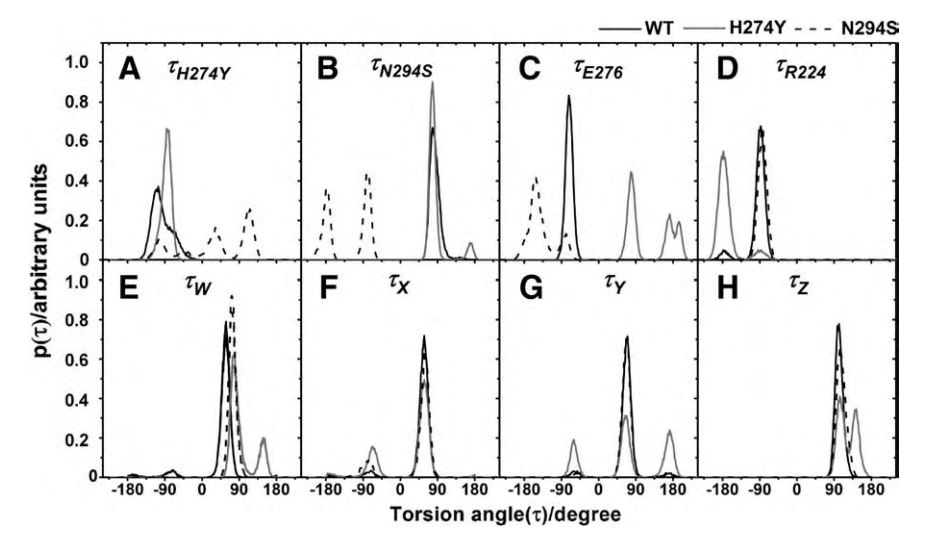


Fig. 5. Distribution plots of the torsional angle of the bulky -OCHEt₂ group of oseltamivir, and the side chains of two mutated residues (H274Y and N294S) and two neighboring residues (E276 and R224). See Fig. 1C for definitions.

the bulkiness of the tyrosine's phenol ring, leads to a large conformational rearrangement of the nearby residue E276 (see Fig. 1C for the initial structure and Fig. 4A for the last MD snapshots). The $\tau_{\rm E276}$ observed in the H274Y system was noticeably split and shifted from a narrow and sharp peak at -80° for the wild-type, into two peaks at 70° and 180° (Fig. 5C). This accordingly causes the rearrangement of the R224 side-chain orientation, where $\tau_{\rm R224}$ was found to consequently rotate by 90° (Fig. 5D) to maintain its hydrogen bonding interactions with the E276 carboxylate group, *i.e.*, the two strongly formed hydrogen bonds indicated by a sharp peak of NE(R224)-OE1(E276) and NH1 (R224)-OE2(E276) at ca. 2.8 Å distance in Fig. 6A and D, respectively. These hydrogen bonds (Fig. 7B) comparable with those found in the

wild-type (Fig. 7A) are in contrast to their crystal structures in which only one carboxylate oxygen (OE1) of E276 interacts with the guanidinium group of R224 (see Fig. 1C). As mentioned above, the rotations of $\tau_{\rm E276}$ and $\tau_{\rm R224}$ towards the inhibitor drastically reduce the hydrophobicity and size of the pocket which accommodates the bulky group of oseltamivir (see Figs. 3A–E and 4A). This is the main reason why the oseltamivir's bulky moiety cannot fit well into the hydrophobic pocket of the H274Y mutant, a notion which is also supported by the high flexibility of the four torsional angles of the particular moiety (τ_W , τ_X , τ_Y and τ_Z , Fig. 5E–H). The results are in good agreement with the previous study on the H274Y N1 mutant [30] where the Y274 phenol ring was found to push the E276 carboxylate group toward the bulky

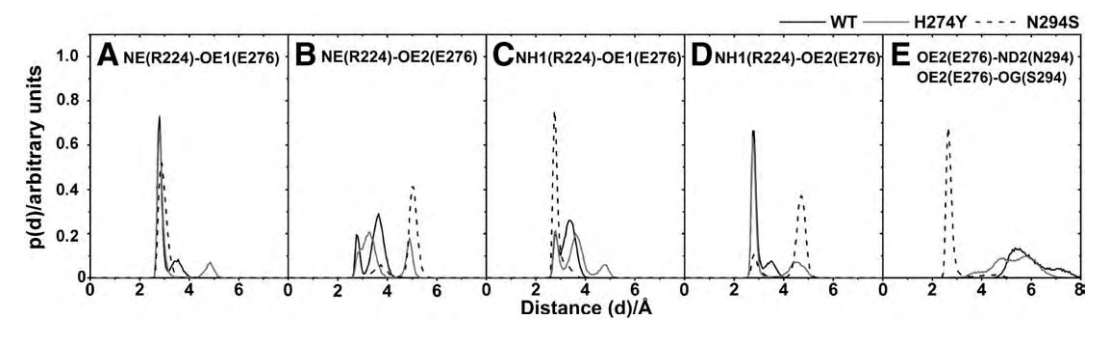


Fig. 6. Distribution plot of the hydrogen bond length of R224-E276 and E276-N294S pairs.

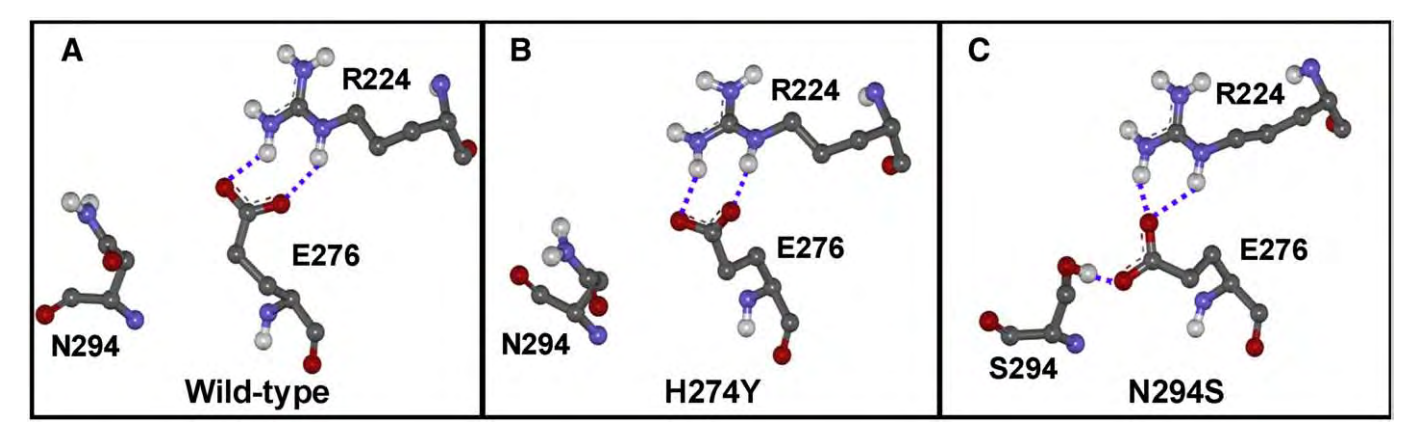


Fig. 7. Hydrogen bonds with E276 in the three simulated systems: (A) OTV-WT, (B) OTV-H274Y, and (C) OTV-N294S.

group of inhibitor; however, the hydrogen bonds between E276 and R224 were not observed.

The remarkable changes in the OTV-N294S complex were originated by the side chain rotation of the mutated residue 294 ($au_{\rm N294S}$) shifting from 78° in the wild-type to form the two preferential conformations at -80° and -180° . This leads accordingly to the primary source of oseltamivir resistance in the N294S mutated N1 strain, in contrast to that observed for the oseltamivir-resistant H274Y mutant. The N294S rotation induces the E276 side chain ($\tau_{\rm E276}$) to turn around in the opposite way (-78° and -152° , Fig. 5C), in comparison to that of the H274Y mutant (78° and ~180°), forming a strong hydrogen bond between the OE2-carboxylate oxygen of E276 and the OGhydroxyl oxygen of the mutated residue S294, as indicated by the intensely sharp peak at ~3 Å in Fig. 6E, which is not detected in either the N1 wild-type or the H274Y mutant. Thus, the E276-S294 hydrogen bond formation largely prevents the side chain rotation of E276 and the strong interaction with R224 which is normally stabilized by the presence of two strong hydrogen bonds (Fig. 6A and D). In other words, only the remaining carboxylate oxygen of E276 (OE1) in the N294S system is able to form the interactions with the NE- and NH1guanidinium nitrogens of R224 (Fig. 6A and C as well as Fig. 7C) agreeing well with the crystallographic structure (yellow in Fig. 1C). This is different from the simulations of the N294S N1 mutant [30] where the two hydrogen bonds formed between E276 and R224 were not changed (from wild-type) by the N294S mutation. Although the H274 side chain seemed to be able to rotate freely leading to the three preferential conformations at -104° , 32° and 110° (Fig. 5A), it did not interfere with the hydrophobic pocket which was constantly constructed by the hydrogen bond network around the center residue E276. Instead, the Y347 phenyl ring sometimes partially occupied the pocket (discussed above) and was also found in the crystal structure (Fig. 1C). Again, in contradiction with that observed for the high-level oseltamivir-resistant H274Y strain, the N294S mutation does not influence the conformations of the R224 side chain and -OCHEt2 group. This statement was supported by the insignificant changes in their torsional angles (τ_{R224} , τ_W , τ_X , τ_Y and τ_Z in Fig. 5C and E–H), in comparison to those of wild-type. These results lead us to conclude that the hydrophobicity and size of the hydrophobic pocket were not disturbed by the N294S mutation.

4. Conclusion

In the present study, multiple MD simulations in combination with the LIE method were applied on the wild-type and the oseltamivirresistant, H274Y and N294S, strains of avian influenza neuraminidase subtype N1. Based on the LIE model derived with Essex coefficients, the predicted inhibitory potencies of oseltamivir against all N1 strains are in good agreement with the experimental observed values. With respect to the OTV-WT complex, the -NH₃⁺ and -OCHEt₂ moieties of oseltamivir dominantly lose their interactions with the H274Y mutated strain by a significantly decreased contribution of the electrostatic and the van der Waals interaction energies, respectively, attributed to the absolute binding energy of OTV-H274Y complex. Loss of interactions at these two moieties accordingly corresponded to the weakened hydrogen bond interactions and changed intermolecular distances with their neighboring residues. In contrast, the N294S mutation showed a slight change in the binding affinities of all of the functional groups of oseltamivir, and most intermolecular interactions with the N1 binding residues were likely to be maintained, except for the -COO⁻ group with a slightly reduced hydrogen bond interaction to Y347.

The likely source of oseltamivir resistance resulting from the single mutation at the two residues positioned close to its bulky group primarily comes from different reasons. Decreases in hydrophobicity and pocket size due to the E276 rotation towards this group, where two hydrogen bonds between E276 and R224 were strongly

maintained, were found in the high-level resistance to oseltamivir in the H274Y mutation. In contrast, the N294S mutation caused the E276 rotation in the opposite direction, to become the centre of the hydrogen network interacting with R224 and the mutated residue S294 which has no direct effect to the oseltamivir bulky group. The above results suggested us to propose that the potent inhibitors against the oseltamivir-resistant strains could contain the hydrophilic group, instead of the oseltamivir bulky moiety, in order to maintain the hydrogen bond interactions with the shifted E276 carboxylate sidechain in H274Y. This hydrophilic group with a longer sidechain is needed to occupy the newly formed space due to the N294S mutation.

Acknowledgements

This work was supported by The Thailand Research Fund (TRF). T.R. thanks the Post-Doctoral Program from the Commission on Higher Education and the funding for New Research (Grant No. TRG5280035) from TRF. P.S. gratefully acknowledges the support from the Emerging Diseases and Bio-Warfare project, the Center of Excellence in Clinical Virology, Chulalongkorn University. We also thank The National Center for National Nanotechnology Center for the use of the Discovery Studio.

References

- O. Ferraris, B. Lina, Mutations of neuraminidase implicated in neuraminidase inhibitors resistance, J. Clin. Virol. 41 (2008) 13–19.
- [2] P.J. Collins, L.F. Haire, Y.P. Lin, J. Liu, R.J. Russell, P.A. Walker, J.J. Skehel, S.R. Martin, A.J. Hay, S.J. Gamblin, Crystal structures of oseltamivir-resistant influenza virus neuraminidase mutants, Nature 453 (2008) 1258–1261.
- [3] J.A. Ives, J.A. Carr, D.B. Mendel, C.Y. Tai, R. Lambkin, L. Kelly, J.S. Oxford, F.G. Hayden, N.A. Roberts, The H274Y mutation in the influenza A/H1N1 neuraminidase active site following oseltamivir phosphate treatment leave virus severely compromised both in vitro and in vivo, Antivir. Res. 55 (2002) 307–317.
- [4] M.Z. Wang, C.Y. Tai, D.B. Mendel, Mechanism by which mutations at His274 alter sensitivity of influenza A virus N1 neuraminidase to oseltamivir carboxylate and zanamivir, Antimicrob. Agents Chemother. 46 (2002) 3809–3816.
- [5] M. Kiso, K. Mitamura, Y. Sakai-Tagawa, K. Shiraishi, C. Kawakami, K. Kimura, F.G. Hayden, N. Sugaya, Y. Kawaoka, Resistant influenza A viruses in children treated with oseltamivir: descriptive study, Lancet 364 (2004) 759–765.
- [6] V.P. Mishin, F.G. Hayden, L.V. Gubareva, Susceptibilities of antiviral-resistant influenza viruses to novel neuraminidase inhibitors, Antimicrob. Agents Chemother. 49 (2005) 4515–4520.
- [7] M.D. de Jong, T.T. Tran, H.K. Truong, M.H. Vo, G.J. Smith, V.C. Nguyen, V.C. Bach, T.Q. Phan, Q.H. Do, Y. Guan, J.S. Peiris, T.H. Tran, J. Farrar, Oseltamivir resistance during treatment of influenza A (H5N1) infection, N. Engl. J. Med. 353 (2005) 2667–2672.
- [8] Q.M. Le, M. Kiso, K. Someya, Y.T. Sakai, T.H. Nguyen, K.H. Nguyen, N.D. Pham, H.H. Ngyen, S. Yamada, Y. Muramoto, T. Horimoto, A. Takada, H. Goto, T. Suzuki, Y. Suzuki, Y. Kawaoka, Avian flu: isolation of drug-resistant H5N1 virus, Nature 437 (2005) 1108.
- [9] H.L. Yen, N.A. Ilyushina, R. Salomon, E. Hoffmann, R.G. Webster, E.A. Govorkova, Neuraminidase inhibitor-resistant recombinant A/Vietnam/1203/04 (H5N1) influenza viruses retain their replication efficiency and pathogenicity in vitro and in vivo, J. Virol. 81 (2007) 12418–12426.
- [10] E. De Clercq, Antiviral agents active against influenza A virus, Nat. Rev. Drug Discov. 5 (2007) 1015–1025.
- [11] M. von Itzstein, The war against influenza: discovery and development of sialidase inhibitors, Nat. Rev. Drug Discov. 6 (2007) 967–974.
- [12] H.J. Schünemann, S.R. Hill, M. Kakad, R. Bellamy, T.M. Uyeki, F.G. Hayden, Y. Yazdanpanah, J. Beigel, T. Chotpitayasunondh, C. Del Mar, J. Farrar, T.T. Hien, B. Özbay, N. Sugaya, K. Fukuda, N. Shindo, L. Stockman, G.E. Vist, A. Croisier, A. Nagjdaliyev, C. Roth, G. Thomson, H. Zucker, A.D. Oxman, WHO rapid advice guidelines for pharmacological management of sporadic human infection with avian influenza A (H5N1) virus, Lancet Infect. Dis. 7 (2007) 21–31.
- [13] R.J. Russell, L.F. Haire, D.J. Stevens, P.J. Collins, Y.P. Lin, G.M. Blackburn, A.J. Hay, S.J. Gamblin, J.J. Skehel, The structure of H5N1 avian influenza neuraminidase suggests new opportunities for drug design, Nature 443 (2006) 45–49.
- [14] M. Malaisree, T. Rungrotmongkol, N. Nunthaboot, O. Aruksakunwong, P. Intharathep, P. Decha, P. Sompornpisut, S. Hannongbua, Source of oseltamivir resistance in avian influenza H5N1 virus with the H274Y mutation, Amino Acids (2009), doi:10.1007/s00726-008-0201-z.
- [15] J. Marelius, K. Kolmodin, I. Feierberg, J. Åqvist, Q: a molecular dynamics program for free energy calculations and empirical valence bond simulations in biomolecular systems, J. Mol. Graph. Model. 16 (1998) 213–225.
- [16] D.A. Case, D.A. Pearlman, J.W. Caldwell, T.E. Cheatham III, J. Wang, W.S. Ross, C.L. Simmerling, T.A. Darden, K.M. Merz, R.V. Stanton, A.L. Cheung, J.J. Vincent, M. Crowley, V. Tsui, H. Gohike, R.J. Radmer, Y. Duan, J. Pitera, I. Massova, G.L. Seibel, U.C. Singh, P.K. Weiner, P.A. Kollman, AMBER 7, University of California, San Francisco, CA, 2002.

T. Rungrotmongkol et al. / Biophysical Chemistry 145 (2009) 29-36

- [17] M. Malaisree, T. Rungrotmongkol, P. Decha, P. Intharathep, O. Aruksakunwong, S. Hannongbua, Understanding of known drug-target interactions in the catalytic pocket of neuraminidase subtype N1, Proteins 71 (2008) 1908–1918.
- [18] W.L. Jorgensen, J. Chandrasekhar, J.D. Madura, R.W. Impey, M.L. Klein, Comparison of simple potential functions for simulating liquid water, J. Chem. Phys. 79 (1983) 926–935.
- [19] H. Li, A.D. Robertson, J.H. Jensen, Very fast empirical prediction and interpretation of protein pKa values, Proteins 61 (2005) 704–721.
- [20] G. King, A. Warshel, A surface constrained all-atom solvent model for effective simulations of polar solutions, J. Chem. Phys. 91 (1989) 3647–3661.
- [21] J.P. Ryckaert, G. Ciccotti, H.J.C. Berendsen, Numerical integration of the Cartesian equations of motion of a system with constraints: molecular dynamics of nalkanes, J. Chem. Phys. 23 (1997) 327–341.
- [22] T. Hansson, J. Aqvist, Estimation of binding free energies for HIV proteinase inhibitors by molecular dynamics simulations, Protein Eng. 8 (1995) 1137–1144.
- [23] J. Åqvist, C. Medina, J.E. Samuelsson, A new method for predicting binding-affinity in computer-aided drug design, Protein Eng. 7 (1994) 385–391.
- [24] I.D. Wall, A.R. Leach, D.W. Salt, M.G. Ford, J.W. Essex, Binding constants of neuraminidase inhibitors: an investigation of the linear interaction energy method, J. Med. Chem. 42 (1999) 5142–5152.

- [25] Y. Abed, B. Nehmé, M. Baz, G. Boivin, Activity of the neuraminidase inhibitor A-315675 against oseltamivir-resistant influenza neuraminidases of N1 and N2, Antivir. Res. 77 (2007) 163–166.
- [26] O. Aruksakunwong, M. Malaisree, P. Decha, P. Sompornpisut, V. Parasuk, S. Pianwanit, S. Hannongbua, On the lower susceptibility of oseltamivir to influenza neuraminidase subtype N1 than those in N2 and N9, Biophys. J. 92 (2007) 798–807.
- [27] P.M. Colman, J.N. Varghese, W.G. Laver, Structure of the catalytic and antigenic sites in influenza virus neuraminidase, Nature 303 (1983) 41–44.
- [28] J.L. McKimm-Breschkin, A. Sahasrabudhe, T.J. Blick, M. McDonald, Mechanisms of resistance of influenza virus to neuraminidase inhibitors, Int. Congr. Ser. 1219 (2001) 855–861.
- [29] A. Moscona, Oseltamivir resistance-disabling our influenza defenses, N. Engl. J. Med. 353 (2005) 2633–2636.
- [30] N.X. Wang, J.J. Zheng, Computational studies of H5N1 influenza virus resistance to oseltamivir. Protein Sci. 18:707–715.

ORIGINAL ARTICLE

Molecular prediction of oseltamivir efficiency against probable influenza A (H1N1-2009) mutants: molecular modeling approach

Thanyada Rungrotmongkol · Maturos Malaisree · Nadtanet Nunthaboot · Pornthep Sompornpisut · Supot Hannongbua

Received: 2 July 2009/Accepted: 14 December 2009/Published online: 27 December 2009 © Springer-Verlag 2009

Abstract To predict the susceptibility of the probable 2009 influenza A (H1N1-2009) mutant strains to oseltamivir, MD/LIE approach was applied to oseltamivir complexed with the most frequent drug-resistant strains of neuraminidase subtypes N1 and N2: two mutations on the framework residues (N294S and H274Y) and the two others on the direct-binding residues (E119V and R292K) of oseltamivir. Relative to those of the wild type (WT), loss of drug-target interaction energies, especially in terms of electrostatic contributions and hydrogen bonds were dominantly established in the E119V and R292K mutated systems. The inhibitory potencies of oseltamivir towards the WT and mutants were predicted according to the ordering of binding-free energies: WT $(-12.3 \text{ kcal mol}^{-1}) > \text{N294S} (-10.4 \text{ kcal mol}^{-1}) >$ $H274Y(-9.8 \text{ kcal mol}^{-1}) > E119 \text{ V}(-9.3 \text{ kcal mol}^{-1}) >$ $R292K (-7.7 \text{ kcal mol}^{-1})$, suggesting that the H1N1-2009

T. Rungrotmongkol and M. Malaisree have equally contributed to this work.

Electronic supplementary material The online version of this article (doi:10.1007/s00726-009-0452-3) contains supplementary material, which is available to authorized users.

T. Rungrotmongkol \cdot M. Malaisree \cdot P. Sompornpisut \cdot S. Hannongbua (\boxtimes)

Computational Chemistry Unit Cell, Department of Chemistry, Faculty of Science, Chulalongkorn University,

Bangkok 10330, Thailand e-mail: supot.h@chula.ac.th

T. Rungrotmongkol Center of Innovative Nanotechnology, Chulalongkorn University, Bangkok 10330, Thailand

N. Nunthaboot Department of Chemistry, Faculty of Science, Mahasarakham University, Mahasarakham 44150, Thailand influenza with R292K substitution, perhaps, conferred a high level of oseltamivir resistance, while the other mutants revealed moderate resistance levels. This result calls for an urgent need to develop new potent anti-influenza agents against the next pandemic of potentially higher oseltamivir-resistant H1N1-2009 influenza.

Keywords 2009-H1N1 influenza A neuraminidase · Oseltamivir resistance · Mutations · Molecular dynamics simulations

Introduction

The 2009 influenza A (H1N1) virus has rapidly spread across the world with an evidence of human to human transmission. The probable mutation in the neuraminidase (NA) genes could cause resistance to the available drugs, especially oseltamivir. A new drug-resistant strain probably leads to a large scale outbreak of novel pandemic flu and an increase the national and global public health concerns. Common mutations in N1 (a subtype in NA group 1) are detected at N294S and H274Y, while the E119V and R292K mutations are mostly found in the N2 and N9 subtypes (in NA group 2), with oseltamivir resistance levels relative to the wild type (WT) of 20-80, 700-1,700, 20-1,000 and 1,500-10,000-fold higher, respectively (Abed et al. 2008; Collins et al. 2008; Yen et al. 2005, 2007). To date, oseltamivir has been found to effectively inhibit this new virus [2009 A (H1N1)] due to the following reasons: the N1 of the new H1N1 influenza and N9 share an identical active site (Rungrotmongkol et al. 2009a, b), and oseltamivir was designed to fit well to the active site of the NA group 2. With an increase in medical use and stockpile of oseltamivir for the recent



T. Rungrotmongkol et al.

outbreak, the question arises, and is the main goal of this study, can we predict the inhibitory activity of oseltamivir with respect to those frequent mutations that take place in the influenza A (H1N1-2009) strain, and thus the potential evolution and spread of resistant strains. The oseltamivir-resistant influenza NA mutants would perhaps serve as the emergence of a potential pandemic strain of the 2009-H1N1 virus.

Oseltamivir is an antiviral drug against NA that functions by preventing viral replication in the last step of the viral life cycle. It was found to directly interact with the catalytic residues of the NA active site, while the framework residues stabilized the enzyme structure (Fig. 1) (Ferraris and Lina 2008). Mutations at the conserved residues of NA appear to associate with oseltamivir resistance in a subtype specific manner. Thus, the mutated framework residues H274Y and N294S are regularly indentified in N1, while in the N2 and N9 sub-types, mutations on the binding residues (E119V and R292K) of oseltamivir were detected after treatment in infected patients with high oseltamivir resistance (Abed et al. 2008; Boivin and Goyette 2002; Collins et al. 2008; Mishin et al. 2005; Zürcher et al. 2006).

To provide information at the molecular level to aid the control and prevention of emerging potential pandemic strains of the 2009-H1N1 influenza, multi-molecular dynamics (MD) simulations in conjunction with the linear interaction energy (LIE) method have been performed on complexes of oseltamivir bound to each of the four most likely 2009-H1N1-mutated strains; that is, with the H274Y, N294S, E119V and R292K substitutions. The structural property, drug-target interaction and the binding affinity of oseltamivir against the mutated models are extensively discussed and compared with those recently published for the wild-type strain of the 2009-H1N1 influenza A virus (Rungrotmongkol et al. 2009a, b).

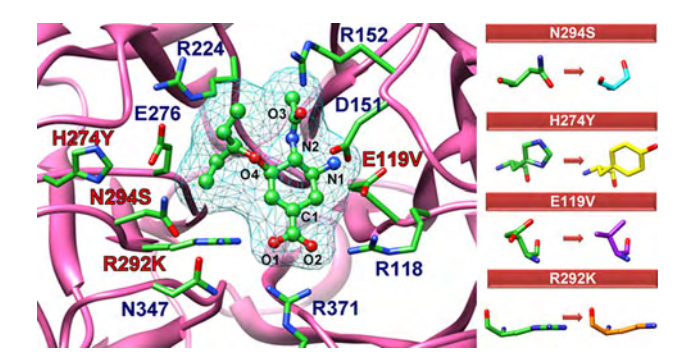


Fig. 1 Modeled structure of oseltamivir bound to the wild-type strain of 2009-H1N1 influenza neuraminidase. Among the labeled residues, four residues colored in *red* are singly mutated for investigation in this work: there are N294S, H274Y, E119V and R292K mutations. The selected atoms of oseltamivir are numbered for simplicity in the discussion



Springer

Materials and methods

The homology model of oseltamivir bound to the wild-type NA (OTV-WT) of the 2009-H1N1 virus (Rungrotmongkol et al. 2009a, b) was used as the initial structure for the modeling of the four single mutations: N294S, H274Y, E119V and R292K. To prepare each mutant, the specific residue was changed using the LEaP module of the AMBER 10 program package (Case et al. 2008), keeping the backbone and identical side chain atoms. All mutated NA strains with oseltamivir bound were then set-up and treated in accordance with the 20-ns MD simulations for the wild-type novel H1N1 influenza (Rungrotmongkol et al. 2009a, b), as follows.

Each simulated system was performed by MD simulations with spherical boundary condition under the surface constrained all atom solvent model (King and Warshel 1989) using the Q-program (Marelius et al. 1998), version 5. The atomic charges of oseltamivir were taken from our previous study (Malaisree et al. 2008). The AMBER force field (Case et al. 2008) was applied to the amino acid and inhibitor atoms. To set-up the environment for oseltamivir to be the most similar in all simulated systems and to take the conformational change of the oseltamivir into consideration, the C1 atom of oseltamivir was then chosen to be the center of simulation and the whole oseltamivir structure was thus considered as ligand. In the simulations, the system was capped by a 25 Å sphere of TIP3P water molecules centered on the C1 atom of oseltamivir (see Fig. 1 for atomic label). Atoms positioned further than 25 Å from the C1 center were taken into consideration as structural restrains. All acidic and basic side chains of residues lying within a 22 Å sphere were fully charged. In contrast, these ionizable residues positioning between 22 Å and 25 Å distances were neutralized, except for the pairs of charged residues with a probable formation of hydrogen-bonding interactions. The rest ionizable residues located outside a 25 Å sphere were considered as uncharged entities. Local reaction field approximation was employed for calculating the long-range electrostatic (ES) interactions, with a 10-Å cut-off radius for the non-bonded interactions. The SHAKE algorithm (Ryckaert et al. 1977) was applied to fix all bonds involving hydrogen atom. The NVT ensemble was performed, and a 2-fs time step was used. Initially, locations of the water molecules were simulated by MD simulations at 5 K, keeping all other atoms fixed to their initial positions, and the whole structure was then relaxed by four steps of simulations. Afterwards, the system was heated to 298 K over 300 ps, followed by equilibration phase. At last, the four equilibrated structures were randomly chosen for employing a production phase of 5-ns simulation.

To predict the binding-free energies ($\Delta G_{\rm bind}$) of osel-tamivir towards the NA mutants, the LIE method (Åqvist

Table 1 Changes in the electrostatic and van der Waals interactions for the four substituent functional groups of oseltamivir in the bound states of the modeled H1N1 mutant relative to those of wild type

				• 1					
Functional group $\langle \Delta \Delta U^{\rm ES} \rangle_{\rm bound}$ (kcal mol ⁻¹)									
	N294S	H274Y	E119V	R292K					
(a) Electrostatic interactions									
-COO-	8.3 ± 0.2	11.3 ± 0.1	5.4 ± 0.1	14.1 ± 0.2					
$-NH_3^+$	-2.7 ± 0.4	-2.8 ± 0.5	11.1 ± 0.6	2.3 ± 1.2					
-NHAc	3.0 ± 0.1	2.0 ± 0.1	6.0 ± 0.1	4.2 ± 0.2					
-OCHEt2	1.3 ± 0.6	0.6 ± 0.6	1.5 ± 0.9	4.3 ± 1.2					
Oseltamivir	10.0 ± 0.6	11.1 ± 0.6	23.9 ± 0.9	24.9 ± 1.2					
Functional group $\langle \Delta \Delta U^{\mathrm{vdW}} \rangle_{\mathrm{bound}}$ (kcal mol ⁻¹)									
	N294S	H274Y	E119V	R292K					
(b) Van der Waals interactions									
$-COO^-$	0.3 ± 0.0	0.3 ± 0.0	0.3 ± 0.0	0.8 ± 0.3					
$-NH_3^+$	0.6 ± 0.1	0.6 ± 0.0	-0.3 ± 0.1	0.8 ± 0.1					
-NHAc	0.2 ± 0.1	1.0 ± 0.1	1.1 ± 0.0	-0.7 ± 0.1					
-OCHEt ₂	1.4 ± 0.1	1.5 ± 0.0	0.1 ± 0.0	3.2 ± 0.2					

Means and standard deviations are derived from four separate 5-ns simulations

 1.2 ± 0.0

 4.2 ± 0.2

 2.5 ± 0.0 3.4 ± 0.0

Oseltamivir

et al. 1994; Hansson et al. 1998) was used. The total binding-free energy, which includes the van der Waals (vdW) ($U^{\rm vdW}$) and the ES interaction energies ($U^{\rm ES}$), of the two simulated states: (1) the solvated ligand (free state), and (2) the ligand bound to the solvated protein (bound state) were evaluated using the equation:

$$\begin{split} \Delta G_{\rm bind} &= \alpha \left(\langle U^{\rm vdW} \rangle_{\rm bound} - \langle U^{\rm vdW} \rangle_{\rm free} \right) \\ &+ \beta \left(\langle U^{\rm ES} \rangle_{\rm bound} - \langle U^{\rm ES} \rangle_{\rm free} \right) + \gamma \end{split} \tag{1}$$

where α and β are the empirical scaling coefficients for the vdW and ES interaction energies, respectively, and γ is a constant. Here, Wall's coefficients ($\alpha = 0.472$, $\beta = 0.122$ and $\gamma = 2.603$), which were efficiently derived from a statistical analysis of the inhibitor sets binding to the relevant NA enzyme (Wall et al. 1999) were chosen to fit the LIE equation due to the three following reasons. (1) Because the outbreak of the novel H1N1 pandemic flu was just arisen in April 2009, the experimental inhibitory activities required for the construction and validation the LIE model for the training set are not available. (2) This set of coefficients was successfully applied on the avian influenza A (H5N1) virus in prediction, the inhibitory activity of oseltamivir against both WT and mutant strains (Rungrotmongkol et al. 2009a, b). (3) The four single mutated strains of 2009-H1N1 neuraminidase virus in the present study were built by a specific mutation on the wild-type strain modeled from the crystal structure of the H5N1 neuraminidase with the sequence identity of 91%

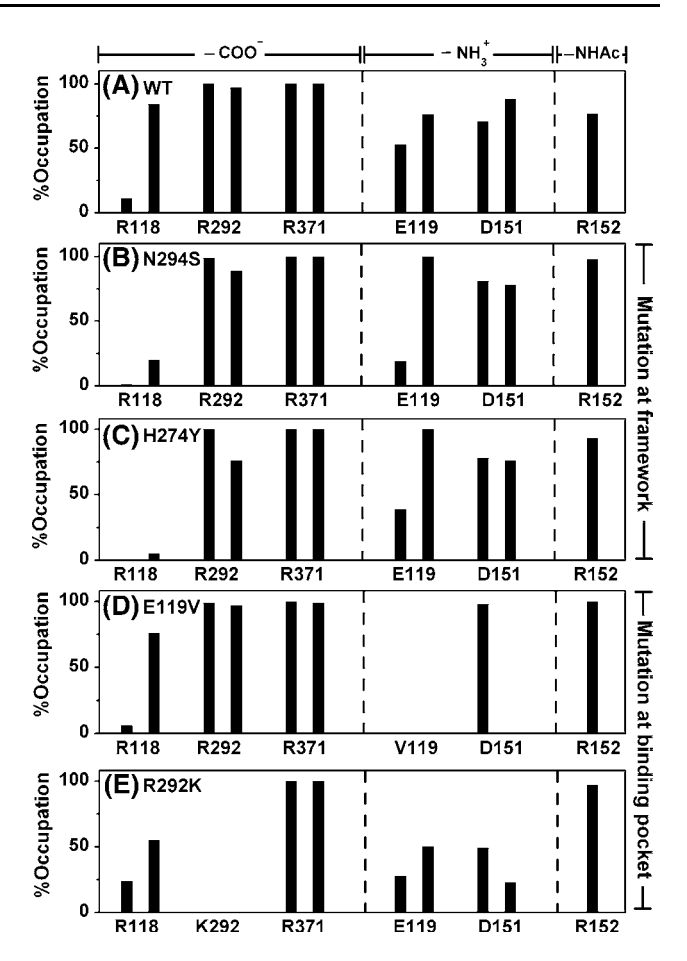


Fig. 2 Percentage occupation of H-bonds between the functional groups of oseltamivir and the NA residues (see Fig. 1 for residue positions) in the mutant models with the single substitution at two district regions: the framework residues closed to the hydrophobic pocket (N294S and H274Y), and the direct-binding residues (E119V and R292K)

(Rungrotmongkol et al. 2009a, b). Therefore, both WT and mutant NA strains of 2009-H1N1 are relatively similar to the H5N1 NA enzyme.

Results and discussion

Reduced oseltamivir binding to probable H1N1-2009 mutants

To examine oseltamivir susceptibility within the neuraminidase pocket of the 2009-H1N1 mutant models, intermolecular hydrogen-bond (H-bond), ES and vdW interactions between the oseltamivir's side chains and the NA residues were evaluated and compared with those of the WT (Rungrotmongkol et al. 2009a, b). The ES and vdW energetic differences were evaluated using Eqs. 2a and 2b, and are summarized in Table 1:



T. Rungrotmongkol et al.

$$\begin{split} \langle \Delta \Delta U^{\rm ES} \rangle_{\rm bound} &= \langle U^{\rm ES} \rangle_{\rm bound} [{\rm mutant}] \\ &- \langle U^{\rm ES} \rangle_{\rm bound} [{\rm wild~type}]. \end{split} \tag{2a}$$

$$\begin{split} \langle \Delta \Delta U^{\rm vdW} \rangle_{\rm bound} &= \langle U^{\rm vdW} \rangle_{\rm bound} [\rm mutant] \\ &- \langle U^{\rm vdW} \rangle_{\rm bound} [\rm wild \ type]. \end{split} \tag{2b}$$

The positive and negative values of the energy components indicate that the selected moiety of oseltamivir in the mutants decreases and increases its binding potency, relative to that of the WT, respectively. The H-bonds were calculated according to the two criteria that (1) the proton donor (D) and acceptor (A) distance is \leq 3.5 Å and (2) the D–H...A angle is \geq 120°. The results are shown in Fig. 2, whereas the descriptions are given in Table S1 of the supplementary materials. The schematic views of hydrogen bonds formed between oseltamivir and

its binding residues extracted from the simulations were given in Fig. 3.

Lower oseltamivir binding-free energies to the probable H1N1-2009 mutants were observed in terms of the H-bonds, $\Delta U^{\rm ES}$ and $\Delta U^{\rm vdW}$ energies relative to the WT, depending on where the mutation is located. As expected, the ES effect of single mutation at the framework residues (H274Y and N294S) is drastically less than that at the direct-binding residues (E119V and R292K), which leads to the $\Delta U^{\rm ES}$ reduction being in the range of c.a. 10–11 and 24–25 kcal mol⁻¹, respectively (Table 1a).

For the H1N1 WT, the strong oseltamivir–NA interactions were found via five, three and one H-bonds (\geq 75%) with the $-COO^-$, $-NH_3^+$ and -NHAc moieties, respectively (Figs. 2a, 3a). In the two framework region mutations, it can be seen that the $-COO^-$ group of oseltamivir

Fig. 3 Electrostatic potential of five different NA strains complexed with oseltamivir where negative regions are in *red* and positive regions are in *blue*: a wild type, b N294S, c H274Y, d E119V and e R292K. Closeup of oseltamivir, hydrogen bonds to its binding residues are represented by *red dashed line*

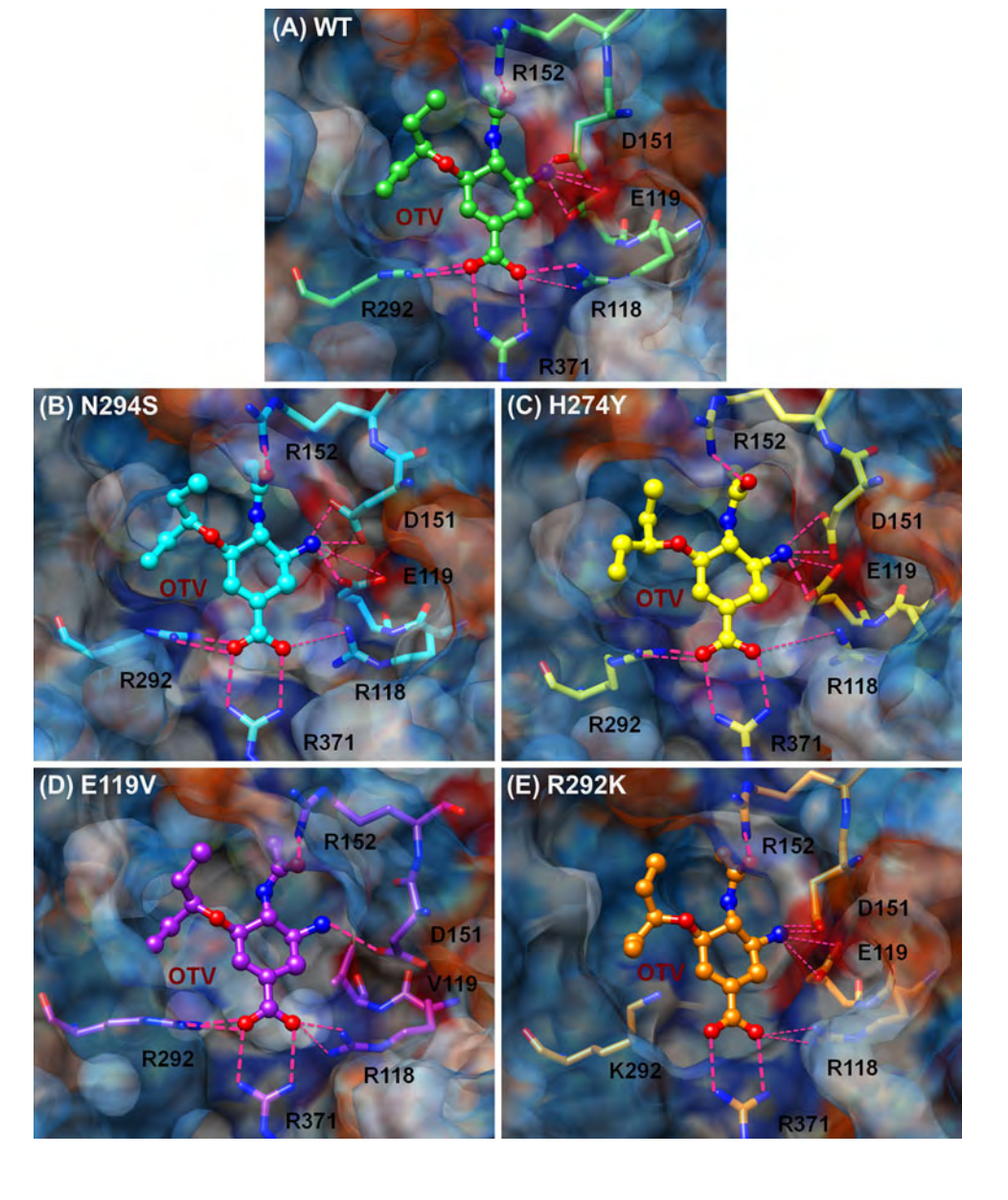




Table 2 MD/LIE binding-free energies (ΔG_{bind}) of oseltamivir towards the 2009-H1N1 influenza neuraminidases [A/California/04/2009(H1N1)] for the wild type (WT) and the probable single mutations: N294S, H274Y, E119V and R292K

NA strain	$\Delta G_{ m bind}~({ m kcal}~{ m mol}^{-1})$						
	WT	N294S	H274Y	E119V	R292K		
Predictive							
A/California/04/2009(H1N1)	-12.8 ± 0.9	-10.4 ± 0.9	-9.8 ± 1.0	-9.3 ± 0.8	-7.7 ± 0.7		
Experimental ^a							
A/WSN/33 (H1N1) ^b	-12.1	-9.3	-8.5	_	— -		
A/Puerto Rico/8/34 (H1N1) ^c	-11.4	-8.8	-8.1	_	_		
A/Vietnam/1203/04 (H1N1) ^c	-13.0	-11.2	-8.6	_	_		
A/Vietnam/1203/04 (H5N1) ^d	-13.1	-10.5	-9.8	_	_		
A/Sydney/5/97 (H3N2) ^b	-12.8	-8.3	_	-8.6	-7.3		
A/Wuhan/359/95 (H3N2) ^e	-12.4	_	_	-9.1	-6.2		

Means and standard deviations are derived from four separate 5-ns simulations

The experimental ΔG_{bind} for different strains of N1 and N2, converted from the K_{I} inhibitory and IC₅₀ values, are also given for comparison $^{\text{a}}$ $\Delta G_{\text{experiment}}$ was calculated from the experimental data using the following references: (b) Abed et al. 2008, (c) Yen et al. 2007, (d) Collins et al. 2008 and (e) Yen et al. 2005

has almost lost the H-bonds with R118 (see Figs. 2b, 3b for N294S; Figs. 2c, 3c for H274Y) in correspondence with the $\Delta U^{\rm ES}(-{\rm COO}^-)$ reduction of 11.3 kcal mol⁻¹ in H274Y and 8.3 kcal mol⁻¹ in N294S (Table 1a). As expected (Table 1b), the decreased ΔU^{vdW} (oseltamivir) $2.5 \text{ kcal mol}^{-1}$ by N294S and of $3.4 \text{ kcal mol}^{-1}$ by H274Y were mainly contributed from the loss of vdW interactions at the bulky OCHEt₂ group ($\sim 1.5 \text{ kcal mol}^{-1}$). Previous theoretical studies on the influenza NA mutants have already explained how the H274Y mutation confers oseltamivir resistance by a meaningful change of E276's sidechain conformation with a consequent effect upon the shape and size of the hydrophobic pocket for the -OCHEt₂ moiety (Malaisree et al. 2009; Rungrotmongkol et al. 2009a, b; Wang and Zheng 2009) while E276 in the N294S mutant acted as the center of H-bond network between R224 and S294 (Rungrotmongkol et al. 2009a, b) similar to that found in the crystal structure of the oseltamivir-resistant H5N1 N294S variant (Collins et al. 2008).

With a relatively high reduction in the ES contribution to oseltamivir in the mutations at the binding residues (E119V and R292K, Table 1a), the mutated residues V119 and K292 showed a complete loss of H-bond interactions with the $-\mathrm{NH_3}^+$ and $-\mathrm{COO}^-$ moieties of oseltamivir (Figs. 2d, 3d for E119V; Figs. 2e, 3e for R292K), supported by an increase in the $\Delta U^{\mathrm{ES}}(-\mathrm{NH_3}^+)$ by 11.1 kcal mol⁻¹ and in the $\Delta U^{\mathrm{ES}}(-\mathrm{COO}^-)$ by 14.1 kcal mol⁻¹. In addition, only one H-bond with D151 in the E119V mutant was maintained, while lower H-bond strengths in the R292K mutant were observed at R118, E119 and D151. Moreover, a reduced vdW interaction of 3.2 kcal mol⁻¹ was found at the $-\mathrm{OCHEt_2}$ group in the R292K mutant

because the side chain of K292 (Fig. 3e) is smaller and shorter than that of R292 (Fig. 3a). The results of the R292K mutation were somewhat comparable to the computational study of the sialic acid analogs binding to the R292K mutated NA subtype N9 (Chachra and Rizzo 2008).

Prediction of inhibitory activity against the H1N1 mutated strains

Based on the MD/LIE approach, the binding affinities of oseltamivir towards different mutant models of the 2009-H1N1 influenza [A/California/04/2009(H1N1)], according to Eq. 1, were predicted and are summarized in Table 2. As expected, oseltamivir's binding-free energy against the WT is the most favorable one at -12.8 kcal mol⁻¹. Only moderate binding-free energy values were found for the N294S, H274Y and E119V mutated strains, in which the corresponding $\Delta G_{\rm bind}$ of -10.4, -9.8 and $-9.3 \text{ kcal mol}^{-1}$, respectively. The lowest favorable binding of oseltamivir is found in the R292K mutant with a predicted $\Delta G_{\rm bind}$ of -7.7 kcal mol⁻¹. All the calculated binding-free energies were found to fall within the ranges of those experimentally determined for various WT and mutant strains of the other influenza N1 and N2 subtypes (Table 2) (Abed et al. 2008; Boivin and Goyette 2002; Collins et al. 2008; Mishin et al. 2005; Zürcher et al. 2006).

Taking all the above data into consideration, it seems likely that oseltamivir will be significantly less potent an inhibitor for all the modeled mutants of the 2009-H1N1 strains, with the ranked order of: R292K < E119V < H274Y < N294S.



T. Rungrotmongkol et al.

Conclusions

In the present study, multi-MD simulations in conjunction with the LIE method was performed on oseltamivir–NA-bound complexes for the four probable NA mutants of influenza A (H1N1-2009): two mutations on the framework residues (N294S and H274Y) and the two others on the direct-binding residues (E119V and R292K) of oseltamivir. Reduction in the oseltamivir–enzyme interaction energies, particularly in the ES term, and in the hydrogen bonding were both observed in the two mutated systems with substitution on the direct-binding residues, E119V and R292K.

Based on the MD/LIE approach, the inhibitory potencies of oseltamivir towards the WT and mutants were predicted in accordance with their derived binding-free energies (ΔG_{bind}) with: WT ($-12.3 \text{ kcal mol}^{-1}$) > N294S $(-10.4 \text{ kcal mol}^{-1}) > \text{H274Y} (-9.8 \text{ kcal mol}^{-1}) > \text{E119 V}$ $(-9.3 \text{ kcal mol}^{-1}) > \text{R292 K} \quad (-7.7 \text{ kcal mol}^{-1}).$ This means that oseltamivir (which, to date, effectively inhibits the current H1N1-2009 wild-type strain) is less effective in protection and/or treatment of patients with these probable mutants, and especially with the R292K variant. Therefore, surveillance of any mutations in the influenza A (H1N1-2009) needs to be closely watched, and prompt action taken for preparation for the next pandemic of potentially higher oseltamivir-resistant H1N1 influenza strains. This calls for the urgent development of new potent anti-influenza agents against both native and mutants forms of H1N1-2009.

Acknowledgments This work was supported by the Thailand Research Fund (TRF). T.R. thanks the TRF Grant for New Research (Grant No. TRG5280035) and M.M. thanks the Royal Golden Jubilee Ph.D. Program (Grant No. 3.C.CU/48/F.1) from the TRF. T.R. also thanks the Post-Doctoral Program from the Commission on Higher Education. The Computational Chemistry Unit Cell, Chulalongkorn University, provided the computing facilities. The Center of Excellence for Petroleum, Petrochemicals, and Advanced Materials, Chulalongkorn University, is acknowledged.

References

- Abed Y, Nehmé B, Baza M, Boivin G (2008) Activity of the neuraminidase inhibitor A-315675 against oseltamivir-resistant influenza neuraminidases of N1 and N2 subtypes. Antiviral Res 77:163–166
- Åqvist J, Medina C, Samuelsson JE (1994) A new method for predicting binding affinity in computer-aided drug design. Protein Eng 7:385–391
- Boivin G, Goyette N (2002) Susceptibility of recent Canadian influenza A and B virus isolates to different neuraminidase inhibitors. Antiviral Res 54:143–147
- Case DA, Darden TA, Cheatham TE, Simmerling CL, Wang J, Duke RE, Luo R, Crowley M, Walker RC, Zhang W, Merz KM, Wang B, Hayik S, Roitberg A, Seabra G, Kolossváry I, Wong KF,

- Paesani F, Vanicek J, Wu X, Brozell SR, Steinbrecher T, Gohlke H, Yang L, Tan C, Mongan J, Hornak V, Cui G, Mathews DH, Seetin MG, Sagui C, Babin V, Kollman PA (2008) AMBER10 University of California San Francisco
- Chachra R, Rizzo RC (2008) Origins of resistance conferred by the R292K neuraminidase mutation via molecular dynamics and free energy calculations. J Chem Theory Comput 4:1526–1540
- Collins PJ, Haire LF, Lin YP, Liu J, Russell RJ, Walker PA, Skehel JJ, Martin SR, Hay AJ, Gamblin SJ (2008) Crystal structures of oseltamivir-resistant influenza virus neuraminidase mutants. Nature 453:1258–1261
- Ferraris O, Lina B (2008) Mutations of neuraminidase implicated in neuraminidase inhibitors resistance. J Clin Virol 41:13–19
- Hansson T, Marelius J, Aqvist JJ (1998) Ligand binding affinity prediction by linear interaction energy methods. J Comput Aided Mol Des 12:27–35
- King G, Warshel A (1989) A surface constrained all-atom solvent model for effective simulations of polar solutions. J Chem Phys 91:3647–3661
- Malaisree M, Rungrotmongkol T, Decha P, Intharathep P, Aruksakunwong O, Hannongbua S (2008) Understanding of known drug-target interactions in the catalytic pocket of neuraminidase subtype N1. Proteins 71:1908–1918
- Malaisree M, Rungrotmongkol T, Nunthaboot N, Aruksakunwong O, Intharathep P, Decha P, Sompornpisut P, Hannongbua S (2009) Source of oseltamivir resistance in avian influenza H5N1 virus with the H274Y mutation. Amino Acids 37:725–732
- Marelius J, Kolmodin K, Feierberg I, Åqvist J (1998) Q: a molecular dynamics program for free energy calculations and empirical valence bond simulations in biomolecular systems. J Mol Graph Model 16:213–225
- Mishin VP, Hayden FG, Gubareva LV (2005) Susceptibilities of antiviral-resistant influenza viruses to novel neuraminidase inhibitors. Antimicrob Agents Chemother 49:4515–4520
- Rungrotmongkol T, Intharathep P, Malaisree M, Nunthaboot N, Kaiyawet N, Sompornpisut P, Payungporn S, Poovorawan Y, Hannongbua S (2009a) Susceptibility of antiviral drugs against 2009 influenza A (H1N1) virus. Biochem Biophys Res Commun 385:390–394
- Rungrotmongkol T, Udommaneethanakit T, Malaisree M, Nunthaboot N, Intharathep P, Sompornpisut P, Hannongbua S (2009b) How does each substituent functional group of oseltamivir lose its activity against virulent H5N1 influenza mutants? Biophys Chem 145:29–36
- Ryckaert JP, Ciccotti G, Berendsen HJC (1977) Numerical integration of the Cartesian equations of motion of a system with constraints: molecular dynamics of n-alkanes. J Comput Phys 23:327–341
- Wall ID, Leach AR, Salt DW, Ford MG, Essex JW (1999) Binding constants of neuraminidase inhibitors: an investigation of the linear interaction energy method. J Med Chem 42:5142–5152
- Wang NX, Zheng JJ (2009) Computational studies of H5N1 influenza virus resistance to oseltamivir. Protein Sci 18:707–715
- Yen HL, Herlocher LM, Hoffmann E, Matrosovich MN, Monto AS, Webster RG, Govorkova EA (2005) Neuraminidase inhibitor-resistant influenza viruses may differ substantially in fitness and transmissibility. Antimicrob Agents Chemother 49:4075–4084
- Yen HL, Ilyushina NA, Salomon R, Hoffmann E, Webster RG, Govorkova EA (2007) Neuraminidase inhibitor-resistant recombinant A/Vietnam/1203/04 (H5N1) influenza viruses retain their replication efficiency and pathogenicity in vitro and in vivo. J Virol 81:12418–12426
- Zürcher T, Yates PJ, Daly J, Sahasrabudhe A, Walters M, Dash L, Tisdale M, McKimm-Breschkin JL (2006) Mutations conferring zanamivir resistance in human influenza virus N2 neuraminidases compromise virus fitness and are not stably maintained in vitro. J Antimicrob Chemother 58:723–732



Computational Studies of Influenza A Virus at Three Important Targets: Hemagglutinin, Neuraminidase and M2 Protein

Thanyada Rungrotmongkol^{1,2a}, Pathumwadee Yotmanee^{1,2a}, Nadtanet Nunthaboot^{3a} and Supot Hannongbua¹*

¹Computational Chemistry Unit Cell, Department of Chemistry, Faculty of Science, Chulalongkorn University, Phayathai Road, Patumwan, Bangkok, 10330, Thailand, ²Center of Innovative Nanotechnology, Chulalongkorn University, Bangkok, 10330, Thailand, ³Department of Chemistry, Faculty of Science, Mahasarakham University, Mahasarakham, 44150, Thailand

Abstract: While the seasonal influenza viruses spreading around the world cause the annual epidemics, the recent outbreaks of influenza A virus subtype H5N1 and pandemic H1N1 have raised global human health concerns. In this review, the applicabilities of computational techniques focused on three important targets in the viral life cycle: hemagglutinin, neuraminidase and M2 proton channel are summarized. Protein mechanism of action, substrate binding specificity and drug resistance, ligand-target interactions of substrate/inhibitor binding to these three proteins either wild-type or mutant strains are discussed and compared. Advances on the novel anti-influenza agents designed specifically to combat the avian H5N1 and pandemic H1N1 viruses are introduced. A better understanding of molecular inhibition and source of drug resistance as well as a set of newly designed compounds is greatly useful as a rotational guide for synthetic and medicinal chemists to develop a new generation of anti-influenza drugs.

Keywords: Avian influenza H5N1 virus, pandemic influenza H1N1 virus, hemagglutinin, neuraminidase, M2 channel, theoretical calculations, computer-aided drug design.

1. INTRODUCTION

The pandemic of influenza virus has caused global public health concern and occasionally leads to millions of death around the world. Among the three different types A, B and C of influenza viruses which can infect humans, only class A is frequently observed to cause pandemics and severe disease [1-3]. The most devastating influenza A pandemic of 1918 Spanish flu killed around 40 million people worldwide [2, 3]. Since late 2003, the appearance of a high virulent avian H5N1 influenza virus or a commonly known "bird flu" and its direct transmission from avian to human species caused a severe disease in human with a high fatality rate of over 50% [4, 5]. The ability of this high pathogenic strain of avian flu to spread among humans could result in a disastrous pandemic influenza [6, 7]. Moreover, the recent outbreak of a novel strain of swine-origin H1N1 influenza virus and its sustained human to human transmission leads to the fear of morbidity and mortality because this new virus strain may lead to a high potential influenza virus pandemic.

Influenza A viruses in the family of *Orthomyxoviridae* are composed of eight segments of single-stranded negative sense RNA molecule encoding eleven known proteins (PB2, PB1, PB1-F2, PA, HA, NP, NA, M1 and M2, and NS1A and NS2, Fig. 1) [8]. A lipid envelop of the viral particle contains two spike glycoproteins, hemagglutinin (HA) and neuraminidase (NA), and the transmembrane protein M2. HA is responsible for the viral entry into target cells while NA plays a critical role in the release of newly synthesized viral particles. The integral membrane protein M2 has a multifunction including proton selective and ion channel. There are 16 antigenically distinct HA (H1-H16) and 9 NA (N1-N9) subtypes. A combination of these HA and NA subtypes is used to identify different strains of influenza virus such as H1N1, H2N2, and H5N1.

This review aims to provide an overview of the recent applications of computational approaches employed to the HA, NA, and M2 protein of the influenza A virus subtypes H5N1 and pandemic

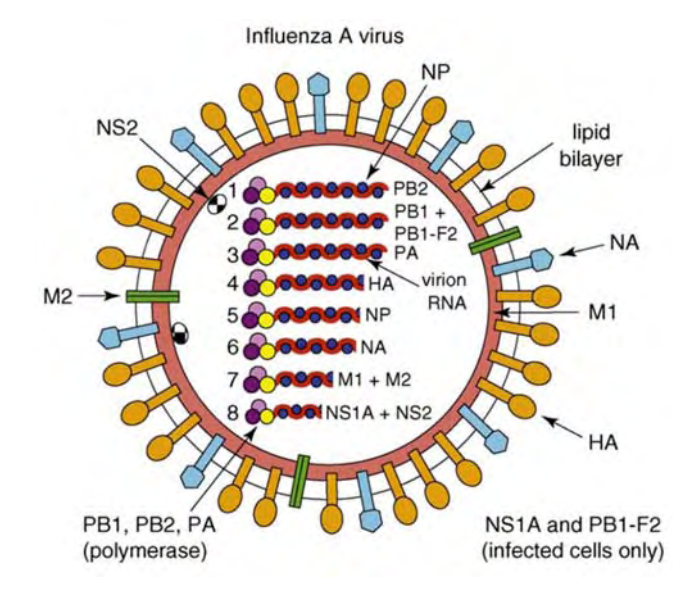


Fig. (1). Schematic representation of influenza A virus particle (Reprinted with permission from Krug and Aramini [8], copyright 2009 Elsevier)

H1N1 in particular the mechanism of protein functions and drug inhibition, source of drug resistance and inhibitor development.

2. HEMAGGLUTININ (HA)

2.1. Roles of HA

The initial step of virus infection involves HA binding to host cell receptor containing glycans linkage with the terminal sialic acid (SA). The efficiency of HA-receptor binding is specific and depends on the nature of the unique linkage between SA and carbohydrates of host target. Avian and human viruses preferentially recognize SA with $\alpha\text{-}2,3\text{-}$ and $\alpha\text{-}2,6\text{-}$ linkages to galactose (Gal), respectively, while swine virus can bind to both linkages. The alternation in host specificity of SA linked to Gal from $\alpha\text{-}2,3\text{-}$ (SA- $\alpha\text{-}2,3\text{-}\text{Gal}$) to $\alpha\text{-}2,6\text{-}$ (SA- $\alpha\text{-}2,6\text{-}\text{Gal}$) linkage is supposed to be a major barrier for influenza viruses to cross species barriers and adapt to new hosts [3, 9-11]. Despite the role of host cell receptor attachment,

^{*}Address correspondence to this author at the Computational Chemistry Unit Cell, Department of Chemistry, Faculty of Science, Chulalongkom University, Phayathai Road, Patumwan, Bangkok, 10330, Thailand; Tel: +66 22 187602; Fax: +66 22 187603; E-mail: supot.h@chula.ac.th

^aThese authors have equally contributed to this work.

HA proteolytic activation is necessary for viral infectivity and spreading of the influenza virus through host's organ. Without proteolysis, the fusion peptide cannot be generated and hence the virus is non-infectious. Computational studies in HA-receptor binding specificity and the cleavage mechanism of action are discussed in the next sections.

2.2. HA and Influenza Pathogenicity

HA, a homotrimer glycoprotein embedded in viral surface, is synthesized as precursor polypeptide (HA0) and cleaved into two disulfide-linked subunits (HA1 and HA2). HA1 is responsible for viral budding to host cell while HA2 promotes the release of viral RNA genome complexed with polymerase through membrane fusion. The pathogenicity of the influenza virus is associated with the cleavage ability of an inactive HA precursor protein [3, 9-11]. In low pathogenic influenza virus (LPIV), the HA cleavage site is cleaved by tripsin-like protease enzymes which are principally found in the respiratory system, thus causing the relatively mind respiratory illness. On the other hand, this particular site of high pathogenic influenza virus (HPIV) is specifically cleaved by proprotein-processing endoproteases PC6 and furin which are found in every part of host organs, thereby leading to a widespread systematic and virulent infection. Structure analyses suggested that the HA cleavage site of LPIV contains a single basic amino acid residue (Q/E-X-R) while the insertion of polybasic amino acids (R-X-R/K-R) leads to the HPIV (Fig. 2). Among all HA subtypes, only H5 and H7 are observed to cause the HPIV [1, 7].

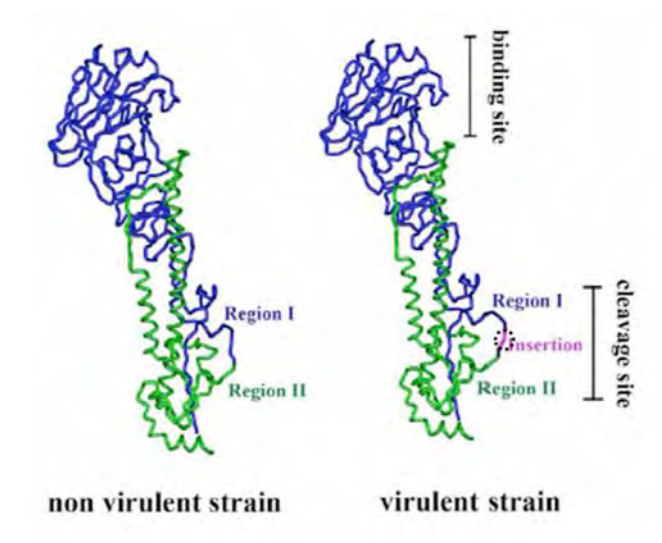


Fig. (2). Modeled structures of LPIV and HPIV HA strains. Amino acid residues near the cleavage site are divided into two regions, Region I and Region II. The insertion of polybasic amino acids in Region I is in circle.

2.3. HA Catalytic Reaction Mechanism

Similar to other members of serine proteases, one of the important catalytic function domains for furin is the catalytic triad including amino acids D153, H194 and S368 or the so-called D/H/S (H/D/S; D102, H57 and S195 for trypsin and chymotrypsin peptidases). Although the order of the active site residues is different, the proteolytic mechanism of furin protease is similar to that of trypsin and chymotrypsin [12], where serine is the nucleophile, histidine functions as the general base or acid and aspartate involves in the stabilization of the positive imidazolium ion of histidine during the transition process. Typically, the reaction mechanism takes place via acylation and deacylation processes (Fig. 3). In the acylation

step, the catalytic H194 acts as a general base to accept a proton from S368 (Fig. 3A) and the deprotonated S368 then becomes a nucleophile to directly attack the scissile carbonyl carbon of the substrate with the formation of the first tetrahedral intermediate (INT-1, Fig. 3B). This resulting tetrahedral intermediate is stabilized through hydrogen bonding interactions with the carboxamide and backbone nitrogen atoms of oxyanion hole formed by residues N295 and S368, respectively. Then, the protonated side chain of H194 acts as a general acid to donate a proton to the backbone nitrogen of the substrate to break down the tetrahedral intermediate. This follows with the elimination of amine product and the formation of acyl-enzyme intermediate (EA, Fig. 3C). The deacylation reaction takes place through the reverse reaction pathway of acylation process by using an activated water molecule as a nucleophile instead of the catalytic serine residue via the formation of the second tetrahedral intermediate (INT-2, Fig. 3D). The produced second tetrahedral intermediate then collapses to release the newly generated carboxyl group and to restore the S195 to its initial form [13,

Although the enzymatic reaction mechanisms carried out by serine protease have been extensively studied [13-15], the detailed mechanism of proteolytic activation of HPIV and LPIV HAs by the specific host proteases is still not well understood. A lack of experimental structures of HA-substrate complex is one of the major problems leading to an unclear insight of HA catalytic mechanism. Recently, molecular dynamics (MD) simulations of the three different HA-furin complexes were carried out with the aim of investigation why HPIV H5 was better recognized and cleaved by ubiquitious subtilisin-like protease than LPIV [16]. The modeled structures of furin complexed with non- and high-virulent HA strain of influenza viruses were constructed using a manual docking of different HA insertion loops within the furin active site (Fig. 4). The cleavage loop of the HPIV HA was hypothesized to bind firmly with the furin active region. The presence of the basic residues in particular at positions S2 (lysine), S4 (arginine) and S6 (arginine) of the high pathogenic avian influenza virus subtype H5 (H5-HPIV) was found to enhance more and strong hydrogen bonding interactions with the furin residues including D154, D264, Y308, E236, V231, D233 and E236. On the other hand, less and non-stable hydrogen bonding interactions with furin were detected in the other two low pathogenic influenza viruses (H5-LPIV and H3-LPIV). In addition, the observation from this work suggested that the shorter bond-making distance between S386 and S1-R of H5-HPIV (3.05 Å) provided a suitable conformation for the nucleophilic attack of the catalytic serine residue in comparison to that of the H5-LPIV (3.45 Å) and H3-LPIV (3.75 Å).

Another study of HA enzymatic reaction mechanism was conducted using the hybrid quantum mechanics/molecular mechanics (QM/MM) [17]. This particular approach was employed to investigate the first step of the acylation process in furin where its substrate was the cleavage site of the HPIV subtype H5N1. In this work, the QM region contains the fragments of H194 and S368 of furin and S1-R (capped by S2-K) and S1'-G of HPIV HA while the rest of system was treated by molecular mechanics. This study showed the reaction pathway of a concerted reaction composing of a two stepwise mechanisms: (i) the proton transfer from S368 to H194 and (ii) neucleophilic attack on the carbonyl carbon of the susceptible bond of the HPIV HA S1-R. The proposed tetrahedral intermediate structure is depicted in Fig. 5. Strong hydrogen bonds were observed between oxygen atom of S1-R and the N295's carboxamide moiety as well as the S368's backbone nitrogen. D153 was observed to significantly stabilize the protonated H194 through electrostatic and hydrogen bonding interactions. The energy profile of the concerted reaction with the activation energy barrier of 16.2 kcal·mol⁻¹ was estimated at the B3LYP/6-31+G*//PM3-CHARMM22 level of theory.

Fig. (3). The proposed HPIV proteolytic mechanism by furin protease starting from the (A) enzyme-substrate (ES) complex, (B) tetrahedral intermediate 1 (INT-1), (C) acyl-enzyme intermediate (EA) to (D) tetrahedral intermediate 2 (INT-2), adapted from ref. 14.

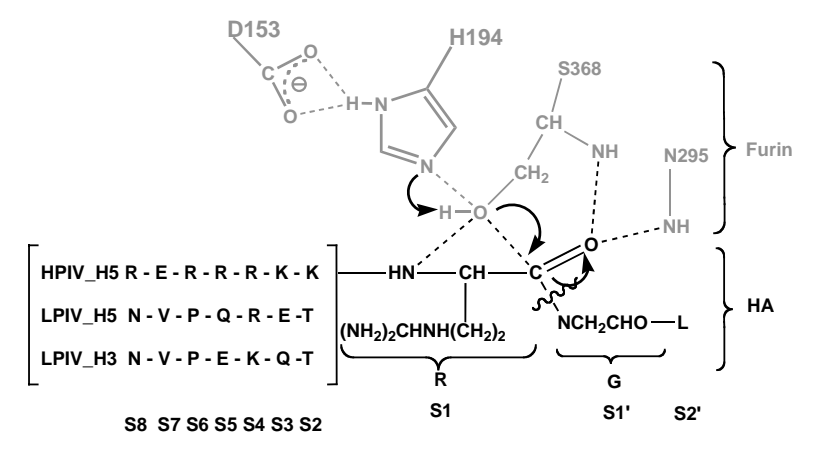


Fig. (4). Schematic representation of the proposed mechanism of three different strains of HAs by furin. Residues of furin and HA cleavage loops are shown in grey and black, respectively, adapted from ref. 16.

2.4. HA-receptor Binding Specificity

Receptor binding preference of HA is a critical factor determining the host range specificity. Li and Wang [18] applied molecular docking and MD simulations to identify the binding characteristics of influenza H5N1 HA with either avian or human receptors. They found that the SA- α -2,3-Gal and SA- α -2,6-Gal bound with HA active residues via *trans* and *cis* conformations, respectively. The HA residues interacted with SA- α -2,3-Gal stronger than that observed in SA- α -2,6-Gal which showed a relatively weak hydrophobic and hydrogen bonds interactions. In the study by Iwata and

colleagues [19], *ab initio* fragment molecular orbital method (FMO) at MP2/6-31G level was applied to examine the binding specificity of different HAs of human H1, swine H1, avian H3 and avian H5 to avian and human receptor analogues. Binding energies and interaction patterns showed that the swine and human H1 HAs were predicted to strongly bind with human receptor compared to the avian one. In contrast, the avian H3 and H5 HAs exhibited more preferentially favorable to avian receptor than the human analogue.

The glycan topology has been hypothesized to be involved in the switching of receptor binding preference. Xu et al. [20, 21]

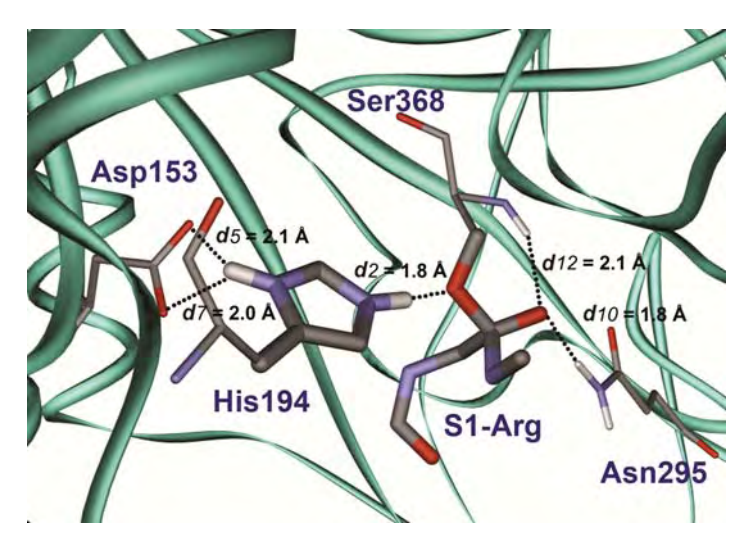


Fig. (5). Tetrahedral intermediate structure of H5N1-furin complex where the QM and MM atoms are represented by thick and thin stick models, respectively [17], copyright 2009 Wiley-Liss, Inc., A Wiley Company)

performed MD simulations of trimeric forms of avian H3, avian H5 and swine H9 complexed with avian and human receptors by taking into consideration the pentasaccharides SA-α-2,3-Gal and SA-α-2,6-Gal receptor analogues (Fig. 6). By analyzing the angle between the first trisaccharides (SA1, Gal2 and Nag3), the authors indicated that a long SA-α-2,3-Gal linkage with the cone-like topology was favorable in avian influenza virus while a long α-2,6 glycan linkage with a unique umbrella-like topology was preferred in human influenza virus. Analysis of binding free energies based molecular mechanics generalized Born surface area (MM-GBSA) implied that the avian H3 and H5 HAs preferentially bound to avian receptors. However, the swine H9 was able to bind both avian and human receptors equally, thereby possibly acting as intermediate hosts for introduction of influenza reassortment acquiring to human. Electrostatic interaction played a major role in stabilizing the HAglycan bound. In all complexes, the HA binding area is composed of residues member of 190-helix and 130- and 220-loops. Relative to avian H3 and H5 subtypes, the large receptor binding domain of swine H9 HA effectively provided optimal contacts with both types of receptor analogues. Among five glycan units, SA strongly interacted with HA receptor binding residues, thereby exhibiting the highest contribution to stabilize protein-glycan affinity.

Mutations of HA key residues were reported to be associated with the change of receptor recognition. For H2, H3, and H5 subtypes, mutations of the two critical amino acids Q226 and G228 in avian influenza virus to L226 and S228 (Q226L and G228S) were found to greatly enhance the human receptor specificity. A different route was detected in H1 subtype which the mutations of E190 and G225 in avian strain to D190 and D225 caused a switch from avian to human specificity [5, 7, 22, 23].

Binding energy and interactions between a single mutation Q226L of avian H3 and SA-α-2,3-Gal or SA-α-2,6-Gal were studied by Sawada and coworkers [24-26]. By comparing the binding energy based ab initio FMO method, the avian Q226 H3 bound to avian-type receptor stronger than that observed in human-type analogue (by 8.2 kcal•mol⁻¹ at FMO-HF/STO-3G or ~15-16 kcal•mol⁻¹ at FMO-MP2/6-31G). Residue Q226 was found to strongly interact with the avian receptor through many hydrogen bond interactions, relatively weak in the case of human receptor. The authors also tried to compare the binding specificity of avian L226 complexed with either avian or human receptors. The binding affinity of L226 avian H3 and SA-α-2,6-Gal was stabilized through hydrophobic interaction between this particular residue and the Gal unit of human receptor. However, introduction of L226 led to steric clash in the case of H3-avian receptor bound, thus reducing the receptor binding capability. The same research group continued their study on the role of these key HA mutations by employing a high accuracy QM/MM approach [27]. The results agreed well with what was already observed in the previous work, i.e., the avian H3 bound to SA- α -2,3-Gal stronger than SA- α -2,6-Gal does. The O226 played a critical role by forming hydrogen bonding interaction with one of hydroxyl moieties of Gal. In the mutant avian H3, the presence of L226 led to small entropic penalty and a dispersion interaction between L226 and SA-α-2,6-Gal, hence improving the binding affinity to human type receptor.

Besides the mutation of residues 226 and 228, another double mutation L129V and A134V of avian H5N1 HA was reported to be a potential route for H5 to adapt the human receptor specificity [28]. Furthermore, Das et al. [29] used free energy perturbation simulation to examine the other mutations that possibly lead to receptor specificity switch of avian H5N1 HA. This study considered either single or double mutations of many HA key residues at positions 135, 137, 138, 143, 186, 190, 192, 197, 225, 226, 227, and 228. A novel combination of V135S and A138S was predicted to significantly increase the human receptor binding preference due to its high contribution of electrostatic interaction. Substitutions of serine at both positions 135 and 138 resulted in a conformational rearrangement in the HA-glycan binding area, therefore accommodating the stable hydrogen bonds between HA and SA-α-2,6-Gal receptor.

Recently, the outbreak of a novel 2009 H1N1 influenza virus leads to a global concern because it could potentially introduce a more dangerous influenza flu pandemic. In the early work, Nunthaboot et al. [30] constructed a three dimensional structure of the 2009 H1N1 HA-human receptor bound and investigated its structural property. Similar to other HAs, SA showed the most contacts with HA residues and the key interactions between the human sialopentasaccharide receptor and HA binding residues member of 190-helix and 130- and 220-loops were conserved. In their continued work, structures and binding behavior of a novel 2009 H1N1 complex were further compared to those of three different HAs of Spanish 1918, swine 1930, and seasonal 2005 [31]. The HA receptor binding domain of a novel 2009 virus was found to exhibit higher hydrophilicity than that of the other three HAs. Introduction of a positively charged K145 residue in a novel 2009 HA was observed to form a unique and potential lysine fence with residues K133, K156, and K222. Residue K145 improved the proteinreceptor binding efficiency by making a strong hydrogen bond with

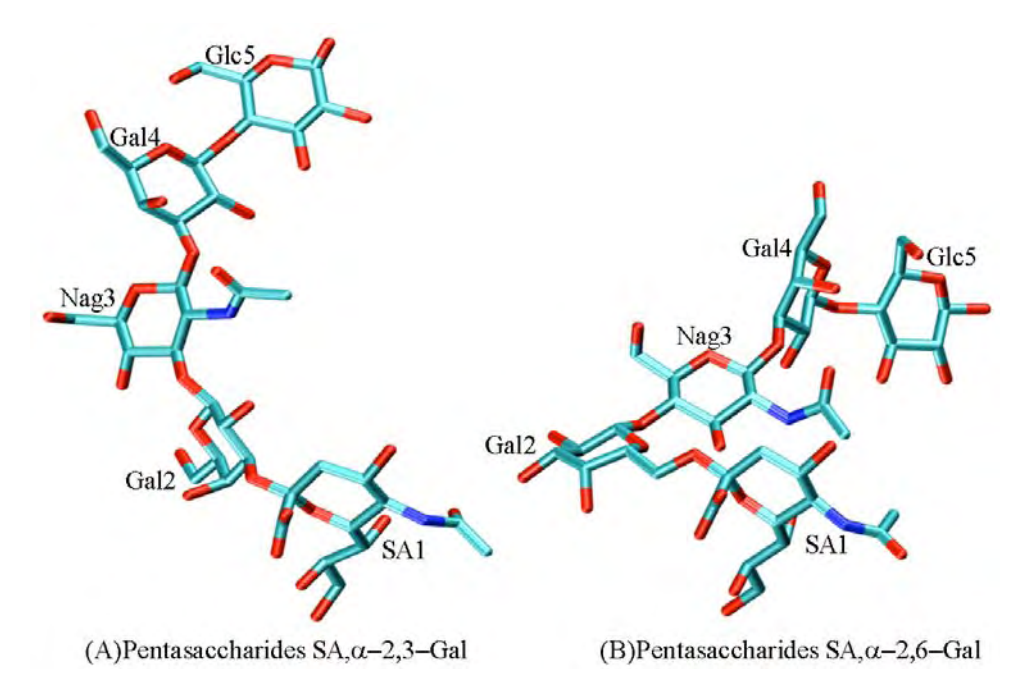


Fig. (6). Structure of pentasaccharides (A) SA-α-2,3–Gal and (B) SA-α-2,6–Gal receptor analogues.

the terminal SA. At the receptor binding QXG site, the presence of a negatively charged E227 residue leads to a formation of QEG sequences in the 2009 H1N1 HA while the QAG pattern was noticed in the other previous H1N1 HAs. Relative to the non-charged A227, the enhanced negative electrostatic isosurface of E227 significantly stabilized K222 conformation to establish a strong hydrogen bond interaction with Gal unit, thereby increasing the binding affinity of HA to human receptor analogue. Substitution of A227E was likely being an evolution of the new H1N1 HA from the previous strains. Furthermore, the replacement of D225 in the two pandemic strains of 1918 and 2009 H1N1 HAs resulted in their larger and stronger hydrogen boding interactions with Gal of human receptor than that detected in the 1930 swine and 2005 seasonal viruses where residue G225 exists instead. The binding efficiency of a novel 2009 H1N1 HA to human receptor was predicted to greater than the other three previous HA strains of H1N1 subtype. In the study by de Vries et al. [32], substitutions of T200A and E227A into the crystal structure of the new pandemic human H1N1 HA were detected to disturb hydrogen bond formation with the 190-helix residue Q191 and the second galactose unit, respectively, thereby reducing the human receptor specificity.

The behavior of a human receptor bound to HA of the 1918 and a novel 2009 H1N1 influenza viruses was also studied by Lee and coworker [33]. Both 1918 and 2009 complexes were predicted to have a similar binding free energy (-7.30 and -8.04 kcal•mol⁻¹ for 1918 and 2009, respectively). Therefore, the authors concluded that the human receptor exhibited no binding preference between the 1918 and 2009 H1N1 HAs. This conclusion is apparently different from those of the previous work [31], possibly due to the use of different starting protein structures.

2.5. Progress on HA Inhibitor Development

Currently, anti-influenza drugs targeting on NA (oseltamivir (OTV), zanamivir (ZNV), peramivir (PRV) and laninamivir (LNV)) and the membrane M2 channel (amantadine (AMT) and rimantadine (RMT)) are clinically available; however, their efficiency is limited owing to the emergence of drug resistance [34-41]. Due to a critical role of HA in the influenza life cycle, it has become an attractive target for drug design and development of anti-influenza drugs and vaccines. Up to now, no drug active against HA has been

approved by FDA, and this fact leads to great efforts in research in this field aimed to discover high selective and effective HA inhibitors. One of the factors to hamper the development of HA inhibitors is the HA-subtype dependent activity. The HA inhibitors could possibly divided into three different groups; (i) fusion inhibitor, (ii) receptor binding inhibitor, (iii) peptide and non-peptide fusion/entry inhibitor. Among these, the fusion inhibitors showed the most advance progress [1, 3]. Compounds such as benzoquinones and hydroquinones were reported to prevent the low-pH induced conformational change of HA [42, 43]. The tert-butyl hydroquinone (TBHQ, Fig. 7A) showed potent activity with IC_{50} values of 5 to 10 µM against the conformational rearrangement of H3N2. The experimentally resolved structures of TBHQ bound to H3 and H14 HAs demonstrated that the inhibitor bound in a hydrophobic area at the interface between HA monomers [43]. This study highlighted an understanding of the protein-ligand interaction and drug mechanism of action.

Using a ligand-based similarity approach, 1-phenyl-cyclopentanecarboxylic acid (4-cyano-phenyl)-methyl-amide (4t) (Fig. **7B**) with the IC_{50} value of 98 nM against H1N1 was identified [44]. A novel class of influenza A virus fusion inhibitor was identified by Vanderlinden and colleagues [45]. The most active compound, 4c (Fig. **7C**) exhibited 50% antiviral effective concentration (EC_{50}) value of 3-23 μ M. This type of compound showed activity against H3 but not the H1, H5 and H7 subtypes. However, either single or a combination of three substitutions D112N (in HA2), R220S (in HA1) and E57K (in HA2) could induce drug resistance mutation of this particular compound.

In addition to the aforementioned three main classes of anti HA viral compounds, a novel group of post-translational inhibitors was suggested. In the study by Rossignol *et al.* [46], thiazolides inhibited the replication of H1N1 virus by blocking the maturation of viral HA at the post-translation level. Compound RM5014 (Fig. **7D**) was the most potent inhibitor with the EC_{50} value of 0.1 µg/ml, 10 times more active than the parent nitazoxanide compound (Fig. **7E**).

As demonstrated above, much progress in the discovery and development of inhibitors against the HA viral could bring to the hope of a successful finding new anti- influenza drugs.

Fig. (7). Chemical structures of HA fusion inhibitors.

3. NEURAMINIDASE (NA)

3.1. Roles of NA

Neuraminidase (NA), one of two glycoproteins on the surface of influenza virus, is responsible for cleaving the terminal sialic acid from the host receptors in the viral replication cycle. By blocking the NA activity, the new infectious virions cannot be released from the host cell, therefore, NA is an important target for antiinfluenza agents in the treatment and prophylaxis of influenza infections. NA predominantly existed as a tetramer of high molecular weight, 240 kDa, as shown in Fig. 8. Based on its phylogenetic tree, the nine subtypes of NA, named N1-N9, are classified into two groups, group-1 (N1, N4, N5 and N8) and group-2 (N2, N3, N6, N7 and N9). The main discrepancy in the structural feature between the two NA groups was revealed by Russell et al. in 2006 [47]. The 150-cavity, formed by open conformation of the 150-loop (residues 147-152), was found adjacent to the sialic acid binding pocket in the group-1 NA (Fig. 8). However, the viral influenza pandemic H1N1 NA recently crystallized lacks this cavity [48]. The highly conserved active site in all subtypes consists of the catalytic residues (R118, D151, D152, R224, E276, R292, R371 and Y406) and the framework residues (E119, R156, W178, S179, D198, I222, E227, H274, E277, N294, and E425).

Up to date, the four anti-influenza drugs (zanamivir, oseltamvir, peramivir and laninamivir in Fig. 9) targeting NA are available to combat the influenza virus. Zanamivir (trade name Relenza® marketed by GlaxoSmithKline) used by oral inhalation is the first NA agent developed through rotational drug design. Oseltamivir (Tamiflu® tablet from Roche) is the most common used for influenza treatment. Peramivir (Rapiacta, brand name in Japan) developed by BioCryst Pharmaceuticals was issued by the Food and Drug Administration as emergency use to treat patients infected by pandemic H1N1 in October 2009. Laninamivir (Inavir made by Daiichi Sankyo Co. Ltd.) recently approved and released in Japan in September 2010 shows the long-acting inhibitory activity against the influenza virus.

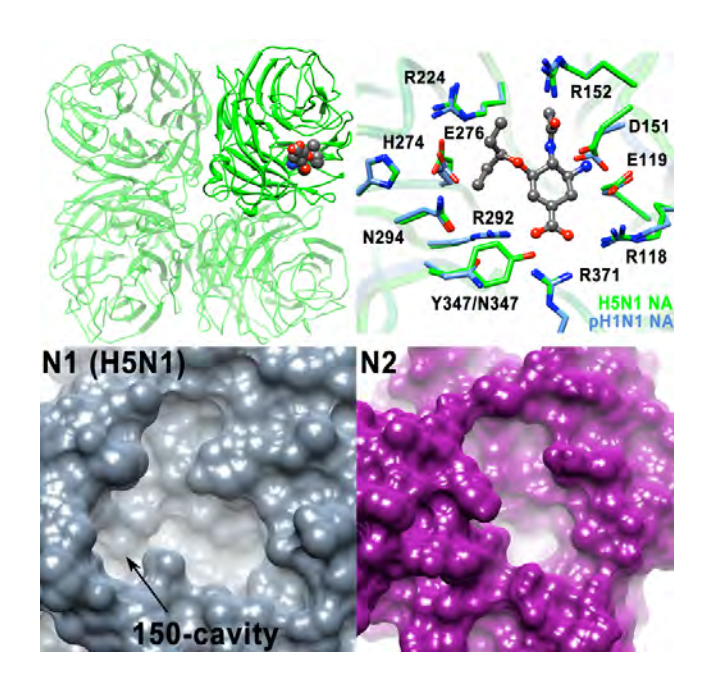


Fig. (8). Tetrameric neuraminidase with drug bound. Close up of oseltamivir and its surrounding residues in NA subtype N1 of the influenza H5N1 and pH1N1 viruses. The active site cavity of NA subtypes N1 and

3.2. Substrate Binding Specificity in Neuraminidase

While the HA specific binding to sialylated glycan on the target cell-surface receptor is widely known, the NA substrate specificity has been rarely reported. Recently, Raab and Tvaroška [49] had revealed the NA substrate specificity for H5N1 virus using SA and two trisacchrides, SA-α2,3-Gal-Glc (3SL) and SA-α2,6-Gal-Glc (6SL). The results shown that the transition from the B_2 to the 2C_5 conformation was found in SA while the distorted boat conformation was adopted for both trisaccharide. With comparable ligandprotein binding in the three complexes via the E276, R292, Y347, R371 and Y406 residues (Fig. 10), the SA1 unit of the two trisaccharides were proposed to stronger interact with the binding pocket than the sialic acid alone. The Gal2 unit of 3SL was stabilized by the N247 and Y347 residues and its sialic acid, whereas the last unit, Glc, of 6SL had partial interactions with the 150-loop residues, D151 and R152 as well as its SA. Therefore the α2,3 linkage was more likely stable than α2,6 linkage. The strength of the substrate binding is in the following order: 3SL > 6SL >> sialic acid. This might be a reason that an avian N1 was experimentally found to cleave the SA-α2,3-Gal glycoconjugates better than the SA-α2,6-Gal [50-52].

3.3. Oseltamivir Efficiency Toward the Group-1 and Group-2 **NA Strains**

To understand why the most widely used NA inhibitor, oseltamivir (OTV), has lower effectiveness for the inhibition of N1 subtype (NA group-1) than N2 and N9 (NA group-2), OTV binding to these three NA subtypes in aqueous solution was studied using MD simulations [53]. Although the hydrophobic pocket was formed for the three complexes via the hydrogen bond between N1 R224 and E276 residues to accommodate the -OCHEt2 group of OTV, lower drug-target interactions at the N1 active site was found relative to those of the N2 and N9 complexes. This is due to the dramatic changes in drug conformation at the -NHAc and -OCHEt2 moieties, i.e., their conformations in the N1 binding pocket were rotated by 40-60 degree from those of N2 and N9. These changes had induced an adjustment in the position and orientation of

Fig. (9). Chemical structures of the four available anti-influenza drugs (OTV, ZNV, PRV and LNV) and the new potent inhibitors against influenza NA target.

Fig. (10). Schematic representation of three substrates, sialic acid (SA), SA- α 2,3-Gal-Glc (3SL) and SA- α 2,6-Gal-Glc (6SL) interacting with the binding residues of H5N1 NA shown with the most preferential intermolecular distances (Å) approximated from the last 2.5 ns of simulations [49].

the surrounding amino acids. In addition, the calculated binding free energy based on molecular mechanics Poisson-Boltzmann surface area (MM-PBSA) reveals the lower susceptibility of OTV to influenza NA subtype N1 than those of in N2 and N9. This is may be due to the rotational design of commercial NA inhibitors is primarily based on the NA group-2. Therefore, designs of novel antiviral agents according to the N1 crystal structure are needed and reviewed hereafter.

3.4. Key Binding Interactions at the Sialic Acid Site in N1 3.4.1. Avian Influenza A H5N1 Virus

Identification of key inhibitor-binding residues is a key factor for understanding the enzyme function as well as for developing the new potent inhibitors. The MD simulation approach was extensively used of a powerful tool for this purpose.

Malaisree *et al.* [54] had conducted MD simulations for the three commercially available NA drugs (OTV, ZNV and PRV as shown in Fig. 9) in the closed conformation of H5N1 NA protein.

The -COO group of inhibitor generally interacted with the three conserved arginines, R118, R292 and R371, as well as Y347 through hydrogen bond formations. Long range interaction with R118 was found instead of hydrogen bond in OTV system. In contrast, hydrogen bonds with the three conserved arginines were totally disappeared in the PRV-N1 simulation using the GROMOS force field and SPC water model [55]. Lawrenz et al. [56] demonstrated that, without Ca2+ binding near the NA active site, Y347 flipped out of the pocket and unable to interact with the -COO group of inhibitor leading to a reduced affinity of drug binding by 3-5 kcal•mol⁻¹. At the positively charged side chain of inhibitors, the E119, D151 and W178 residues stabilize the ammonium group of OTV and the guanidinium group of ZNV and PRV. Although the longer guanidinium group also formed hydrogen bonds with E227, only that of PRV with different orientation (Fig. 8) had two more binding residues, E277 and Y406. The R152 and E277 provide hydrogen bond interactions to the -NHAc group of all three drugs. The E276 and R224 form hydrophobic pocket to accomodate the -

OCHEt2 of OTV and PRV, while the R224, E276 and E277 stabilize the hydrophilic group of ZNV via hydrogen bonds. In agreement with those proposed by Malaisree et al. [54], the -OH substituent on the 5-membered ring of PRV firmly forms a hydrogen bond with D151 closely resemble to the natural NA substrate, sialic acid [57].

The tamiphosphor, the phosphonate congener of OTV, and its analogs showed more inhibitory potency than OTV against the native NA strains of the H1N1 and H5N1 influenza viruses [58]. Udommaneethanakit et al. [59] had adopted this idea and utilized MD technique to study the three known NA drugs and their phosphonate analogues (OTP, ZNP and PRP in Fig. 9) in both closed and open forms of NA of the H5N1 virus. The replacement of the - COO° group by the $-PO_3^{2-}$ group led to more effective interactions with the surrounding residues, R118, Y347 and Y406, resulting in a stronger binding affinity with N1 enzyme. However, the negative net charge of the phosphonate compounds could repel the negatively charged D151 residue of the flexible 150-loop away from the active site causing the more likely open N1 form. The 13b compound, tamiphosphor with the large basis group (Fig. 9), showed more preferential binding potential to this residue of the 150-loop [60]. The OTV-2 compound with -CH₂NH₃⁺ substitution on the C3 position of OTV (Fig. 9) was suggested to be a drug candidate since it showed highly predicted binding affinity through an additional interaction with E119 as well as good bioavailability [61].

3.4.2. Pandemic Influenza A H1N1 Virus

In February 2009, the pandemic influenza A H1N1 virus (pH1N1) emerged from swines in Maxico and rapidly spread worldwide had raised a global human health concern. This new influenza virus already contains the adamantine-resistant mutation in M2 protein. After a couple months of outbreak, Rungrotmongkol et al. [35] had modeled the complex structure of the A/California/ 04/2009 (H1N1) NA strain with the most important anti-influenza drug, OTV, using homology modeling and multiple MD simulations. Among the active site and framework N1 residues (Fig. 8), the main difference between the H5N1 and pH1N1 NAs is the important residue Y347 in the H5N1 NA replaced by asparagine in the pH1N1 NA. Although the hydrogen bond interaction with N347 cannot be formed, the -COO moiety could strongly interact by the argentine triad including R118. This finding together with the other drug-target interactions conserved could explain the OTV ability for treatment of infected pH1N1 patients. The comparative study of OTV and ZNV in the N1 cavity of Spanish H1N1, H5N1 and pH1N1 viruses presented a relatively conserved and unique drug binding pattern among all different N1 strains [62]. More intermolecular interaction through hydrogen bonds with ZNV than OTV was detected.

3.5. Source of Oseltamivir Resistance

The NA inhibitors are effective for treatment of the current nonseasonal influenza viruses, H5N1 and pH1N1, however, the emergence and spread of drug-resistant strain remains a major concern on the national and global public health. Beside the single amino acid replacements, E119V/I and R292K, in N2 and N9 conferring OTV resistance [37, 64-66], the H274Y and N294S (H275Y and N295S in N1 numbering) single substitutions on the framework residues are the most frequent OTV-resistant mutations in N1 subtype [38, 40, 67, 68]. The reduction in the inhibitory potency of OTV was found in treatment of patients infected with the H274Y and N294S H5N1 and the H274Y pH1N1 variants [69-71]. To develop new potent antiviral agents to be used for treatment of both native and drug-resistant influenza H5N1 and pH1N1 virus infections, a clear understanding of OTV resistance due to these known mutations in molecular level is required.

Using MD technique, Malaisree et al. [34] simulated the 3Dstructural model of avian H5N1 NA with H274Y mutation in complex with OTV. The simulated results indicated that replacement on the framework residue 274 from histidine to tyrosine pushed the E276 side chain much closer to the -OCHEt2 group of OTV (Fig. 11A). This phenomenon led to a formation of significantly reduced pocket size and hydrophilicity in the area around the drug bulky moiety which was unsuitable to accommodate the OTV molecule. In addition, the rotated E276 firmly formed hydrogen bonds with R224 better than those in wild type. With the stability of E276-R224 hydrogen bond pair, Park and Jo [72] suggested that water penetration to the region between the -OCHEt2 group and E276 may cause the resistance of H274Y mutant to OTV. Rungrotmongkol et al. [63] reported the reduction of the electrostatic and the van der Waals interaction energies at the -NH3 and -OCHEt2 groups of OTV, respectively, in correspondence with the decreased hydrogen bond strengths and increased distances with their surrounding residues in the H274Y mutant of H5N1 NA. This differs for N294S mutation, i.e., diminutive changes of functional group contribution in binding energies and intermolecular interactions with N1 residues. Moreover, the E276 conformation in N294S was dissimilar to that of H274Y, since it served as the hydrogen network center interacting with R224 and S294, the mutated residue (Fig. 11B). Almost all results were consistent with Wang and Zheng's study [39] except the absence of the salt bridge between E276 and R224 formed at the end of H274Y simulation while this interaction was maintained in N294S. Altogether, the information revealed from

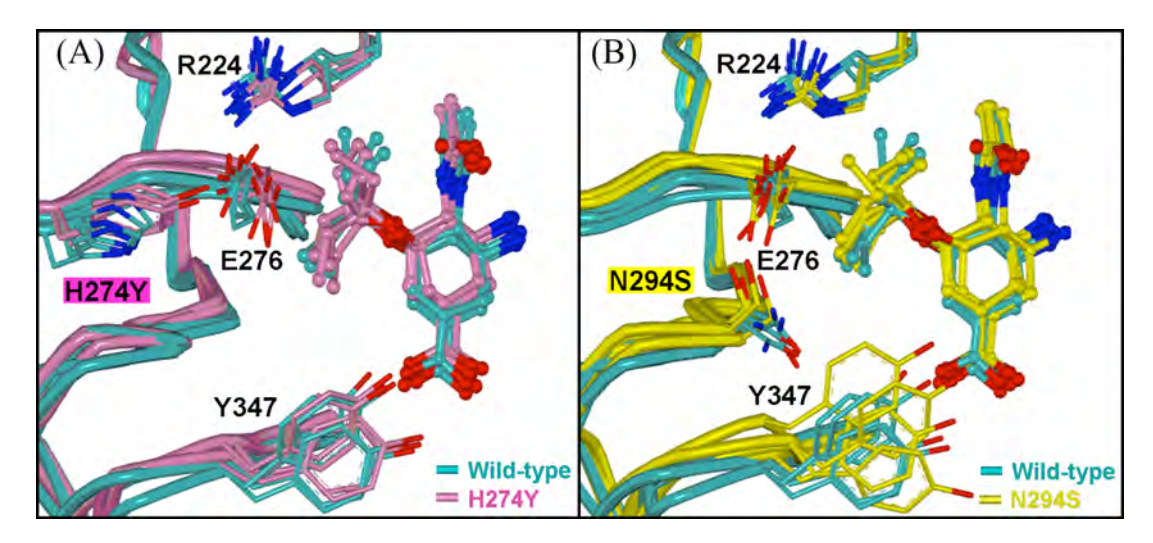


Fig. (11). Structural alignment between the MD snapshots of the wild-type and mutant strains, H274Y and N294S [63] (copyright 2009 Elsevier).

MD simulations considerably is in contrast to the hypothesis of reduction in OTV susceptibility over the single NA mutants R292K, H274Y and N294S [73-75].

3.6. Prediction of Drug Efficiency to Probable pH1N1 NA Mutants

After the pH1N1 outbreak, the strains of influenza resistance to the current anti-influenza drugs were not unexpected. Prediction of drug inhibitory potency against the probable pH1N1 NA mutants could provide the useful data in drug design and preparation for the next epidemic and pandemic of potential drug-resistant pH1N1 strains. Rungrotmongkol et al. [36] had modeled and evaluated the OTV efficiency over the four single substitutions H274Y, N294S, E119V and R292K in pH1N1 NA. In Fig. 12, the mutations at the binding site of OTV, E119V and R292K, had noticeably caused a loss of drug-target interactions energies particularly in terms of electrostatic interactions at the -NH₃⁺ and -COO groups of OTV, respectively, corresponding to the disappearance of hydrogen bonds with the mutated residue. In contrast, the other two mutations occurring at the framework site, H274Y and N294S, had decreased the van der Waals interaction at the -OCHEt2 side chain of OTV and the weakened hydrogen bond with R118 and E119. Based on linear interaction energy (LIE) method, the OTV-resistant level was predicted according to the reduced binding free energy relative the wild type strain: $R\overline{2}92K > E119V \approx H274Y > N294S$. It is noteworthy that, WHO received the first report of OTV-resistant (H274Y) pH1N1 virus in July 2009. Later on, the predictive ZNV affinity towards the series of the possible pH1N1 NA mutants R292K, R152K, E119A/D, and H274Y was studied by Pan et al. [76]. In contrast to OTV, the pH1N1 H274Y variant does not confer the resistance to ZNV. ZNV will lose its inhibitory activity over the four single substitutions on the drug binding residues in pH1N1 NA (R292K, R152K and E119A/D) due to the loss of polar interactions with the mutated residue. This is similar to what found in E119V and R292K OTV-resistant models [36]. Furthermore, the order of reduced ZNV activity predicted against the mutated models is $R292K >> R152K \approx E119D > E119A$.

3.7. Progress on Development of New NA Inhibitors

The discovery of the open N1 conformation with the 150-cavity and 430-cavity adjacent the sialic acid binding site has provided the new opportunity for drug design of anti-influenza inhibitors [47, 77]. Using the open N1 as receptor for docking, Du et al. [78] had suggested that the modified OTV analogs with different numbers of hydroxyl group substitutions on the hydrophobic side chain and – NHC(=NH₂⁺)NH₂ replacement on -NH₃⁺ group showed increased binding affinity and favorable conformation in the active cavity. Cheng et al. [79] had performed the ensemble based virtual screening of the National Center Institute diversity set on either crystal structure or the apo and holo MD snapshots of influenza A subtype N1 [77]. It is interesting that, among the 27 top hits, 14 of them cannot be found by docking to the crystal structure alone, since their favorable binding site was in the 150-cavity and/or 430-cavity. Rungrotmongkol et al. had applied the computer-assisted combinatorial techniques to design, focus and in silico screen a virtual library of OTV analogs [80] and the pyrrolidine analogs [81]. From the large diversity combinatorial library, the small highly focused combinatorial subset of both designed analogs was proposed to contain NA inhibitors with considerably higher potencies toward the N1 enzyme than their parent inhibitors, OTV and A-315675 (Fig. 9). The R-groups of the designed analogs (Fig. 13) are useful as a guideline for developing a next generation of antiviral agents.

4. M2 PROTEIN CHANNEL

The structures and functions of the M2-channel were initially studied since the early 1900s using different techniques such as

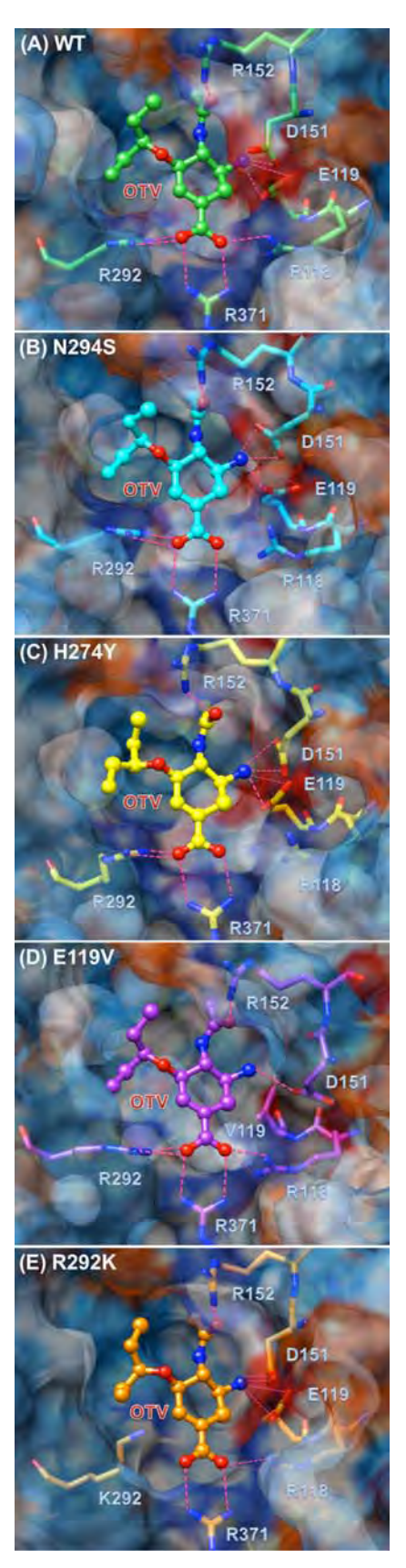


Fig. (12). Hydrogen bonds formed with OTV, represented by red dashed line, in (a) wild-type and (B-E) four possible mutants of pandemic H1N1 virus (adapted from ref. 36).

functional mutagenesis [82-84], site-directed infrared dichroism [85], solution NMR (solNMR) [86], solid-state NMR (ssNMR) [87-93], X-ray crystallography [90, 94] and computational modeling [95-99]. Several aspects including the M2 function in viral life cycle, structural characteristics, proton transport mechanism, drug inhibition and drug resistance were identified.

4.1. Roles of M2 Channel

The influenza A virus M2 protein, a tetrameric type III integral transmembrane (TM) protein, is known to play an essential role in viral replication by mediating the acidification and uncoating of endosomally entrapped virus. The tetrameric M2 in the viral membrane functions as pH-dependent proton channels [83, 100, 101] to equilibrate pH across the viral membrane during entry and across the trans-Golgi membrane of infected cells during viral maturation [102-104]. After endocytosis and before HA mediated fusion between viral and endosomal membrane, the M2 channels are activated by the low pH of the endosome to conduct protons to acidify the viral interior. The acidification was suggested to weaken electrostatic interaction between ribonucleoprotein (RNP) complexes and matrix proteins. Consequently, membrane fusion can release the uncoated RNPs into the cytosol for transporting into the nucleus [105]. However, this proposed mechanism is not yet validated by further experimental evidence. At a later stage, the following processes take place during viral assembly, (i) the newly synthesized viral proteins are transported to the cell surface by trans-Golgi network (TGN), (ii) the viral membrane proteins are topologically inverted in the TGN membrane, and (iii) the functional domain of HA is exposed to the low pH of the Golgi lumen and it is susceptible to premature rearrangement to the fusion-active conformation. To preserve the high pH form of nascent HA, protons were transferred out of the TGN through the M2 channels [102]. Note that proton specific conductance of M2 is activated by low pH, evidenced by the channel recordings [104, 106, 107].

4.2. Structures of the M2 Channel

The M2 protein channel consists of 97 residues: (i) an ectodomain (residues 1-24); (ii) the pore-forming TM helix (residues 25-43); (iii) an amphiphilic C-terminal helix (residues 47-60); and (iv) a cytoplasmic tail (residues 61-97). Both experimental and computational approaches were used to determine the structures of M2 channel, discussed below.

4.2.1. Experimental Structure of the M2 Channel

A number of experimental studies were carried out and revealed dramatically different structures of the M2 transmembrane domain with/without C-terminal at different pH conditions where H37 can be non-protonated (0H), one-protonated (1H) and two-protonated (2H) for high pH ($pH \sim 6.5$ -8) as well as three-protonated (3H) and fully-protonated (4H) for low pH ($pH \sim 5$ -6). Even now, the recent high faithful techniques have provided a similar topology of elementary M2/TM structure as previous, in which the TM helices gather into a left-handed twist in four-helix bundle protein. Its residues exhibit a repeating helical periodicity of 3.6 amino acids per

oseltamivir scaffold

Aliphatic and Aromatic Alcohols-R₄

Aliphatic Acyl Halides and Anhydrides-R2

Aliphatic Andehydes and Ketones and Thioureas-R3

$$H_2N$$
 NH_2
 NH_2

$$R_2O$$
 R_3
 R_1
 R_1
 R_2
 R_3
 R_4

pyrrolidine scaffold

Grignard Reagents (R₁-groups)

Aliphatic & Acyl Halides (R2-groups)

Grignard Reagents (R3-groups)

Amines & Aliphatic Oxide (R4-groups)

Fig. (13). List of the most favorable R-groups obtained from the final combinatorial subset [80, 81].

Fig. (14). Comparisons of the recent experimental structures: X-ray (3BKD, 3C9J and 3LBW), ssNMR (2KQT and 2L0J) and solNMR (2RLF).

turn. The M2 pore is lined by polar residues S31, G34, H37 and W41 and a non-polar residue V27 of the TM sequence. The imidazole ring of H37 acted as *pH* sensors [108]. The pore constriction is found at two places, V27 positioned near the N-terminal end and H37/W41 closed to the C-terminal end. In other words, the H37/W41 gating residue plays an important role in M2 channel [109], while the secondary gate was formed by V27 at the channel entrance [110]. The cavity formed between these two important residue regions is the drug binding site [91, 108, 110]. Among experimentally resolved 3D-structures of M2/TM (Fig. 14), they are considerably different in details for describing the mechanism of proton conduction, drug inhibiting and drug resistance.

The first M2/TM (residues 22-46) crystal structures (3BKD and 3C9J) were explicated by Stouffer et al. [90], in which the two forms in the absence and presence of the AMT channel-blocking were crystallized in β -octylglucoside (OG) detergent environment at resolutions of 2.05 Å and 3.5 Å, respectively. The free channel at pH 7.3 (3BKD) was suggested as a mixed protonation state of H37 tetrad on the basis of the known pKa value. Their isolated models called as A4- and D4-models represent open and closed channel conformations that pull in the C-terminal gating region diverse and converse of four-helix bundle, while they are tightly packed at the N-terminal end. The closed D4-model exhibited the R45-D44 salt bridge, while this was not detected in the spray out of the open A4model. The M2-bound form (3C9J) was crystallized at a lower pH of 5.3 supporting the open channel structure with a presence of AMT. The crystal structures of the AMT-bound at low pH (3C9J) and the drug-free at high pH M2/TM (3BKD) showed a nearly identical drug-binding site in consistent with AMT inhibitory ability at pH 5-8 [111-113].

In 2008, Schnell et al. [86] determined the solNMR structure of the closed conformation of M2 residues 18-60 in complex with four RMTs located in the lipid-facing pocket at pH of 7.5 in dihexanoyl-phosphatidyl-choline (DHPC) detergent micelles (2RLF). Each subunit has N-terminus (residues 18-23), TM helix (residues 25-46), short flexible loop (residues 47-50) and C-terminal amphipathic helix (residues 51-59). The TM helix has a twist angle of 23° leading to the extremely narrow channel that cannot accommodate an inhibitor. At high pH, TM helices were tightly locked by intermolecular interactions between W41 and D44. This TM packing is destabilized by pH reduction leading to an unlocked gate conformation, and the proton conduction through waters is consequently occurred. The extended loop (residues 47-50) at C-terminal end is connected with amphipathic helix lying almost perpendicular (~82°) to the TM helices using a packing mode right-handed to form the channel base (Fig. 14, 2RLF). This segment could adopt a more stable conformation in the viral membrane when C50 is mutated to S to avoid the disulphide formation.

In 2010, Cady *et al.* [108] had proposed the ssNMR structure (2KQT) of AMT binding to M2/TM (residues 22-46) at *pH* condition of 7.5 in dimyristoylphosphatidylcholine (DMPC) which is expected to better mimic a biological membrane than micelle. The four helices of this M2/TM structure are kinked at G34, with the helical axis tilted by 30° for the N-terminal segment and 19° for the C-terminal segment, in consistent with ¹⁵N ssNMR orientational constraints [92]. The narrowest points of the pore lie at the N-terminal V27 and C-terminal H37/W41, which are involved in *pH* sensing and proton-conducting activity of M2 channel [109].

Furthermore, Acharya and coworkers [94] presented a high-resolution (1.65 Å) crystallographic structure of the M2/TM protein (residues 25–46) in apo form at *pH* 6.5 (3LBW). This corresponds

В Viral Exterior I. Histidine-Locked State Viral exterior н **Viral Interior Acid Activation** Conductance Viral interior H_2O III. Conducting State **II. Activated State**

Fig. (15). The recent proposed mechanisms of proton transportation through the M2 channel via the H37 from A) Hirata group [126] and B) Sharma et al. [115].

Tryptophan Gating

to an intermediate protonation state (with diprotonated histidines, 2H) of the channel [114], providing a pathway for proton conduction. A network of hydrogen bonds from water molecules favorably contributed to the M2 channel from below the pore lying residues 27 to almost interior of the virus, excepting for the W41 region.

Recently, Sharma et al. [115] reported the apo M2 structure with spanning residues from 22 to 62 (2L0J) in 1,2-dioleoyl-snglycero-3-phosphatidylcholine: 1,2-dioleoyl-sn-glycero-3 phosphoethanolamine (DOPC: DOPE) bilayers solved by ssNMR at pH of 7.5. This structure is spectacularly different from the earlier solNMR M2 structure (residues 18-60) in detergent micelles (2RLF) [86]. Within residues 26-46, the kinked TM helix at G34 is comparatively similar to the kinked TM domain with AMT bound [92], where the N-terminal and C-terminal ends showed tilt angles of ~32° and ~22° relative to the bilayer normal, respectively. The C-terminal of the amphipathic helices is situated with allowance to form the tetrameric M1 binding domain.

4.2.2. Dynamical View of the M2 Channel Structures

As mentioned earlier, different techniques used such as ssNMR, solNMR and X-ray led to different M2 structures. In the MD studies using the ssNMR structure, H37/W41 gate was almost found in closed form at low protonation state and open form at high protonation state [96, 97, 99], in which the V27 is always opened. It was also proposed by Arkin group that proton transfer is appreciably taken place only in the system with two or more charged histidines in which the gate can be opened because of the electrostatic repulsion between the charged histidines [96]. Intharathep et al. [116] have shown that the channel is closed at low protonation state while at high protonation state, the electrostatic repulsion of the charged histidine leads to the pore opening and thus enhancing the accessibility of water into the pore. Chen et al. [97] and Hu et al. [114] reported that the highest proton permeability is the triply protonation state of H37. In addition, the secondary gate was found at V27, in which the water wire was alternatively broken by the primary (H37/W41) or secondary (V27) gates, i.e., the two gates were broken one by one. This fact was supposed to be a reason supporting the evidence of very low proton conductance in M2 channel. Leonov et al. [99] performed MD simulations using the X-ray (3BKD), ssNMR (1NYJ) and solNMR (2RLF) structures. They found that the X-ray one is the most stable, however, the water conductance was not correlate to the protonation state of the channel since it always closes at V27 in the 0H and 2H states and even at low pH in the 3H state. Khurana et al. [98] have conducted MD simulation using D4-model in which the tetrameric M2 channel was duplicated from D4-bundle of the X-ray structure (3BKD). They found that at high pH the channel is opened at the V27 and closed at H37 gates, and in vice versa at the low pH.

4.3. The M2 Gating-Like Mechanism

From the 97 amino acids of M2, the C-terminal amphipathic helices is found to stabilize the tetramer by intermolecular contacts. The two intermonomer disulfide bonds between residues C17 and C19 of the ectodomain of M2 are thought to stabilize oligomeric assembly, helping in incorporation into budding virus particles [83, 100]. In addition, a cytoplasmic tail was found to facilitate virus assembly by binding to the M1 protein [117, 118].

As known the H37 tetrad of the M2 channel has been indicated important in its gating mechanism. Mutants of the M2 channel at this residue replaced H by G, S, or T residues lead to the loss of their proton selectivity [119]. This function can be restored upon addition of imidazole group indicating its important role in proton selectivity. Regarding the pH controlled gating mechanism, it was suggested that the H37 was found to act as a pH sensor switch to turn the gate "on" and "off", in which only protons are allowed to penetrate through this highly selective filter [114]. The pKa's of the four histidines at the gating region are different from one another, in which the triply and quadruply protonated histidines are determined for the open forms of the M2. In addition, when W41 is replaced by the smaller size residues such as A, C, or F, the higher proton conductivity was observed compared to that of wild type. With Raman spectroscopy, a cation- π interaction between the protonated imidazole of H37 and the indole of W41 was found to play an important role to turn the gate "on" and "off". Recently, V27 was proposed to form a secondary gate [110], however, the data from the mutagenesis are not conclusive. Pinto and coworkers reported an increase of proton transport when V27 was replaced by A or D while the reductivity was found for the replacement by residues S, T, G, K, R, F or W [120]. In contrast, Holsinger et al. showed that the mutation of V27 to A, S, or T does not change the current of protons [121].

The unknown function of the C-terminal which might plays a critical role in membrane assembly was also studied by cystein mutagenesis. Previously, Tobler *et al.* [122] demonstrated that the C-terminal could be deleted without effecting proton conductivity,

although it was found that shorter fragments had poor surface expression in oocytes. Recently, the fragment residues 21-61, 21-51 and 22-46 in *Xenopus* oocytes were studied and compared. The results showed that the assembly, drug binding and proton translocation in both micelles and bilayer can be studied with confidence by using the short fragment M2/TM only.

4.4. The Proton Transport Mechanism

As known, the M2 channels are very selective for protons [106, 122-124]. The rate of transportation of wild-type M2 channel of c.a. 105 protons per tetramer per second at pH 5.7 was found in endosomes [106, 122]. The mechanism of proton transport through the aqueous pore of the channel is actually not known yet. The two acceptable mechanisms are the shuttling and gating (or shutter). The first mechanism requires at least one non-protonated H37 that orients its two nitrogen atoms toward the channel pore surface [125]. A proton is proposed to transfer to the imidazole ring of H37 which is, then, releases to a neighboring water molecule. In the final state, the imidazole ring was flipped (or tautomerization) to the initial configuration to accept the next proton. Based on threedimensional reference interaction site model (3D-RISM) method, Hirata group [126] suggested that this model seems to be uncertain because two nitrogen atoms of the same histidine exposed to water inside the pore were not found. The MD simulation studies from Intharathep el al. [116] also did not found any histidine residue in such conformation. The second mechanism, "gating" or "shutter", claimed that water can form a proton wire through the channel in the open state [97, 127]. A proton transport from the hydronium ion to an adjacent water molecule is possible via the hydrogen bond formation between them, so-called Grotthuss (GT) mechanism [128]. The likelihood of the GT mechanism with a low proton conductance was suggested by the MD simulated results from Voth group [97].

Hirata group [126] proposed the new proton transport mechanism describing the low proton conductance of the M2 channel through two histidines, one protonated and another non-protonated (Fig. 15A). A hydronium ion and a water molecule attach the nitrogen atom of the non-protonated and protonated imidazole, respectively (step I in Fig. 15A). The proton transportation from a hydronium ion to the N_e atom of H37 imidazole ring, and the other protonated H37 releases the proton to a nearby water molecule. Consequently, these two H37 residues switch their protonation states from protonated to non-protonated and in vice versa (step II in Fig. 15A). Afterward, the two H37 residues move to the appropriate positions due to conformational fluctuations of protein (step III in Fig. 15A) to organize the next process of proton transfer (step IV in Fig. 15A). They also suggested that this mechanism is achievable only in the 3H state owing to the two reasons. Firstly, at least one non-protonated H37 is needed to bond respectively with a water and with a hydronium ion; therefore the possibility of the 4H state is excluded. Secondly, W41 tetrad in the closed 1H and 2H channels completely prevent water accessible from the gating area. This is thus no water molecules available in making a hydrogen bond with the imidazole ring of H37 inside the pore.

Recently, the crystallographers [115] proposed the M2 proton transport mechanism involving 2H state with two diagonal histidines protonated corresponding to closed conformation at $pH \sim 7.0$ [114]. This model clarifies the process of shuttling mechanism using the three states for the proton conducting: (i) histidine-locked-state, (ii) activated state, and (iii) conducting state. In histidine-locked-state (I), each dimer of adjacent H37 has shared proton via strong hydrogen bond between the N_{d1} and N_{e2} atoms on the imidazole ring (step I in Fig. 15B) with an energetically favorable situation [129]. The other two N_{d1} and two N_{e2} sites are pointed to the C-terminal end (step I and II in Fig. 15B). These protons on N_{e2} atoms make the hydrogen bond interactions with the indole rings of the W41 gating residues (step I in Fig. 15B), while hydrogen bonds

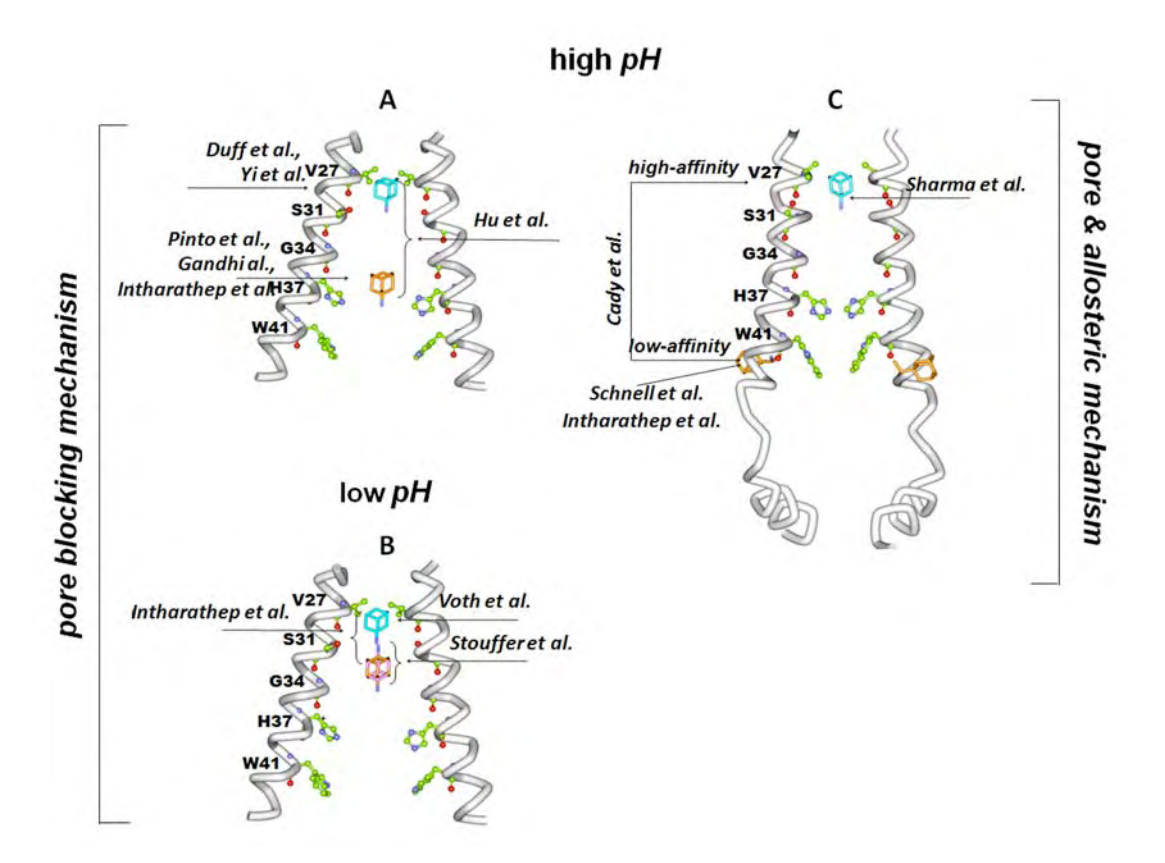


Fig. (16). The drug binding sites proposed based on structural, functional, and computational simulation data at high and low pH. The protein structure shown here is the structure from X-ray (3C9J) for blocking-model and solNMR (2RLF) for two sites, pore and allosteric-model.

were formed between the two protons on N_{d1} atoms and the backbone carbonyl oxygens themselves (step II in Fig. 15B). In activated state (II), a proton transfer process is taken place between the hydronium ion and the N_{d1}-N_{e2} hydrogen bond site with resulting in of the rotation of two imidazolium rings. This allows the protonated N_{d1} forming a hydrogen bond with water in the N-terminal pore while the protonated N_{e2} moving downward to form an ion- π interaction with the W41 indole ring, thereby blocking water accessible from the C-terminal pore (step II in Fig. 15B). The conducting state (III) is obtained when the indole moves away and exposes the Ne2 proton to a water molecule in the C-terminal pore. Once the Ne2 proton is released to C-terminal water, the HxxxW quartet then returns to the (I) state [115].

4.5. Inhibition of the M2 Ion Channel

As known, the proton conductivity can be inhibited by amantadine (AMT) and rimantadine (RMT), the first effective drugs licensed for influenza virus [130]. However, the main and urgent issue for the treatment of the M2 channel is the drug resistance [35, 41]. To study new and more potent inhibitors, mechanisms of action of known drug are essential. Fig. 16 shows the current issue of sciencetific research focusing to the location of drug binding to the M2 protein. AMT was found to inhibit the M2 with a 1: 1 stoichiometry [111]. The drug binding sites are often predicted by the location of drug-resistance to the mutant viruses L26, V27, A30, S31 and G34 (Fig. **16A-B**) [102, 104, 121, 123, 131].

It was suggested by Hay group that interaction between AMT polar group and S31 is the key feature of action of this inhibitor [83, 102]. However, the neutron diffraction studied by Duff et al. [132] indicated that AMT behaves as a 'blocker' in which its adamantyl group interacts with V27 via van der Waals interactions, while the charged amine group forms hydrogen bonds with S31. This is supported by the molecular modeling results by Sansom et al. [127] and Yi et al. [110]. Alternatively, based on Pinto et al. [82] and Gandhi et al. [84], AMT was proposed to bind at a location deeper in the channel where its ammonium group was found to interact with the nonprotonated nitrogen atoms on the H37 side chain via hydrogen bond. In addition, Hu et al. [92] suggested that the amino group of AMT was involved equally to interact with S31 and H37 side chains at high pH. The suggested binding site describing above is shown in Fig. 16A.

Based on the MD simulations studied by Voth group, the 3H triply protonated H37 was found to be the most likely open state in which the AMT primarily bound at A29, therefore reducing the proton conductance by 99.8% [97]. MD studies of the entirely six protonation states of M2 complexed with AMT and RMT by Intharathep et al. [116] suggested that the preferential position of the two drugs depends on number of charged His37. At low protonation states, polar group of inhibitor was found to point to the neutral H37 imidazole ring (Fig. 16A), while increasing the number of charged H37, the inhibitor was shifted up to the mount of the pore drawing the hydrogen bond between inhibitor's NH₃⁺ and S31 hydroxyl group. In addition, the two orientations of drug molecule can be inward and outward for high and low pH at the S31 of the M2 pore, that facilitate a large apolar group of the drugs to fit-well inside the hydrophobic pockets formed by V27- and G34-tetrad of the M2, respectively (Fig. 16B). In agreement with the experimental IC_{50} value, it was also found in this simulation study that water density in the open channel was inhibited more effective by RMT than AMT.

Based on crystallographic study, Stouffer et al. [86] have demonstrated that a single molecule of AMT was located in the Nterminal pore lumen. The drug was found to locate on the axis of the pore adjacent to S31. Two orientations of the drug, the amine

Fig. (17). The current M2 drugs, amantadine (AMT) and rimantadine (RMT), and the newly designed M2 inhibitors.

group either pointing inward or outward the aqueous pore was also observed depending on where the water is more hydrated. However, the inward orientation is recognizable as the preferential one. Here, a large apolar group snugly fits into the N-terminal end of the aqueous cavity, while its polar end projects toward, but does not directly contact with H37 (Fig. 16B). This is consistent with that observed experimentally where inhibitory activity is increased when the amino group of AMT is substituted by a more bulky alkylamines. Although Wang et al. [111] suggested that determining the structure of the drug complexed M2 protein at neutral pH is more important than the low pH state because the protein is only temporary populated in acidifying endosomes, while the drug firstly binds with high affinity to the protein near neutral pH. However, the existing of complexed structures at both low and high pH is important to provide much informative for understanding its mechanism of inhibition [108].

Beside the pore binding site mechanism described above, the drug molecules were also proposed to inhibit the activity of the M2 channel by locating outside the M2 pore (Fig. 16C). This mechanism is firstly proposed by Schnell et al. [86] and known as the allosteric mechanism where all drug molecules were observed to contact with the lipid membrane. They showed a solNMR structure at high pH of residues 18 to 60 (TM plus C-terminal) with four RMTs bound to the C-terminal lipid-facing pocket of the helices. Drug binding includes interactions with residues 40-45 from one TM (TMⁱ) and the adjuscent TM (TMⁱ⁺¹). A RMT polar group forms important hydrogen bond to D44ⁱ that further interact with W41ⁱ⁺¹ to lock the gate, while an andamantane bulky group lies within the hydrophobic pocket composed of $I42^i$, $L40^{i+1}$ and $L43^{i+1}$. Drug inhibition at the lipid binding pocket assists to stabilize the close conformation of the pore at high pH. This packing of TM helices was destabilized and unlocked the W41 gate when pH decreases. Based on this proposed drug binding approach, Intharathep et al.[133] have used MD simulations to study this allosteric mechanism at three pHs, i.e., RMT-M2 complexes at 0H, 1H and 3H protonation states. They found that at a neutral protonation state, a narrow channel with the RMT-D44-W41 hydrogen bond network was formed. This network is weaken at the 1H state and vanished when the number of charged H37 residue increases, i.e., the hydrogen bond network is less stable, allowing the W41 gate to easily open. Thus, the M2 channel at allosteric site can be effectively blocked at high pH only.

Recently, Cady et al. [108] have demonstrated based on ssNMR structure (2KQT) that two AMT-binding sites exist, one inside and another one outside the M2 pore. The high affinity site locates in

the N-terminal channel lumen. This site can be occupied by a single AMT in which its bulky apolar group is most likely oriented against the hydrophobic V27 side chains and the polar amine points toward the cavity near S31 residues. The second one is the external binding site, observed on the C-terminal protein. It has a low-affinity, taken place only when the drug in the bilayer reaches high concentrations.

The complex of AMT-M2 (residues 18-62) solved by Sharma et al. (Fig. 14, 2L0J) [115] showed drug binding inside the pore in a related way to the classical binding of drug. This is in contrast to the RMT binding site found at the hydrophobic pocket closed to D44 on the external surface at C-terminal end (Fig. 14, 2RLF) [86]. With larger tilt of 13° to the previous 2RLF structure, the relatively wider lipid-facing hydrophobic pocket filled by the I51 and F54 side chains in the amphipathic helix prevents the drug binding at D44 outside the channel (Fig. 14, 2L0J). This suggested that RMT bound at the protein exterior may be an artifact of the detergent environment used. The D44A and R45A mutations were shown to disturb the binding of RMT and confer a RMT-insensitive channel, but the single mutant, D44A, is still sensitive to AMT. This information led them to conclude that the drug binding site on the external surface of channel is not primary binding site in consistent with the pharmacological inhibition of M2 [120], but differs from the functional and structural experiments studied by Pielak et al. [107].

4.6. M2 Drug Resistance

The first class of anti-influenza A virus targeting the M2 protein channel, AMT, was introduced to the market since 1967. Twenty-six year later, the second M2 blocker, RMT, was consequently released. Although, clinical studies have demonstrated that either AMT or RMT effectively reduced the total number of influenza A cases by 60-70 %, their serious problems are corresponding to many neuropsychiatric side effects and the widespread of drug resistance [134]. A frequency of a global adamantane-resistant H3N2 influenza A virus was increased; 1% – 2% before 2002, 15% during the 2004–2005 influenza season, and 90.5% during the 2005–2006 season [135]. However, the H1N1 (25 % during the 2005-2006 seasons) virus displayed a lower degree of AMT resistance compared with H3N2 [41].

Single amino acid substitution at positions 26, 27, 30, 31 or 34 in the transmembrane region of the M2 proton channel predominately reduced drug inhibitory efficiency [95, 108, 111, 123]. The AMT-resistant H3N2 viruses were frequently detected at position 31 (70-80%) and a relatively low percentages were observed at the other sites; 10 % at either position 27 or 30 and 1-2% at position 26 [136]. The specific AMT-resistant mutations are likely to depend

upon viral subtypes. The S31N mutant was predominated in H3N2 and H5N1 strains while V27A was often found in H1N1 virus [137].

The recent outbreak of 2009 H1N1influenza A virus appears a combination of double V27A/S31N mutation, fully resistant to both AMT and RMT [138, 139]. Abed et al. [140] used reverse genetics to create and to characterize the recombination influenza A H1N1 mutations of L26F, V27A, A30T, S31N, and G34E in M2 gene. These mutant strains exhibited the IC_{50} values of 154- to 3300-fold higher than those of the wild type. The A30T mutant showed the very high-level resistance to AMT with a 3300-fold, while introductions of S31N, V27A and double V27A/S31N mutations were reported to be 267-, 1829-, and 154-fold, respectively. Furthermore, the high mortality percentage values of 87.5% and 68.75% in V27A/S31N and S31N mutants, respectively, were reported. The efficiency of AMT against the M2 mutants such as A30T and S31N was consequently investigated by means of MD simulation [141]. The A30T showed a water density higher than that of S31N. Furthermore, with the wider pore diameter, the important hydrogen bonding interactions between AMT and pore lining residues of A30T were eliminated, causing to AMT run out of the pore while the AMT in S31N mutant was observed to locate at the pore opening region and bond with V27 instead of S31 [141]. The results supported a high-level resistance of AMT to A30T in comparison with S31N.

Recently, Rungrotmongkol et al. [35] have suggested that the early 2009 H1N1 isolated from infected patients in southern California, A/California/04/2009 (H1N1), harboring mainly with V28I, S31N and L43T had strong resistance to AMT, which completely lost hydrogen bonding with the M2 residues. Substitutions of bigger amino acids, weaken and widen of the pore channel, were apparently associated with the reduced drug potency. Their results are corresponding to the proposed pore blocking resistance mechanism by increasing the channel diameter of the M2 mutation: (i) the channel is no longer binding to the inhibitor, (ii) channel is remain binding with the inhibitor but may not able to block the pore [95]. In addition, Pielak and co-workers [107] revealed that introductions of bulkier S31N and smaller V27A significantly reduce the helix-helix packing and hydrophobic interactions at the N-terminal ends of the membrane, respectively. In the models of allosteric drug resistance and pore blocking mechanisms, the M2 channel was proposed to destabilize the drug binding site at D44 and to decrease the hydrophobic interaction between inhibitor and the pore region, respectively.

4.7. Progress of Development of New M2 Inhibitors

On the urgent need to development of new anti-influenza, the discovery of new types of M2 inhibitor for replacement of the AMT and RMT becomes a crucial issue. This is due to the fact that the usage of these two current drugs was limited by central nervous system side effects and the rapid emergence of drug-resistant viruses. Over the past decade, nearly all reported M2 inhibitors were AMT derivatives, such as compounds 3-5 (Fig. 17) [142-144]. Compound 6 is one of the very few examples of nonadamantanebased M2 inhibitors designed [39, 84, 120].

Recently, Hu et al. [145] have reported the identification of several new hits as M2 inhibitors through the focused screening of a small primaryamine library [146]. The hits were as active as AMT against wild-type influenza A virus as determined by three kinds of assays, including cell-based, viral inhibition and patch clamp assays. Among them, compound 7 is the most potent inhibitor and is three times more active than AMT for viral inhibition ($IC_{50} = 1.363$ mM vs. 5.960 mM). Encouraged by these results, Zhao et al. decided [147] to modify the hit to further increase its potency. By keeping the scaffold constant and modifying the amino functionality, 14 analogs were made and evaluated for viral inhibition, as assessed by A/WS/33 (H1N1, AMT resistant) and A/Hong Kong/8/68 (H3N2, AMT sensitive) viruses [148, 149]. Most of the compounds in this study exhibited antiviral inhibition as good as AMT, and compound 8 was identified to be the most potent; it was nearly 240-fold more potent than AMT.

Based on nonadamantane compound 6, Wang et al. [150] have been searching for new classes of M2 inhibitors. With a structureactivity relation, the spiro-piperidine 9 was found as the most active with low IC_{50} of 0.92±0.11 µM. They also suggest based on that this spiro-piperidine 9 binds more extensive with M2 channel, thus leading to stronger inhibitory potentcy.

As reviewed above, a better understanding of the protein mechanism of action as well as drug-target interaction is expected to help the design of new and more effective drug; especially ones enable to fight the drug resistant variants.

ACKNOWLEDGMENTS

This work was supported by the Higher Education Research Promotion and National Research University Project of Thailand, Office of the Higher Education Commission (HR1155A), and the Thai Government Stimulus Package 2 (TKK2555) under the Project for Establishment of Comprehensive Center for Innovative Food, Health Products and Agriculture. . T.R. and P.Y. thanks the postdoctoral fellowship from the Ratchadaphiseksomphot Endowment Fund from Chulalongkorn University. N.N. (Grant No.MRG 5380255) and T.R. (Grant No. TRG5280035) acknowledge the funding for New Research from Thailand Research Fund. The Center of Excellence for Petroleum, Petrochemicals and Advanced Materials, Chulalongkorn University is acknowledged. The authors wish to thank Dr. S.T. Dubas for proofreading the manuscript, and A. Meeprasert, C. Rungnim and W. Khuntawee for their kind preparations of figures.

LIST OF ABBREVIATIONS

AMT Amantadine 3D Three-dimension

3D-RISM Three-dimensional reference interaction site

model

DHPC Dihexanoyl-phosphatidyl-choline **DMPC** Dimyristoylphosphatidylcholine

DOPC 1,2-dioleoyl-sn-glycero-3-phosphatidylcholine **DOPE** 1,2-dioleoyl-sn-glycero-3 phosphoethanolamine

ES Enzyme-substrate

FDA (U.S.) food and drug administration **FMO** Fragment molecular orbital method

Gal Galactose Glc Glucose GTGrotthus HA Hemagglutinin H-bond Hydrogen bond

HPIV High pathogenic influenza virus

INT Intermediate

LIE linear interaction energy **LPIV** Low pathogenic influenza virus

LNV Laninamivir MD Molecular dynamics

MM-GBSA Molecular mechanics generalized Born surface

MM-PBSA Molecular mechanics Poisson-Boltzmann sur-

face area

NA Neuraminidase

NMR Nuclear magnetic resonance OG = β -octylglucoside

OTP = Oseltamivir phosphonate

OTV = Oseltamivir

pH1N1 = Pandemic influenza H1N1 virus

PRP = Peramivir phosphonate

PRV = Peramivir

QM/MM = Quantum mechanics/molecular mechanics

TBHQ = tert-butyl hydroquinone
TGN = Trans-Golgi network
TM = Transmembrane
RMT = Rimantadine

RNP = Ribonucleoprotein

SA = Sialic acid 3SL = SA- α 2,3-Gal-Glc

 $6SL = SA-\alpha 2,6-Gal-Glc$

solNMR = Solution nuclear magnetic resonance ssNMR = Solid-state nuclear magnetic resonance

X-ray = crystallographic spectroscopy ZNP = Zanamivir phosphonate

ZNV = Zanamivir

REFERENCES

- Gong J, Fang H, Li M, et al. Potential targets and their relevant inhibitors in anti-influenza fields. Curr Med Chem 2009; 16: 3716-39.
- [2] Prakash S. Swine flu diagnosis and treatment edn First. Delhi: Biotech Books; 2009.
- [3] Jiang S, Li R, Du L, Liu S. Roles of the hemagglutinin of influenza A virus in viral entry and development of antiviral therapeutics and vaccines. Protein Cell 2010; 4: 342-54.
- [4] Bewley CA. Illuminating the switch in influenza viruses. Nat Biotechnol 2008; 26: 60-2.
- [5] Taubenberger JK. Influenza hemagglutinin attachment to target cells: 'birds do it, we do it'. Future Virol 2006; 1: 415-8.
- [6] Fouchier R, Kuiken T, Rimmelzwaan G, Osterhaus A. Global task force for influenza. Nature 2005; 435: 419-20.
- [7] Stevens J, Blixt O, Tumpey TM, Taubenberger JK, Paulson JC, Wilson IA. Structure and receptor specificity of the hemagglutinin from an H5N1 Influenza virus. Science 2006; 312: 404-10.
- [8] Krug RM, Aramini JM. Emerging antiviral targets for influenza A virus. Trends Pharmacol Sci 2009; 30: 269-77.
- [9] Skehel JJ, Wiley DC. Receptor binding and membrane fusion in virus entry: the influenza hemagglutinin. Annu Rev Biochem 2000; 69: 531-69.
- [10] Neumann G, Noda T, Kawaoka Y. Emergence and pandemic potential of swine-origin H1N1 influenza virus. Nature 2009; 459: 931-9
- [11] Gamblin SJ, Skehel JJ. Influenza hemagglutinin and neuraminidase membrane glycoproteins. J Biol Chem 2010; 285: 28403-9.
- [12] Ekici ÖD, Paetzel M, Dalbey RE. Unconventional serine proteases: variations on the catalytic Ser/His/Asp triad configuration. Protein Sci 2008: 17: 2023-37.
- [13] Hedstrom L. Serine protease mechanism and specificity. Chem Rev 2002: 102: 4501-24.
- [14] Ishida T, Kato S. Theoretical perspectives on the reaction mechanism of serine proteases: the reaction free energy profiles of the acylation process. J Am Chem Soc 2003; 125: 12035-48.
- [15] Ishida T, Kato S. Role of Asp102 in the catalytic relay system of serine proteases: a theoretical study. J Am Chem Soc 2004; 126: 7111-8.
- [16] Decha P, Rungrotmongkol T, Intharathep P, *et al.* Source of high pathogenicity of an avian influenza virus H5N1: why H5 is better cleaved by furin. Biophys J 2008; 95: 128-34.
- [17] Rungrotmongkol T, Decha P, Sompornpisut P, et al. Combined QM/MM mechanistic study of the acylation process in furin complexed with the H5N1 avian influenza virus hemagglutinin/s cleavage site. Proteins 2009; 76: 62-71.

- [18] Li M, Wang B. Computational studies of H5N1 hemagglutinin binding with SA-alpha-2,3-Gal and SA-alpha-2, 6-Gal. Biochem Biophys Res Commun 2006; 347: 662-8.
- [19] Iwata T, Fukuzawa K, Nakajima K, et al. Theoretical analysis of binding specificity of influenza viral hemagglutinin to avian and human receptors based on the fragment molecular orbital method. Comput Biol Chem 2008; 32: 198-211.
- [20] Xu D, Newhouse EI, Amaro RE, et al. Distinct glycan topology for avian and human sialopentasaccharide receptor analogues upon binding different hemagglutinins: a molecular dynamics perspective. J Mol Biol 2009; 387: 465-91.
- [21] Newhouse EI, Xu D, Markwick PRL, et al. Mechanism of glycan receptor recognition and specificity switch for avian, swine, and human adapted influenza virus hemagglutinins: a molecular dynamics perspective. J Am Chem Soc 2009; 131: 17430-42.
- [22] Matrosovich M, Tuzikov A, Bovin N, et al. Early alterations of the receptor-binding properties of H1, H2, and H3 avian influenza virus hemagglutinins after their introduction into mammals. J Virol 2000; 74: 8502-12.
- [23] Glaser L, Stevens J, Zamarin D, et al. A single amino acid substitution in 1918 influenza virus hemagglutinin changes receptor binding specificity. J Virol 2005; 79: 11533-6.
- [24] Sawada T, Hashimoto T, Nakano H, Suzuki T, Ishida H, Kiso M. Why does avian influenza A virus hemagglutinin bind to avian receptor stronger than to human receptor? Ab initio fragment molecular orbital studies. Biochem Biophys Res Commun 2006; 351: 40-3.
- [25] Sawada T, Hashimoto T, Tokiwa H, et al. Ab initio fragment molecular orbital studies of influenza virus hemagglutinin– sialosaccharide complexes toward chemical clarification about the virus host range determination. Glycoconj J 2008; 25: 805-15.
- [26] Sawada T, Hashimoto T, Tokiwa H, et al. Ab initio base fragment molecular orbital studies of influenza viral hemagglutinin HA1 full-domains in complex with sialoside receptors. J Mol Genet Med 2008; 3: 133-42.
- [27] Sawada T, Fedorov DG, Kitaura K. Role of the key mutation in the selective binding of avian and human influenza hemagglutinin to sialosides revealed by quantum-mechanical calculations. J Am Chem Soc 2010; 132: 16862-72.
- [28] Auewarakul P, Suptawiwat O, Kongchanagul A, et al. An avian influenza H5N1 virus that binds to a human-type receptor. J Virol 2007; 81: 9950-5.
- [29] Das P, Li J, Royyuru AK, Zhou R. Free energy simulations reveal a double mutant avian H5N1 virus hemagglutinin with altered receptor binding specificity. J Comput Chem 2009; 30: 1654-63.
- [30] Nunthaboot N, Rungrotmongkol T, Malaisree M, et al. Molecular insights into human receptor binding to 2009 H1N1influenza A hemagglutinin. Monatsh Chem 2010; 141: 801-7.
- [31] Nunthaboot N, Rungrotmongkol T, Malaisree M, et al. Evolution of human receptor binding affinity of H1N1 hemagglutinins from 1918 to 2009 pandemic influenza A virus. J Chem Inf Model 2010; 50: 1410-7.
- [32] de Vries RP, de Vries E, Moore KS, Rigter A, Rottier PJM, de Haan CAM. Only two residues are responsible for the dramatic difference in receptor binding between swine and new pandemic H1 hemagglutinin. J Biol Chem 2011; 286: 5868-75.
- [33] Lee AN, Hartono YD, Sun T, et al. Molecular dynamics studies of human receptor molecule in hemagglutinin of 1918 and 2009 H1N1 influenza viruses. J Mol Model 2010. DOI: 10.1007/s00894-010-0867-5.
- [34] Malaisree M, Rungrotmongkol T, Nunthaboot N, et al. Source of oseltamivir resistance in avian influenza H5N1 virus with the H274Y mutation. Amino Acids 2009; 37: 725-32.
- [35] Rungrotmongkol T, Intharathep P, Malaisree M, et al. Susceptibility of antiviral drugs against 2009 influenza A (H1N1) virus. Biochem Biophys Res Commun 2009; 385: 390-4.
- [36] Rungrotmongkol T, Malaisree M, Nunthaboot N, Sompornpisut P, Hannongbua S. Molecular prediction of oseltamivir efficiency against probable influenza A (H1N1-2009) mutants: molecular modeling approach. Amino Acids 2010; 39: 393-8.
- [37] Okomo-Adhiambo M, Demmler-Harrison GJ, Deyde VM, et al. Detection of E119V and E119I mutations in influenza A (H3N2) viruses isolated from an immunocompromised patient: challenges in diagnosis of oseltamivir resistance. Antimicrob Agents Chemother 2010; 54: 1834-41.

- [38] Wang B, Dwyer DE, Blyth CC, et al. Detection of the rapid emergence of the H275Y mutation associated with oseltamivir resistance in severe pandemic influenza virus A/H1N1 09 infections. Antiviral Res 2010; 87: 16-21.
- [39] Wang NX, Zheng JJ. Computational studies of H5N1 influenza virus resistance to oseltamivir. Protein Sci 2009; 18: 707-15.
- [40] Yen HL, Ilyushina NA, Salomon R, Hoffmann E, Webster RG, Govorkova EA. Neuraminidase inhibitor-resistant recombinant A/Vietnam/1203/04 (H5N1) influenza viruses retain their replication efficiency and pathogenicity in vitro and in vivo. J Virol 2007; 81: 12418-26.
- [41] Bright RA, Shay DK, Shu B, Cox NJ, Klimov AI. Adamantane resistance among influenza A viruses isolated early during the 2005–2006 influenza season in the United States JAMA 2006; 295: 891-4.
- [42] Bodian DL, Yamasaki RB, Buswell RL, Stearns JF, White JM, Kuntz ID. Inhibition of the fusion-inducing conformational change of influenza hemagglutinin by benzoquinones and hydroquinones. Biochemistry 1993; 32: 2967-78.
- [43] Russell RJ, Kerry PS, Stevens DJ, et al. Structure of influenza hemagglutinin in complex with an inhibitor of membrane fusion. Proc Natl Acad Sci USA 2008; 105: 17736-41.
- [44] Tang G, Qiu Z, Lin X, et al. Discovery of novel 1-phenyl-cycloalkane carbamides as potent and selective influenza fusion inhibitors. Bioorg Med Chem 2010; 20: 3507-10.
- [45] Vanderlinden E, Göktaş F, Cesur Z, et al. Novel inhibitors of influenza virus fusion: structure-activity relationship and interaction with the viral hemagglutinin. J Virol 2010; 84: 4277-88.
- [46] Rossignol JF, Frazia SL, Chiappa L, Ciucci A, Santoro MG. Thiazolides, a new class of anti-influenza molecules targeting viral hemagglutinin at the post-translational level. J Biol Chem 2009; 284: 20708-808
- [47] Russell RJ, Haire LF, Stevens DJ, et al. The structure of H5N1 avian influenza neuraminidase suggests new opportunities for drug design. Nature 2006; 443: 45-9.
- [48] Li Q, Qi J, Zhang W, et al. The 2009 pandemic H1N1 neuraminidase N1 lacks the 150-cavity in its active site. Nat Struct Mol Biol 2010: 17: 1266-8.
- [49] Raab M, Tvaroška I. The binding properties of the H5N1 influenza virus neuraminidase as inferred from molecular modeling. J Mol Model 2010: DOI: 10.1007/s00894-010-0852-z.
- [50] Kobasa D, Kodihalli S, Luo M, et al. Amino acid residues contributing to the substrate specificity of the influenza A virus neuraminidase. J Virol 1999; 73: 6743-51.
- [51] Fran de Barros Jr J, Sales Alviano D, da Silva MH, et al. Characterization of sialidase from an influenza A (H3N2) virus strain: kinetic parameters and substrate specificity. Intervirology 2003; 46: 199-206.
- [52] Mochalova LV, Korchagina EY, Kurova VS, Shtyria JA, Gambaryan AS, Bovin NV. Fluorescent assay for studying the substrate specificity of neuraminidase. Anal Biochem 2005; 341: 190-3.
- [53] Aruksakunwong O, Malaisree M, Decha P, et al. On the lower susceptibility of oseltamivir to influenza neuraminidase subtype N1 than those in N2 and N9. Biophys J 2007; 92: 798-807.
- [54] Malaisree M, Rungrotmongkol T, Decha P, Intharathep P, Aruksakunwong O, Hannongbua S. Understanding of known drug-target interactions in the catalytic pocket of neuraminidase subtype N1. Proteins 2008; 71: 1908-18.
- [55] Lawrenz M, Baron R, McCammon JA. Independent-trajectories thermodynamic-integration free-energy changes for biomolecular systems: determinants of H5N1 avian influenza virus neuraminidase inhibition by peramivir. J Chem Theory Comput 2009; 5: 1106-16.
- [56] Lawrenz M, Wereszczynski J, Amaro R, Walker R, Roitberg A, McCammon JA. Impact of calcium on N1 influenza neuraminidase dynamics and binding free energy. Proteins 2010; 78: 2523-32.
- [57] Varghese JN, McKimm-Breschkin JL, Caldwell JB, Kortt AA, Colman PM. The structure of the complex between influenza virus neuraminidase and sialic acid, the viral receptor. Proteins 1992; 14: 327-32.
- [58] Shie JJ, Fang JM, Wang SY, et al. Synthesis of Tamiflu and its phosphonate congeners possessing potent anti-influenza activity. J Am Chem Soc 2007; 129: 11892-3.
- [59] Udommaneethanakit T, Rungrotmongkol T, Bren U, Frecer V, Stanislav M. Dynamic behavior of avian influenza a virus neuraminidase subtype H5N1 in complex with oseltamivir, zanamivir, pe-

- ramivir, and their phosphonate analogues. J Chem Inf Model 2009; 49: 2323-32.
- [60] Wang P, Zhang JZH. Selective binding of antiinfluenza drugs and their analogues to 'open' and 'closed' conformations of H5N1 neuraminidase. J Phys Chem B 2010; 114: 12958-64.
- [61] Park JW, Jo WH. Computational design of novel, high-affinity neuraminidase inhibitors for H5N1 avian influenza virus. Eur J Med Chem 2010; 45: 536-41.
- [62] Le L, Lee E, Schulten K, Truong TN. Molecular modeling of swine influenza A/H1N1, Spanish H1N1, and avian H5N1 flu N1 neuraminidases bound to Tamiflu and Relenza. PLoS curr 2009; doi: 10.1371/currents.RRN1015.
- [63] Rungrotmongkol T, Udommaneethanakit T, Malaisree M, et al. How does each substituent functional group of oseltamivir lose its activity against virulent H5N1 influenza mutants? Biophys Chem 2009; 145: 29-36.
- [64] Carr J, Ives J, Kelly L, et al. Influenza virus carrying neuraminidase with reduced sensitivity to oseltamivir carboxylate has altered properties in vitro and is compromised for infectivity and replicative ability in vivo. Antiviral Res 2002; 54: 79-88.
- [65] Yen HL, Herlocher LM, Hoffmann E, et al. Neuraminidase inhibitor-resistant influenza viruses may differ substantially in fitness and transmissibility. Antimicrob Agents Chemother 2005; 49: 4075-84.
- [66] Abed Y, Nehme B, Baz M, Boivin G. Activity of the neuraminidase inhibitor A-315675 against oseltamivir-resistant influenza neuraminidases of N1 and N2 subtypes. Antiviral Res 2008; 77: 163-6.
- [67] Ives JAL, Carr JA, Mendel DB, et al. The H274Y mutation in the influenza A/H1N1 neuraminidase active site following oseltamivir phosphate treatment leave virus severely compromised both in vitro and in vivo. Antiviral Res 2002; 55: 307-17.
- [68] de Jong MD, Thanh TT, Khanh TH, et al. Oseltamivir resistance during treatment of influenza A (H5N1) infection. N Engl J Med 200; ,353: 2667-72.
- [69] Earhart KC, Elsayed NM, Saad MD, et al. Oseltamivir resistance mutation N294S in human influenza A(H5N1) virus in Egypt. J Infect Public Heath 2009; 2: 74-80.
- [70] Hurt AC, Holien JK, Parker MW, Barr IG. Oseltamivir resistance and the H274Y neuraminidase mutation in seasonal, pandemic and highly pathogenic influenza viruses. Drugs 2009; 69: 2523-31
- [71] Kawai N, Ikematsu H, Tanaka O, et al. Comparison of the clinical symptoms and the effectiveness of neuraminidase inhibitors for patients with pandemic influenza H1N1 2009 or seasonal H1N1 influenza in the 2007–2008 and 2008–2009 seasons. J Infect Chemother 2010; DOI: 10.1007/s10156-010-0179-9.
- [72] Park JW, Jo WH. Infiltration of water molecules into the oseltamivir-binding site of H274Y neuraminidase mutant causes resistance to oseltamivir. J Chem Inf Model 2009; 49: 2735-41.
- [73] McKimm-Breschkin J, Sahasrabudhe A, Blick T, McDonald M. Mechanisms of resistance of influenza virus to neuraminidase inhibitors. International Congress Series 2001; 1219: 855-61.
- [74] Moscona A: Oseltamivir resistance--disabling Our Influenza Defenses. N Engl J Med. 2005; 353: 2633-6.
- [75] von Itzstein M. The war against influenza: discovery and development of sialidase inhibitors. Nat Rev Drug Discov 2007; 6: 967-74.
- [76] Pan D, Sun H, Bai C, Shen Y, Jin N, Liu H, Yao X. Prediction of zanamivir efficiency over the possible 2009 influenza A (H1N1) mutants by multiple molecular dynamics simulations and free energy calculations. J Mol Model 2010; DOI: 10.1007/s00894-010-0929-8
- [77] Amaro RE, Minh DDL, Cheng LS, et al. Remarkable loop flexibility in avian influenza N1 and its implications for antiviral drug design. J Am Chem Soc 2007; 129: 7764-5
- [78] Du QS, Wang SQ, Chou KC. Analogue inhibitors by modifying oseltamivir based on the crystal neuraminidase structure for treating drug-resistant H5N1 virus. Biochem Biophys Res Commun 2007; 362: 525-31.
- [79] Cheng LS, Amaro RE, Xu D, Li WW, Arzberger PW, McCammon JA. Ensemble-based virtual screening reveals potential novel anti-viral compounds for avian influenza neuraminidase. J Med Chem 2008; 51: 3878-94.
- [80] Rungrotmongkol T, Frecer V, De-Eknamkul W, Hannongbua S, Miertus S. Design of oseltamivir analogs inhibiting neuraminidase of avian influenza virus H5N1. Antiviral Res 2009; 82: 51-8.
- [81] Rungrotmongkol T, Udommaneethanakit T, Frecer V, Miertus S. Combinatorial design of avian influenza neuraminidase inhibitors

- containing pyrrolidine core with a reduced susceptibility to viral drug resistance. Comb Chem High Throughput Screen. 2010; 13: 268-77
- [82] Pinto LH, Dieckmann GR, Gandhi CS, et al. A functionally defined model for the M2 proton channel of influenza A virus suggests a mechanism for its ion selectivity. Proc Natl Acad Sci USA 1997; 94: 11301-6.
- [83] Sugrue RJ, Hay AJ. Structural characteristics of the M2 protein of influenza A viruses: evidence that it forms a tetrameric channel. Virology 1991; 180: 617-24.
- [84] Gandhi CS, Shuck K, Lear JD, et al. Cu(II) inhibition of the proton translocation machinery of the influenza A virus M2 protein. J Biol Chem 1999; 274: 5474-82.
- [85] Kukol A, Adams PD, Rice LM, Brunger AT, Arkin IT. Experimentally based orientational refinement of membrane protein models: a structure for the influenza A M2 H+ channel. J Mol Biol 1999; 286: 951-62.
- [86] Schnell JR, Chou JJ. Structure and mechanism of the M2 proton channel of influenza A virus. Nature 2008; 451: 591-U512.
- [87] Kovacs FA, Denny JK, Song Z, Quine JR, Cross TA. Helix tilt of the M2 transmembrane peptide from influenza A virus: an intrinsic property. J Mol Biol 2000; 295: 117-25.
- [88] Wang JF, Kim S, Kovacs F, Cross TA. Structure of the transmembrane region of the M2 protein H+ channel. Protein Sci 2001; 10: 2241-50.
- [89] Tian CL, Gao PF, Pinto LH, Lamb RA, Cross TA. Initial structural and dynamic characterization of the M2 protein transmembrane and amphipathic helices in lipid bilayers. Protein Sci 2003; 12: 2597-605.
- [90] Stouffer AL, Acharya R, Salom D, et al. Structural basis for the function and inhibition of an influenza virus proton channel. Nature 2008; 451: 596-U513.
- [91] Nishimura K, Kim SG, Zhang L, Cross TA. The closed state of a H+ channel helical bundle combining precise orientational and distance restraints from solid state NMR-1. Biochemistry 2002; 41: 13170-7.
- [92] Hu J, Asbury T, Achuthan S, et al. Backbone structure of the amantadine-blocked trans-membrane domain M2 proton channel from influenza A virus. Biophys. J. 2007; 92: 4335-43.
- [93] Tobler K, Kelly ML, Pinto LH, Lamb RA. Effect of cytoplasmic tail truncations on the activity of the M2 ion channel of influenza A virus. J Virol 1999; 73: 9695-701.
- [94] Acharya R, Carnevale V, Fiorin G, et al. Structure and mechanism of proton transport through the transmembrane tetrameric M2 protein bundle of the influenza A virus. Proc Natl Acad Sci USA 2010; 107: 15075-80.
- [95] Astrahan P, Kass I, Cooper MA, Arkin IT. A novel method of resistance for influenza against a channel-blocking antiviral drug. Proteins 2004; 55: 251-7.
- [96] Kass I, Arkin IT. How pH opens a H+ channel: The gating mechanism of influenza a M2. Structure 2005; 13: 1789-98.
- [97] Chen HN, Wu YJ, Voth GA. Proton transport behavior through the influenza a M2 channel: insights from molecular simulation. Biophys J 2007; 93: 3470-9.
- [98] Khurana E, Dal Peraro M, DeVane R, Vemparala S, DeGrado WF, Klein ML. Molecular dynamics calculations suggest a conduction mechanism for the M2 proton channel from influenza A virus. Proc Natl Acad Sci USA 2009; 106: 1069-74.
- [99] Leonov H, Arkin IT. Structure and dynamics of the influenza A M2 channel: a comparison of three structures. J Mol Model 2009; 15: 1317-28.
- [100] Holsinger LJ, Alams R. Influenza virus M2 integral membrane protein is a homotetramer Stabilized by formation of disulfide bonds. Virology 1991; 183: 32-43.
- [101] Paterson RG, Takeda M, Ohigashi Y, Pinto LH, Lamb RA. Influenza B virus BM2 protein is an oligomeric integral membrane protein expressed at the cell surface. Virology 2003; 306: 7-17.
- [102] Hay AJ, Wolstenholme AJ, Skehel JJ, Smith MH. The molecular basis of the specific anti-influenza action of amantadine. EMBO J 1985; 4: 3021-4.
- [103] Helenius A. Unpacking the incoming influenza virus Cell. Cell. 1992; 69: 577-8.
- [104] Pinto LH, Holsinger LJ, Lamb RA. Influenza virus M2 protein has ion channel activity. Cell 1992; 69: 517-28.

- [105] Martin K, Helenius A. Nuclear transport of influenza virus ribonucleoproteins: the viral matrix protein (M1) promotes export and inhibits import. Cell 1991; 67: 117-30.
- [106] Lin T-I, Schroeder C. Definitive assignment of proton selectivity and attoampere unitary current to the M2 ion channel protein of influenza A virus. J Virol 2001; 75: 3647-56.
- [107] Pielak RM, Schnell JR, Chou JJ. Mechanism of drug inhibition and drug resistance of influenza A M2 channel. Proc Natl Acad Sci USA 2009; 106: 7379-84.
- [108] Cady SD, Schmidt-Rohr K, Wang J, Soto CS, Degrado WF, Hong M. Structure of the amantadine binding site of influenza M2 proton channels in lipid bilayers. Nature 2010; 463: 689-U127.
- [109] Tang YJ, Zaitseva F, Lamb RA, Pinto LH. The gate of the influenza virus M-2 proton channel is formed by a single tryptophan residue. J Biol Chem 2002; 277: 39880-6.
- [110] Yi M, Cross TA, Zhou HX. A secondary gate as a mechanism for inhibition of the M2 proton channel by amantadine. J Phys Chem B 2008; 112: 7977-9.
- [111] Wang C, Takeuchi K, Pinto LH, Lamb RA. Ion channel activity of influenza A virus M2 protein: characterization of the amantadine block. J Virol 1993; 67: 5585-94.
- [112] Czabotar PE, Martin SR, Hay AJ. Studies of structural changes in the M2 proton channel of influenza A virus by tryptophan fluorescence. Virus Res 2004; 99: 57-61.
- [113] Hu J, Fu RQ, Cross TA. The chemical and dynamical influence of the anti-viral drug amantadine on the M2 proton channel transmembrane domain. Biophys J 2007; 93: 276-83.
- [114] Hu J, Fu R, Nishimura K, et al. Histidines, heart of the hydrogen ion channel from influenza A virus: toward an understanding of conductance and proton selectivity. Proc Natl Acad Sci USA 2006; 103: 6865-70.
- [115] Sharma M, Yi MG, Dong H, et al. Insight into the mechanism of the influenza a proton channel from a structure in a lipid bilayer. Science 2010; 330: 509-12.
- [116] Intharathep P, Laohpongspaisan C, Rungrotmongkol T, et al. How amantadine and rimantadine inhibit proton transport in the M2 protein channel. J Mol Graph Model 2008; 27: 342-8.
- [117] McCown MF, Pekosz A. Distinct domains of the influenza A virus M2 protein cytoplasmic tail mediate binding to the M1 protein and facilitate infectious virus production. J Virol 2006, 80: 8178-89.
- [118] Chen BJ, Leser GP, Jackson D, Lamb RA. The influenza virus M2 protein cytoplasmic tail interacts with the M1 protein and influences virus assembly at the site of virus budding. J Virol 2008; 82: 10059-70.
- [119] Venkataraman P, Lamb RA, Pinto LH. Chemical rescue of histidine selectivity filter mutants of the M2 ion channel of influenza A virus. J Biol Chem 2005; 280: 21463-72.
- [120] Balannik V, Carnevale V, Fiorin G, et al. Functional studies and modeling of pore-lining residue mutants of the influenza A virus M2 ion channel. Biochemistry 2010; 49: 696-708.
- [121] Holsinger LJ, Nichani D, Pinto LH, Lamb RA. Influenza A virus M2 ion channel protein: a structure-function analysis. J Virol 1994; 68: 1551-63.
- [122] Mould JA, Drury JE, Frings SM, et al. Permeation and activation of the M-2 ion channel of influenza A virus. J Biol Chem 2000; 275: 31038-50.
- [123] Chizhmakov IV, Geraghty FM, Ogden DC, Hayhurst A, Antoniou M, Hay AJ. Selective proton permeability and pH regulation of the influenza virus M2 channel expressed in mouse erythroleukaemia cells. J Physiol 1996; 494: 329-36.
- [124] Shimbo K, Brassard DL, Lamb RA, Pinto LH. Ion selectivity and activation of the M2 ion channel of influenza virus. Biophys J 1996: 70: 1335-46.
- [125] Duff KC, Ashley RH. The transmembrane domain of influenza A M2 protein forms amantadine-sensitive proton channels in planar lipid bilayers. Virology 1992; 190: 485-489.
- [126] Phongphanphanee S, Rungrotmongkol T, Yoshida N, Hannongbua S, Hirata F. Proton transport through the influenza A M2 channel: three-dimensional reference interaction site model study. J Am Chem Soc 2010; 132: 9782-8.
- [127] Sansom MSP, Kerr ID, Smith GR, Son HS. The influenza A virus M2 channel: A molecular modeling and simulation study. Virology 1997; 233: 163-73.
- [128] Agmon N. The Grotthuss mechanism. Chem Phys Lett 1995; 244: 456-62.

- [129] Krause J. Proline conformations in linear peptides. Structure determination of the methyl ester of N-benzyloxycarbonyl-L-prolyl-D-alanine (N-Z-L-Pro-D-Ala-OMe). Acta Crystallogr C 1991, 47: 1508-12.
- [130] Davies WL, Grunert RR, Haff RF, et al. Antiviral activity of 1-adamantanamine (Amantadine). Science 1964; 144: 862-3.
- [131] Wang C, Lamb RA, Pinto LH. Direct measurement of the influenza A virus M2 protein ion channel activity in mammalian cells. Virology 1994; 205: 133-40.
- [132] Duff KC, Gilchrist PJ, Saxena AM, Bradshaw JP. Neutron diffraction reveals the site of amantadine blockade in the influenza A M2 ion channel. Virology 1994; 202: 287-93.
- [133] Intharathep P, Rungrotmongkol T, Decha P, et al. Evaluating how rimantadines control the proton gating of the influenza A M2proton port via allosteric binding outside of the M2-channel: MD simulations. J Enzyme Inhib Med Chem 2011; 26: 162-8.
- [134] Jefferson T, Demicheli V, Pietrantonj CD, Rivetti D. Amantadine and rimantadine for influenza A in adults. Cochrane Database Syst Rev 2006; 19: CD001169.
- [135] Deyde VM, Xu XY, Bright RA, et al. Surveillance of resistance to adamantanes among influenza A(H3N2) and A(H1N1) viruses isolated worldwide. J Infect Dis 2007; 196: 249-57.
- [136] Suzuki H, Saito R, Masuda H, Oshitani H, Sato M, Sato I. Emergence of amantadine-resistant influenza A viruses: epidemiological study J Infect Chemother 2003; 9: 195-200.
- [137] Saito R, Sakai T, Sato I, Sano Y, Oshitani H, Sato M, Suzuki H. Frequency of amantadine-resistant influenza A viruses during two seasons featuring cocirculation of H1N1 and H3N2. J Clin Microbiol 2003; 41: 2164-5.
- [138] Dawood FS, Jain S, Finelli L, et al. Emergence of a novel swineorigin influenza A (H1N1) virus in humans. N Engl J Med 2009; 360: 2605-15.
- [139] Shinde V, Bridges CB, Uyeki TM, et al. Triple-reassortant swine influenza A (H1) in humans in the United States, 2005-2009. N Engl J Med 2009; 360: 2616-25.

Accepted: May 5, 2011

Received: March 3, 2011

- [140] Abed Y, Goyette N, Boivin G. Generation and characterization of recombinant influenza A (H1N1) viruses harboring amantadine resistance mutations. Antimicrob Agents Chemother 2005; 49: 556-9.
- [141] Laohpongspaisan C, Rungrotmongkol T, Intharathep P, et al. Why amantadine loses its function in influenza M2 mutants: MD simulations. J Chem Inf Model 2009; 49: 847-52.
- [142] Aldrich PE, Hermann EC, Meier WE, et al. Antiviral agents. 2. Structure-activity relationships of compounds related to 1 adamantanamine. J Med Chem 1971; 14: 535-43.
- [143] Kolocouris A, Tataridis D, Fytas G, et al. Synthesis of 2-(2-adamantyl)piperidines and structure anti-influenza virus A activity relationship study using a combination of NMR spectroscopy and molecular modeling. Bioorg Med Chem Lett 1999; 9: 3465-70.
- [144] Zoidis G, Fytas C, Papanastasiou L, et al. Heterocyclic rimantadine analogues with antiviral activity. Bioorg Med Chem 2006; 14: 3341-8
- [145] Hu WH, Zeng SG, Li CF, Jie YL, Li ZY, Chen L. Identification of Hits as matrix-2 protein inhibitors through the focused screening of a small primary amine library. J Med Chem 2010; 53: 3831-4.
- [146] Zoidis G, Kolocouris N, Naesens L, De Clercq E. Design and synthesis of 1,2-annulated adamantane piperidines with anti-influenza virus activity. Bioorg Med Chem 2009; 17: 1534-41.
- [147] Zhao X, Li CF, Zeng SG, Hu WH. Discovery of highly potent agents against influenza A virus. Eur J Med Chem 2011; 46: 52-7.
- [148] Judd AK, Sanchez A, Bucher DJ, Huffman JH, Bailey K, Sidwell RW. In vivo anti-influenza virus activity of a zinc finger peptide. Antimicrob Agents Chemother 1997; 41: 687-92.
- [149] Sidwell RW, Smee DF. In vitro and in vivo assay systems for study of influenza virus inhibitors. Antiviral Res 2000; 48: 1-16.
- [150] Wang J, Cady SD, Balannik V, Pinto LH, DeGrado WF, Hong M. Discovery of spiro-piperidine inhibitors and their modulation of the dynamics of the M2 proton channel from influenza A virus. J Am Chem Soc 2009; 131: 8066-76.

ELSEVIER

Contents lists available at ScienceDirect

Journal of Molecular Graphics and Modelling

journal homepage: www.elsevier.com/locate/JMGM



Molecular insight into the specific binding of ADP-ribose to the nsP3 macro domains of chikungunya and venezuelan equine encephalitis viruses: Molecular dynamics simulations and free energy calculations

Thanyada Rungrotmongkol^{a,b,*}, Nadtanet Nunthaboot^c, Maturos Malaisree^a, Nopporn Kaiyawet^a, Pathumwadee Yotmanee^a, Arthitaya Meeprasert^a, Supot Hannongbua^a

- ^a Computational Chemistry Unit Cell, Department of Chemistry, Faculty of Science, Chulalongkorn University, Bangkok 10330, Thailand
- ^b Center of Innovative Nanotechnology, Chulalongkorn University, Bangkok 10330, Thailand
- ^c Department of Chemistry, Faculty of Science, Mahasarakham University, Mahasarakham 44150 Thailand

ARTICLE INFO

Article history: Received 16 July 2010 Received in revised form 19 September 2010 Accepted 23 September 2010 Available online 29 October 2010

Keywords: Chikungunya Venezuelan equine encephalitis ADP-ribose Molecular dynamics simulations

ABSTRACT

The outbreaks of chikungunya (CHIKV) and venezuelan equine encephalitis (VEEV) viral infections in humans have emerged or re-emerged in various countries of "Africa and southeast Asia", and "central and south America", respectively. At present, no drug or vaccine is available for the treatment and therapy of both viral infections, but the non-structural protein, nsP3, is a potential target for the design of potent inhibitors that fit at the adenosine-binding site of its macro domain. Here, so as to understand the fundamental basis of the particular interactions between the ADP-ribose bound to the nsP3 amino acid residues at the binding site, molecular dynamics simulations were applied. The results show that these two nsP3 domains share a similar binding pattern for accommodating the ADP-ribose. The ADP-ribose phosphate unit showed the highest degree of stabilization through hydrogen bond interactions with the nsP3 V33 residue and the consequent amino acid residues 110-114. The adenine base of ADP-ribose was specifically recognized by the conserved nsP3 residue D10. Additionally, the ribose and the diphosphate units were found to play more important roles in the CHIKV nsP3-ADP-ribose complex, while the ter-ribose was more important in the VEEV complex. The slightly higher binding affinity of ADP-ribose toward the nsP3 macro domain of VEEV, as predicted by the simulation results, is in good agreement with previous experimental data. These simulation results provide useful information to further assist in drug design and development for these two important viruses.

© 2010 Elsevier Inc. All rights reserved.

1. Introduction

Chikungunya (CHIKV) and Venezuelan equine encephalitis (VEEV) viruses are pathogens that are primarily transmitted to humans and/or animals through the bite of infected mosquitoes. With respect to, a diverse array of mosquito vectors exist, but species within the genus *Aedes* are the main vectors for both viruses, and in particular *A. aegypti*. The outbreaks of CHIKV in humans have been distributed in several countries of Africa and southeast Asia [1], while the VEEV outbreaks have occurred in the U.S.A., Mexico, Colombia and Venezuela [2]. Among the four non-structural (nsP1–4) and the main structural (capsids, E1 and E2) proteins encoded in their genomic RNA, the functions and the major role of

E-mail address: t.rungrotmongkol@gmail.com (T. Rungrotmongkol).

the nsP3 protein are not yet clear, although the infection is required at an early stage in the transcription process for viral replication [3]. Here, an understanding at the atomic level of the molecular recognition and interaction between the ADP-ribose molecule and the nsP3 macro domain of CHIKV and VEEV, as model alphaviruses, is the main goal of this study. The simulated results constitute new important data to further assist in the design of inhibitors accommodating at the adenosine-binding site for the inhibition of these two alphaviruses.

CHIKV and VEEV viruses belong to the genus *Alphavirus* in the *Togaviridae* family. As with most other alphaviruses, they are enveloped, single stranded and positive sense RNA viruses. Their genomic RNA encodes for four non-structural proteins (nsP1–4) in the 5′ region and three main structural proteins (capsids, E1 and E2) in the 3′ region. The non-structural proteins have distinct important functions in the early stages of RNA replication, the negative strand synthesis [3–5]. In the latter stage of infection, the negative strand serves as a template for the synthesis of progeny-positive strands, and subgenomic mRNAs coding for the virus structural proteins.

^{*} Corresponding author at: Computational Chemistry Unit Cell, Department of Chemistry, Faculty of Science, Chulalongkorn University, Bangkok, 10330, Thailand. Tel.: +66 22 187602; fax: +66 22 187603.

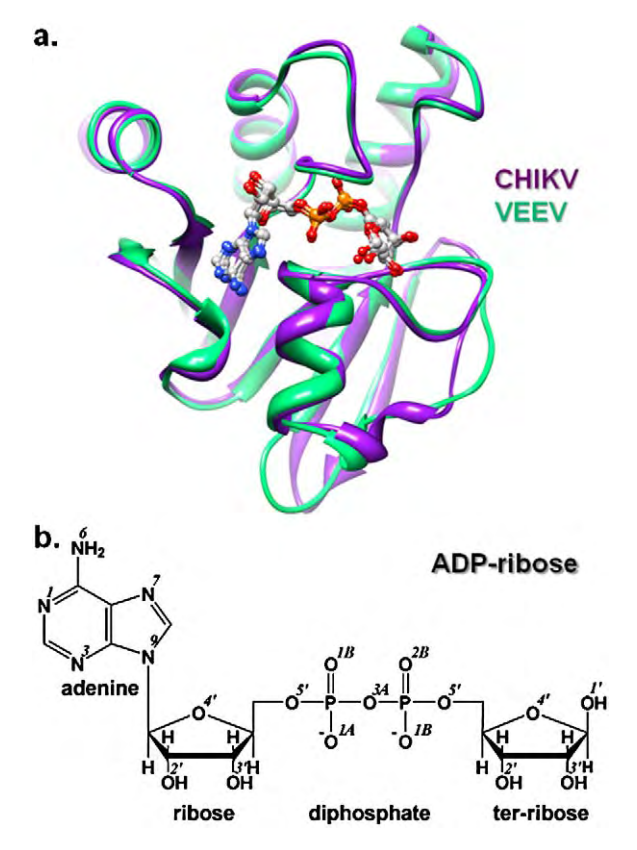
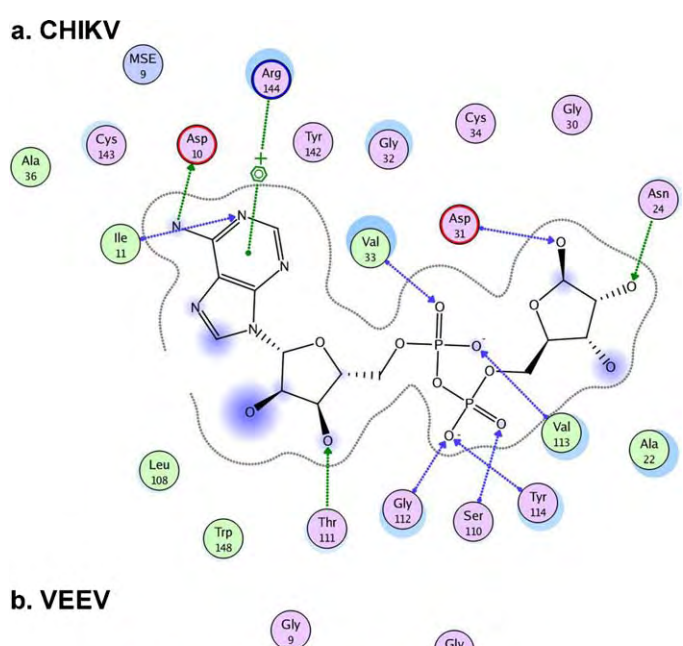


Fig. 1. (a) Structural alignment between the crystal structures of the CHIKV (violet) and VEEV (green) nsP3 macro domains complexed with ADP-ribose. (b) Schematic chemical structure of ADP-ribose containing adenine, ribose, diphosphate and terribose moieties. (For interpretation of the references to color in this figure legend, the reader is referred to the web version of the article.)

The enzymatic machinery of three of the four non-structural proteins has been evaluated. The nsP1 protein is responsible for methylation and capping of viral mRNAs [6,7], directing the replication complex to the membrane [8], and association with the cytoplasmic surface of endosomes and lysosomes [9]. The nsP2 protein is a RNA triphosphatase [10], RNA helicase [11], NTPase [12] and protease [13]. The nsP4 protein is an RNA-dependent RNA polymerase involved in genome replication and transcription [14]. However, in some contrast, all that is known for the nsP3 protein is that it is proposed to be essential as a part of the minus strand replicase and mutations in it can reduce the rate of the minus strand and subgenomic RNA synthesis [15,16]. The nsP3 protein sequence is composed of three domains: (i) the C-terminal region with a poorly conserved sequence [17], (ii) the relatively well conserved serine/threonine rich sequence, and (iii) the N-terminal macro domain sequence. This macrodomain is ancient and is widely distributed throughout all eukaryotic organisms, bacteria and archaea [18]. Moreover, macro domains are also found in many types of positive strand RNA viruses, including hepatitis E, rubella, and those members of the corona- and alpha-viruses. The macro domain contains the binding domain for the ADP-ribose containing molecules: ADPribose, poly ADP-ribose and o-acetyl-ADP-ribose [19–22]. Recently, the crystal structures of the nsP3 macro domain for the VEEV and CHIKV have been reported (Fig. 1a) [23]. Each domain contains the six-stranded β sheet with three α helices. The intermolecular interactions between the residues in the binding pocket of the two enzymes and the ADP-ribose, as analyzed from their crystal structures, are drawn in Fig. 2.

To gain the fundamental knowledge on the structure and binding modes of ADP-ribose in the nsP3 macro domains of CHIKV and



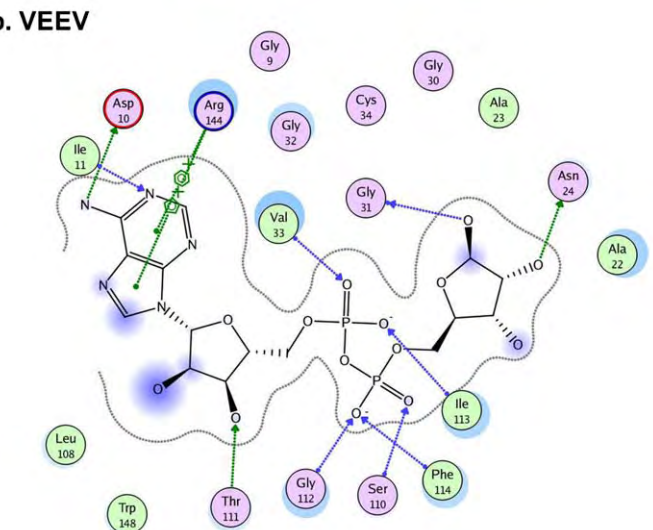


Fig. 2. Schematic representations on intermolecular interactions between ADP-ribose and the residues at the binding pocket of the nsP3 macro domains of (a) CHIKV and (b) VEEV, based on the crystal structures [23].

VEEV in aqueous solution, molecular dynamics (MD) simulations of the ADP-ribose bound with both CHIKV and VEEV macro domains were conducted. The results were extensively analyzed in terms of intermolecular hydrogen bonds, decomposition free energy and its components, and the binding free energy of the complex focused on the ADP-ribose binding pocket.

2. Materials and methods

2.1. System preparation

The recently reported X-ray crystallographic structures of the CHIKV and VEEV nsP3 macro domains complexed with the ADP-ribose [23] (Fig. 1a), taken from the Protein Data Bank (PDB) (entry codes 3GPO and 3GQO, respectively), were used as the starting coordinates for the MD simulations. Initial structure preparations and calculation processes were carried out using the AMBER package suit of programs [24]. The AMBER ff03 force field [25] was applied for amino acid residues while the ADP parameters [26] were used to create the parameters for ADP-ribose. Likewise the protonation states for the five ionizable amino acids (Asp, Glu, Lys, Arg and His) were assigned using the PROPKA program [27].

All missing hydrogen atoms of the proteins and ADP-ribose were added with standard bond lengths and angles by the LEaP module of AMBER. To relieve bad steric interactions, the hydrogen atoms were firstly minimized with 1500 steps of steepest descents (SD) followed by 1500 steps of conjugated gradient (CG). Afterwards, each complex was immersed in a cubic box of TIP3P water molecules [28] and, in the case of CHIKV, a sodium counterion was randomly added to neutralize the electrical charge of the CHIKV. The number of total atoms and the water box size of the CHIKV system were 25,893 atoms and $66 \times 67 \times 74 \,\text{Å}^3$, while those for the VEEV complex were 24,588 atoms and $65 \times 68 \times 69 \,\text{Å}^3$, respectively. Based on a cutoff distance of 12 Å, the added water molecules were consequently energy minimized using 1500 steps each of SD and CG, while the protein and ligand were restrained with a force constant of 500 kcal/molÅ². Finally, the entire structure was fully minimized with 3000 steps each for SD and CG, to search for the optimum conformation.

2.2. Molecular dynamics simulations

All simulations were carried out under the periodic boundary condition with the *NPT* ensemble. The SHAKE algorithm [29] was applied to constrain all covalent bonds involving hydrogen atoms. A time step of 2 fs with residue-based non-bonded interactions truncated at 12 Å was used. The long-range electrostatic interactions [30] were calculated according to the particle mesh Ewald method. A Berendsen coupling time of 0.2 ps was employed to maintain the temperature and standard pressure of the system [31]. Firstly, both complexes were heated up to 298 K for 60 ps. Then, the MD simulations were performed for 10 ns, consisting of the first 4 ns of equilibration and another 6 ns of the production phase. The trajectories, collected every 0.2 ps in the production phase, were used for analysis.

The convergences of energy, temperature, pressure and the global root mean-square displacement (RMSD) were used to verify the system stability. The MD trajectories extracted from the production phase were analyzed in terms of hydrogen bond (H-bond), decomposition of free energies on a per-residue basis ($\Delta G_{bind}^{residue}$), binding free energies (ΔG_{bind}) and their energy components.

2.3. Molecular mechanics/Poisson–Boltzmann Surface Area (MM/PBSA) calculations

The Molecular Mechanics/Poisson–Boltzmann Surface Area (MM/PBSA) approach is a well-accepted method to estimate the binding free energy between a protein and its given ligand [32–34]. This method, as implemented in the AMBER program, was applied to compute the binding free energies for the CHIKV and VEEV nsP3 macro domain complexed with ADP-ribose. Here, changes in the binding free energy in the protein (nsP3 macro domain)–ligand (ADP-ribose) binding is computed as the difference between the free energies of the complex ($\Delta G_{complex}$), protein (ΔG_{ligand}) and ligand (ΔG_{ligand}), as outlined in Eq. (1):

$$\Delta G_{bind} = \Delta G_{complex} - [\Delta G_{protein} + \Delta G_{lig}]$$
 (1)

In general, the total free energy of each species contains the enthalpy and entropy contributions, as shown in Eq. (2):

$$\Delta G = \Delta H - T \Delta S \tag{2}$$

where ΔH of the system is composed of the enthalpy changes in the gas phase upon complex formation (ΔE_{MM}) and the solvated free energy contribution (ΔG_{sol}), while $-T\Delta S$ refers to the entropy contribution to the binding. Eq. (2) can be then approximated as shown in Eq. (3):

$$\Delta G = \Delta E_{MM} + \Delta G_{sol} - T\Delta S \tag{3}$$

where ΔE_{MM} is the summation of the van der Waals (ΔE_{vdW}) and the electrostatic (ΔE_{ele}) interaction energies, and was evaluated by the SANDER module of AMBER using Eq. (4):

$$\Delta E_{MM} = \Delta E_{vdW} + \Delta E_{ele} \tag{4}$$

In addition, ΔG_{sol} , which denotes the solvation free energy, can be computed as the summation of an electrostatic component ($\Delta G_{ele,sol}$) and a nonpolar component ($\Delta G_{nonpolar,sol}$), as shown in Eq. (5):

$$\Delta G_{sol} = \Delta G_{ele,sol} + \Delta G_{nonpolar,sol} \tag{5}$$

The electrostatic component was computed by the Possion-Boltzmann (PB) method [35,36] in the AMBER suite. The dielectric constants for the solute and the surrounding solvent were set to 1 and 80, respectively. The same set of atomic charges on each complex applied in the MD simulations was again used in the PB computation. The nonpolar term in the solvation free energy was computed, as shown in Eq. (6):

$$\Delta G_{nonnolar\ sol} = \gamma SASA + \beta \tag{6}$$

where SASA is the solvent accessible surface area of each given molecule and is determined using a solvent probe radius of 1.4 Å. For the PB model, the values of the surface tension constants γ and β were set to 0.0072 kcal/mol Ų and 0.00 kcal/mol, respectively. The entropy term $T\Delta S$ is required to account for the conformational entropy change of the two binding partners upon complexation. In this study, we performed a normal-mode analysis [37], using the NMODE module, to compute the vibrational, rotational and translational entropies.

2.4. Binding free energy decomposition

The contribution of each residue to the total binding free energy of the protein–ligand complex, according to Eq. (1), was evaluated through the free energy decomposition based on the MM/PBSA method [38,39]. For this purpose, the contribution of atom i to the total electrostatic interaction energy between the two components is given by one half of a pairwise electrostatic interaction energy between the two atoms, each belonging to the protein and ligand complex. This is expressed in Eq. (7) as:

$$E_{ele}^{i} = \frac{1}{2} \sum_{j \neq i} \frac{q_{i}q_{j}}{r_{ii}} \tag{7}$$

where j are the atoms of the part that i does not belong to, whereas r_{ij} is the distance between the two atoms with atomic partial charges of q_i and q_j . Similarly, one half of the pairwise intercomponent van der Waals interaction energies (E^i_{vdW}) between the nsP3 protein and the ADP-ribose ligand was attributed to avoid double counting. The calculation of the internal energy, $\Delta E_{\rm int}$, is equal to zero under the assumption of a single trajectory approach since the internal energies of the complex and the separated parts are calculated from the same trajectory. The SASA of each atom i to the nonpolar solvation term is given by Eq. (8):

$$\Delta G_{nonpolar,sol}^{i} = \gamma \times (SASA^{i,complex} - (SASA^{i,protein} + SASA^{i,ligand}))$$
(8)

where *SASA*^{i,protein} or *SASA*^{i,ligand} is equal to zero depending on which component the atom belongs to. The GB approach was used to calculate electrostatic free energy term by Eq. (9):

$$\Delta G_{ele,sol} = -\frac{1}{2} \left(1 - \frac{e_{GB}^{-\kappa f}}{\varepsilon_{\omega}} \right) \sum_{ij} \frac{q_i q_j}{f_{GB}}$$
 (9)

where ε_{ω} is the dielectric constant of solvent, κ is the Debye–Hückel screening parameter and the double sum runs over all pairs of

atoms. In this study, ε_{ω} and κ were assigned to 80 and 0, respectively, and f_{GB} was defined by Eq. (10):

$$f_{GB} = \left[r_{ij}^2 + \alpha_i \alpha_j \exp\left(\frac{-r_{ij}^2}{4\alpha_i \alpha_j}\right) \right]^{1/2}$$
 (10)

where α_i and α_j are the effective Born radius of atoms i and j, respectively. The contribution of atom i to the electrostatic free energy is obtained by Eq. (11):

$$\Delta G_{ele,sol}^{i} = -\frac{1}{2} \sum_{j} \left(1 - \frac{e^{-\kappa f}}{\varepsilon_{\omega}} \right) \frac{q_{i}q_{j}}{f_{GB_{ij}}(r_{ij})} + \frac{1}{2} \sum_{j \neq i} \frac{q_{i}q_{j}}{r_{ij}}$$
(11)

Finally, the contribution to the total binding free energy for a per-residue basis, $\Delta G_{bind}^{residue}$, can be obtained by summation of the atomic contributions E_{ele}^i , E_{vdW}^i , $\Delta G_{ele,sol}^i$ and $\Delta G_{nonpolar,sol}^i$ over the atoms of a given residue without consideration of the entropy terms. The separated contribution of its backbone, $\Delta G_{bind}^{backbone}$, or the side chain, $\Delta G_{bind}^{side\ chain}$, can be constructed from the related atoms

3. Results and discussion

To determine the system stability of the CHIKV and VEEV nsP3–ADP-ribose complexes, RMSDs of the heavy atoms over 10-ns MD simulation with respect to their starting structures were plotted versus simulation time and given in Fig. S1 (see supplementary data). It can be seen that the two complexes were found to reach equilibrium at 4-ns and thus the MD trajectories taken from the subsequent 6-ns simulations were properly used for analysis.

3.1. Key binding motif of ADP-ribose

To obtain detailed information and insight into the intermolecular interactions of the ADP-ribose and the nsP3 protein, the percentage and the number of hydrogen bond (H-bond) occupations between the ADP-ribose and the binding residues of the CHIKV and the VEEV nsP3 macro domains were identified according to the subsequent criteria: (i) the distance between proton donor (D) and acceptor (A) atoms \leq 3.5 Å; and (ii) the D-H···A angle \geq 120. The results are summarized in Fig. 3, where the strong and medium hydrogen bond interactions are determined by H-bond occupations of higher than 75% and 50%, respectively (dashed lines in Fig. 3). We assume that the strongly detected H-bonds at the binding site of the nsP3 macro domain could provide the important interactions between the binding pocket residues and the ADP-ribose molecule.

The stabilization at the adenine base of ADP-ribose in both viral nsP3-ADP-ribose complexes was mostly contributed from the nsP3 residues D10 and I11. The backbone nitrogen of I11 stabilized the ribose through a very strong hydrogen bond with the N¹-nitrogen (see atomic label in Fig. 1b), which is in good agreement with the schematic view of the protein-ligand interactions determined from the X-ray structures (Fig. 2). Its N⁶-nitrogen established two moderate strength hydrogen bond interactions with the two carboxylate oxygens of D10, while in the crystal structures [23] only the hydrogen bond with the OD1-oxygen of D10 (3.0 Å in CHIKV and 2.7 Å in VEEV) was formed. In addition, it was proposed that the high specificity of the adenine moiety of ADP-ribose in the binding to the alphavirus CHIKV and VEEV nsP3 macro domains was mainly achieved through the conserved residue D10 [23]. A significant decrease in the protein thermal stability for the GDP binding to the CHIKV nsP3 macro domain, compared to that of the ADP-protein complex [23], is most likely caused by a lack of any particular interaction between the nsP3 D10 residue and the GDP guanine base.

By considering the interaction of the connecting ribose (Fig. 3), although the two simulated models exhibited a similar strong hydrogen bond between their O3′-hydroxyl oxygen of the ribose and the hydroxyl moiety of the nsP3 T111 residue, the interaction to the R144 residue was significantly different. In the case of CHIKV, the ribose O2′-hydroxyl oxygen was intensely stabilized by the nsP3 R144 residue through the presence of two strong hydrogen bonds with the gaunidinium group at the NE- and NH2-nitrogens. In contrast, these interactions had almost disappeared in the case of the VEEV nsP3-ADP-ribose complex where only a very weak hydrogen bond with one of the gaunidinium nitrogen's of the R144 residue was observed.

Both the CHIKV and the VEEV nsP3–ADP-ribose complexes shared relatively similar patterns of hydrogen bond interactions at the diphosphate unit (Fig. 3). There was a strong hydrogen bond between the O^{1A}-phosphate oxygen and the backbone nitrogen of the nsP3 V33 residue. The O^{1B}- and O^{2B}-phosphate oxygens established strong and rather weak hydrogen bonds, respectively, to the backbone nitrogen of S110. Furthermore, the O^{2B} atom formed two strong hydrogen bonds, one each with residues G112 and either Y114 (CHIKV) or F114 (VEEV). However, a clear difference between the two viral nsP3–ADP-ribose complexes was found in terms of the interaction with residue 133. In CHIKV, two strong hydrogen bonds were formed between the two phosphate oxygens (O^{2A} and O^{2B}) of the ADP-ribose and the backbone of the nsP3 residue V113, whereas one of these interactions was weaker at the I113 residue in the VEEV nsP3–ADP-ribose complex.

Moreover, interactions between the ADP-ribose and the two viral nsP3 macro domains are remarkably different at the ter-ribose unit. Only one strong hydrogen bond was found between the O^{5'}phosphate connecting oxygen and the backbone nitrogen of the nsP3 Y114 residue in CHIKV (Fig. 3a), while three strong hydrogen bonds to nsP3 residues G31, G32 and F114 were detected in the VEEV nsP3-ADP-ribose complex (Fig. 3b). Conversion of the D31 residue to G31 in the VEEV nsP3 protein leads to the formation of a strong hydrogen bond between the G31 residue and the ter-ribose unit, instead of the two moderate hydrogen bonds seen with the D31 residue through its backbone oxygen and nitrogen atoms as observed in CHIKV. This was subsequently found to affect the adjacent residue where the interaction with G32 in the case of the VEEV nsP3-ADP-ribose complex is markedly stronger than that in the CHIKV case. The O^{5'} atom of the ter-ribose moiety made a stronger hydrogen bond to the nsP3 I113 residue in VEEV than with the V113 residue in CHIKV. Furthermore, the H-bond between the nitrogen backbone of the nsP3 residue Y114 (CHIKV) or F114 (VEEV) and the $O^{5'}$ atom of the ADP-ribose unit was well conserved.

Taking into account all of the above information, the hydrogen bond patterns between the ADP-ribose and the nsP3 macro domains for both CHIKV and VEEV are almost the same. The nsP3 amino acid residues D10, I11, N24, D/G31-C34, S110-Y/F114 and R144 were found to be the key residues for the enzyme-ligand binding. In addition, the ribose and diphosphate units of the ADP-ribose were found to play more important roles in the CHIKV nsP3-ADP-ribose complex, while the strongly stabilized ter-ribose played the main part in the VEEV nsP3-ADP-ribose complex.

3.2. Per residue nsP3 enzyme-ADP-ribose interactions

To provide the basic information on the intermolecular interactions contributed from the individual residues in the CHIKV and VEEV nsP3 macro domains to the ADP-ribose, the pair interaction decomposition of free energy ($\Delta G_{bind}^{residue}$, the per residue total binding free energy) was evaluated using the decomposition energy module in AMBER. The calculation was performed over the 100 MD snapshots taken from the last 6-ns simulation. The summations

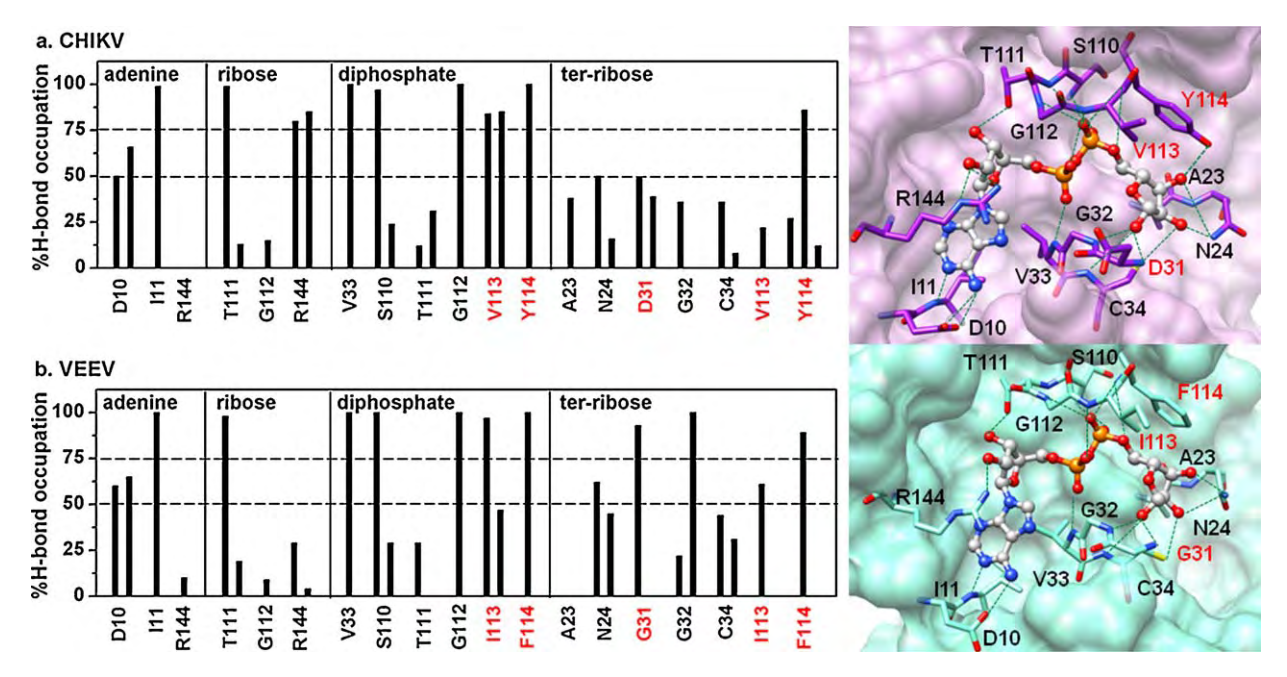


Fig. 3. Left: Percentage occupation of H-bonds between each ADP-ribose moiety (see Fig. 1b for definition) and the key residues in the binding pocket of the (a) CHIKV and (b) VEEV nsP3 macro domains. Right: The schematic view of the ADP-ribose (ligand)-nsP3 protein interaction, taken from the last MD snapshot is also depicted for both viruses, where the nsP3 residues that are different between the two macro domains are shown in red.

of per residue interaction free energies were separated into the residue backbone ($\Delta G_{bind}^{backbone}$) and the side chain ($\Delta G_{bind}^{side\ chain}$). The energy contributions from the selected residues are summarized in Fig. 4.

As shown, the plots for both viral nsP3–ADP-ribose systems show similar trends and almost the same patterns of decomposition energies (Fig. 4). The major contribution to the binding mode of the ADP-ribose, with a $\Delta G_{bind}^{residue}$ of \leq –4 kcal/mol (black column), was obviously gained from the many key nsP3 amino acid residues located in the ADP-ribose binding pocket of the CHIKV and VEEV macro domains. These residues are G32, V33, L109 (VEEV), S110, T111, G112, V133 (CHIKV) or I113 (VEEV), Y114 (CHIKV) or F114 (VEEV), and R144 (CHIKV), which directly face to the diphosphate

moiety of ADP-ribose (see schematic view in Fig. 3). Based on this major contribution, with a $\Delta G_{bind}^{residue}$ of \leq –4 kcal/mol, the energy contribution to the ADP-ribose molecule in VEEV (Fig. 4b) is slightly larger than that for CHIKV (Fig. 4a). In both systems, the interactions of these key residues were mainly achieved from their backbone atoms (light grey column, Fig. 4), which are in good agreement with the formation of many H-bonds with the backbone nitrogen and oxygen atoms, as previously mentioned above. Additionally, an essential contribution to the binding energy in the range of $-4 \leq \Delta G_{bind}^{residue} \leq -2$ kcal/mol was provided by the four nsP3 amino acid residues (I11, A22, N24 and L109) in CHIKV, and the six residues (I11, A22, N24, G30, G31 and C34) in VEEV.

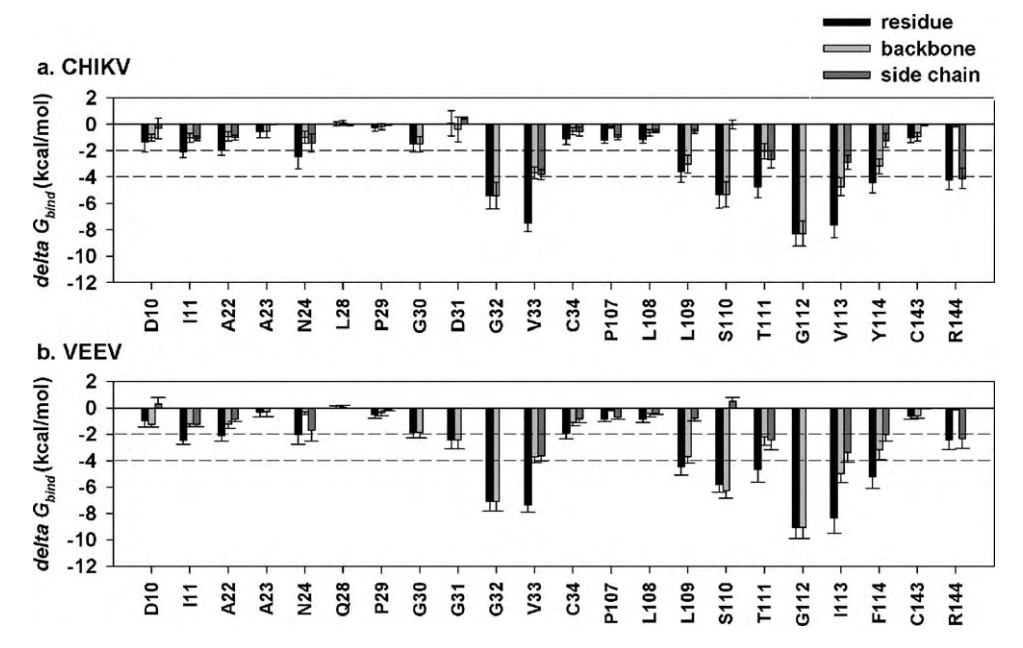


Fig. 4. Decomposition of the free energy on a per-residue basis ($\Delta G_{bind}^{residue}$) into the contributions from the atom groups of the backbone ($\Delta G_{bind}^{backbone}$) and the side chain (ΔG_{bind}^{side} chain) in the (a) CHIKV and (b) VEEV nsP3 macro domains bound to ADP-ribose.

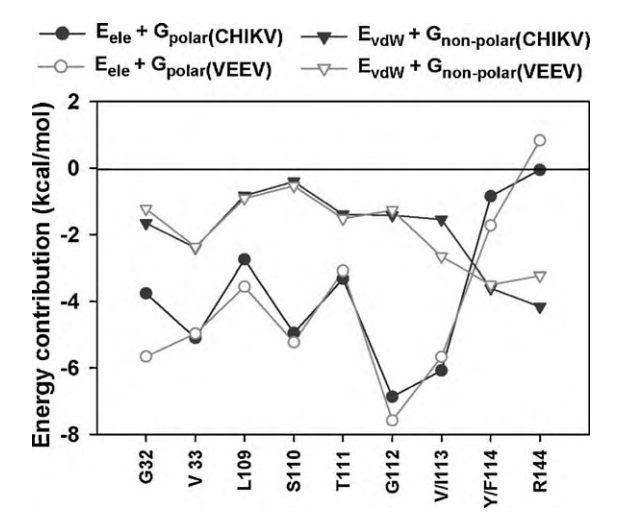


Fig. 5. Energy contribution of electrostatic and van der Waals terms for the key residues of the two nsP3 protein macro domains, CHIKV and VEEV.

To reveal the source of the interaction contribution from each particular residue, the electrostatic ($E_{ele} + G_{polar}$) and van der Waals ($E_{vdW} + G_{nonpolar}$) energy terms of the nine key residues in both alphaviruses were plotted and compared (Fig. 5). Except for the residues Y114 (CHIKV) or F114 (VEEV) and R144, the majority of the decomposed energy interaction originated from the electrostatic contribution apparently through H-bonding interactions, while the van der Waals contribution appeared as a minor influence to those key residues in the ADP-ribose binding process.

3.3. Binding affinity of ADP-ribose

The total binding free energy for the ADP-ribose molecule. ΔG_{bind} , and its detailed energy contributions calculated according to the MM/PBSA approach, are summarized in Table 1. Note that the 100 MD snapshots used in the MM/PBSA calculations were the same set as those used to evaluate the pair interaction decomposition of free energy. The ΔG_{bind} can be divided into polar $(E_{vdW} + G_{nonpolar})$ and nonpolar $(\Delta G_{nonpolar,sol} + \Delta E_{vdW})$ energies, whereupon the free energy of the ADP-ribose binding is revealed to be primarily contributed from the $\Delta G_{nonpolar,sol} + \Delta E_{vdW}$ at -72.6and -71.8 kcal/mol for the CHIKV and VEEV, respectively, while the $\Delta G_{ele.sol} + \Delta E_{ele}$ shows a likely unfavorable contribution at 36.8 and 32.5 kcal/mol for the CHIKV and VEEV, respectively. In the latter case, this is due to the intermolecular electrostatic energy, which is mainly achieved from the many hydrogen bond formations with the ADP-ribose binding residues of the nsP3 macro domain (as discussed above), and is lower than the desolvation energy. This

Table 1 Calculated energy components, binding free energy (kcal/mol) and experimental dissociation constant (K_d , μ M) of ADP-ribose binding to macro domain of (a) CHIKV and (b) VEEV.

	СНІКУ	VEEV
ΔE_{ele}	-316.8 ± 22.0	-376.8 ± 16.7
ΔE_{vdW}	-64.9 ± 4.3	-64.5 ± 3.7
ΔE_{MM}	-381.7 ± 22.7	-441.3 ± 17.1
$\Delta G_{nonpolar,sol}$	-7.7 ± 0.2	-7.3 ± 0.2
$\Delta G_{ele,sol}$	353.6 ± 20.8	409.4 ± 14.9
ΔG_{sol}	345.8 ± 20.9	402.0 ± 14.9
$\Delta G_{ele,sol} + \Delta E_{ele}$	36.8 ± 8.2	32.5 ± 7.3
$\Delta G_{nonpolar,sol} + \Delta E_{vdW}$	-72.6 ± 2.3	-71.8 ± 2.0
ΔG_{total}	-35.9 ± 7.1	-39.3 ± 6.4
$-T\Delta S$	29.7 ± 3.5	30.3 ± 2.1
ΔG_{bind}	-6.2 ± 5.6	-9.0 ± 4.8
K_d (μ M) [23]	5 ± 0.4	3.9 ± 0.65

occurrence has been reported in the previous theoretical studies of the interactions and binding free energies between ligands and proteins in an aqueous solution [40–43]. With the summation of the solute entropy term (\sim 30 kcal/mol), an estimated ΔG_{bind} of -6.2 kcal/mol and -9.0 kcal/mol was found for the CHIKV and VEEV complexes, respectively, suggesting that the ADP-ribose binds to and interacts with the binding site of the VEEV nsP3 macro domain slightly stronger than that with CHIKV. These simulation based results are in a good agreement with the experimental dissociation constant (K_d) of ADP-ribose binding to the nsP3 macro domain of these two alphaviruses [23].

4. Conclusions

In this study, molecular dynamics simulations were used to identify the key residues at the ADP-ribose binding site of the CHIKV and NEEV nsP3 macro domains for the design of potent inhibitors against these viruses. The likely binding motif for the ADP-ribose in both nsP3 enzyme targets was found to be considerably similar, involving the potential binding residues of D10, I11, N24 and R144, D/G31-C34, and S110-Y/F114. Among the four subunits of the ADP-ribose, the negatively charged $PO_4^{\ 2-}$ moiety showed the strongest interactions with the above residues in the binding pocket of enzyme. In addition, the ribose and the diphosphate units were found to play more important roles in the CHIKV nsP3-ADPribose complex, while the ter-ribose moiety was more important in the corresponding VEEV complex. The per-residue decomposition energies suggested that the particular interactions between the ADP-ribose and the nsP3 macro domain were mostly derived from the electrostatic contributions, apparently through hydrogen bond interactions with the residue backbone. In addition, the binding efficiency of the ADP-ribose towards the nsP3 macro domain of CHIKV was predicted to be slightly lower than that for VEEV, which concurs with the experimental data. An understanding of the specific interactions between the ADP-ribose and the nsP3 macro domain at the molecular level is useful information to further assist in drug design and development for these two important viruses.

Acknowledgments

This work was supported by The Thailand Research Fund, and the Thai Government Stimulus Package 2 (TKK2555), under the Project for Establishment of Comprehensive Center for Innovative Food, Health Products and Agriculture. T.R. thanks the Ratchadaphiseksomphot Endowment Fund from Chulalongkorn University for Postdoctoral fellowship, and the TRF Grant for New Research (Grant No. TRG5280035). The Computational Chemistry Unit Cell at Chulalongkorn University provided the computing facilities. The Center of Excellence for Petroleum, Petrochemicals and Advanced Materials, Chulalongkorn University, is acknowledged.

Appendix A. Supplementary data

Supplementary data associated with this article can be found, in the online version, at doi:10.1016/j.jmgm.2010.09.010.

References

- [1] S.K. Lam, K.B. Chua, P.S. Hooi, M.A. Rahimah, S. Kumari, M. Tharmaratnam, S.K. Chuah, D.W. Smith, I.A. Sampson, Chikungunya infection—an emerging disease in Malaysia, Southeast Asian J. Trop. Med. Public Health 32 (2001) 447–451.
- [2] J.G. Estrada-Franco, R. Navarro-Lopez, J.E. Freier, D. Cordova, T. Clements, A. Moncayo, W. Kang, C. Gomez-Hernandez, G. Rodriguez-Dominguez, G.V. Ludwig, S.C. Weaver, Venezuelan equine encephalitis virus, southern Mexico, Emerg. Infect. Dis. 10 (2004) 2113–2121.
- [3] Y.F. Wang, S.G. Sawicki, D.L. Sawicki, Alphavirus nsP3 functions to form replication complexes transcribing negative-strand RNA, J. Virol. 68 (1994) 6466–6475.

- [4] J.A. Lemm, T. Rümenapf, E.G. Strauss, J.H. Strauss, C.M. Rice, Polypeptide requirements for assembly of functional Sindbis virus replication complexes: a model for the temporal regulation of minus- and plus-strand RNA synthesis, EMBO J. 13 (1994) 2925–2934.
- [5] Y. Shirako, J.H. Strauss, Regulation of Sindbis virus RNA replication: uncleaved P123 and nsP4 function in minus-strand RNA synthesis, whereas cleaved products from P123 are required for efficient plus-strand RNA synthesis, J. Virol. 68 (1994) 1874–1885.
- [6] P. Laakkonen, M. Hyvönen, J. Peränen, L. Kääriäinen, Expression of Semliki Forest virus nsP1-specific methyltransferase in insect cells and in *Escherichia coli*, J. Virol. 68 (1994) 7418–7425.
- [7] T. Ahola, L. Kääriäinen, Reaction in alphavirus mRNA capping: formation of a covalent complex of nonstructural protein nsP1 with 7-methyl-GMP, Proc. Natl. Acad. Sci. U.S.A. 92 (1995) 507–511.
- [8] T. Ahola, A. Lampio, P. Auvinen, L. Kääriäinen, Semliki Forest virus mRNA capping enzyme requires association with anionic membrane phospholipids for activity, EMBO J. 18 (1999) 3164–3172.
- [9] J. Peränen, P. Laakkonen, M. Hyvönen, L. Kääriäinen, The alphavirus replicase protein nsP1 is membrane-associated and has affinity to endocytic organelles, Virology 208 (1995) 610–620.
- [10] L. Vasiljeva, A. Merits, P. Auvinen, L. Kääriäinen, Identification of a novel function of the alphavirus capping apparatus RNA 5'-triphosphatase activity of nsP2, J. Biol. Chem. 275 (2000) 17281–17287.
- [11] M. Gomez de Cedróna, N. Ehsani, M.L. Mikkola, J.A. Garcıĭaa, L. Kääriäinen, RNA helicase activity of Semliki Forest virus replicase protein nsP2, FEBS Lett. 448 (1999) 19–22.
- [12] D.L. Sawicki, S. Perri, J.M. Polo, S.G. Sawicki, Role for nsP2 proteins in the cessation of alphavirus minus-strand synthesis by host cells, J. Virol. 80 (2006)
- [13] D.J. Barton, S.G. Sawicki, D.L. Sawicki, Demonstration in vitro of temperaturesensitive elongation of RNA in Sindbis virus mutant ts6, J. Virol. 62 (1988) 3597–3602.
- [14] J.K. Rubach, B.R. Wasik, J.C. Rupp, R.J. Kuhn, R.W. Hardy, D.W. Smith, Characterization of purified Sindbis virus nsP4 RNA-dependent RNA polymerase activity in vitro, Virology 384 (2009) 201–208.
- [15] I. De, C. Fata-Hartley, S.G. Sawicki, D.L. Sawicki, Functional analysis of nsP3 phosphoprotein mutants of Sindbis virus, J. Virol. 77 (2003) 13106– 13116
- [16] M.W. LaStarza, J.A. Lemm, C.M. Rice, Genetic analysis of the nsP3 region of Sindbis virus: evidence for roles in minus-strand and subgenomic RNA synthesis, J. Virol. 68 (1994) 5781–5791.
- [17] J.H. Strauss, E.G. Strauss, The alphaviruses: gene expression, replication, and evolution, Microbiol. Rev. 58 (1994) 491–562.
- [18] J.R. Pehrson, R.N. Fuji, Evolutionary conservation of histone macroH2A subtypes and domains, Nucleic Acids Res. 26 (1998) 2837–2842.
- [19] L.R. Comstock, J.M. Denu, Synthesis and biochemical evaluation of O-acetyl-ADP-ribose and N-acetyl analogs, Org. Biomol. Chem. 5 (2007) 3087– 3091.
- [20] M.P. Egloff, H. Malet, A. Putics, M. Heinonen, H. Dutartre, A. Frangeul, A. Gruez, V. Campanacci, C. Cambillau, J. Ziebuhr, T. Ahola, B. Canard, Structural and functional basis for ADP-ribose and poly(ADP-ribose) binding by viral macro domains, J. Virol. 80 (2006) 8493–8502.
- [21] G.I. Karras, G. Kustatscher, H.R. Buhecha, M.D. Allen, C. Pugieux, F. Sait, M. Bycroft, A.G. Ladurner, The macro domain is an ADP-ribose binding module, EMBO I. 24 (2005) 1911–1920.
- [22] G. Kustatscher, M. Hothorn, C. Pugieux, K. Scheffzek, A.G. Ladurner, Splicing regulates NAD metabolite binding to histone macroH2A, Nat. Struct. Mol. Biol. 12 (2005) 624–625.
- [23] H. Malet, B. Coutard, S. Jamal, H. Dutartre, N. Papageorgiou, M. Neuvonen, T. Ahola, N. Forrester, E.A. Gould, D. Lafitte, F. Ferron, J. Lescar, A.E. Gorbalenya, X. de Lamballerie, B. Canard, The crystal structures of Chikungunya and Venezuelan equine encephalitis virus nsP3 macro domains define a conserved adenosine binding pocket, J. Virol. 83 (2009) 6534–6545.

- [24] D.A. Case, T.A. Darden, T.E.I. Cheatham, C.L. Simmerling, J. Wang, R.E. Duke, R. Luo, W. Crowley, R.C. Walker, W. Zhang, K.M. Merz, B. Wang, S. Hayik, A. Roitberg, G. Seabra, I. Kolossváry, K.F. Wong, F. Paesani, J. Vanicek, X. Wu, S.R. Brozell, T. Steinbrecher, H. Gohlke, L. Yang, C. Tan, J. Mongan, V. Hornak, G. Cui, D.H. Mathews, M.G. Seein, C. Sagui, V. Babin, P.A. Kollman, AMBER 10 (2008).
- [25] Y. Duan, C. Wu, S. Chowdhury, M.C. Lee, G. Xiong, W. Zhang, R. Yang, P. Cieplak, R. Luo, T. Lee, J. Caldwell, J. Wang, P. Kollman, A point-charge force field for molecular mechanics simulations of proteins based on condensed-phase quantum mechanical calculations, J. Comput. Chem. 24 (2003) 1999–2012.
- [26] K.L. Meagher, L.T. Redman, H.A. Carlson, Development of polyphosphate parameters for use with the AMBER force field, J. Comput. Chem. 24 (2003) 1016–1025.
- [27] H. Li, A.D. Robertson, J.H. Jensen, Very fast empirical prediction and rationalization of protein pKa values, Proteins 61 (2005) 704–721.
- [28] W.L. Jorgensen, J. Chandrasekhar, J.D. Madura, R.W. Impey, M.L. Klein, Comparison of simple potential functions for simulating liquid water, J. Chem. Phys. 79 (1983) 926–935.
- [29] J.P. Ryckaert, G. Ciccotti, H.J.C. Berendsen, Numerical integration of the Cartesian equations of motion of a system with constraints: molecular dynamics of n-alkanes, J. Comput. Phys. 23 (1997) 327–341.
- [30] D.M. York, T.A. Darden, L.G. Pedersen, The effect of long-range electrostatic interactions in simulations of macromolecular crystals: a comparison of the Ewald and truncated list methods, J. Chem. Phys. 99 (1993) 8345–8348.
- [31] H.J.C. Berendsen, J.P.M. Postma, W.F.V. Gunsteren, A. DiNola, Molecular dynamics with coupling to an external bath, J. Chem. Phys. 81 (1984) 3684–3690.
- [32] M. Malaisree, T. Rungrotmongkol, P. Decha, P. Intharathep, O. Aruksakunwong, S. Hannongbua, Understanding of known drug-target interactions in the catalytic pocket of neuraminidase subtype N1, Proteins 71 (2008) 1908–1918.
- [33] P.A. Kollman, I. Massova, C. Reyes, B. Kuhn, S. Huo, L. Chong, M. Lee, T. Lee, Y. Duan, W. Wang, O. Donini, P. Cieplak, J. Srinivasan, D.A. Case, T.E. Cheatham, Calculating structures and free energies of complex molecules: combining molecular mechanics and continuum models, Acc. Chem. Res. 33 (2000) 889–897
- [34] J. Srinivasan, T.E. Cheatham, P. Cieplak, P.A. Kollman, D.A. Case, Continuum solvent studies of the stability of DNA RNA, and phosphoramidate—DNA helices, J. Am. Chem. Soc. 120 (1998) 9401–9409.
- [35] G. Lamm, Reviews in computational chemistry, in: B. Kenny, R.L. Lipkowitz, R.C. Thomas (Eds.), The Poisson–Boltzmann equation, 2003, pp. 147–365.
- [36] N.A. Baker, Biomolecular applications of Poisson–Boltzmann methods, in: B. Kenny, R.L. Lipkowitz, R.C. Thomas (Eds.), Reviews in Computational Chemistry, 2005, pp. 349–379.
- [37] J. Kottalam, D.A. Case, Langevin modes of macromolecules: applications to crambin and DNA hexamers, Biopolymers 29 (1990) 1409–1421.
- [38] H. Gohlke, C. Kiel, D.A. Case, Insights into protein-protein binding by binding free energy calculation and free energy decomposition for the Ras-Raf and Ras-RalGDS complexes, J. Mol. Biol. 330 (2003) 891–913.
- [39] V. Zoete, M. Meuwly, M. Karplus, Study of the insulin dimerization: binding free energy calculations and per-residue free energy decomposition, Proteins 61 (2005) 79–93.
- [40] O. Aruksakunwong, M. Malaisree, P. Decha, P. Sompornpisut, V. Parasuk, S. Pianwanit, S. Hannongbua, On the lower susceptibility of oseltamivir to influenza neuraminidase subtype N1 than those in N2 and N9, Biophys. J. 92 (2007) 798–807.
- [41] M. Malaisree, T. Rungrotmongkol, N. Nunthaboot, O. Aruksakunwong, P. Intharathep, P. Decha, P. Sompornpisut, S. Hannongbua, Source of oseltamivir resistance in avian influenza H5N1 virus with the H274Y mutation, Amino Acids 37 (2009) 725–732
- [42] S. Miyamoto, P.A. Kollman, What determines the strength of noncovalent association of ligands to proteins in aqueous solution? Proc. Natl. Acad. Sci. U.S.A. 90 (1993) 8402–8406.
- [43] W. Wang, P.A. Kollman, Free energy calculations on dimer stability of the HIV protease using molecular dynamics and a continuum solvent model, J. Mol. Biol. 303 (2000) 567–582.

ORIGINAL PAPER

Molecular insights into human receptor binding to 2009 H1N1 influenza A hemagglutinin

Nadtanet Nunthaboot · Thanyada Rungrotmongkol · Maturos Malaisree · Panita Decha · Nopporn Kaiyawet · Pathumwadee Intharathep · Pornthep Sompornpisut · Yong Poovorawan · Supot Hannongbua

Received: 25 September 2009/Accepted: 2 May 2010/Published online: 27 May 2010 © Springer-Verlag 2010

Abstract The current pandemic of the viral 2009 H1N1 influenza and its sustained human–human transmission has raised global concern for human health. The binding of the viral glycoprotein hemagglutinin (HA) and the human α-2,6-linked sialopentasaccharide (SIA-2,6-GAL) host cell receptor is a critical step in the viral replication cycle. Here, the complex structure of the 2009 H1N1 HA bound to the SIA-2,6-GAL sialopentasaccharide receptor was constructed by using homology modeling and molecular dynamic simulations. The receptor was found to fit very well within the HA binding pocket and formed hydrogen bonds with the residues of the 130-loop, 190-helix, and 220-loop. Most receptor binding residues play a significant role in stabilizing the protein–receptor complex with major

contributions being provided by V135, T136, A137, K222, and Q226. The results are similar to the human SIA-2,6-GAL sialopentasaccharide receptor binding to H1 HA subtype, but are slightly different from those of H3, H5, and H9 HAs.

Keywords Computational chemistry · Hydrogen bonds · Molecular modelling · Sialopentasaccharide receptor · Per residue interactions · Molecular dynamics simulations

Introduction

Since the first identification of the novel A (H1N1) influenza virus in April 2009, the outbreak of this virus has rapidly spread and encircled over 100 countries worldwide, causing more than 3,000 human deaths (April–September 2009) [1]. The World Health Organization (WHO) announced a worldwide pandemic alert level at phase 6, indicating that a global human pandemic of this virus isolate is under way [1–3]. In the primary step of the viral replication cycle, influenza infection is initiated by the viral surface homotrimeric glycoprotein hemagglutinin (HA) binding to the host membrane sialylated glycans, which act as cell receptors. Understanding of this attachment and interaction can provide a basic knowledge of how the emerging virus infects humans and is thus the main goal of this study.

Hemagglutinin is an important target for the development of both vaccines and antiviral drugs against influenza viruses. Each monomer of the homotrimer is composed of two subunits, HA1 and HA2. Whilst HA1 is known to be responsible for the viral attachment to host cell, HA2 is associated with the release of the viral RNA complexed with the RNA polymerase through membrane fusion [4–7], and thus HA is essential to both host cell targeting and cell

N. Nunthaboot

Department of Chemistry, Faculty of Science, Mahasarakham University, Mahasarakham 44150, Thailand

T. Rungrotmongkol · M. Malaisree · P. Decha · N. Kaiyawet · P. Intharathep · P. Sompornpisut · S. Hannongbua (☒) Computational Chemistry Unit Cell, Department of Chemistry, Faculty of Science, Chulalongkorn University, Bangkok 10330, Thailand e-mail: supot.h@chula.ac.th

T. Rungrotmongkol

Center of Innovative Nanotechnology, Chulalongkorn University, Bangkok 10330, Thailand

Y. Poovorawan

Center of Excellence in Clinical Virology, Faculty of Medicine, Chulalongkorn University, Bangkok 10330, Thailand

S. Hannongbua

Center of Excellence for Petroleum, Petrochemicals, and Advanced Materials, Chulalongkorn University, Bangkok 10330, Thailand



entry (infection). HA1 binds to host cell membrane receptors, glycans containing the terminal sialic acid which are attached to surface membrane proteins or lipids [6, 8, 9]. The specific topology, determined principally but not exclusively by the specific linkage of the terminal sialic acid to the galactose subunit and the glycan chain length, identifies the species and tissue specificity and avidity of binding, and thus its infectability and transmission rates [10]. The avian influenza virus preferentially recognizes the sialic acid α -2,3-galactose (SIA- α -2,3-GAL) linkage with a long glycan chain and cone-like topology, whilst the adopted sialic acid α-2,6-galactose (SIA-α-2,6-GAL) linkage is more favorable for both human and swine influenza viruses with longer glycan chains and an umbrella topology [10–14]. It is supposed that the alternation in host specificity of sialic acid linked to galactose from α -2,3- to α -2,6linkage is a major barrier for influenza viruses to cross species barriers and adapt to a new host [7, 10, 15–18].

From the available information, it is clear that the binding domain of HA with the glycan receptors comprises several key structural components including the 190-helix, 130- and 220-loop domains, and several other conserved residues that give species and tissue specificity [9]. However, how this is derived is not clear and to date, the H1N1-2009 HA structures, either as free-form or receptor-bound conformation, have not yet been experimentally solved. Recently, a theoretically modeled structure of the HAreceptor complex has been published [19]. However, it represents a static view of protein-receptor interactions without dynamic capture of time-dependent properties. Therefore, in the present study, molecular dynamics (MD) simulations were performed on the homology modeled structure of the novel H1N1 HA complexed with the SIA-2,6-GAL sialopentasaccharide, a human preferential receptor, to investigate the fundamental structural characteristics, the role of conserved binding residues, and receptor binding specificity. Extensive analysis was focused on the structural properties and, in particular, on the enzyme-receptor interactions in terms of hydrogen bonding and per residue-receptor interactions.

Results and discussion

MD simulation of the novel H1N1 HA complexed with the SIA-2,6-GAL sialopentasaccharide, a human preferential receptor, was carried out over a period of 4 ns. In the last 2.5-ns simulation, the whole system is fairly stable as indicated by the small magnitude of root mean square deviation (RMSD) fluctuation of ca. 0.5 Å (Fig. 1). The simulation run could thus provide a suitable basis for the subsequent analyses.

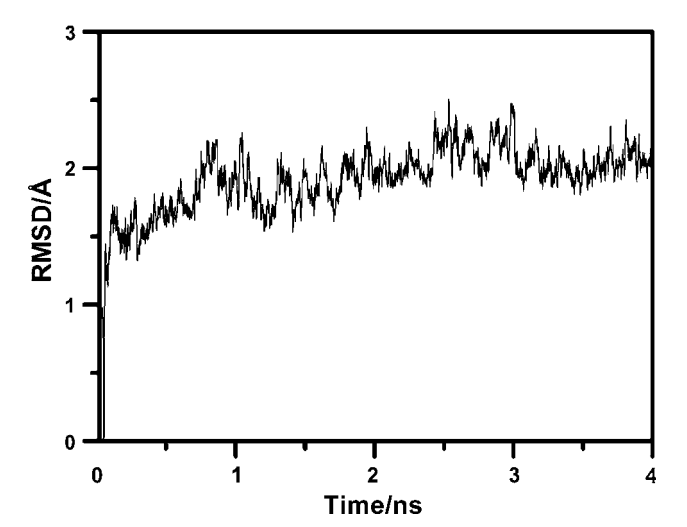


Fig. 1 Root mean square deviation (*RMSD*) of all heavy atoms of hemagglutinin and human SIA- α -2,6-GAL pentasaccharide receptor to the starting structure as a function of simulation time

The obtained human SIA-2,6-GAL sialopentasaccharide receptor was found to properly occupy the binding pocket of the 2009 H1N1 hemagglutinin, similar to what has been observed experimentally in the other viral influenza HA strains [21, 28–30], where the potentially important contact residues of the 130-loop (K133a, N133, V135, T136, and A137), 190-helix (H183, D190, and S193), and 220-loop (K222, D225, Q226, and E227) as well as Y95 (see Fig. 2a for residue positions) were revealed. Structural properties, hydrogen bonds, and per residue–receptor interactions are extensively discussed in the following sections.

Sialopentasaccharide receptor conformation

To investigate the conformational character of the human SIA-2,6-GAL sialopentasaccharide receptor, the distribution of eight important torsion angles, defined in Fig. 3a, from (1) $\tau I - \tau 4$ bridging between the saccharide units and (2) $\tau 5 - \tau 8$ of the functional groups of the terminal sialic acid, were measured and plotted in Fig. 3b and c, respectively.

It can clearly be seen in Fig. 3b that the $\tau 1$ and $\tau 2$ torsions of the first three saccharide units (SIA1, GAL2, and NAG3) show a single preferential and sharp peak, suggesting the high stability of these units which were well oriented and occupied in the binding pocket of the enzyme (Fig. 2a, b) and, therefore, that many hydrogen bonds with the HA residues were firmly formed (Fig. 4a, discussed later). The most probable glycosidic torsion angle ($\tau 1$, black line in Fig. 3b) was found at ca. -68° indicating the adopted *cis*-conformation of the α -2,6-linked terminal sialic acid (SIA1) to the galactose (GAL2) of the receptor. This proposed conformation is consistent with what has



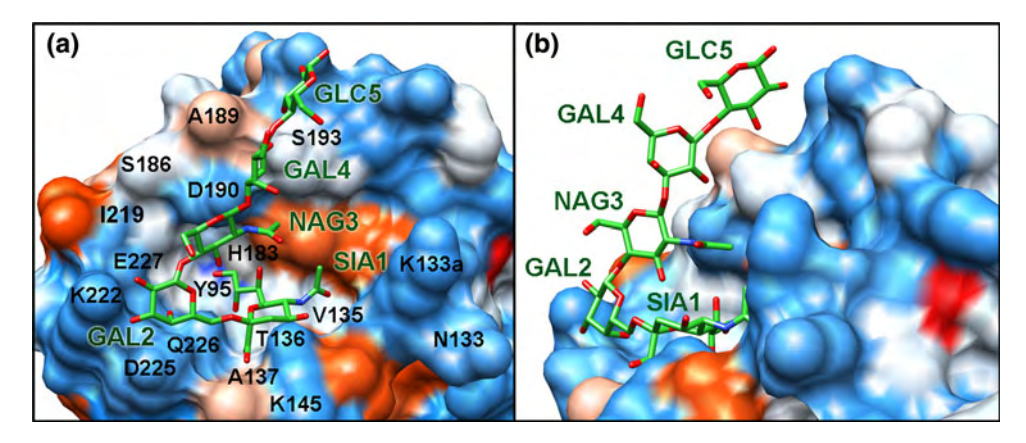
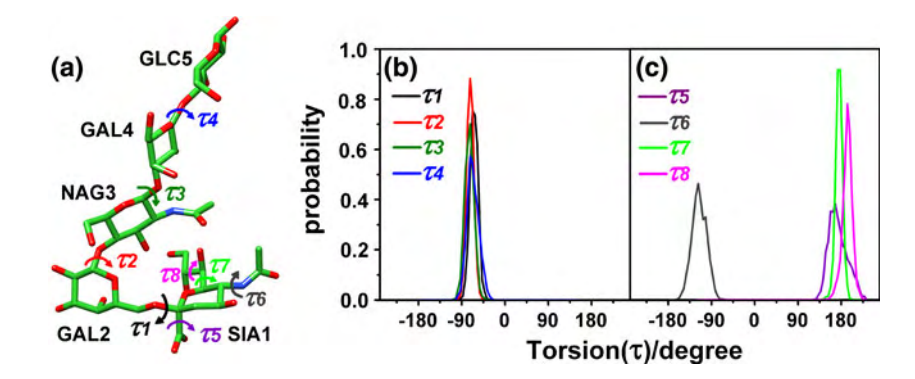


Fig. 2 a Top and b side views of the human SIA-2,6-GAL sialopentasaccharide receptor bound to the binding pocket of the 2009 H1N1 influenza HA. The potential contact residues and five units of the receptor (SIA1, GAL2, NAG3, GAL4, and GLC5) are labeled.

Residue K133a is an inserted amino acid specific to the 2009 H1N1 HA. Blue and orange surfaces indicate the hydrophilic and hydrophobic features, respectively (color figure online)

Fig. 3 a Definition of torsion angles of the human SIA-2, 6-GAL sialopentasaccharide receptor. Probability distributions of the b torsion angles $(\tau I - \tau 4)$ linking between each saccharide unit and **c** torsion angles $(\tau 5 - \tau 8)$ of the functional groups of the terminal sialic acid



been observed both experimentally and theoretically for the human SIA-2,6-GAL receptor binding to the influenza HA subtypes H1, H3, and H5, whose glycosidic torsion angles were observed to fall within the range of between -50° and -70° [21, 30–33]. In the same fashion, the $\tau 3$ and $\tau 4$ angles linking between the last three saccharides (NAG3, GAL4, and GLC5) showed the single preferential sharp peak at ca. -73° (Fig. 3b) indicating their high rigidity throughout the simulation period.

To reveal the conformational change of the terminal sialic acid SIA1, the torsion angles of its functional groups were further evaluated and the results are shown in Fig. 3c. Amongst the four angles, $\tau 5$ and $\tau 6$ are slightly broader than the other two angles, $\tau 7$ and $\tau 8$. This indicates that the -COO- and -NHAc groups could feasibly rotate rather than the hydrophilic group.

Enzyme-receptor hydrogen bonds

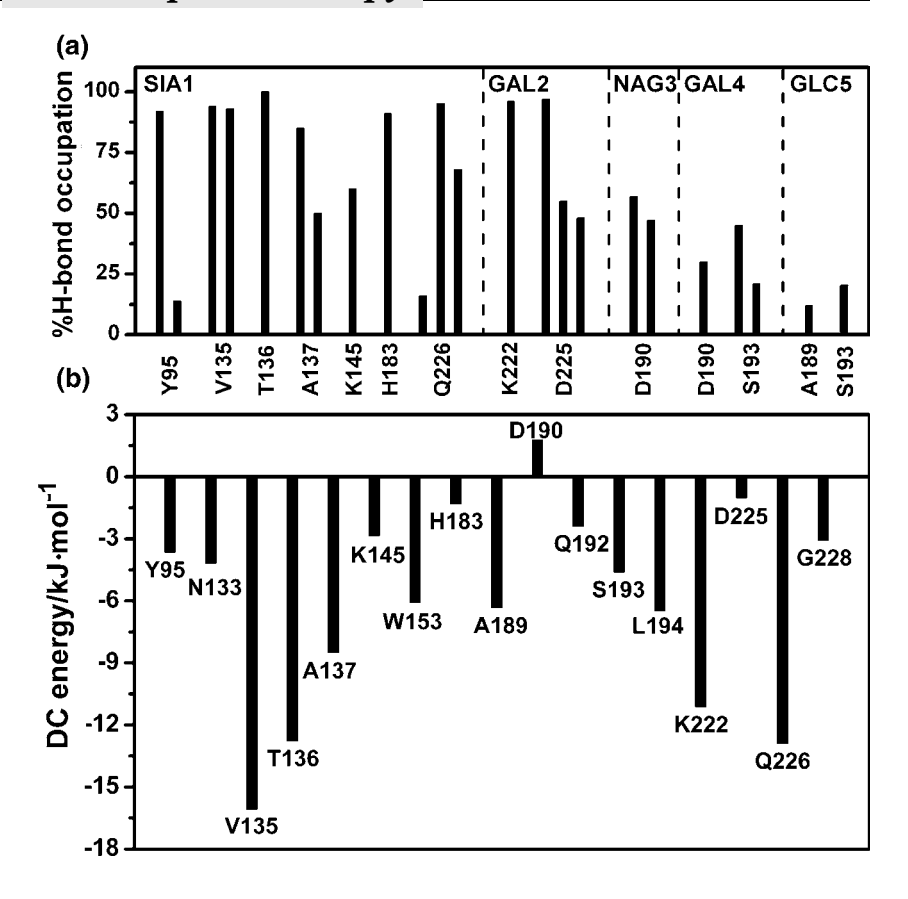
To determine the protein-receptor interactions, hydrogen bonding between the HA residues and the human SIA-α-2,6-GAL sialopentasaccharide receptor were calculated according to the two criteria: (1) a proton donor (D) and acceptor (A) distance of 3.5 Å or less and (2) a D-H···A angle of 120° or more.

The number and percentage of hydrogen bond occupation of each of the 2009 HA binding residues and all five saccharides of the receptor were evaluated, and the results are shown in Fig. 4a (see description in Table 1). At the terminal sialic acid (SIA1, see Fig. 2a), extensive interactions were found with Y95 and the highly conserved residues of the 130-loop (V135, T136, and A137), 190helix (H183), and 220-loop (Q226). The hydroxyl oxygen of the hydrophilic group forms a strong hydrogen bond to the phenyl group of Y95. Three strong hydrogen bonds were detected between the terminal sialic acid -COOgroup and the three HA residues, T136 and A137 in the 130-loop and Q226 in the 220-loop, whilst the -NHAc moiety established two strong hydrogen bonds with the backbone nitrogen and oxygen atoms of residue V135 in the 130-loop. In addition, the hydroxyl oxygen atoms of hydrophilic side chain form strong and moderate hydrogen bonds with the imidazole ring of H183 in the 190-helix and the amide group of Q226 in the 220-loop, respectively.



Fig. 4 a Hydrogen bonding occupation and **b** decomposition (*DC*) energy in kJ mol⁻¹ of the individual residues of the 2009 H1N1 HA towards the human SIA-2,6-GAL sialopentasaccharide receptor

(see Fig. 2 for residue labels)



Based on the numbers of hydrogen bonds (see Fig. 4a), the 130-loop is more likely to be in contact with SIA1 than the 190-helix and 220-loop, which is comparable to that of the other hemagglutins complexed with the human receptor [21, 30, 33].

For the second unit of the human SIA-2,6-GAL sialopentasaccharide receptor (GAL2), two strong hydrogen bonds were formed with the ammonium group of K222 and the backbone oxygen of D225. These hydrogen bonds were also detected in the case of the H5 HA-receptor complex, but not in the H3 and H9 HA-receptor complexes [33]. Moreover, two moderate hydrogen bonding interactions between the hydroxyl moieties of this saccharide and the carboxylate group of D225 were also found. Instead, G225, as in the crystal structure of the H1 HA-receptor complex [21, 30], forms hydrogen bonds through its backbone oxygen with the GAL2 unit. Finally, considering the other three units (NAG3, GAL4, and GLC5) of the sialopentasaccharide, they were all found to establish medium to rather weak hydrogen bond networks to the two 190-helix residues, D190 and S193, which are in agreement with the published results of the swine H1-receptor structure [21]. Interestingly, they are, however, different from what has been reported for the H3, H5, and H9 HA-receptor complexes where the last three glycans explicitly interact with the 150-loop and 190-helix [33].

Taking into account all the simulation results shown above, all important hydrogen bonds between the SIA-2,6-GAL sialopentasaccharide receptor and the residues of the 130-loop, 190-helix, and 220-loop are considerably conserved and are more likely to be similar to those observed in the H1 HA–receptor complex structure [21, 30], indicating the likely reliability of the simulated structures of the human receptor bound to the pocket of the viral H1N1-2009 HA. In addition, the results also confirm the potentially important role of the 130-loop, 190-helix, and 220-loop of the viral surface HA in attaching to SIA-2,6-GAL sialopentasaccharide glycan, which is the main receptor found in human respiratory tract host cells.

Per residue HA enzyme—SIA-2,6-GAL receptor interactions

To reveal the fundamental basis of the binding between the human SIA-2,6-GAL sialopentasaccharide receptor and the influenza HA, the interaction energies between each of the individual residues and the SIA-2,6-GAL sialopentasaccharide were evaluated by using the decomposition (DC) energy module implemented in AMBER 10. The energetic contribution was averaged over a set of 100 MD snapshots, taken at every 25 ps from the last 2.5-ns simulation.



Table 1 Hydrogen bond descriptions and interactions detected between heavy atoms of the human SIA-α-2,6-GAL pentasaccharide receptor and 2009-H1N1 hemagglutinin residues

Pentasaccharide	НА	Туре	Occupation (%)
SIA1	Y95	Y95_OH_HO8_SIA1	92
	Y95	Y95_OH···H_O9_SIA1	14
	V135	V135_N_H···O5N_SIA1	94
	V135	V135_OH_N5_SIA1	93
	T136	T136_OG1_H···O1B_SIA1	100
	A137	A137_N_H···O1A_SIA1	85
	A137	A137_N_H···O1B_SIA1	50
	K145	K145_NZ_H···O4_SIA1	60
	H183	H183_NE2···H_O9_SIA1	91
	Q226	Q226_NE2_H···O1A_SIA1	16
	Q226	Q226_NE2_H···O1B_SIA1	95
	Q226	Q226_OE1···H_O8_SIA1	68
GAL2	K222	K222_NZ_H···O3_GAL2	96
	D225	D/G225_O···H_O4_GAL2	97
	D225	D225_OD1···H_O3_GAL2	55
	D225	D225_OD2···H_O3_GAL2	48
NAG3	D190	D190_OD1···H_N2_NAG2	57
	D190	D190_OD2···H_N2_NAG2	47
GAL4	D190	D190_OD1···H_O2_GAL4	30
	S193	S193_OG···H_O2_GAL4	45
	S193	S193_OG_H···O2_GAL4	21
GLC5	A189	T189_O···H_O6_GLC5	12
	S193	S193_OG···H_O3_GLC5	20

The evaluated DC energies of the HA residues located in the binding pocket are plotted in Fig. 4b, where the per residue interaction energies are seen to vary within the range of 2 to -17 kJ mol^{-1} . The major contribution to the enzyme-receptor interactions was gained from the conserved residues which are the members of the 130- and 220-loops: V135, T136, A137, K222, and Q226. The corresponding DC energies of less than -8 kJ mol^{-1} due to these residues agree well with the hydrogen bond data discussed above (Fig. 4a) and corroborate their important role in attaching the viral coat HA to the human SIA-2,6-GAL sialopentasaccharide receptor of susceptible host cells. The higher negative values of the DC data in Fig. 4b for the remaining residues of these two loops and the 190helix residues (except for D190) also indicate their likely responsibilities in stabilizing the human receptor-HA complex. In some contrast, and in agreement with a previous theoretical report [34], the D190 residue was found to destabilize the protein-receptor complex.

Interestingly, as determined from their DC energies, the D225 and D190 residues do not significantly improve the enzyme-receptor binding affinity, although they interact explicitly via three hydrogen bonds with the GAL2, NAG3, and GAL4 saccharides of the SIA-2,6-GAL sialopentasaccharide, respectively (as discussed above). This can then be best understood in terms of their total interactions with the neighboring residues, since the DC energy is a summation of all interactions between a central residue and its environment, including the SIA-2,6-GAL receptor and all the residues of the respective HA enzyme. In other words, the D225 and D190 hydrogen bond energies can be destabilized by their repulsions with the other residues of the HA.

Conclusions

In the present study, the three-dimensional structure of the human SIA-2,6-GAL sialopentasaccharide receptor bound to the recently detected 2009 H1N1 HA was modeled based on a homology modeling approach and consequently performed by molecular dynamic simulations. The structural properties and protein-receptor interactions, in terms of the receptor conformation, hydrogen bonds, and per residue interaction energies, were extensively discussed and compared to the binding between the human SIA-2,6-GAL sialopentasaccharide receptor and the other HAs. Basically, comparative molecular dynamics are complementary to experimental results (tissue binding, glycan microarrays, Scatchard analysis) and do not suffer the drawback of crystallographic methods in that the glycan and HA protein show considerable flexibility in conformation which is missed, by being only a single snapshot, by crystallography methods.

Conformational analysis of the human SIA-2,6-GAL sialopentasaccharide receptor orientation throughout the simulation period confirms the adopted preferential cisconformation of this receptor, as indicated by the glycosidic torsion angle between the terminal sialic acid (SIA1) and the adjacent galactose (GAL2) of ca. -68°. The simulated model of the 2009 H1 HA bound to the human SIA-2,6-GAL sialopentasaccharide receptor showed a well-oriented conformation of the receptor in the binding pocket of the HA enzyme and lays in the conserved regions including the 130-loop, 190-helix, and 220-loop. The sialic acid forms many strong hydrogen bonds with the HA residues V135, T136, A137, H183, and Q226. Furthermore, the GAL2 unit of the receptor was found to interact with the HA K222 and D225 residues, whilst the last three glycans established hydrogen bonds with D190 and S193. Based on a per residue interaction analysis, most receptor binding residues (especially V135, T136, A137, K222, and Q226) of the viral surface HA were found to play a stabilizing role in attaching to the human SIA-2,6-GAL sialopentasaccharide receptor of the host cell.



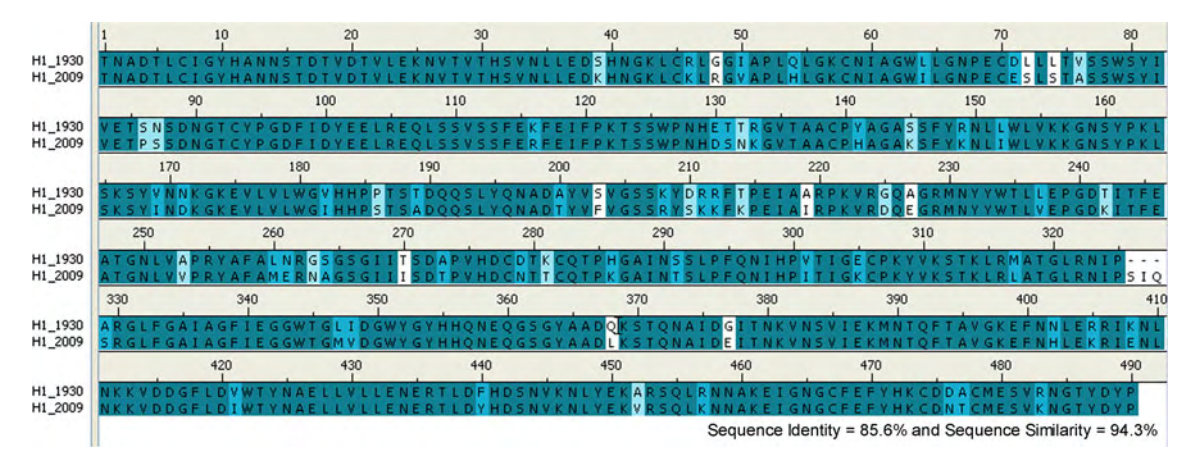


Fig. 5 Sequence alignment of 1930 and 2009 H1 hemagglutinins of influenza A (H1N1) viruses

In comparison to the other influenza HAs-human SIA-2,6-GAL sialopentasaccharide receptor complexes, the simulated results of this receptor binding to the 2009 H1N1 influenza HA provided the highest similarity to those from the structure of the H1-receptor complex. This is mainly due to the fact that they belong to the identical HA subtype and so are likely to share the highest conformational as well as primary sequence similarity. In addition, the results also show somewhat similar properties to those evaluated and observed for the H3 and H5, and H9 HAs-SIA-2,6-GAL complexes. Although many experimental aspects of the 2009 H1N1 outbreak including its virulence and pandemic potential are still uncertain, our molecular information could provide a better understanding of the first step of the viral life cycle based on how the viral surface glycoprotein HA of the 2009 influenza A (H1N1) efficiently attaches and tightly binds with the human SIA-2,6-GAL sialopentasaccharide receptor.

Materials and methods

Model of 2009 H1N1 influenza hemagglutinin complexed with human receptor

The initial structure of the 2009 H1N1 influenza HA bound with the human SIA-2,6-GAL sialopentasaccharide receptor was modeled based on the sequence which was recently isolated from children in Southern California, A/California/04/2009(H1N1) [20]. To seek the most relevant structure of the 2009 HA protein, its amino acid sequence was preliminarily aligned to all seven available crystallographic H1N1 HA structures [21]. It was found that the highest amino acid sequence similarity, at 86% identical, was with the 1930 swine H1N1 HA structure (Fig. 5). Therefore, this HA enzyme structure complexed with the human SIA-2,6-GAL sialopentasaccharide receptor (Protein Data Bank

entry code 1RVT) was chosen as the template [21] for building up the HA-2009 structure by homology modeling performed by using the module implemented in Discovery Studio 2.0 [22]. The novel H1N1 HA–receptor complex was then further refined by using energy minimization and followed by multiple stepwise MD simulations.

Molecular dynamics simulations

All simulations of HA-receptor complex were carried out using the SANDER module of the AMBER 10 software package [23]. The HA protein and SIA-2,6-GAL sialopentasaccharide were parameterized by using the AMBER03 [24] and the GLYCAM06 force fields [25], respectively. All missing hydrogen atoms were added by using the LEaP module [23] and the system was subsequently solvated by a cubic box with dimensions of $66 \times 69 \times 141 \text{ Å}^3$ filled with TIP3P water molecules. Normal charge states of ionizable amino acids corresponding to pH 7.0 were treated and 5 Cl⁻ counterions were further added to maintain neutrality on the system. A periodic boundary condition in the isobaric-isothermal (NPT) ensemble with a constant pressure of 1 atm and a temperature of 310 K was set up, whilst a Berendsen coupling time of 0.2 ps was employed to control the temperature. The SHAKE algorithm [26] was applied to constrain all hydrogen bonds using a time step of 2 fs. Non-bonded interactions were calculated with a 12-Å residue-based cutoff and the particle mesh Ewald method [27] was applied to treat the long-range electrostatic interactions. To remove unfavorable contact, the structure of the HA-receptor complexes was relaxed by performing 3,000 steps of conjugated gradient energy minimization. The whole system was subsequently heated from 0 to 310 K over 100 ps. The system was pre-equilibrated for two steps of 200-ps simulations with position restraints on the receptor atoms with the factors of 80 and 40 kJ mol⁻¹ \mathring{A}^{-2} ,



Human receptor binding to 2009 H1N1 influenz Author's personal copy

to maintain their coordinates inside the protein binding pocket. Afterwards, the complex was fully simulated for 4 ns.

Acknowledgments This work was financially supported by the Thailand Research Fund (TRF) and the Commission Higher Education (CHE). N.N. (Grant No. MRG5180298) and T.R. (Grant No. TRG5280035) acknowledge the funding for New Research from TRF. The authors are grateful for the partial support by the Rachadapisek Sompoch Endowment Fund "Emerging Health Risk Cluster", Chulalongkorn University. The Center of Excellence for Petroleum, Petrochemicals, and Advanced Materials, Chulalongkorn University, is acknowledged.

References

- 1. World Health Organization (2010) Global Alert and Response (GAR). http://www.who.int/csr/disease/swineflu/en/index.html. Accessed 2 May 2010
- 2. Zarocostas J (2009) World Health Organization declares A (H1N1) influenza pandemic. Available via http://www.bmj.com/ cgi/content/extract/338/jun12_1/b2425. Accessed 2 May 2010
- Centers for Disease Control and Prevention (2010) 2009 H1N1 flu. http://www.cdc.gov/h1n1flu/. Accessed 2 May 2010
- 4. Steinhauer DA (1999) Virology 258:1
- 5. Horimoto T, Kawaoka Y (2001) Clin Microbiol Rev 14:129
- 6. Cross KJ, Burleigh LM, Steinhauer DA (2001) Exp Rev Mol Med
- 7. Stevens J, Blixt O, Tumpey TM, Taubenberger JK, Paulson JC, Wilson IA (2006) Science 312:404
- 8. Wiley DC, Skehel JJ (1987) Annu Rev Biochem 56:365
- 9. Skehel JJ, Wiley DC (2000) Anun Rev Biochem 69:531
- 10. Chandrasekaran A, Srinivasan A, Raman R, Viswanathan K, Raguram S, Tumpey TM, Sasisekharan V, Sasisekharan R (2008) Nat Biotechnol 26:107
- 11. Bateman AC, Busch MG, Karasin AI, Bovin N, Olsen CW (2008) J Virol 82:8204
- 12. Gambaryan AS, Karasin AI, Tuzikov AB, Chinarev AA, Pazynina GV, Bovin NV, Matrosovich MN, Olsen CW, Klimov AI (2005) Virus Res 114:15
- 13. Matrosovich MN, Gambaryan AS, Teneberg S, Piskarev VE, Yamnikova SS, Lvov DK, Robertson JS, Karlsson KA (1997) Virology 233:224
- 14. Rogers GN, D'Souza BL (1989) Virology 173:317
- 15. Suzuki Y, Ito T, Suzuki T, Holl RE, Chambers TM, Kiso M, Ishida H, Kawaoka Y (2000) J Virol 74:11825

- 16. Russell RJ, Stevens DJ, Haire LF, Gamblin SJ, Skehel JJ (2006) Glycoconjugate J 23:85
- 17. van Riel D, Munster VJ, de Wit E, Rimmelzwaan GF, Fouchier RA, Osterhaus AD, Kuiken T (2007) Am J Pathol 171:1215
- 18. Nicholls JM, Bourne AJ, Chen H, Guan Y, Peiris JSM (2007) Respir Res 8:73
- 19. Soundararajan V, Tharakaraman K, Raman R, Raguram S, Shriver Z, Sasisekharan V, Sasisekharan R (2009) Nat Biotechnol 27:510
- 20. National Center for Biotechnology Information (NCBI) (2010) GenBank sequences from pandemic (H1N1) 2009 viruses. http://www.ncbi.nlm.nih.gov/genomes/FLU/SwineFlu.html. Accessed 2 May 2010
- 21. Gamblin SJ, Haire LF, Russell RJ, Stevens DJ, Xiao B, Ha Y, Vasisht N, Steinhauer DA, Daniels RS, Elliot A, Wiley DC, Skehel JJ (2004) Science 303:1838
- 22. Discovery Studio 2.0, Accelrys Inc., San Diego, CA, USA
- Case DA, Darden TA, Cheatham TE, Simmerling CL, Wang J, Duke RE, Luo R, Crowley M, Walker RC, Zhang W, Merz KM, Wang B, Hayik S, Roitberg A, Seabra G, Kolossváry I, Wong KF, Paesani F, Vanicek J, Wu X, Brozell SR, Steinbrecher T, Gohlke H, Yang L, Tan C, Mongan J, Hornak V, Cui G, Mathews DH, Seetin MG, Sagui C, Babin V, Kollman PA (2008) AMBER 10, University of California, San Francisco
- 24. Duan Y, Wu C, Chowdhury S, Lee MC, Xiong G, Zhang W, Yang R, Cieplak P, Luo R, Lee T, Caldwell J, Wang J, Kollman P (2003) J Comput Chem 24:1999
- 25. Tessier MB, DeMarco ML, Yongye AB, Woods RJ (2008) Mol Simulat 34:349
- 26. Ryckaert JP, Ciccotti G, Berendsen HJC (1977) J Comput Phys 23:327
- 27. Darden T, York D, Pedersen L (1993) J Chem Phys 98:10089
- 28. Ha Y, Stevens DJ, Skehel JJ, Wiley DC (2001) Proc Natl Acad Sci U S A 98:11181
- 29. Ha Y, Stevens DJ, Skehel JJ, Wiley DC (1968) Virology 309:209
- 30. Lin T, Wang G, Li A, Zhang Q, Wu C, Zhang R, Cai Q, Song W, Yuen KY (2009) Virology 392:73
- 31. Kumari K, Gulati S, Smith DF, Gulati U, Cummings RD, Air GM (2007) Virol J 4:42
- 32. Li MY, Wang BH (2006) Biochem Biophys Res Commun 347:662
- 33. Xu D, Newhouse EI, Amaro RE, Pao HC, Cheng LS, Markwick PRL, McCammon JA, Li WW, Arzberger PW (2009) J Mol Biol
- 34. Iwata T, Fukuzawa K, Nakajima K, Aida-Hyugaji S, Mochizuki Y, Watanabe H, Tanaka S (2008) Comput Biol Chem 32:198



Evolution of Human Receptor Binding Affinity of H1N1 Hemagglutinins from 1918 to 2009 Pandemic Influenza A Virus

Nadtanet Nunthaboot,[†] Thanyada Rungrotmongkol,^{‡,§} Maturos Malaisree,[‡] Nopporn Kaiyawet,[‡] Panita Decha,^{||} Pornthep Sompornpisut,[‡] Yong Poovorawan,[⊥] and Supot Hannongbua*,[‡]

Department of Chemistry, Faculty of Science, Mahasarakham University, Mahasarakham, 44150, Thailand, Computational Chemistry Unit Cell, Department of Chemistry, Faculty of Science, Chulalongkorn University, Bangkok, 10330, Thailand, Center of Innovative Nanotechnology, Chulalongkorn University, Bangkok, 10330, Thailand, Computational Chemistry Research Unit, Department of Chemistry, Faculty of Science, Thaksin University, Phatthalung 93110, Thailand, and Center of Excellence in Clinical Virology, Faculty of Medicine, Chulalongkorn University, Bangkok, 10330, Thailand

Received January 27, 2010

The recent outbreak of the novel 2009 H1N1 influenza in humans has focused global attention on this virus, which could potentially have introduced a more dangerous pandemic of influenza flu. In the initial step of the viral attachment, hemagglutinin (HA), a viral glycoprotein surface, is responsible for the binding to the human SIA α2,6-linked sialopentasaccharide host cell receptor (hHAR). Dynamical and structural properties, based on molecular dynamics simulations of the four different HAs of Spanish 1918 (H1-1918), swine 1930 (H1-1930), seasonal 2005 (H1-2005), and a novel 2009 (H1-2009) H1N1 bound to the hHAR were compared. In all four HA—hHAR complexes, major interactions with the receptor binding were gained from HA residue Y95 and the conserved HA residues of the 130-loop, 190-helix, and 220-loop. However, introduction of the charged HA residues K145 and E227 in the 2009 HA binding pocket was found to increase the HA—hHAR binding efficiency in comparison to the three previously recognized H1N1 strains. Changing of the noncharged HA G225 residue to a negatively charged D225 provides a larger number of hydrogen-bonding interactions. The increase in hydrophilicity of the receptor binding region is apparently an evolution of the current pandemic flu from the 1918 Spanish, 1930 swine, and 2005 seasonal strains. Detailed analysis could help the understanding of how different HAs effectively attach and bind with the hHAR.

INTRODUCTION

The emerging influenza pandemic of the 2009 influenza A/H1N1 virus, with readily detected human-human transmission rates, has raised serious global concern for human health in recent times. Among the known targets determining the virus life's cycle, the initial step of viral attachment is mediated by HA binding the virion to the host cell receptor, α2,6 linked sialopentasaccharide (SIA-2,6-GAL; hHAR) in the case of humans. Amino acid mutations in the HA receptor binding domain could potentially introduce an outbreak of a new influenza virus. Relative to the 1918 Spanish (H1-1918), the 1930 swine (H1-1930), and the 2005 seasonal (H1-2005) H1N1 viruses, the HA binding pocket of the 2009 H1N1 (H1-2009) virus was found to display a notably higher hydrophilicity than the other three viral HAs. Such types of electronic effects, in cooperation with the structural differences due to the amino acid components (Table 1) in the binding pocket of the four HAs, are supposed to affect their susceptibility. A detailed and comparative understanding of the HA-hHAR binding among the four H1N1 strains is, then, the rational goal of this study.

On June 11, 2009, the WHO raised the alert status of the 2009 influenza A/H1N1 to level 6.1 This novel H1N1 pandemic has caused at least 18 000 deaths in many countries around the world (as of July 2010). The most devastating influenza pandemic, 1918 H1N1 Spanish Flu, killed more than 40 million people worldwide. ²⁻⁴ The replication cycle of influenza virus is initiated by the attachment of the viral HA to sialylated glycans on the target cell-surface receptor, allowing for viral penetration into the host cell. While the adopted sialic acid α2,3-galactose linkage with a short glycan chain and cone-like topology is more favorable in avian influenza virus, the human and swine influenza viruses preferentially recognizes the sialic acid α2,6-galactose with longer glycan chains and an umbrella like topology, 5-10 hereafter referred to the hHAR. Besides HA functions, the M2-proton channel and neuraminidase (NA) are associated with the proton transport and the release of the newly synthesized viral particles in the viral replication cycle. Although the antiviral drugs approved against M2 ion channel and NA proteins are currently used for the treatment of influenza virus infections, the limitation of drug resistances because of amino acid mutations has led to an effort to

^{*} To whom correspondence should be addressed. Tel: +66 22 187602. Fax: +66 22 187603. E-mail: supot.h@chula.ac.th.

[†] Department of Chemistry, Faculty of Science, Mahasarakham University.

‡ Computational Chemistry Unit Cell, Department of Chemistry, Faculty of Science, Chulalongkorn University.

[§] Center of Innovative Nanotechnology, Chulalongkorn University.

[&]quot;Computational Chemistry Research Unit, Department of Chemistry, Faculty of Science, Thaksin University.

¹ Center of Excellence in Clinical Virology, Faculty of Medicine, Chulalongkorn University.

Table 1. Comparison of Amino Acids in the HA Receptor Binding Domain of the Four Different H1N1 Influenza Viruses: The 1918 Spanish Flu (H1-1918), 1930 Swine Flu (H1-1930), 2005 Seasonal Flu (H1-2005), and 2009 Novel Flu (H1-2009)^a

114 (111 2005)	ana 2007 110	3 (e1 1 1a (111 2	2007)	
		H1N1 H	A strains	
residue ID	H1-1918	H1-1930	H1-2005	H1-2009
95	Y	Y	Y	Y
133	T	T	N	$\underline{\mathbf{N}}$
133a	K	$\frac{\mathbf{R}}{\mathrm{G}}$	<u>N</u> <u>R</u> G	$\overline{\mathbf{K}}$
134	G	$\overline{\mathbf{G}}$		G
135	V	V	V	V
136	T	T	T	T
137	A	A	A	A
138	A	A	A	A
145	S	S	$\underline{\mathbf{N}}$	$\underline{\mathbf{K}}$
153	W	W	W	W
155	T	$\frac{\mathbf{V}}{\mathrm{H}}$	$\frac{\mathbf{V}}{\mathbf{H}}$	$\frac{\mathbf{V}}{\mathbf{H}}$
183	H			
185	P	P	P	$rac{\mathbf{P}}{\mathbf{S}}$ $rac{\mathbf{A}}{\mathbf{D}}$
186	P	P	P	$\underline{\mathbf{S}}$
189	T	T	T	$\underline{\mathbf{A}}$
190	D	D	D	
192	Q S	Q S	Q S	Q
193		S		Q S L <u>I</u> K
194	L	L	L	L
219	A	A	$\frac{\mathbf{E}}{\mathbf{K}}$	Ī
222	K	K	K	K
225	D	$\underline{\mathbf{G}}$	<u>G</u> Q A	D
226	Q	<u>G</u> Q A	Q	Q
227	A		A	Q <u>E</u> G
228	G	G	G	G

^a Residues are numbered (residue ID) according to 1918 Spanish flu sequence. Using H1-1918 as the reference, the residue differences in the other three isolates are shown in bold and underlined. Residue K133a is an inserted amino acid specific to H1.

discover new potent inhibitors. Impacts of drug-resistant mutant strains of these two targeted proteins and their relevant commercial agents have been extensively studied. 11-14

The viral genetic sequences in the HA receptor binding domain of the four different H1N1 influenza viruses, that is, the 1918 Spanish flu, 1930 swine flu, 2005 seasonal flu, and 2009 novel flu, are compared and are summarized in Table 1 (see multiple sequence alignment in Figure S1, Supporting Information). Using the original 1918 H1N1 HA as the reference, the amino acids at 7 Å spherical radius around the hHAR in the binding pockets of the H1-1930, H1-2005, and H1-2009 HAs contain three (K133aR, T155V, and D225G), six (T133N, K133aR, S145N, T155V, A219E, and D225G), and seven (T133N, S145K, T155V, P186S, T189A, A219I, and A227E) substitutions (shown in bold and underlined in Table 1), respectively. From a comparison of the hydrophobic plots (Figure 1), the 2009 HA binding pocket displays considerably higher hydrophilic characteristics (represented by the blue surface) than those of the other three HA strains. Since the residues 190 and 225 are known to be a key factor determining the HA-hHAR binding in all H1N1 subtypes, 15-20 and the HAs of all H1N1 strains contain D190, therefore, interest is focused on residue 225 in which G225 was found in the 1930 swine and 2005 seasonal viruses, whereas D225 was detected in the HAs of the two pandemic strains, H1-1918 and H1-2009 (Table 1). In addition, residue A227, which is the receptor binding site that is commonly conserved as "Q226-A227-G228" (QAG) was replaced by E227 in the novel 2009 influenza virus. Substitution of A227 by the negatively charged E227 residue (OEG) is supposed to affect the orientation of the surrounding residues. 18 As a consequence, the increase of the hydrophilicity and the replacement of the QAG by the QEG receptor binding site of the H1-2009 HA are possibly involved in the recognition and familiarity-strength in the binding to the hHAR of the newly emerged flu.

To examine the influence of the electronic and structural changes in the four HA binding pockets, molecular dynamics (MD) simulations of the hHAR bound to the four HA A/H1N1 influenza viruses were carried out. The HA-hHAR binding, as well as the structural and dynamical properties, were analyzed and are extensively discussed. The observed information at the atomic level could essentially provide a better understanding and a prediction of the new H1N1 influenza pathogenesis.

MATERIALS AND METHODS

System Preparation. The cocrystal structure of the 1930 swine influenza A/H1N1 HA (H1-1930) with the hHAR and the crystal structure of the apo form of the 1918 influenza A/H1N1 HA (H1-1918), were retrieved from the Protein Data Bank (PDB entry codes 1RVT and 1RUZ, respectively)²¹ and were used as the starting structures for the MD simulations. To prepare the hHAR bound to the H1-1918 HA, superposition of the H1-1930 and the H1-1918 HA proteins over the backbone carbon atoms was performed, and the H1-1930 coordinates were then removed, retaining the coordinates of hHAR. The structure of the 2005 seasonal H1N1 HA complexed with the hHAR was prepared in a similar fashion of the H1-2009.²² Briefly, using the structure of 1930 swine flu²¹ as a template and amino acid sequences of the isolated Influenza A/swine/Chachoengsao/NIAH587/ 2005(H1N1),²³ the 3D-structure of the 2005 HA protein was created by homology modeling technique using the module implemented in Discovery Studio 2.0.²⁴ The hHAR bound to the H1-2005 HA was set up in a similar manner to that of the aforementioned H1-1918.

Molecular Dynamics Simulations. All calculations of the HA-hHAR complexes were carried out using the AMBER 10 software package. ²⁵ The HA proteins and the hHAR were parametrized using the AMBER03²⁶ and GLYCAM06 force fields,²⁷ respectively. Protonation of the ionizable amino acids was assigned at pH 7.0 using the PROPKA program. ^{28,29} All missing hydrogen atoms were added using the LEaP module implemented in AMBER 10.25 The simulated system was subsequently solvated by TIP3P water molecules in a cubic box with dimensions of $65 \times 68 \times 143 \text{ Å}^3$ for H1-1918, $65 \times 68 \times 141 \text{ Å}^3$ for H1-1930, and $67 \times 68 \times 141$ $\rm Å^3$ for H1-2005. This is almost comparable to that of 66 \times $69 \times 141 \text{ Å}^3$ used before for the H1-2009 complex.²² The electroneutrality of the simulated systems was treated by adding 1, 0, 4, and 5 chloride counterions for H1-1918, H1-1930, H1-2005, and H1-2009, respectively. The periodic boundary condition in the isobaric-isothermal (NPT) ensemble with a constant pressure of 1 atm and temperature of 310 K was set up, whereas a Berendsen coupling time of 0.2-ps was employed to control the temperature. Nonbonded interactions were calculated with a 12 Å residue-based cutoff, and the Particle Mesh Ewald method³⁰ was applied to treat the long-range electrostatic interactions. A 2-fs step size with the SHAKE algorithm³¹ was used along the simulations.

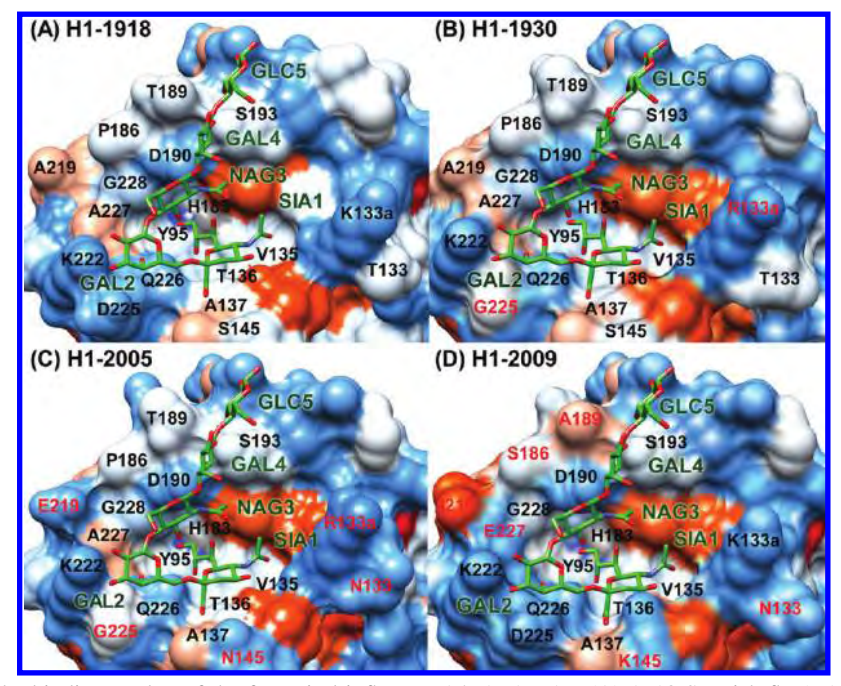


Figure 1. The hHAR in the binding pocket of the four viral influenza A/H1N1 HAs: (A) 1918 Spanish flu (H1-1918), (B) 1930 swine flu (H1-1930), (B) 2005 seasonal flu (H1-2005), and (D) 2009 novel pandemic flu (H1-2009). For H1-1930, H1-2005, and H1-2009, the residues that differ from the reference H1-1918 sequence are shown in red. The hydrophilic and hydrophobic surfaces are colored by blue and orange, respectively.

The water molecules were first relaxed with 500 steps of steepest descent (SD) and 1000 steps of conjugated gradient minimizations, while the HA and hHAR coordinates were kept fixed. The whole system was consequently optimized by performing 1,000 steps of SD and 1,000 steps of conjugated gradient minimizations. Afterward, the systems was heated to 310 K over 100-ps simulation and preequilibrated for 400 ps with position restraints on the hHAR atoms with factors of 20 and 10 kcal·mol⁻¹·Å⁻² to maintain their coordinates inside the receptor-binding pocket. Finally, 6.5-ns simulations were carried out for each HA-hHAR complex and the structural coordinates from the last 5-ns (1.5–6.5-ns) simulations, a production period, were collected for analysis.

RESULTS AND DISCUSSION

Changes of the Receptor Conformation Inside the H1 Binding Pocket. The attachment of the viral surface homotrimeric glycoprotein HA to the host membrane via the hHAR is believed to be the primary step in the viral replication cycle. To differentiate the receptor's conformation in the binding pocket of the HAs of the Spanish flu (H1-1918), swine flu (H1-1930), seasonal flu (H1-2005), and a novel pandemic flu (H1-2009), the distributions of the torsion angles $(\tau 1 - \tau 9)$ in Figure 2) were measured and are plotted in Figure 3. As defined in Figure 2, $\tau 1 - \tau 9$ were classified in three important regions providing three different characters of the receptor binding: (i) $\tau 1 - \tau 3$, conformations of terminal sialic acid (SIA1) α2,6-linked to galactose (GAL2) of the hHAR; (ii) $\tau 4 - \tau 6$, orientations of the three side chains of the SIA1 functional groups; and (iii) $\tau 7 - \tau 9$, bridging between the saccharide units 2-5 of the receptor.

The distributions of the torsion angle plots (Figure 3), excluding $\tau 9$ of H1-1930 and $\tau 4$ of H1-2005, reveal clearly that all torsion angles of the four HA-hHAR systems show

a sharp peak at almost the same position, suggesting that the hHAR adapts itself very well to reach its optimal structure within the four H1NI HA binding sites.

The $\tau 1 - \tau 3$ angles on the single bonds linking between the six-membered rings of the SIA1 terminus and the GAL2 unit show a sharp peak at approximately -65° , -165° and 70°, respectively, indicating an identical orientation of these two sugars puckered into the HA pocket site. The $\tau 1$ glycosidic torsion of approximately -65° represents their cis-conformation on the α-ketosidic linkage corresponding to those commonly observed in the SIA-α2,6-GAL receptor (hHAR) bound to other HAs by both experimental and theoretical studies.^{21,32–35} Considering the orientations of the three side chains of the SIA1, the difference was only found at the carboxylate group of the H1-2005 in which its τ 4 was detected at \sim 30° relative to \sim 180° for the other HAs, that is, in difference from the other systems, the O1A group (see Figure 2) of the H1-2005 was rotated into the binding site to interact with the HA residues. The $\tau \theta$ angle of the hydrophilic moiety displayed a sharper peak than the $\tau 4$ of the $-COO^-$ and $\tau 5$ of the -NHAc groups, indicating that these two side chains are slightly more flexible in a narrow range in comparison with the hydrophilic group of the terminal SIA1.

For the remaining sugar moieties lying on the surface-exposed region of the hHAR protein (see Figure 1), the structural conformations of the NAG3 and GAL4 were found to be similar among the four HAs, as presented by the same degrees of τ 7 and τ 8 angles (-70° and -80° , respectively, in Figure 3). However, the orientation of the last glycan unit, GLC5, in the H1-1930 (τ 9 of 65°, red line) was somewhat different from the other three HAs (τ 9 of -65°). Therefore, different intermolecular interactions of the terminal GLC5 sugar of the saccharide chain with the protein surface residues

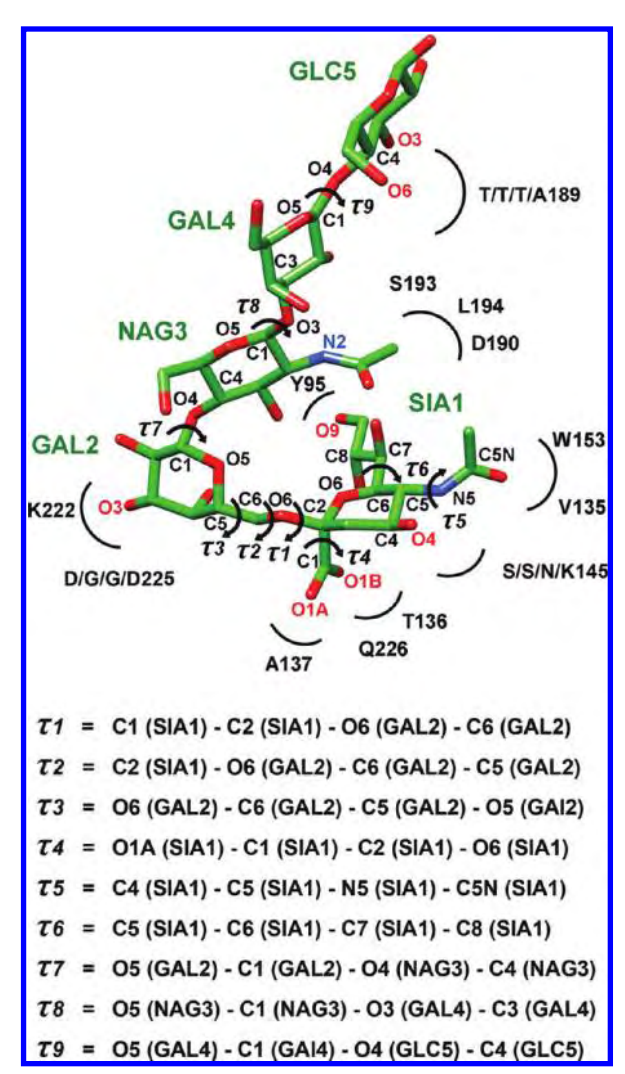


Figure 2. Schematic representation and definitions of the $\tau 1 - \tau 9$ torsion angles of the hHAR in the binding site of the HA subtype H1. Some labeled atoms used in the results and discussion are also shown. The labels, such as S/S/N/K145, were used to represent the four different amino acids in the same sequence number of the 1918-, 1930-, 2005- and 2009-H1N1 HAs, respectively.

are to be expected in the H1-1930 case (details in the following sections).

Enzyme-Receptor Interactions. To gain insight into the efficiency of the hHAR binding to the HAs of H1-1918, H1-1930, H1-2005, and H1-2009, the percentage and number of hydrogen bonds between this receptor and the contact residues of HAs were measured according to the subsequent criteria: (i) the distance between proton donor (D) and acceptor (A) atoms of ≤ 3.5 Å and (ii) the D-H···A angle of ≥120°. The results are shown in Figure 4 and the hydrogen bond descriptions are given in Table S1 (Supporting Information).

As shown in Figure 4, hydrogen bonds between the hHAR and the HA residues in all systems can be firmly formed in the three important binding HA regions, 130-loop, 190-helix, and 220-loop, especially at the sialic acid terminus which is inserted directly into the receptor-binding pocket of the HA. Strong hydrogen bonds are almost conserved at the residues Y95, V135, T136, A137, and Q226 of the four HA strains. Note that major interactions between the SIA1 and the T136 and Q226 are maintained although different hydrogen bonding pattern was detected, that is, the interaction takes

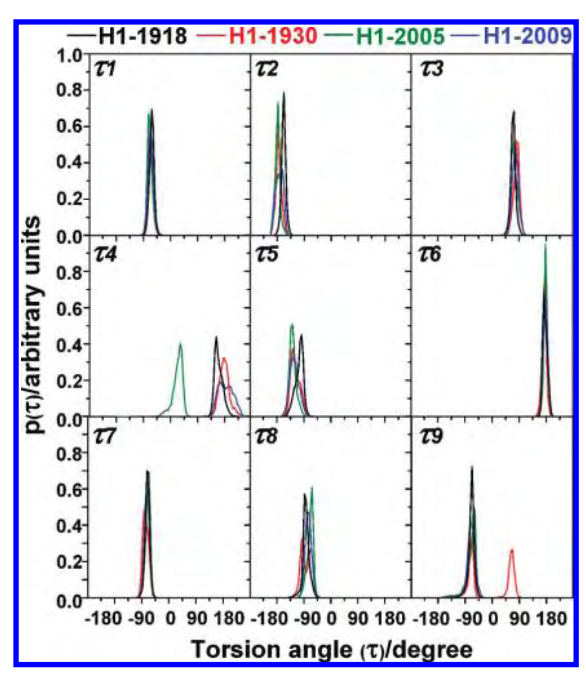


Figure 3. Distribution plots of the torsion angles $(\tau 1 - \tau 9)$ of the hHAR lying within the binding pocket of the HA of the four H1N1 strains (H1-1918, H1-1930, H1-2005, and H1-2009).

place via the O1A in the H1-2005 and the O1B in the other HAs (see Table S1, Supporting Information). Noticeably change was found when the S/S/N145, a polar residue with noncharged side chain, in the H1-1918, H1-1930, and H1-2005 was replaced by the K145, a positively charged residue in a novel HA. This makes the H1-2009 capable of establishing one moderate hydrogen bond to the O4 of SIA1. The observed results lead to conclusion that introducing of the fourth lysine (K145) of the lysine fence (K133, K156, and K222) in the HA of the 2009 facilitates stronger enzyme-receptor binding by better anchoring the SIA1 terminus. This observation is in agreement with the recently proposed hypothesis.³⁶ Furthermore, a strong hydrogen bond between the H183 and the O9 of SIA1 was observed in the H1-1930, H1-2005, and H1-2009 complexes, whereas this kind of interaction was disappeared in the case of H1-1918 system.

A major difference was additionally found at the connecting GAL2 unit, where the number and percentage of hydrogen bonding interactions detected at the HA 220-loop on residues K222 and D/G/G/D225 are much stronger for H1-1918 and H1-2009 than those of H1-1930 and H1-2005 (Figure 4). It is clear that for the D/G/G/D225 binding, the direct electrostatic effects because of the negatively charged D225 residue, lead to a more effective interaction in the H1-1918 and the H1-2009 viral HAs than the noncharged G225 in the HA of the H1-1930 and H1-2005 viruses. For the K222-GAL2 binding, the moderate and strong hydrogen bonds between O3 of this particular unit and the K222 residue in the HA of H1-1918 and H1-2009 were observed. This is possibly affected by the indirect effects caused by the presence of one (D225) and two (D225 and E227) negatively charged residues (see also Table 1) in the binding pocket of H1-1918 and H1-2009, respectively. In 2009 influenza pandemic strain, the orientation of the K222 residue was mainly stabilized by both D225 and E227 residues through electrostatic and salt-bridge interactions, respectively

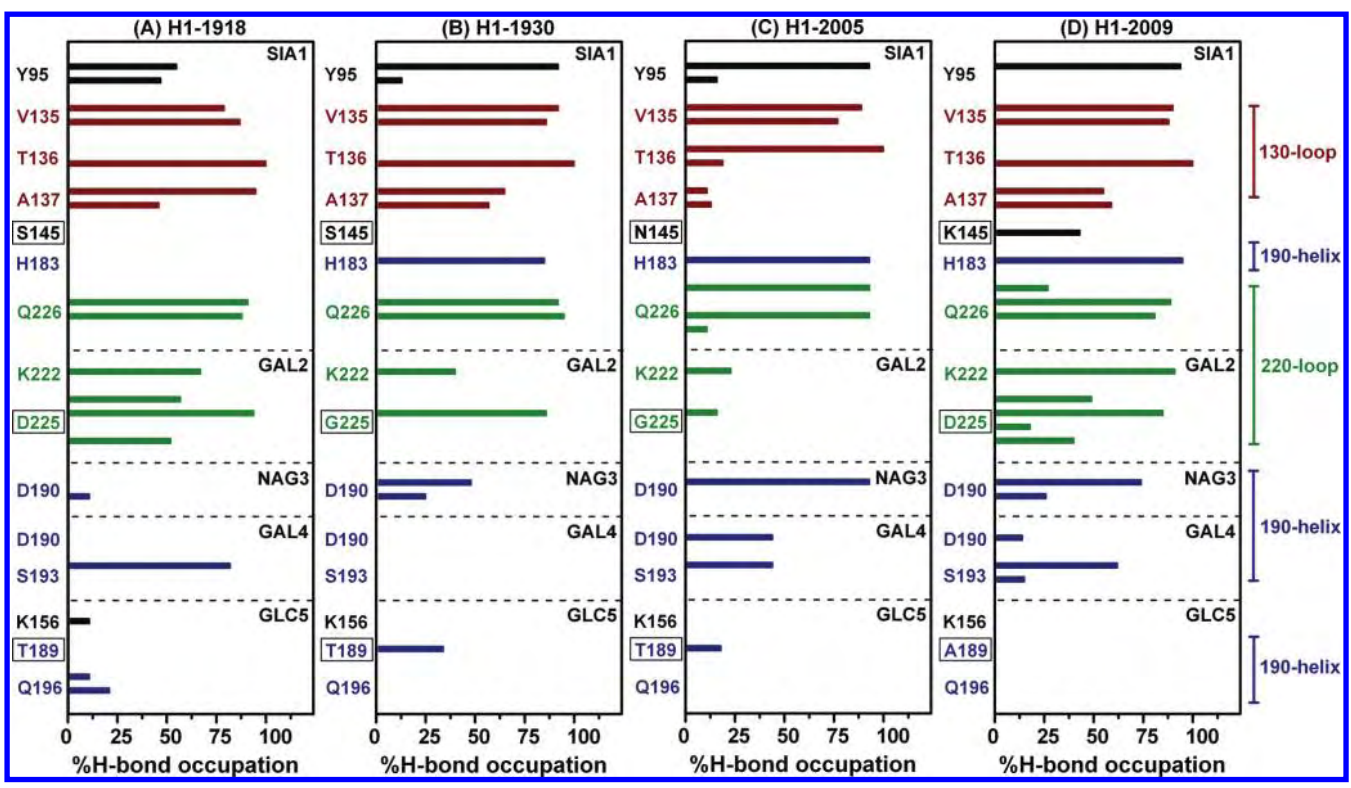


Figure 4. Hydrogen bond occupation between the five saccharide units (SIA1, GAL2, NAG3, GAL4, and GLC5) of the hHAR and the HA binding residues of (A) Spanish flu (H1-1918), (B) swine flu (H1-1930), (C) seasonal flu (H1-2005), and (D) a novel flu (H1-2009). The residues which are different among the four HAs are shown with a box around the label (see Figure 1 for residue positions). Residues of the 130-loop, 190-helix, and 220-loops are colored by red, blue, and green, respectively.

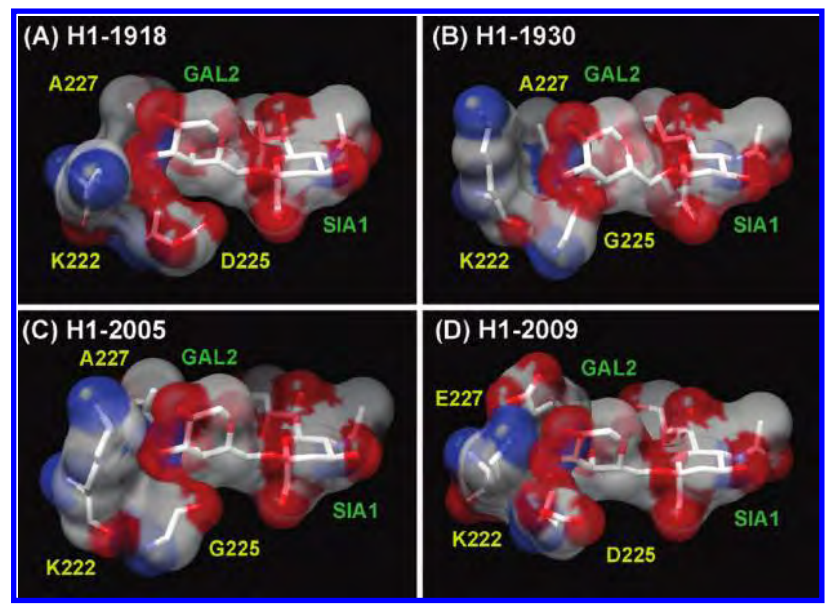


Figure 5. Electrostatic potential map of hHAR and HA binding residues K222, D/G/G/D225 and A/A/E227 of (A) Spanish flu (H1-1918), (B) swine flu (H1-1930), (C) seasonal flu (H1-2005), and (D) novel flu (H1-2009). Positive and negative electrostatic potentials are represented by blue and red, respectively.

(see Figure 5D and more discussion in the next section), whereas only D225 was observed to stabilize K222 in the case of H1-1918. This is in contrast with what was found for the H1-1930 and H1-2005 viruses, where both the G225 and A227 residues are hydrophobic, leading to a lowering of the electrostatic potential in this region, relative to those of the other two systems. This provides a clear reason why K222 could not form a stable hydrogen bond with GAL2 in the H1-1930 and H1-2005 HAs (Figure 4B and C, respectively). This hypothesis is further analyzed in terms of the

electrostatic potential plot in the next section. A crucial role of residue 225 has been reported previously, ^{16–18} with the additional hypothesis that mutation of this residue could result in a reduced viral binding affinity to the hHAR. It has also been experimentally found that the presence of the G225 residue in the HA of H1-1930 and H1-2005 apparently reduced the binding efficiency of the virus to the hHAR. ^{3,16,18}

With respect to the NAG3, GAL4, and GLC5 saccharide units, which lay on the surface exposed region (Figure 1), far from the binding pocket, and are supposed to play only

a minor role in holding the receptor in place, a lower percentage and number of hydrogen bonds were found (Figure 4) in comparison to those observed at the first two units (SIA1 and GAL2) of the receptor. Their interactions were moderately strong with 190-helix residues T/T/T/A189, D190, and S193.

Taking into account all the above given data, the order of hydrogen bond strengths of the hHAR binding to the H1N1 HAs was H1-2009 > H1-1918 > H1-2005 \approx H1-1930. The increase of binding affinity in the novel H1-2009 (H1N1) HA to the hHAR is mainly because of the higher hydrophilicity at the receptor binding domain, in which residues 145, 225, and 227 were found to play a critical role. The transmissibility of the 2009 H1N1 virus (depending upon several external factors and determined by the basic reproduction number, R_0 of 1.2–1.6) falls within the range of the 1918 Spanish flu (R_0 of 1.4–2.8) but is higher than that of seasonal influenza virus (R_0 of 0.9–2.1). This transmission ability is supposed to relate, somewhat, to the predicted enzyme-receptor binding affinity. Note that the pathogenesis and transmission studies of the 2009 H1N1 influenza virus indicated that a novel flu was observed to be more pathogenic than the seasonal H1N1 virus. 38,39 Since the 2009 influenza virus could deeply penetrate into the airways and exhibits more extensive viral replication in the respiratory tract, its severity could potentially increase in comparison with seasonal virus. 38,39

Effect of Charged Residues on the Receptor Binding **Affinity.** As already mentioned, hydrogen bond analysis revealed that introduction of charged amino acids in the receptor binding domain of the novel HA influenza virus could effectively contribute to the binding with the hHAR, in particular HA residues 222, 225, and 227. Therefore, to provide an additional perspective on the contribution of the polar residues to the hHAR-HA binding, the electrostatic isosurface maps of the hHAR and the HA 222, 225, and 227 residues were plotted in Figure 5. The positive and negative electrostatic potentials are indicated by blue and red, respectively.

In all systems, the negative electrostatic potentials (Figure 5, red) were found around the SIA1 and GAL2 units of the hHAR, while a positive electrostatic potential was generated over the K222 residue (Figure 5, blue). Differences between the four viral HAs are clearly and obviously observed in the region around the 225 and 227 residues. Here, changing the negatively charged D225 residue in the 1918- and 2009-H1N1 models to a nonpolar G225 residue (Table 1) leads to the negative electrostatic potential around residue 225 almost totally disappearing (the red regions in Figure 5A and D change to white in Figure 5B and C, respectively). In addition, the substitution of a nonpolar A227 residue of the 1918-, 1930-, and 2005-H1N1 HAs (Table 1) with a negatively charged E227 residue in the HA of H1-2009 leads additionally to an enhanced negative electrostatic potential around the 227 residue (the red region, which is only observed in Figure 5D).

As a consequence, the electrostatically negative potentials near residues D225 and E227 are unique in the H1-2009 H1N1 isolate (of the four studied) and the enhanced electronegative isosurface could potentially stabilize the ionic network of the 220-loop residues K222, D225, and E227. This helps the K222 residue to adjust its conformation to be in optimal contact with the GAL2 moiety of the hHAR, leading to the formation of a strong hydrogen bond in the H1-2009 HA-hHAR complex (Figure 4D), as previously discussed. On the other hand, the electrostatic potentials that result from the combination of the charged- and noncharged residues (D225 and A227) can potentially induce the moderate K222-GAL2 hydrogen bond formation in the H1-1918 HA-hHAR interaction (Figure 4A). This is not the case for the H1-1930 and H1-2005 HAs (Figure 4B and C, respectively), where this hydrogen bond is very weak because both G225 and A227 are fully uncharged and could not establish such ionic network with the K222.

Role of the Nonconserved Residue 227. Although residue 227 was found to vary between the influenza A viral strains, the receptor binding residues Q226 and G228 are highly conserved, forming a "Q226-X227-G228" pattern or socalled "QXG" site, where QSG and QGG sites are found in the avian H3 or H5 and H2 influenza virus HAs, respectively. 18,40 In this study, both the 1918-, 1930-, and 2005-H1N1 strains contain the QAG sequences, whereas the 2009-novel flu (H1-2009) shows a unique QEG site. The increased hydrophilicity in the receptor binding region is apparently the development of the current pandemic flu from the 1918 Spanish, the 1930 swine, and the seasonal 2005 influenzas. As shown and described in the previous sections, substitution of the noncharged A227 residue with the negatively charged E227 improves the binding of HA to the hHAR, and this is potentially attained by establishing the ionic network with the K222 and D225 residues. This finding thus indicates that the nonconserved residue 227 possibly plays a critical role in the evolution of a new and potentially more pathogenic H1N1 influenza virus. Note that among the three residues in the HA QXG site of the four H1 strains under this study, Q226 is the only residue that interacts directly with the hHAR via strong hydrogen bonds (Figure 4).

Human HAR Solvation. Solvation of the hHAR was monitored in terms of atom-atom radial distribution functions, RDFs, $g_{xy}(r)$, the probability of finding a particle of type y within a sphere radius r around the particle of type x. The RDFs from all heteroatoms of the hHAR to the oxygen atom of water were evaluated. The selected RDFs and the corresponding running coordination numbers, n(r), are shown in Figure 6.

For all HA-hHAR complexes, the major differences in the g(r) at the SIA1 terminus takes place only on the O1B atom (see Figure 2 for atomic label), where the plot for the H1-2005 complex shows the first sharp peak at \sim 2.7 Å with the corresponding coordination number n(r) integrated up to its first minimum of 2.8 water molecules (Figure 6B, right axis). This indicates that the water was firmly coordinated to the O1B atom of the H1-2005, but not in the HA-hHAR systems of H1-1918, H1-1930, and H1-2009. This is because of the interchange of the O1A and O1B positions due to the rotation of the τ 4 angle (see Figure 3).

Although no significant difference was found in terms of the peak position of the RDFs of the other atoms of the SIA1 (Figure 6A, C, and D), the n(r) of the H1-1918, H1-1930, and H1-2005 show a higher average number of water molecules located around this glycan unit than that detected in the H1-2009. In other words, the SIA1 of the hHAR in the HA-hHAR complex of the H1-2009 virus is less solvated than that with the other three HAs. This is consistent with the hydrogen bond

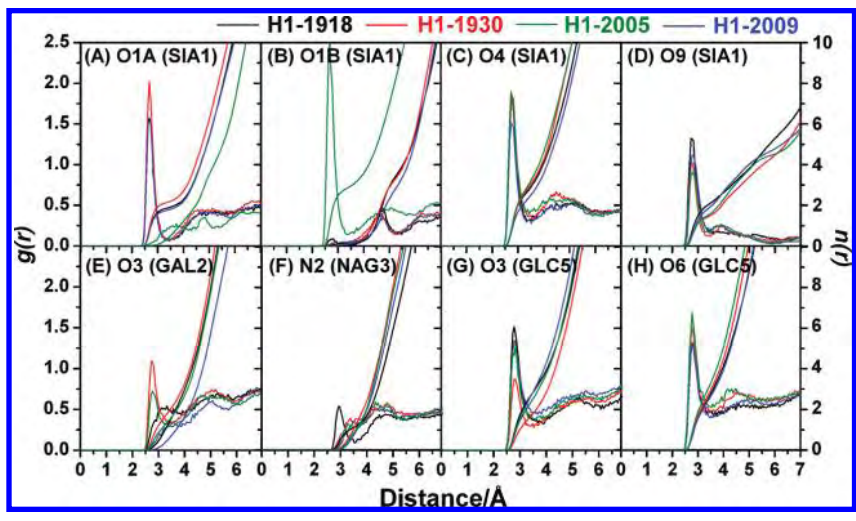


Figure 6. Radial distribution function, g(r), centered on the selected heteroatoms of the hHAR (see Figure 2 for atomic labels) to oxygen atoms of water molecules and the running coordination number, n(r), for the four simulated HA—hHAR systems.

data (Figure 4), where a greater level of direct contact leads to the formation of more hHAR—HA hydrogen bonds with the H1-2009 than with the other three viral strains. A clear example is the moderate hydrogen bonding between the O4 atom of SIA1 of the hHAR and the guanidinium group of the HA K145 residue that only takes place in H1-2009 (Figure 4D). Another example that supports the degree of the solvation of O9 atom (Figure 6D) is the strong hydrogen bonding between this oxygen and the HA H183 residue, which is in a reverse order of the first shell coordination numbers for O9 of 1.5 1.5, 2.0, and 2.5 water molecules for H1-2005, H1-1930, H1-2009, and H1-1918, respectively.

For the other four glycan units, the following significant differences were found: O3 of GAL2 (Figure 6E), N2 of NAG3 (Figure 6F), and O3 of GLC5 (Figure 6G), in which the degree of solvation also supports the hydrogen bond data discussed previously (Figure 4).

CONCLUSION

In the present work, MD simulations of the hHAR bound to the four different HAs of the 1918-, 1930-, 2005-, and 2009-H1N1 influenza viruses were studied and compared in terms of hydrogen bond formation, receptor conformational changes, the role of the receptor binding residues and the receptor solvation level.

In all complexes, the glycosidic torsion angle linking the terminal sialic acid and the adjoining GAL2 of apprximately −65° confirmed the preferentially favorable cis-conformation of the hHAR, similar to that detected with other HA strains. 34,35 The SIA1 terminus was found to interact strongly with the HA Y95 residue and with the conserved residues of the HA receptor binding domain, which consists of the 130-loop (V135, T136 and A137), 190-helix (H183, except for H1-1918), and 220loop (K222 and Q226) through many strong hydrogen bonds, whereas the GAL2 and the last three glycan units (NAG3, GAL4 and GLC5) of the hHAR established hydrogen bonds with amino acids in the HA 220-loop and 190-helix, respectively. More importantly, the crucial presence of a positively charged K145 residue in the HA of the novel H1-2009 can potentially make a lysine fence with residues K133, K156, and K222 and provides an optimal contact to hydrogen bond with the SIA1 of the hHAR. Because of the presence of an uncharged S/S/N145 residue in place of the K145, such an ionic network was not created in the Spanish 1918, swine 1930, or seasonal 2005 virions, resulting in the lower potency of HA-hHAR binding. As observed in the all H1N1 strains, 15,18,20 HA residue 225 plays a critical role in the hHAR GAL2 binding efficiency. The presence of a negatively charged D225 residue in the HAs of the H1-1918 and H1-2009 could provide a larger number of hydrogen bonds in the HA-hHAR complex than that observed in H1-1930 and H1-2005, where a noncharged G225 residue exists instead. Q226 of the QAG (1918-, 1930-, and 2005-H1N1) or QEG (2009-H1N1) HA sequence directly interacts with the hHAR SIA1 terminus via hydrogen bonds, while the nonconserved 227 residue was found to play a role in stabilizing the enzyme structure around the K222 residue. Introduction of the negatively charged HA E227 residue in the H1-2009 substantially enhanced the HA-hHAR binding efficiency through hydrogen bonds formation between the HA K222 residue and the GAL2 unit of the hHAR. The lower hydrogen bonding interactions in the H1-1918, H1-1930, and H1-2005 HAs were compensated by a higher degree of water accessibility to the hHAR.

In conclusion, the efficiency of the hHAR binding to the HA of the novel 2009 H1N1 viral strain is greater than that in the 1918 Spanish and the 2005 seasonal (which is comparable to the 1930 swine) influenza viruses, respectively. A major contribution to the virion HA-cellular hHAR binding in H1-2009 is apparently gained from the charged residues existing in the HA binding pocket. Our simulated results provide a better understanding of how the viral surface glycoprotein HA of different H1N1 strains efficiently attach and bind to the hHAR.

ACKNOWLEDGMENT

This work was financially supported by the Thailand Research Fund (TRF), the Commission Higher Education (CHE), and the Thai Government Stimulus Package 2 (TKK2555), under the Project for Establishment of Comprehensive Center for Innovative Food, Health Products and Agriculture. N.N. (grant No. MRG5180298) and T.R. (grant No. TRG5280035) acknowledge the TRF grant for the new research. P.S. gratefully acknowledges the support from the Emerging Diseases and Bio-Warefare project, the Center of Excellence in Clinical Virology, Chulalongkorn University.

Supporting Information Available: Multiple sequence alignment of all four H1N1 strains and hydrogen bond descriptions. This information is available free of charge via the Internet at http://pubs.acs.org/.

REFERENCES AND NOTES

- World Health Organization. Global Alert and Response (GAR). http://www.who.int/csr/disease/swineflu/en/index.html (accessed July 10, 2010).
- (2) Neumann, G.; Noda, T.; Kawaoka, Y. Emergence and pandemic potential of swine-origin H1N1 influenza virus. *Nature* 2009, 459, 931–939.
- (3) Shen, J.; Ma, J.; Wang, Q. Evolutionary trends of A(H1N1) influenza virus hemagglutinin since 1918. PLoS One 2009, 4, e7789.
- (4) Krug, R. M.; Aramini, J. M. Emerging antiviral targets for influenza A virus. Trends Pharmacol. Sci. 2009, 30, 269–277.
- (5) Chandrasekaran, A.; Srinivasan, A.; Raman, R.; Viswanathan, K.; Raguram, S.; Tumpey, T. M.; Sasisekharan, V.; Sasisekharan, R. Glycan topology determines human adaptation of avian H5N1 virus hemagglutinin. *Nat. Biotechnol.* 2008, 26, 107–113.
- (6) Bateman, A. C.; Busch, M. G.; Karasin, A. I.; Bovin, N.; Olsen, C. W. Amino acid 226 in the hemagglutinin of H4N6 influenza virus determines binding affinity for 2,6-linked sialic acid and infectivity levels in primary swine and human respiratory epithelial cells. J. Virol. 2008. 82, 8204–8209.
- (7) Gambaryan, A. S.; Karasin, A. I.; Tuzikov, A. B.; Chinarev, A. A.; Pazyninab, G. V.; Bovinb, N. V.; Matrosovich, M. N.; Olsen, C. W.; Klimove, A. I. Receptor-binding properties of swine influenza viruses isolated and propagated in MDCK cells. *Virus. Res.* 2005, 114, 15– 22.
- (8) Matrosovich, M. N.; Gambaryan, A. S.; Teneberg, S.; Piskarev, V. E.; Yamnikova, S. S.; Lvov, D. K.; Robertson, J. S.; Karlsson, K. A. Avian influenza A viruses differ from human viruses by recognition of sialyloligosaccharides and gangliosides and by a higher conservation of the HA receptor-binding site. *Virology* 1997, 23, 224–234.
- (9) Rogers, G. N.; D'Souza, B. L. Receptor binding properties of human and animal H1 influenza virus isolates. *Virology* 1989, 173, 317–322.
- (10) Bewley, C. A. Illuminating the switch in influenza viruses. *Nat. Biotechnol.* **2008**, *26*, 60–62.
- (11) Laohpongspaisan, C.; Rungrotmongkol, T.; Intharathep, P.; Malaisree, M.; Decha, P.; Aruksakunwong, O.; Sompornpisut, P.; Hannongbua, S. Why amantadine loses its function in influenza M2 mutants: MD simulations. J. Chem. Inf. Model. 2009, 49, 847–852.
- (12) Ghosh, A.; Nandy, A.; Nandy, P.; Gute, B. D.; Basak, S. C. Computational study of dispersion and extent of mutated and duplicated sequences of the H5N1 influenza neuraminidase over the period 1997–2008. J. Chem. Inf. Model. 2009, 49, 2627–2638.
- (13) Udommaneethanakit, T.; Rungrotmongkol, T.; Bren, U.; Frecer, V.; Stanislav, M. Dynamic behavior of avian influenza A virus neuraminidase subtype H5N1 in complex with oseltamivir, zanamivir, peramivir, and their phosphonate analogues. J. Chem. Inf. Model. 2009, 49, 2323–2332.
- (14) Rungrotmongkol, T.; Intharathep, P.; Malaisree, M.; Nunthaboot, N.; Kaiyawet, N.; Sompornpisut, P.; Payungporn, S.; Poovorawan, Y.; Hannongbua, S. Susceptibility of antiviral drugs against 2009 influenza A (H1N1) virus. *Biochem. Biophys. Res. Commun.* 2009, 385, 390– 304
- (15) Glaser, L.; Stevens, J.; Zamarin, D.; Wilson, I. A.; García-Sastre, A.; Tumpey, T. M.; Basler, C. F.; Taubenberger, J. K.; Palese, P. A single amino acid substitution in 1918 influenza virus hemagglutinin changes receptor binding specificity. *J. Virol.* 2005, 79, 11533–11536.
- (16) Stevens, J.; Blixt, O.; Tumpey, T. M.; Taubenberger, J. K.; Paulson, J. C.; Wilson, I. A. Structure and receptor specificity of the hemagglutinin from an H5N1 influenza virus. *Science* 2006, 312, 404–410.
- (17) Taubenberger, J. K. Influenza hemagglutinin attachment to target cells: "Birds do it, we do it". Future Virol. 2006, 1, 415–418.
- (18) Matrosovich, M.; Tuzikov, A.; Bovin, N.; Gambaryan, A.; Klimov, A.; Castrucci, M. R.; Donatelli, I.; Kawaoka, Y. Early alterations of the receptor-binding properties of H1, H2, and H3 avian influenza virus hemagglutinins after their introduction into mammals. *J. Virol.* 2000, 74, 8502–8512.
- (19) Yang, Z. Y.; Wei, C. J.; Kong, W. P.; Wu, L.; Xu, L.; Smith, D. F.; Nabel, G. J. Immunization by avian H5 influenza hemagglutinin mutants with altered receptor binding specificity. *Science* 2007, 317, 825–828.

- (20) Stevens, J.; Blixt, O.; Glaser, L.; Taubenberger, J. K.; Palese, P.; Paulson, J. C.; Wilson, I. A. Glycan microarray analysis of the hemagglutinins from modern and pandemic influenza viruses reveals different receptor specificities. J. Mol. Biol. 2006, 355, 1143–1155.
- (21) Gamblin, S. J.; Haire, L. F.; Russell, R. J.; Stevens, D. J.; Xiao, B.; Ha, Y.; Vasisht, N.; Steinhauer, D. A.; Daniels, R. S.; Elliot, A.; Wiley, D. C.; Skehel, J. J. The structure and receptor-binding properties of the 1918 influenza hemagglutinin. *Science* 2004, 303, 1838–1842.
- (22) Nunthaboot, N.; Rungrotmongkol, T.; Malaisree, M.; Decha, P.; Kaiyawet, N.; Intharathep, P.; Sompornpisut, P.; Poovorawan, Y.; Hannongbua, S. Molecular insights into human receptor binding to 2009 H1N1 influenza A hemagglutinin. *Monatsh. Chem.* 2010, 141, 801–807.
- (23) Influenza virus resource. http://www.ncbi.nlm.nih.gov/genomes/FLU/SwineFlu.html (accessed Apr 25, 2009).
- (24) Discovery Studio 2.0; Accelrys Inc: San Diego, CA, 2007.
- (25) Case, D. A.; Darden, T. A.; Cheatham, III, T. E.; Simmerling, C. L.; Wang, J.; Duke, R. E.; Luo, R.; Crowley, M.; Walker, R. C.; Zhang, W.; Merz, K. M.; Wang, B.; Hayik, S.; Roitberg, A.; Seabra, G.; Kolossváry, I.; Wong, K. F.; Paesani, F.; Vanicek, J.; Wu, X.; Brozell, S. R.; Steinbrecher, T.; Gohlke, H.; Yang, L.; Tan, C.; Mongan, J.; Hornak, V.; Mathews, G. C. D. H.; Seetin, M. G.; Sagui, C.; Babin, V.; Kollman, P. A. AMBER10; University of California: San Francisco, CA, 2008.
- (26) Duan, Y.; Wu, C.; Chowdhury, S.; Lee, M. C.; Xiong, G.; Zhang, W.; Yang, R.; Cieplak, P.; Luo, R.; Lee, T.; Caldwell, J.; Wang, J.; Kollman, P. A point-charge force field for molecular mechanics simulations of proteins based on condensed-phase quantum mechanical calculations. J. Comput. Chem. 2003, 24, 1999–2012.
- (27) Tessier, M. B.; Demarco, M. L.; Yongye, A. B.; Woods, R. J. Extension of the GLYCAM06 biomolecular force field to lipids, lipid bilayers and glycolipids. *Mol. Simulat.* 2008, 34, 349–364.
- (28) Li, H.; Robertson, A. D.; Jensen, J. H. Very fast empirical prediction and rationalization of protein pKa values. *Proteins* **2005**, *61*, 704–721.
- (29) Bas, D. C.; Rogers, D. M.; Jensen, J. H. Very fast prediction and rationalization of pKa values for protein-ligand complexes. *Proteins* 2008, 73, 765–783.
- (30) Darden, T.; York, D.; Pedersen, L. Particle mesh Ewald: an N-log(N) method for Ewald sums in large systems. *J. Chem. Phys.* **1993**, *98*, 10089–10092.
- (31) Ryckaert, J.; Ciccotti, G.; Berendsen, H. J. C. Numerical integration of the cartesian equations of motion of a system with constraints: Molecular dynamics of *n*-alkanes. *J. Comput. Phys.* **1977**, 23, 327–341.
- (32) Lin, T.; Wang, G.; Li, A.; Zhang, Q.; Wu, C.; Zhang, R.; Cai, Q.; Song, W.; Yuen, K. Y. The hemagglutinin structure of an avian H1N1 influenza A virus. *Virology* **2009**, *392*, 73–81.
- (33) Kumari, K.; Gulati, S.; Smith, D. F.; Gulati, U.; Cummings, R. D.; Air, G. M. Receptor binding specificity of recent human H3N2 influenza viruses. Virol. J. 2007, 4, 42–53.
- (34) Li, M.; Wang, B. Computational studies of H5N1 hemagglutinin binding with SA-alpha-2, 3-Gal and SA-α-2, 6-Gal. *Biochem. Biophys. Res. Commun.* 2006, 347, 662–668.
- (35) Xu, D.; Newhouse, E. I.; Amaro, R. E.; Pao, H. C.; Cheng, L. S.; Markwick, P. R.; McCammon, J. A.; Li, W. W.; Arzberger, P. W. Distinct glycan topology for avian and human sialopentasaccharide receptor analogues upon binding different hemagglutinins: A molecular dynamics perspective. J. Mol. Biol. 2009, 387, 465–491.
- (36) Soundararajan, V.; Tharakaraman, K.; Raman, R.; Raguram, S.; Shriver, Z.; Sasisekharan, V.; Sasisekharan, R. Extrapolating from sequence-the 2009 H1N1 "swine" influenza virus. *Nat. Biotechnol.* 2009, 27, 510–513.
- (37) Coburn, B. J.; Wagner, B. G.; Blower, S. Modeling influenza epidemics and pandemics: insights into the future of swine flu (H1N1). *BMC*. *Med.* **2009**, 7, 30–37.
- (38) Munster, V. J.; de Wit, E.; van den Brand, J. M.; Herfst, S.; Schrauwen, E. J.; Bestebroer, T. M.; van de Vijver, D.; Boucher, C. A.; Koopmans, M.; Rimmelzwaan, G. F.; Kuiken, T.; Osterhaus, A. D.; Fouchier, R. A. Pathogenesis and transmission of swine-origin 2009 A(H1N1) influenza virus in ferrets. *Science* **2009**, *325*, 481–483.
- (39) Maines, T. R.; Jayaraman, A.; Belser, J. A.; Wadford, D. A.; Pappas, C.; Zeng, H.; Gustin, K. M.; Pearce, M. B.; Viswanathan, K.; Shriver, Z. H.; Raman, R.; Cox, N. J.; Sasisekharan, R.; Katz, J. M.; Tumpey, T. M. Transmission and pathogenesis of swine-origin 2009 A(H1N1) influenza viruses in ferrets and mice. *Science* 2009, 325, 484–487.
- (40) Chen, J.; Fang, F.; Yang, Z.; Liu, X.; Zhang, H.; Zhang, Z.; Zhang, X.; Chen, Z. Characterization of highly pathogenic H5N1 avian influenza viruses isolated from poultry markets in central China. *Virus. Res.* 2009, 146, 19–28.

Author's personal copy

Journal of Molecular Graphics and Modelling 29 (2011) 591-596

FISFVIFR

Contents lists available at ScienceDirect

Journal of Molecular Graphics and Modelling

journal homepage: www.elsevier.com/locate/JMGM



How do carbon nanotubes serve as carriers for gemcitabine transport in a drug delivery system?

Uthumporn Arsawang^a, Oraphan Saengsawang^{b,c}, Thanyada Rungrotmongkol^{b,c}, Purinchaya Sornmee^a, Kitiyaporn Wittayanarakul^{b,c,e}, Tawun Remsungnen^d, Supot Hannongbua^{b,c,*}

- ^a Department of Mathematics, Faculty of Science, Chulalongkorn University, Bangkok 10330, Thailand
- ^b Computational Chemistry Unit Cell, Department of Chemistry, Faculty of Science, Chulalongkorn University, Bangkok 10330, Thailand
- ^c Center of Innovative Nanotechnology, Chulalongkorn University, Bangkok 10330, Thailand
- ^d Department of Mathematics, Faculty of Science, Khon Kaen University, Khonkaen 40002, Thailand
- e Program of Natural Resource and Environmental Management, School of Science and Technology, Khon Kaen University, Nongkhai Campus, Nongkhai 43000, Thailand

ARTICLE INFO

Article history: Received 24 June 2010 Received in revised form 1 November 2010 Accepted 1 November 2010 Available online 11 November 2010

Keywords:
Carbon nanotube
Gemcitabine
Drug delivery
Molecular dynamics simulations
Steered molecular dynamics simulations

ABSTRACT

Aiming at understanding the molecular properties of the encapsulation of the anticancer drug gemcitabine in the single-walled carbon nanotube (SWCNT), molecular dynamics (MD) simulations were applied to the two scenarios; that of gemcitabine filling inside the SWCNT, and that of the drug in the free state. Inside the SWCNT, the cytosine ring of gemcitabine was found to form a π - π stacking conformation with the SWCNT surface, and this movement is not along the centerline of the tube from one end to the other of the tube where the distance from the center of gravity of the molecule to the surface is 4.7 Å. A tilted angle of 19° was detected between the cytosine ring of gemcitabine and the inner surface of SWCNT. In comparison to its conformation in the free form, no significant difference was observed on the torsion angle between the five- (ribose) and the six- (cytosine) membered rings. However, gemcitabine inside the SWCNT was found to have a lower number of solvating water molecules but with a stronger net solvation than the drug in the free state. This is due to the collaborative interactions between gemcitabine and the surface of the SWCNT. In addition, the steered molecular dynamics simulation (SMD) approach was employed to investigate the binding free energy for gemcitabine moving from one end to another end throughout the SWCNT. In excellent agreement with that yielded from the classical MD, the SMD energy profile confirms that the drug molecule prefers to locate inside the SWCNT.

© 2010 Elsevier Inc. All rights reserved.

1. Introduction

Since the discovery of carbon nanotubes (CNTs) in 1991 [1], they have been considered as the ideal material for a variety of applications owing to their unique properties. These properties include their potential biocompatibility in pharmaceutical drug delivery systems [2–4] and their excellent role as drug carriers with a highly site-selective delivery and sensitivity [5–10]. To accelerate the optimal development of CNT as a new effective drug transporter, it is required to better understand the structural properties of the drug–CNT complex.

As reported by the Centers for Disease Control and Prevention (CDC), cancer is the second leading cause in the number of deaths worldwide [11], and ovarian cancer, found in the female

reproductive malignant cells [12], is the fifth most common cancer. Gemcitabine, in combination with carboplatin, is the main anticancer drug used to treat ovarian cancer [13]. Gemcitabine is a pro-drug, and as the active di- and tri-phosphate nucleosides, exhibits cell phase specificity, primarily killing cells undergoing DNA synthesis (S-phase) and also blocking the progression of cells through the G1/S-phase boundary. The cytotoxic effects of gemcitabine are exerted through incorporation of gemcitabine triphosphate (dFdCTP) into DNA, resulting in the inhibition of DNA synthesis and induction of apoptosis. However, this is not cancer cell specific and so the main problem, common to most cancer treatments and therapy, is the serious side effects to normal cells. Bone marrow toxicity is one such effect in patients who show adverse reactions to gemcitabine. To avoid such effects, the development of a drug delivery system to transport the drug molecules efficiently and specifically to the targeted tumor cells, without harming the surrounding tissue is one promising approach. This can lead to a more sustained and localized delivery of the drug, reducing the systemic loads and side effects to non-target cells. To this end CNTs have been found to show good carrier properties by serving as a

^{*} Corresponding author at: Computational Chemistry Unit Cell, Department of Chemistry, Faculty of Science, Chulalongkorn University, Bangkok 10330, Thailand. Tel.: +66 22 187602; fax: +66 22 187603.

E-mail address: supot.h@chula.ac.th (S. Hannongbua).

U. Arsawang et al. / Journal of Molecular Graphics and Modelling 29 (2011) 591–596

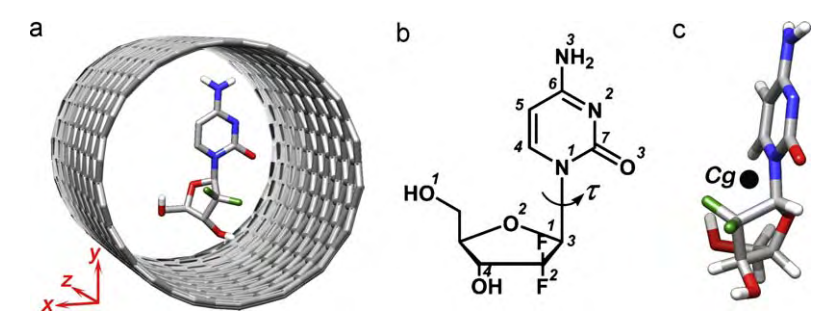


Fig. 1. (a) The structure of the (18,0) single-walled carbon nanotube (SWCNT) complexed with the gemcitabine drug. (b) The atomic labels and torsion angle, τ , of drug are defined. The origin of the Cartesian coordinate for the complex was centered at the center of gravity (*Cg*) of the SWCNT where (c) the *Cg* position of drug molecule is also shown

transporter of bio-molecules to the target site of a diverse array of compounds, including drugs [14–18], vaccines [19,20], small peptides [21,22], proteins [23–26], nucleic acids [27–30], vitamins and sugars [31,32]. Basically, these molecules are attached on either the inner or outer tube wall surfaces, which are the so-called filling or wrapping modes of binding, respectively. Functionalized CNTs were also proposed as promising materials as they were found to reduce the toxic nature of the pristine (non-functionalized) CNT in both *in vitro* and *in vivo* applications [33–35].

The present study aims to examine the structure, orientation, conformation, solvation and movement of the anticancer drug gemcitabine inside a pristine zigzag (18,0) single-walled carbon nanotube (SWCNT) in aqueous solution using a molecular dynamics simulation approach. The properties of gemcitabine in the free form (without SWCNT bound) in aqueous solution were also studied and compared. In addition, the steered molecular dynamics simulation (SMD) [36] was applied to examine the binding free energy profile when gemcitabine moves, from one end to another end, throughout the SWCNT.

2. Model and method

2.1. Preparation of the starting structures

Zigzag (18,0) SWCNT with a diameter of 14Å was used as the model carrier to examine the gemcitabine–SWCNT drug carrier. The SWCNT structure was generated from the Nanotube Modeler package [37] with chiral vectors m=18, n=0 and 34Å in length (Fig. 1a). The molecular dynamics simulations were carried out for two systems; free gemcitabine and its complex with SWCNT, both solvated in an aqueous solution.

To construct the molecular geometry of the gemcitabine–SWCNT complex, the crystal structure of gemcitabine bound to human deoxycytidine kinase (Protein Data Bank (PDB) [38], code 2NO0) was used to excise the gemcitabine structure and this was then placed in the middle of the pore of a pristine SWCNT (Fig. 1a). Hydrogen atoms were added to the drug molecule and both ends of the tube using the LEaP module in the AMBER 9 software package [39].

The parameters of the SWCNT were taken from the AMBER 99 force field [40] where the atom type CA was chosen to represent the aromatic carbon atoms. A general comment on the applicability of this force field to CNT can be found elsewhere [41,42]. For the gemcitabine molecule, the parameters for the 5- and 6- membered rings were, respectively, created by considering those of the ribose and cytosine, while the parameters involving the fluorine atoms were generated from the Generalized AMBER Force Field (GAFF) [40]. To obtain the atomic charges of gemcitabine, the following procedures were carried out. Firstly, the molecular structure

of the gemcitabine was fully optimized using the Gaussian03 program [43] at the Hartree-Fock level of theory using the 6-31G* basis set. Then, the electrostatic potentials (ESP) surrounding the compound were computed at the same basis set and level of theory. The RESP charge-fitting procedure was applied and the partial charges of equivalent atoms were fitted into the identical value using the RESP module of AMBER 9.

The drug in free state and the drug–SWCNT complex were both solvated with a SPC/E [44] octagonal box over 12 Å from the system surface. Any water molecules in which the oxygen atoms sterically overlapped with the heavy atoms of the drug and the SWCNT molecules were removed. Here, the systems of the free drug and its complex with SWCNT contain 3296 and 14627 atoms in total, respectively.

2.2. Classical molecular dynamics (MD) simulations

The simulations were performed using the SANDER module in the AMBER 9 program package with the *NPT* ensemble at 1 atm and a time step of 2 fs. The SHAKE algorithm [45] was applied to all bonds involving hydrogen atoms to constrain their motions. The periodic boundary conditions were applied and the cutoff function was set at 12 Å for nonbonded interactions and particle mesh Ewald method [46,47]. The whole system was heated from 100 K to 300 K for 25 ps and equilibrated at 300 K for 600 ps. Then, the production stage was performed for 10 ns in which the structural coordinates were saved every 1 ps for analysis.

2.3. Steered molecular dynamics (SMD) simulations

Basic concept of the SMD technique [36] is to apply the external forces to particles in a selected direction by employing a harmonic (spring-like) restraint to the system in order to create greater change of the particle coordinates, relative to classical MD. In this study, the gemcitabine was generated to locate at 25 Å far from one end of the SWCNT on the vector which pointing through the Cg of the SWCNT and parallel to the tube axis. The external forces were then employed to all drug atoms in the direction along the selected vector. The pulling atoms were harmonically constrained with a force F = -k(x - vt), where k, x, v and t are the spring constant, atom coordinates, atom velocities, and integration time step, respectively [48,49]. The value of k was set to $7k_BT/Å^2$, which relates to a thermal fluctuation of the pulling atoms of 0.38 Å, $(k_BT/k)^{1/2}$ where T denotes temperature in Kelvin and $k_{\rm B}$ is Boltzman's constant [48,49]. A dielectric constant of 1 and an integration time step of 2 fs were set throughout the SMD simulation. Switching distance required for smoothing between electrostatic and van der Waals interactions is within the range 10–12 Å. With the applied velocity of $0.0035 \,\text{Å}\,\text{ps}^{-1}$, drug was found to exit the SWCNT at 600 ps. U. Arsawang et al. / Journal of Molecular Graphics and Modelling 29 (2011) 591-596

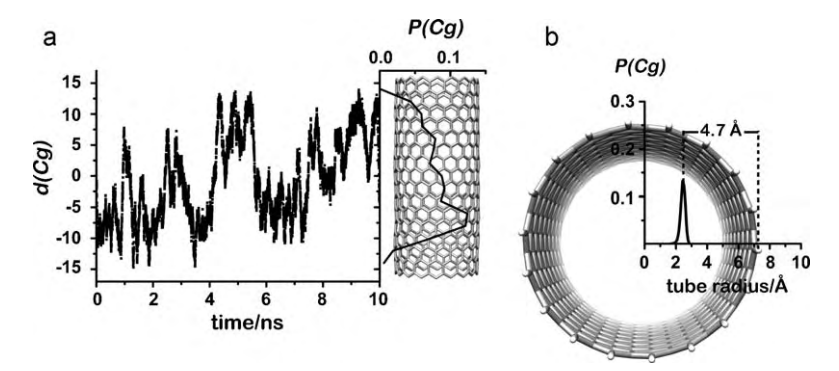


Fig. 2. (a) Displacement of the center of gravity of gemcitabine, d(Cg), as a function of the simulation time (horizontal plot), and the probability of finding the gemcitabine Cg (vertical plot), P(Cg), projected onto the SWCNT z-axis. (b) The P(Cg) in directions perpendicular to the SWCNT surface (x- and y-axis).

Note that, the other atoms in the system, including the explicit water molecules, were treated by the classical MD approach. The coordinates of system were collected every 0.2 ps.

3. Results and discussion

3.1. Localization of gemcitabine within the drug-SWCNT complex

To examine the feasibility of using SWCNT as a nano-container for gemcitabine delivery applications, the drug–SWCNT complex was monitored in terms of the gemcitabine center of gravity (Cg) distribution inside the SWCNT. Along the SWCNT's axis (z-axis defined in Fig. 1a), the displacement of the gemcitabine Cg, d(Cg), as a function of simulation time is shown in the horizontal plot in Fig. 2a, while the probability of finding the gemcitabine Cg, P(Cg), is illustrated in the vertical plot of the same figure. To monitor the movement of the drug in the direction perpendicular to the SWCNT surface, the averaged projection of the P(Cg) to the tube x-and y-axis (defined in Fig. 1a) were also calculated, and are shown in Fig. 2b.

In Fig. 2a, the d(Cg) in the horizontal plot shows that at the initial step (t=0), the gemcitabine was located at the center of the SWCNT (Cg=0). Regular movement of the drug molecule from one end $(d(Cg)=-12.5\,\text{Å})$ to the other $(d(Cg)=+12.5\,\text{Å})$ of the 34 Å SWCNT can be clearly seen. In addition, gemcitabine was never found at the inner surface at a distance of <4.5 Å from the two ends of the tube, *i.e.*, the gemcitabine is able to move freely and remain only inside its container. This is likely due to breaking the π - π interactions between the cytosine group and the tube wall at the ends. The observed event was well supported by the P(Cg) plot (the vertical plot in Fig. 2a), where the probability was found to increase exponentially as a function of the distance from the two ends of the SWCNT. Note that a symmetric distribution of the P(Cg) plot is expected if the sampling size is large enough, with a long enough simulation time.

In the same manner, the probability of finding the gemcitabine Cg in the direction perpendicular to the tube surface (x- and y-axis) showed only one distinct peak at 2.3 Å from the origin of the coordinate system, indicating that gemcitabine does not prefer to move at the center along the tube z-axis but rather that the favorite motion is \sim 4.7 Å away from the inner surface instead. It is, therefore, likely that an aromatic stacking interaction between the gemcitabine and the SWCNT surface was formed (discussed in the next section). Taking into account all the above mobility data, gemcitabine was found to coordinate inside the SWCNT, forming the drug–SWCNT complex, during the whole simulation time of 10 ns. Therefore, the SWCNT terminated by the hydrogen atoms is assumed to be suitable as a drug container for a gemcitabine delivery system.

3.2. Conformation of gemcitabine in the free and SWCNT-complexed forms

To examine the conformation as well as the flexibility of gemcitabine in the free state and that when inside the SWCNT, the relative orientation of the ribose ring (five-membered ring) and cytosine ring (six-membered ring), defined as the $C^7-N^1-C^3-O^2$ torsion angle (τ) in Fig. 1b, was calculated and compared. No significant difference was found between the gemcitabine conformations in these two states (Fig. 3), where the most probable torsion angle of the free and SWCNT-complexed forms was observed at 210° and 215°, respectively. Note that the distribution plot showed a broad peak covering the range of 80°, precisely from 170° to 250° for the free form and from 180° to 260° for the complex. This suggested that the drug molecule is rather flexible and insensitive to the environment, both when free in the aqueous solution and when complexed inside the SWCNT. Therefore, utilizing CNT as the gemcitabine carrier does not affect the conformation of the drug itself and so, presumably, does not affect its stability and bioactivity.

To understand more details of the molecular alignment of gemcitabine inside the SWCNT, the atom–atom radial distribution functions (RDFs), expressed as $g_{ij}(r)$ the probability of finding a particle of type j in a sphere of radius, r, around a particle of type i, were calculated. Interest here was focused onto the cytosine (six-membered) ring whose π -aromatic system was expected to preferably be deposited and to directly interact with the inner surface of the SWCNT. Therefore, in this study i denotes the backbone atoms of the cytosine ring (C^4 – C^7 , N^1 and N^2) and j represents the carbon atoms of the SWCNT. The calculated RDFs are summarized in Fig. 4a, whilst a schematic representation of the drug–SWCNT complex, where vector \bar{a} lies parallel to the SWCNT surface and vector \bar{b} points from C^6 to N^1 atoms, is shown in Fig. 4b.

The six RDF plots (Fig. 4a) can be classified into three sets, $\{C^5, C^6, N^2\}$, $\{C^4, C^7\}$ and $\{N^1\}$, in which their g(r)s were detected for the first time $(g(r) \neq 0)$ at 3.0 Å, 3.4 Å and 3.8 Å with the maxima

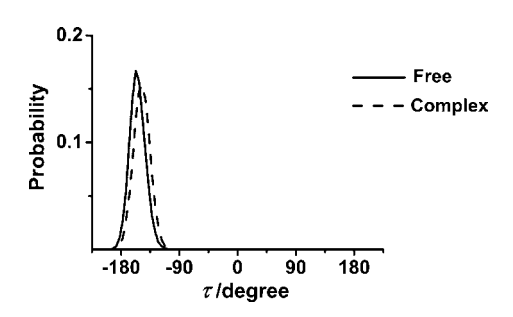


Fig. 3. Distribution of the $C^7 - N^1 - C^3 - O^2$ torsion angle, τ (see Fig. 1b for its definition and atomic labels), of the gemcitabine in the free (solid line) and SWCNT-complexed (dash line) forms.

U. Arsawang et al. / Journal of Molecular Graphics and Modelling 29 (2011) 591-596

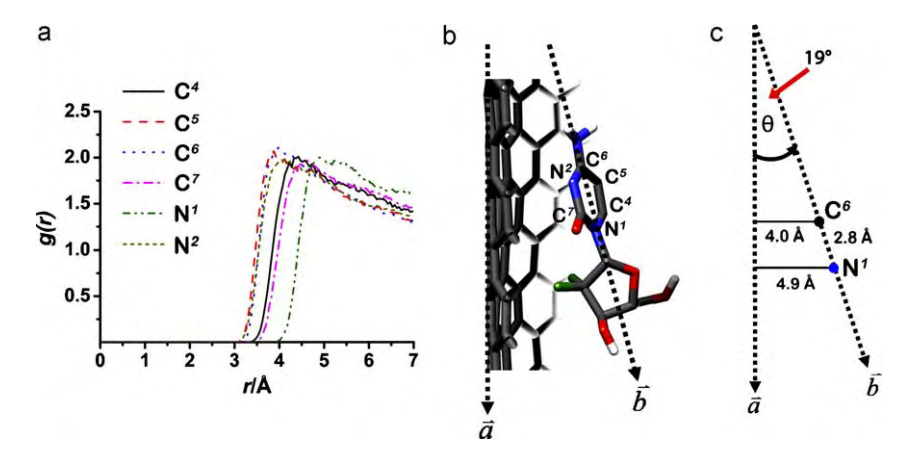


Fig. 4. (a) RDFs centered at the atoms in the cytosine (six-membered) ring of the gemcitabine drug (C^4-C^7 , N^1 and N^2) to the carbon atoms of the SWCNT. (b) Schematic representation of the gemcitabine–SWCNT complex where vector \bar{a} lies parallel to the SWCNT surface and vector \bar{b} points from the C^6 to the N^1 atoms. (c) Estimated angle between vectors \bar{a} and \bar{b} (see text for details of the related distances).

at \sim 4.0 Å, \sim 4.5 Å and 4.9 Å, respectively. Using the most probable distances from the C⁶ (\sim 4.0 Å maximum of the C⁶–C RDF) and N¹ (\sim 4.9 Å maximum of the N¹–C RDF) atoms to the SWCNT surface, and the N¹–C⁶ distance (2.8 Å), the angle between the vectors \bar{a} and \bar{b} can be estimated (Fig. 4c). The obtained value of 19° indicates the tilted angle representing the configuration of the π – π stacking interaction between the cytosine ring of the gemcitabine and the inner surface of the SWCNT. This interaction is supposed to be the main reason why the preferential mobility of the drug molecule along the molecular *z*-axis of the SWCNT takes place at \sim 4.7 Å far from the surface of the SWCNT (Fig. 2b).

3.3. Solvation of gemcitabine in free solution and complexed with SWCNT

The ligand solvation was monitored by the atom–atom radial distribution functions. Here, the RDFs to the oxygen atom of water around the heteroatom in the gemcitabine were evaluated and plotted in Fig. 5 for gemcitabine in both the free solvated and SWCNT-complexed forms. The corresponding running integration numbers, n(r), were also calculated and are shown. The first shell coordination number, CN, around the atoms of drug (defined in Fig. 1b) in both systems, which were obtained from the integration up to the first minimum of the RDF, are summarized in Table 1.

The plots for both systems showed almost sharp first peaks, indicating a strong solvation and high water accessibility, to the central atoms of the drug molecule. Among all oxygens, the $\rm O^2$ atom is much less accessible than the others owing to the steric hindrance to solvation in 5-membered ring. Remarkable changes were found

Table 1 First shell coordination number, CN, around the atoms of gemcitabine in the free and SWCNT-complexed forms, obtained from the integration up to the first minimum of the atom-atom RDF, g(r), shown in Fig. 5.

Atom	CN	
	Free	Complex
O ¹	2.5	2.4
O^2	0.7	0.6
O_3	3.0	2.3
O^4	2.6	2.5
N^1	=	0.8
N^2	1.5	1.0
N^3	3.8	3.3
F^1	4.7	_
F^2	6.5	2.3

on the RDFs of the fluorine atoms, especially F^1 . In the complex form, the first shell RDF of F^2 atom displayed the lower intensity while that of F^1 atom was almost disappeared; *i.e.*, water molecules cannot feasibly gain access to these two atoms. This is due to the fact that these gemcitabine atoms in the SWCNT-complexed form were turned to approach to the SWCNT surface (see Fig. 4b). Moreover, a considerable difference was also observed in the height of the g(r) in the region between the first and the second peaks of almost all RDFs, which denotes the feasibility of water exchange between the two shells. These values for the drug in the free form (Fig. 5a, c, and e) were noticeably higher than those in the SWCNT-complexed forms, which imply that water molecules in the first hydration shell bind stronger to the drug atoms in the complex form than those in the free form. The likely reason for this finding is because of the col-

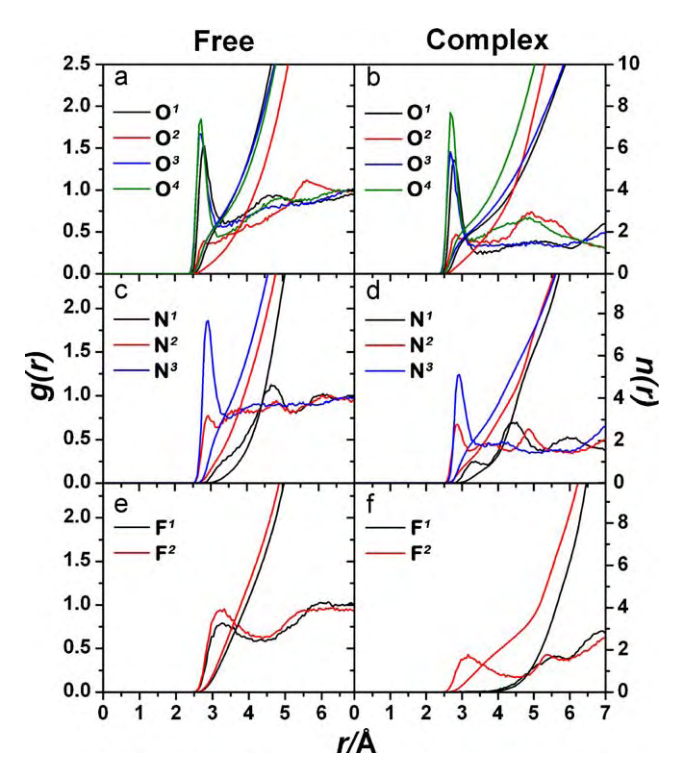


Fig. 5. Radial distribution functions, g(r), centered on the inhibitor atoms (see Fig. 1b for atomic labels) to the oxygen atoms of the modeled water for gemcitabine in the free and SWCNT-complexed systems, including the running integration number up, n(r).

U. Arsawang et al. / Journal of Molecular Graphics and Modelling 29 (2011) 591-596

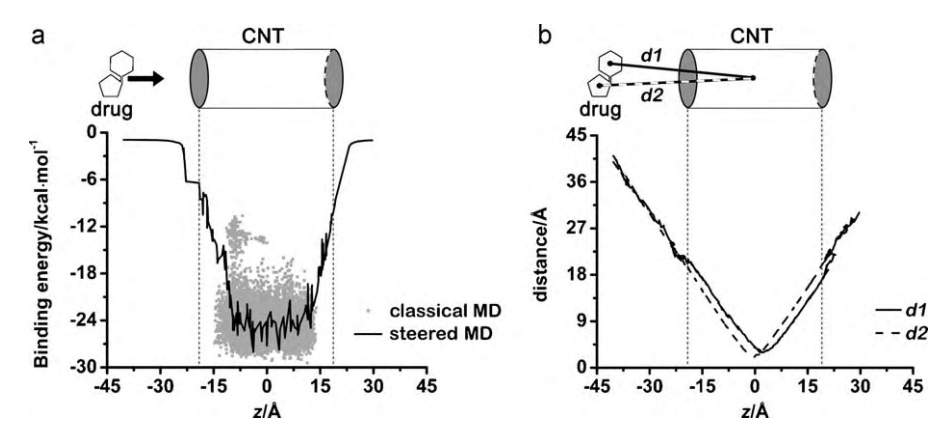


Fig. 6. (a) Binding free energies between the SWCNT and the gemcitabine drug obtained from the classical and the steered MD simulations, and (b) the d1 and d2 distances (defined in the inset) from Cg of the SWCNT to Cgs of the six- (cytosine) and five- (ribose) of drug molecule, respectively, as a function of the distance along tube (z) axis.

laborative effect due to the aromatic stacking interactions with the inner surface of the SWCNT (see also Fig. 4b), as discussed above.

Changes in the first shell coordination numbers of gemcitabine, in comparison between its free and SWCNT-complexed states (Table 1), can be classified into three sets; notably a marked decrease $\{F^1, F^2\}$, a slightly decreased $\{O^3, N^1, N^2, N^3\}$ and lastly those that were almost the same $\{O^1, O^2, O^4\}$. This is a consequence of the conformational changes of gemcitabine, where the three sets of atoms in the complexed form were located in the following three configurations relative to the SWCNT surface (Fig. 4b); (i) $\{F^1, F^2\}$ was tabbed between the SWCNT inner surface and the fivemembered ring (almost no space is available for the solvent); (ii) $\{O^3, N^1, N^2, N^3\}$ were positioned in the plane of the six-membered ring that is coordinated in the stacked conformation to the SWCNT surface (only half of the space around the atoms can be solvated); and (iii) {O¹, O², O⁴} was tilted to point away from the SWCNT surface and the atoms in the SWCNT-gemcitabine complex are fully solvated, the same as that found as in the free form.

3.4. Binding free energy profile via the movement through the SWCNT

To examine characteristics of the gemcitabine's movement from one end to another end throughout the tube, binding free energy profile from the steered MD simulations was evaluated using the MM/PBSA procedure successfully applied in our previous works [50–52]. The results were given in Fig. 6a in comparison with those yielded from the classical MD. To monitor drug's conformation along the steered MD energy profile, the two distances d1 and d2 measured from *Cgs* of the six- (cytosine) and five- (ribose) rings of drug to *Cg* of the SWCNT were, respectively, defined in an inset in Fig. 6b. Changes of those distances as a function of the tube axis (*z*-axis) were calculated and shown in the same figure.

As expected, the SMD binding free energy (solid line in Fig. 6a) is almost zero when gemcitabine locates outside $(-40 \, \text{Å} \le z \le -27 \, \text{Å})$, and decreases rapidly after the molecule enters the SWCNT $(-15 \, \text{Å} \le z \le -10 \, \text{Å})$. The energy remains constant with the average of about $-25 \, \text{kcal mol}^{-1}$ in the range $-10 \, \text{Å} \le z \le 10 \, \text{Å}$ and increase again afterward. This is in excellent agreement with that yielded from the classical MD (grey dot in Fig. 6a) when the drug molecule moves within the SWCNT. The two independent sources of energy data indicate clearly that drug molecule prefers to locate inside the SWCNT with a rather high energy barrier of $-25 \, \text{kcal mol}^{-1}$ to exit from the tube. In terms of the drug's conformation, d1 (defined in an inset) is about 3.82 Å longer than d2 at $z < 0 \, \text{Å}$ (Fig. 6b) and in *vice versa*. This indicates evidently that the ribose ring of gemcitabine points to enter into one end and exit from another end of the tube.

4. Conclusions

MD simulations provide insight into the structural properties of SWCNT serving as a gemcitabine drug carrier. The conformation, orientation and solvation of gemcitabine, as well as its movement inside the SWCNT, was extensively investigated in comparison to those of the drug in the free solvated state. According to the local density distributions of the drug projected to the diameter (xyplane) and the length (z-axis) of the SWCNT, gemcitabine was able to simultaneously translocate from one end to the other of the SWCNT. This movement is not along the centerline of the tube, but rather the displacement is at a distance from the C(g) of gemcitabine of 4.7 Å from the inner surface of the tube, where the cytosine ring of gemcitabine is oriented with a 19° tilted angle to the SWCNT inner surface. This information indicates that the drug molecule always exists inside the tube and is in the π - π stacking conformation between its cytosine ring and the tube surface. Although, the relative conformations between the cytosine and ribose rings in both the free and SWCNT-complexed states were almost identical, the loss of drug solvation around the drug molecule, especially the F¹ and F² atoms, were found in the drug-SWCNT complex. This is a result of the collaborative interaction with the surface of the tube. In addition, the binding free energy profile of the gemcitabine via its movement from outside through the SWCNT was also investigated using steered MD. The result is in good agreement with that obtained from the classical MD, i.e., drug molecule prefers to locate inside the SWCNT.

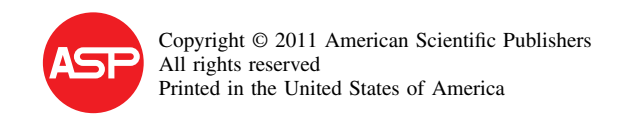
Acknowledgments

This work was supported by The Thailand Research Fund (TRF), and the Thai Government Stimulus Package 2 (TKK2555), under the Project for Establishment of Comprehensive Center for Innovative Food, Health Products and Agriculture. U.A. would like to acknowledge the M.Sc. program from the Development and Promotion of Science and Technology Talents project (DPST) and the graduate school Chulalongkorn University. O.S. thanks the Commission on Higher Education, and T.R. and K.W. thank the Ratchadaphiseksomphot Endowment Fund from Chulalongkorn University for the Post Doctoral Program. T.R. also thanks the TRF Grant for New Research (Grant No. TRG5280035). The HPC service at National Electronics and Computer Technology Center (NECTEC) and the Applied Mathematics Research Group (AMRG) at Khon Kaen University provided the computing facilities. The Center of Excellence for Petroleum, Petrochemicals and Advanced Materials, Chulalongkorn University, is acknowledged.

References

- [1] S. Iijima, Helical microtubules of graphitic carbon, Nature 354 (1991) 56-58.
- [2] A. Bianco, K. Kostarelos, C.D. Partidos, M. Prato, Biomedical applications of functionalised carbon nanotubes, Chem. Commun. (2005) 571–577.
- [3] S.K. Smart, A.I. Cassady, G.Q. Lu, D.J. Martin, The biocompatibility of carbon nanotubes, Carbon 44 (2006) 1034–1047.
- [4] A.M. Popov, Y.E. Lozovik, S. Fiorito, L.H. Yahia, Biocompatibility and applications of carbon nanotubes in medical nanorobots, Int. J. Nanomed. 2 (2007) 361–372.
- [5] S. Banerjee, T. Hemraj-Benny, S.S. Wong, Covalent surface chemistry of singlewalled carbon nanotubes, Adv. Mater. 17 (2005) 17–29.
- [6] G. Pastorin, W. Wu, S.B. Wieckowski, J.-P. Briand, K. Kostarelos, M. Prato, et al., Double functionalisation of carbon nanotubes for multimodal drug delivery, Chem. Commun. (2006) 1182–1184.
- [7] C. Klumpp, K. Kostarelos, M. Prato, A. Bianco, Functionalized carbon nanotubes as emerging nanovectors for the delivery of therapeutics, Biochim. Biophys. Acta: Biomembr. 1758 (2006) 404–412.
- [8] K. Kostarelos, L. Lacerda, G. Pastorin, W. Wu, J. Wieckowski Sebastien, Luangsivilay, et al., Cellular uptake of functionalized carbon nanotubes is independent of functional group and cell type, Nat. Nanotechnol. 2 (2007) 108–113.
- [9] V. Raffa, G. Ciofani, S. Nitodas, T. Karachalios, D. D'Alessandro, M. Masini, et al., Can the properties of carbon nanotubes influence their internalization by living cells? Carbon 46 (2008) 1600–1610.
- [10] X. Zhang, L. Meng, Q. Lu, Z. Fei, P.J. Dyson, Targeted delivery and controlled release of doxorubicin to cancer cells using modified single wall carbon nanotubes, Biomaterials 30 (2009) 6041–6047.
- [11] http://www.cdc.gov/nchs/FASTATS/deaths.htm.
- 12] http://www.reuters.com/article/idUKN1930660220080220.
- [13] M.F. Kose, M.M. Meydanli, G. Tulunay, Gemcitabine plus carboplatin in platinum-sensitive recurrent ovarian carcinoma, Expert Rev. Anticancer Ther. 6 (2006) 437–443.
- [14] A. Bianco, K. Kostarelos, M. Prato, Applications of carbon nanotubes in drug delivery, Curr. Opin. Chem. Biol. 9 (2005) 674–679.
- [15] R.P. Feazell, N. Nakayama-Ratchford, H. Dai, S.J. Lippard, Soluble single-walled carbon nanotubes as longboat delivery systems for platinum (IV) anticancer drug design, J. Am. Chem. Soc. 129 (2007) 8438–8439.
- [16] Z. Liu, X.M. Sun, N. Nakayama-Ratchford, H.J. Dai, Supramolecular chemistry on water-soluble carbon nanotubes for drug loading and delivery, ACS Nano 1 (2007) 50–56.
- [17] Z. Liu, K. Chen, C. Davis, S. Sherlock, Q.Z. Cao, X.Y. Chen, et al., Drug delivery with carbon nanotubes for *in vivo* cancer treatment, Cancer Res. 68 (2008) 6652–6660.
- [18] C. Srinivasan, Carbon nanotubes in cancer therapy, Curr. Sci. 94(2008) 300–301.
- [19] A. Bianco, M. Prato, Can carbon nanotubes be considered useful tools for biological applications? Adv. Mater. 15 (2003) 1765–1768.
- [20] C. Salvador-Morales, E. Flahaut, E. Sim, J. Sloan, M.L.H. Green, R.B. Sim, Complement activation and protein adsorption by carbon nanotubes, Mol. Immun. 43 (2006) 193–201.
- [21] D. Pantarotto, C.D. Partidos, R. Graff, J. Hoebeke, J.-P. Briand, M. Prato, et al., Synthesis, structural characterization, and immunological properties of carbon nanotubes functionalized with peptides, J. Am. Chem. Soc. 125 (2003) 6160-6164.
- [22] D. Pantarotto, C.D. Partidos, J. Hoebeke, F. Brown, E. Kramer, J.-P. Briand, et al., Immunization with peptide-functionalized carbon nanotubes enhances virus-specific neutralizing antibody responses, Chem. Biol. 10 (2003) 961–966.
- [23] D. Pantarotto, J.-P. Briand, M. Prato, A. Brianco, Translocation of bioactive peptides across cell membranes by carbon nanotubes, Chem. Commun. (2004) 16–17
- [24] N.W.S. Kam, H. Dai, Carbon nanotubes as intracellular protein transporters: generality and biological functionality, J. Am. Chem. Soc. 127 (2005) 6021–6026.
- [25] K. Yanagi, K. Iakoubovskii, S. Kazaoui, N. Minami, Y. Maniwa, Y. Miyata, et al., Light-harvesting function of beta-carotene inside carbon nanotubes, Phys. Rev. B 74 (2006) 155420.
- [26] K. Yanagi, Y. Miyata, H. Kataura, Highly stabilized β-carotene in carbon nanotubes, Adv. Mater. 18 (2006) 437–441.
 [27] H. Gao, Y. Kong, D. Cui, C.S. Ozkan, Spontaneous insertion of DNA oligonu-
- [27] H. Gao, Y. Kong, D. Cui, C.S. Ozkan, Spontaneous insertion of DNA oligonu cleotides into carbon nanotubes, Nano Lett. 3 (2003) 471–473.
- [28] N.W.S. Kam, Z. Liu, H. Dai, Functionalization of carbon nanotubes via cleavable disulfide bonds for efficient intracellular delivery of siRNA and potent gene silencing, J. Am. Chem. Soc. 127 (2005) 12492–12493.

- [29] Y. Liu, D.-C. Wu, W.-D. Zhang, X. Jiang, C.-B. He, T.S. Chung, et al., Polyethylenimine-grafted multiwalled carbon nanotubes for secure noncovalent immobilization and efficient delivery of DNA, Angew. Chem. Int. Ed. 44 (2005) 4782–4785.
- [30] Z. Liu, M. Winters, M. Holodniy, H.J. Dai, siRNA delivery into human T cells and primary cells with carbon-nanotube transporters, Angew. Chem. Int. Ed. 46 (2007) 2023–2027.
- [31] Y.H. Xie, A.K. Soh, Investigation of non-covalent association of single-walled carbon nanotube with amylose by molecular dynamics simulation, Mater. Lett. 59 (2005) 971–975.
- [32] J. Xie, Q. Xue, Q. Zheng, H. Chen, Investigation of the interactions between molecules of [beta]-carotene, vitamin A and CNTs by MD simulations, Mater. Lett. 63 (2009) 319–321.
- [33] V.L. Colvin, The potential environmental impact of engineered nanomaterials, Nat. Biotechnol. 21 (2003) 1166–1170.
- [34] C.M. Sayes, F. Liang, J.L. Hudson, J. Mendez, W. Guo, J.M. Beach, et al., Functionalization density dependence of single-walled carbon nanotubes cytotoxicity in vitro, Toxicol. Lett. 161 (2006) 135–142.
- [35] M. Prato, K. Kostarelos, A. Bianco, Functionalized carbon nanotubes in drug design and discovery, Acc. Chem. Res. 41 (2007) 60–68.
- [36] M. Gao, M. Wilmanns, K. Schulten, Steered molecular dynamics studies of titin II domain unfolding, Biophys. J. 83 (2002) 3435–3445.
- [37] http://www.jcrystal.com/products/wincnt/, Nanotube Modeler, JCrystalSoft Ed., 2004–2005.
- [38] http://www.drugbank.ca/.
- [39] D.A. Case, T.A. Darden, I.T.E. Cheatham, C.L. Simmerling, J. Wang, R.E. Duke, et al., AMBER 10, U.O. California Ed., San Francisco, 2008.
- [40] J. Wang, R.M. Wolf, J.W. Caldwell, P.A. Kollman, D.A. Case, Development and testing of a general amber force field, J. Comput. Chem. 25 (2004) 1157–1174.
- [41] Y. Cheng, D. Li, B. Ji, X. Shi, H. Gao, Structure-based design of carbon nanotubes as HIV-1 protease inhibitors: atomistic and coarse-grained simulations, J. Mol. Graphics Modell. 29 (2010) 171–177.
- [42] C. Wei, Adhesion and reinforcement in carbon nanotube polymer composite, Appl. Phys. Lett. 88 (2006) 093108-1-093108-3.
- [43] M.J.T. Frisch, G.W. Trucks, H.B. Schlegel, G.E. Scuseria, M.A. Robb, J.R. Cheeseman Jr., J.A. Montgomery, T. Vreven, K.N. Kudin, J.C. Burant, J.M. Millam, S.S. Iyengar, J. Tomasi, V. Barone, B. Mennucci, M. Cossi, G. Scalmani, N. Rega, G.A. Petersson, H. Nakatsuji, M. Hada, M. Ehara, K. Toyota, R. Fukuda, J. Hasegawa, M. Ishida, T. Nakajima, Y. Honda, O. Kitao, H. Nakai, M. Klene, X. Li, J.E. Knox, H.P. Hratchian, J.B. Cross, V. Bakken, C. Adamo, J. Jaramillo, R. Gomperts, R.E. Stratmann, O. Yazyev, A.J. Austin, R. Cammi, C. Pomelli, J.W. Ochterski, P.Y. Ayala, K. Morokuma, G.A. Voth, P. Salvador, J.J. Dannenberg, V.G. Zakrzewski, S. Dapprich, A.D. Daniels, M.C. Strain, O. Farkas, D.K. Malick, A.D. Rabuck, K. Raghavachari, P. Foresman, I. Komaromi, R.L. Martin, D.J. Fox, T. Keith, M.A. Al-Laham, C.Y. Peng, A. Nanayakkara, M. Challacombe, P.M.W. Gill, B. Johnson, W. Chen, M.W. Wong, C. Gonzalez, J.A. Pople, Gaussian 03 Revision C. 02, Gaussian Inc., Wallingford, CT, 2004.
- [44] H.J.C. Berendsen, J.R. Grigera, T.P. Straatsma, The missing term in effective pair potentials, J. Phys. Chem. 91 (1987) 6269–6271.
- [45] S. Miyamoto, P.A. Kollman, Settle: an analytical version of the SHAKE and RAT-TLE algorithm for rigid water models, J. Comput. Chem. 13 (1992) 952–962.
- [46] T. Darden, D. York, L. Pedersen, Particle mesh Ewald: an N [center-dot] log(N) method for Ewald sums in large systems, J. Chem. Phys. 98 (1993) 10089–10092.
- [47] U. Essmann, L. Perera, M.L. Berkowitz, T. Darden, H. Lee, L.G. Pedersen, A smooth particle mesh Ewald method, J. Chem. Phys. 103 (1995) 8577–8593.
- [48] J.C. Phillips, R. Braun, W. Wang, J. Gumbart, E. Tajkhorshid, E. Villa, et al., Scalable molecular dynamics with NAMD, J. Comput. Chem. 26 (2005) 1781–1802.
- [49] S. Kumar, C. Huang, G. Zheng, E. Bohm, A. Bhatele, J.C. Phillips, et al., Scalable molecular dynamics with NAMD on the IBM Blue Gene/L system, IBM J. Res. Dev. 52 (2008) 177–188.
- [50] T. Rungrotmongkol, N. Nunthaboot, M. Malaisree, N. Kaiyawet, P. Yotmanee, A. Meeprasert, et al., Molecular insight into the specific binding of ADP-ribose to the nsP3 macro domains of chikungunya and venezuelan equine encephalitis viruses: molecular dynamics simulations and free energy calculations, J. Mol. Graphics Modell. (2010), doi:10.1016/j.jmgm.2010.09.2010.
- [51] O Aruksakunwong, M. Malaisree, P. Decha, P. Sompornpisut, V. Parasuk, S. Pianwanit, et al., On the lower susceptibility of oseltamivir to influenza neuraminidase subtype N1 than those in N2 and N9, Biophys. J. 92 (2007) 798–807.
- [52] M. Malaisree, T. Rungrotmongkol, P. Decha, P. Intharathep, O. Aruksakunwong, S. Hannongbua, Understanding of known drug-target interactions in the catalytic pocket of neuraminidase subtype N1, Proteins 71 (2008) 1908–1918.



Understanding the Molecular Properties of Doxorubicin Filling Inside, and Wrapping Outside, Single-Walled Carbon Nanotubes

Purinchaya Sornmee¹, Thanyada Rungrotmongkol^{2, 3}, Oraphan Saengsawang^{2, 3}, Uthumporn Arsawang¹, Tawun Remsungnen⁴, and Supot Hannongbua^{2, *}

¹Department of Mathematics, Chulalongkorn University, Bangkok, 10330, Thailand ²Computational Chemistry Unit Cell, Department of Chemistry, Chulalongkorn University, Bangkok, 10330, Thailand ³Center of Innovative Nanotechnology, Chulalongkorn University, Bangkok, 10330, Thailand ⁴Department of Mathematics, Khon Kaen University, Khon Kaen, 40002, Thailand

Molecular dynamics (MD) simulations were applied in order to examine the molecular properties of the anticancer drug, doxorubicin (DOX), carried by single-walled carbon nanotubes (SWCNT) in an aqueous solution. The models evaluated were the two DOX-SWCNT complexes based upon DOX being inside (DOX_{in}-SWCNT) or outside (DOX_{out}-SWCNT) the pristine SWCNT, and these were compared to that for the aqueous free form (DOX_{free}). It was found that DOX in the DOX_{in}-SWCNT complex was less flexible than DOX_{free} and DOX_{out}-SWCNT, which was expected due to its collaborative interaction with the surface of the tube. Interestingly, in both complexes with SWCNT DOX was found to move from one end of the SWCNT to the other, in the $\pi-\pi$ stacking conformation between the three aromatic hydroxyanthraquinonic rings of the DOX and the surface of the SWCNT. This configuration is better established in the DOX_{out}-SWCNT complex than in the DOX_{in}-SWCNT complex, with their respective distances from the DOX center of mass to the nearest carbon atom of the SWCNT being 4.0 Å and 4.5 Å. Due to the curvature effect and the volume constraints, the ordering of water accessibility around DOX was observed in the following order: DOX_{free} \gg DOX_{out}-SWCNT > DOX_{in}-SWCNT.

Keywords: Drug Delivery System, Carbon Nanotube, Doxorubicin Anticancer Drug, Molecular Dynamics Simulations.

1. INTRODUCTION

Treating cancer with systemic chemotherapy usually shows undesirable side effects in patients because the drug affects all rapidly dividing cells including normal cells. Many side effects can be controlled or reduced by targeting the drug delivery, 1,2 which then ideally brings the right amount of drug directly and specifically to the site of the disease, such as the specific tissue or even cancer cells. The selection of effective drug carriers is one of the best biomedical aspects for an effectively targeted drug delivery system and many such approaches for delivery systems have been proposed, based on various drug carriers. Here, the single-walled carbon nanotube (SWCNT) was considered as the drug transporter 3-5 for carrying the anti-cancer drug, doxorubicin (DOX), through two different modes of

drug binding; DOX either filling into the pore or wrapping on the outer surface of the SWCNT. The molecular information obtained could assist further design efforts for more effective and selective drug carriers for the treatment of cancer with reduced side effects.

DOX is one of the most potent and widely used drugs for the treatment of many types of cancer.⁶ It intercalates with double stranded nucleic acids and so inhibits the synthesis of DNA within cells and thus the growth of certain cancers is slowed down or stopped.⁷ However, amongst diverse side effects, it produces severe cardiotoxicity and myelosuppression. To avoid these and other such side effects, much attention has been paid to improving the delivery of DOX to the target cancer cells. For example, encapsulation and micellar delivery of DOX in glucosamine(ethyleneglycol) was shown to provide the ability to protect and carry this drug to the target.⁸ Moreover, Janes et al.⁷ developed chitosan nanoparticles as

^{*}Author to whom correspondence should be addressed

colloidal carriers of DOX into the cells in its active form. They showed that DOX could be complexed to chitosan by incubation and subsequently, once separated, the dextran and DOX conjugates encapsulated in chitosan nanoparticles of ~100 nm diameter provided decreased tumor volumes in mice, whereas the treatment with DOX alone did not.9 Two-layer porous silicon10 and mesoporous thin silica films¹¹ can be used as a drug carrier for controlled delivery of DOX. As to SWCNT as a carrier, Liu et al. 12 showed an extremely high drug loading ability for the innovative, easy-to-make SWCNT-DOX complex, where, allowing for the weight of the phospholipid-poly(ethylene glycol) coating, the SWCNT-DOX complex contained \sim 50–60% (w/w) of DOX, a level that is remarkably higher than that for liposomes and dendrimer based drug carriers. Furthermore, the DOX-SWCNT complex, when functionalized with a target specific monoclonal antibody and a fluorescent marker, was successfully transported to human cancer cells, followed by drug release and translocation into the nucleus.¹³

In the present study, we focused on trying to understand the basic knowledge of the DOX-SWCNT complex in terms of serving as a drug delivery vehicle for transportation of this anti-cancer drug to target cells. Molecular dynamics (MD) simulations were performed on the DOX loaded to either the inner or the outer surfaces of SWCNT and compared to the free drug, all in an aqueous state. The structural and dynamics properties of the free DOX and the two DOX-SWCNT complexes were analyzed and compared in terms of drug conformation, drug solvation and curvature effect.

2. EXPERIMENTAL DETAILS

2.1. Modeled Systems

The (28,0) zigzag type of SWCNT was constructed using the Nanotube Modeler program.¹⁴ The modeled SWCNT has finite length of 38.89 Å with a diameter of 21.94 Å, a C-C bond length of 1.42 Å, and the two ends of the SWCNT were terminated with hydrogen atoms. The tube model used for carrying the DOX drug consists of 1,008 carbon atoms and 56 hydrogen atoms. The atomic coordinates of DOX were regained from the Drug Data Bank Database (entry code: DB00997)^{15, 16} and the missing hydrogen atoms were then added by considering the hybridization of the covalent bonds. Due to the relatively high pKa (8.3) of DOX^{17, 18}, its chemical structure was treated in the protonated form as a weak base (Fig. 1). To prepare the starting structures of the DOX-SWCNT complexes, the DOX was placed inside (DOX_{in}-SWCNT; Fig. 2(a)) or outside (DOX_{out}-SWCNT; Fig. 2(b)) the SWCNT.

The AMBER99 force fields¹⁹ involving atom type CA, designed for aromatic carbon atoms, were applied for the SWCNT. To construct the atomic charges and parameters

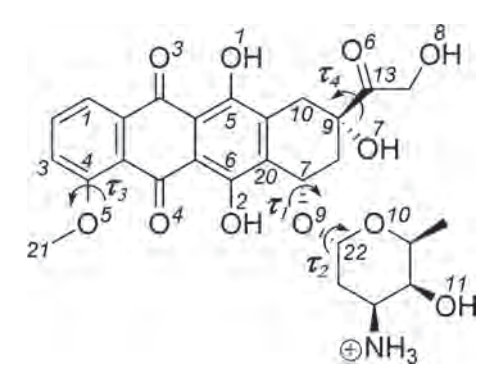


Fig. 1. Chemical structure of DOX, in its protonated form, showing the torsional angles and atomic labels.

for DOX, the structure optimization was performed with the HF/6-31G(d) calculation to refine the drug geometry using the Gaussian03 program.²⁰ Consequently, the electrostatic potentials surrounding the drug molecule were calculated using the same level of theory and basis set as applied in the optimization step. The RESP charges were generated by the RESP module of the AMBER 10²¹ program, with the partial charge distributions among identical atoms being fitted into the same value. The force fields of DOX were assigned using the Antechamber suite of the program and the missing parameters were obtained from the Generalized AMBER Force Field (GAFF).²²

2.2. Molecular Dynamics (MD) Simulations

To examine the feasibility of using SWCNT as a drug carrier for drug delivery applications, MD simulations were carried out for: (i) free DOX in bulk water (DOX_{free})

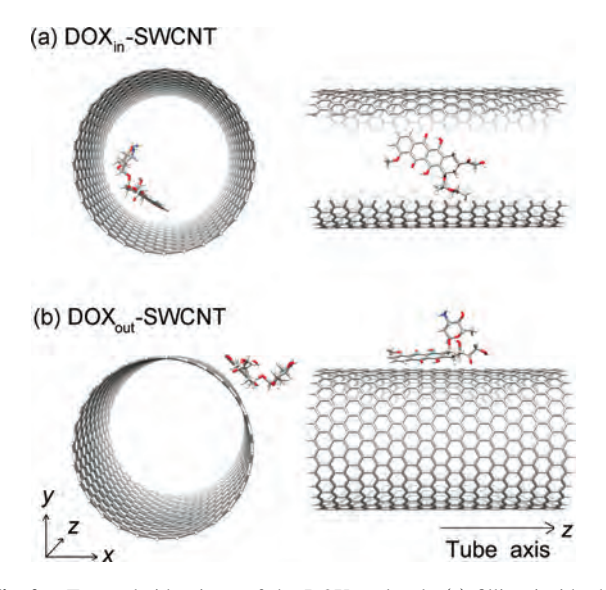


Fig. 2. Top and side views of the DOX molecule (a) filling inside the pore (DOX $_{\text{in}}$ -SWCNT) and (b) wrapping on the outer surface (DOX $_{\text{out}}$ -SWCNT) of the (28,0) zigzag SWCNT, where the origin of the Cartesian coordinate is at the center of the gravity of the SWCNT and the *z*-axis is parallel to the tube-axis.

(ii) DOX bound inside the SWCNT (DOX_{in}-SWCNT) and (iii) DOX bound outside the SWCNT (DOX_{out}-SWCNT).

The three models studied were separately prepared using the LEaP module of the AMBER10 software package.²¹ Each system was solvated with the simple point charge (SPC) water model in the truncated octagonal box and neutralized by a chloride ion. This leads to a total of 5,017, 18,420 and 19,698 atoms for the DOX_{free}, DOX_{in}-SWCNT and DOX_{out}-SWCNT systems, respectively. The simulations were performed under periodic boundary conditions with the *NPT* ensemble using AMBER10. The particle mesh Ewald method²³ was used to handle the long-range electrostatic interactions, whilst the SHAKE algorithm²⁴ was employed to constrain all bonds involving hydrogen atoms. A time step of 2 fs and pressure of 1atm were applied with a cutoff of 12 Å for nonbonded interactions.

To relieve bad steric contacts prior to the simulation process, three minimizationsteps were applied. Firstly, the hydrogen atoms were minimized with all the heavy atoms fixed, followed secondly by the optimization of the added water molecules and then finally the minimization of the whole structure. The system was heated from 100 K to 300 K with a subsequent equilibration phase at 300 K for 500 ps and a final production phase of 9.5 ns. The MD trajectories were stored every 200 steps and only the snapshots extracted from the production phase were used for analysis. The convergence of energies, temperature and root mean square deviation (*RMSD*) were used to verify the stability of each system.

3. RESULTS AND DISCUSSION

3.1. Change in DOX Conformation

To examine the conformation of DOX in free and the two SWCNT-complexed forms, four torsional angles, $\tau_1 - \tau_4$, of DOX (defined in Fig. 1) in the three states were investigated and compared (Fig. 3).

By considering the lilted angles, τ_1 and τ_2 , between the tetracyclic and the aminoglycosidic groups of DOX (see Fig. 1 for definition), the DOX inside the tube was less flexible than those in the other two forms, the $\mathrm{DOX}_{\mathrm{free}}$ and $\mathrm{DOX}_{\mathrm{out}}\text{-SWCNT}$ complex, as indicated by the sharp and narrow peaks at $\tau_1 = -125^{\circ}$ and $\tau_2 = -78^{\circ}$ (Figs. 3(a and b)). The most flexible form is DOX_{free} where three and two favorable conformations, represented by τ_1 (-156°, -123° and -77°) and τ_2 (-154° and -70°), respectively, were found. With respect to the DOX_{out}-SWCNT complex, the DOX conformation was characterized by the two peaks of τ_1 (-153° and -85°) and the two peaks of τ_2 (-159° and -62°). The flexibility of the -OCH₃ and -COCH₂OH side chains of DOX is monitored by the τ_3 and τ_4 values, respectively. As indicated (Fig. 3(c)) by the two separated peaks ($\tau_3 = -77^{\circ}$ and 79°), the two overlapped peaks ($\tau_3 = 11^\circ$ and 77°) and the one broad peak ($\tau_3 = 38^{\circ}$), the $-OCH_3$ group in the free

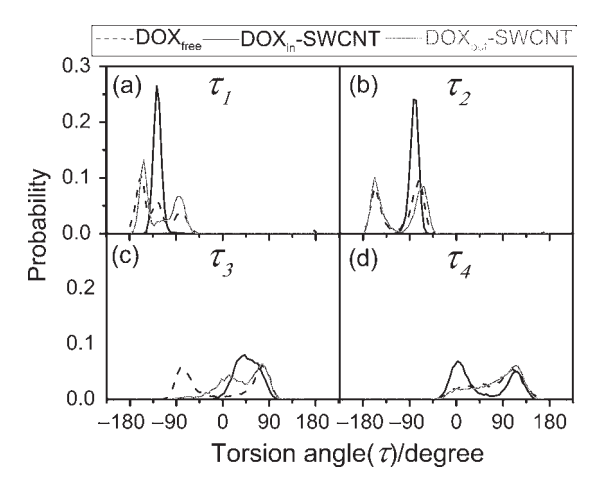


Fig. 3. Distribution of the torsional angles $(\tau_1 - \tau_4)$; defined in Fig. 1) of the free DOX in bulk water (dash black), and of DOX bound inside (solid black) or outside (solid grey) of the SWCNT.

form is, as expected, more flexible than that in either the DOX wrapping outside or filling the inside of the SWCNT. Interestingly, the $-\text{COCH}_2\text{OH}$ group of DOX inside the SWCNT clearly shows two distinct and almost symmetric conformations of $\tau_4 = 1^\circ$ and 121°. This is due to the large steric hindrance with the aminoglycosidic ring when the DOX tetracyclic group in the DOX_{in}-SWCNT complex binds almost in parallel to the inner surface of the SWCNT (see also snapshots in Figs. 6(b and c)).

3.2. Translation of DOX Inside and Outside of the SWCNT

3.2.1. DOX Inside the SWCNT

To verify whether the SWCNT is capable for being used as nano-container in drug delivery applications, the probability of finding the DOX drug, P(Cg), represented by its center of gravity (Cg) projected to the tube-axis (z-axis; defined in Fig. 2(b)) and averaged to the x- and y-axes of the SWCNT was evaluated. The results are shown in Figure 4 where the distance from the origin of the Cartesian coordinate (defined in Fig. 2(b)) and the DOX Cg as a function of the simulation time is also shown as an inset.

The P(Cg) along the tube-axis (Fig. 4(b)) decreases exponentially as a function of the distances from the two ends of the tube, indicating that DOX is able to move freely along the 39 Å length of the SWCNT and remains solely inside the SWCNT. Noticeably, the drug never visits at a distance of <4.5 Å from the two ends. This is because the drug molecule cannot overcome the energy barrier from the repulsion with the hydrogen atoms at both ends. Note, that the symmetric distribution of the P(Cg) plot is expected if the simulation time is long enough. As a function of simulation time, DOX was found to move freely from one end to the other end of the SWCNT (inset

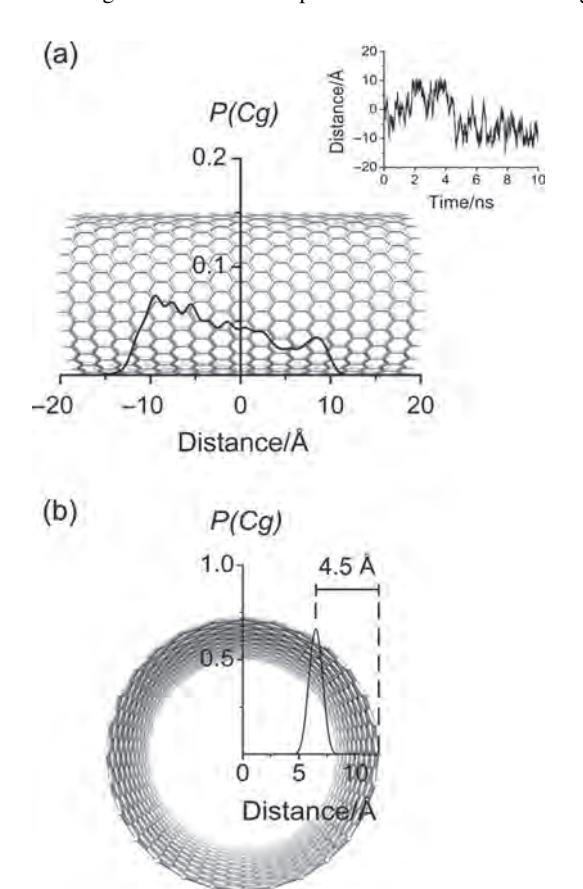


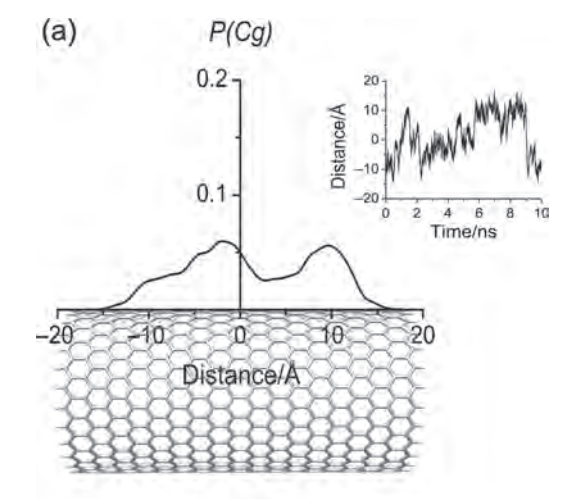
Fig. 4. Probability distributions of the center of gravity, P(Cg), of DOX encapsulated inside the SWCNT (DOX_{in}-SWNT) (a) projected to the tube-axis (*z*-axis; defined in Fig. 2(b)), where the distance from the origin of the Cartesian coordinate and the DOX Cg as a function of simulation time is given in the inset, and (b) averaged and projected to the x- and y-axes.

of Fig. 4(a)), corresponding with the P(Cg) plot shown in Figure 4(a).

In the same manner, a single sharp peak at 6.50 Å of the averaged probability plot of the DOX Cg in the direction perpendicular to the SWCNT surface (Fig. 4(b)), indicates the most probable distance of DOX is far away from the tube-axis. In other words, the preferential coordinate of the drug molecule is \sim 4.5 Å from the inner surface of the SWCNT when the diameter of the tube is 21.94 Å. In summary, the data from the Cg distribution plots suggest that DOX moves parallel to the inner surface of the SWCNT (with the distance to the Cg of \sim 4.5 Å) from one end to the other end of the SWCNT (Fig. 4(a)).

3.2.2. DOX Outside the SWCNT

Similar to that seen for the DOX_{in} -SWCNT complex, the probability of finding the DOX Cg binding outside the SWCNT (DOX_{out}-SWCNT) were calculated and are shown in Figure 5. The plot representing DOX movement in the direction perpendicular to the tube surface (Fig. 5(b)) shows a pronounced peak centered at 15 Å



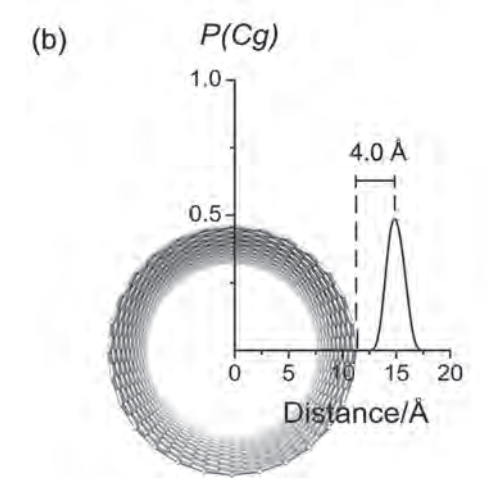


Fig. 5. Probability distributions of the center of gravity, P(Cg), of DOX bound outside of the SWCNT (DOX_{out}-SWNT) (a) projected to the tubeaxis (*z*-axis;defined in Fig. 2), where the distance from the origin of the Cartesian coordinate and the DOX Cg as a function of the simulation time is given in the inset and (b) averaged and projected to the x- and y-axes.

from the origin, i.e., \sim 4.0 Å from the outer surface of the tube. Along the tube-axis, the plot shows two broad peaks centered at \sim -2 Å and 10 Å without access to the two ends (Fig. 5(a)). The formation of these two peaks, the two regions where DOX spent more time than in the other areas, are because of the interaction between DOX and the H atoms at the two ends. The asymmetry of these two peaks is due to the asymmetry of the drug molecule, i.e., its Cg is not at the center of the molecule. The observed result is consistent with the distribution plot as a function of the simulation time (Fig. 5(a) inset) in which the drug molecule was found to move freely from one end to the other end.

Taken together, the distribution plots in Figures 4 and 5 clearly indicate that the SWCNT, when terminated with H atoms, shows a potential to serve as a drug-container in which the drug is able to bind to both the inside and the outside of the SWCNT during the whole simulation.

3.3. Drug Orientation Inside and Outside the SWCNT

To monitor the probable aromatic stacking interactions between DOX and the wall surface of the SWCNT drug carrier, the atom-atom radial distribution functions (RDFs, $g_{ij}(r)$), that is the probability of finding a particle of type j within a sphere radius r around the particle of type i, were calculated. Here, i represents the selected carbon atom of DOX and j denotes all the carbon atoms of the SWCNT. The results for the two complexes, DOX_{in}-SWCNT and DOX_{out}-SWCNT, were plotted and compared in Figure 6. Their corresponding drug bound structures taken from the MD snapshots are also depicted. Here, the four carbon atoms, C^1 and C^4 – C^6 (defined in Fig. 1) were used to represent the planarity of the three aromatic hydroxyan-thraquinonic rings of the DOX molecule.

The RDF plots for the C^1 and C^4 – C^6 atoms of DOX in the DOX_{in}-SWCNT complex (Fig. 6(a)) show clear peaks with maxima at 3.6, 3.7, 4.0 and 3.8 Å, respectively. This means that the distances from those DOX C atoms to the nearest atom of the SWCNT are almost the same, indicating the aromatic stacking orientation of the tetracyclic portion has an alignment that is almost parallel to the inner surface of the SWCNT. Schematic representations of such conformations, taken from the MD snapshots (Figs. 6(b and c)) confirm such conclusions. Such a tilled orientation, with the four distances being slightly different, is due to the steric hindrance between the inner surface curvature of the SWCNT and the drug side chains.

For the DOX_{out} -SWCNT complex (Fig. 6(d)), the curvature effect on the drug structure was not observed. Here, the orientation of the three aromatic hydroxyan-thraquinonic rings of the DOX molecule was found to be parallel to the *z*-axis of the SWCNT, i.e., it is well aligned on the curvature of the outer surface. This conclusion was indicated by the maxima of the C^1 and C^2 - C^4 *RDFs* which take place at the same distance of \sim 3.9 Å. A schematic representation of the DOX_{out} -SWCNT (Figs. 6(e and f))

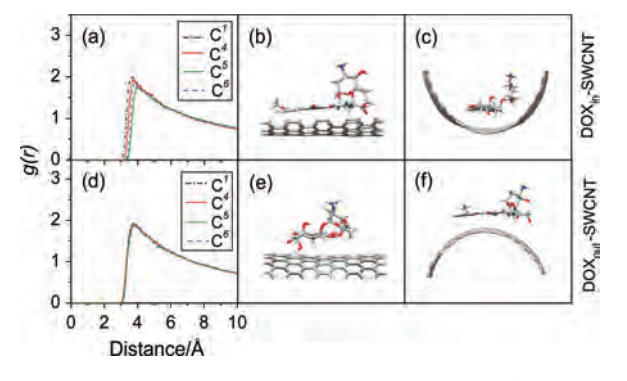


Fig. 6. RDFs from the four carbon atoms, C^1 and C^4 – C^6 (defined in Fig. 1), on the three-aromatic hydroxyanthraquinonic rings of DOX to the C atoms of the SWCNT for the (a) DOX_{in}-SWCNT and (d) DOX_{out}-SWCNT complexes. The corresponding drug bound structures are shown in ((b) and (c)) for the DOX_{in}-SWCNT and ((e) and (f)) for the DOX_{out}-SWCNT.

reveals that, in contrast to that of the DOX_{in} -SWCNT, the aromatic hydroxyanthraquinonic ring of the drug molecule in the DOX_{out} -SWCNT complex is not positioned along the tube axis (compare Figs. 6(b and f)). The data for both complexes suggest that the π - π stacking interactions between the aromatic rings of the DOX and its transporter are better formed in the DOX_{out} -SWCNT than that in the DOX_{in} -SWCNT systems. This could then be the reason why the DOX_{out} -SWCNT is more often proposed as the drug binding mode in drug delivery applications. ^{11, 25}

3.4. Solvation Structure of Drug

The probability of finding water molecules around the heteroatoms of DOX were considered and determined in terms of the atom-atom radial distribution functions. The RDF plots for the three systems studied ($\mathrm{DOX}_{\mathrm{free}}$, $\mathrm{DOX}_{\mathrm{in}}$ -SWCNT and $\mathrm{DOX}_{\mathrm{out}}$ -SWCNT) are shown in Figure 7 together with the corresponding running integration numbers, n(r).

The *RDF* plots in Figure 7 denote the distribution of the water oxygen around the selected DOX heteroatoms. The peak at \sim 3 Å usually represents the first solvation shell, and sharpening of the first peak signifies how strong the solvent coordinates to the central atom are, whilst the height of the first minimum refers to the resident time (how long the solvent molecule stays in the first hydration shell). As can be seen in Figure 7, the plots for the three systems, either with or without the SWCNT drug carrier, show a first peak at \sim 3 Å indicating that almost all atoms were considerably solvated by water molecules. As expected, among the three systems, the drug in free form, DOX $_{\rm free}$, was better solvated than that in the DOX $_{\rm out}$ -SWCNT and the DOX $_{\rm in}$ -SWCNT, respectively. Detailed

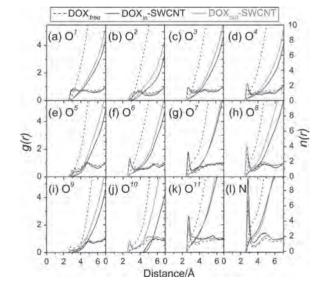


Fig. 7. The *RDFs* of water molecules around the DOX heteroatoms for the three systems; DOX_{free} , DOX_{in} -SWCNT and DOX_{out} -SWCNT.

comparisons, especially amongst the two DOX-SWCNT complexes, are discussed below.

The RDFs plots can be classified according to their features into three sets; (i) a sharp and narrow first peak at $\sim 2.7-2.8$ Å with a clear minimum of the $[O^6, O^7, O^8]$ O¹¹ and N], exhibits their firm hydration shell (Figs. 7(fh, k and l)); (ii) a broad peak at ~ 3 Å of the $[O^1, O^3,$ O⁴ and O¹⁰] denotes a movable solvation (Figs. 7(a, c, d and i)); (iii) a disappearing of the peak at the region \sim 3 Å of the $[O^2, O^5]$ and O^9 means that those atoms cannot be accessed by solvent (Figs. 7(b, e and i)). Interest is paid on the O¹⁰ atom of the six-membered ring oxygen (Fig. 7(i)) in which no water was detected within a distance of $\leq \sim 4.5$ Å in the DOX_{in}-SWCNT, i.e., the water was totally shielded by the inner surface of the SWCNT (see Figs. 6(b and c) for the schematic orientation). For the DOX_{out}-SWCNT, this atom was partially shielded, leading to the CN of 1 water molecule (Fig. 7(j), grey line, and see also Figs. 6(e and f)). This is not the case for the DOX_{free}, where the O10 atom in this state was found to be solvated by two water molecules (Fig. 7(j), dashed line). Note that the CN is the n(r) integrated up to the first minimum of the RDF, i.e., this number represents the number of water molecules positioning in the first hydration shell around the central atom.

In terms of the running integration number, n(r), it is clear from almost all atoms that the plots for the DOX_{free} (dashed lines in Fig. 7) is much higher than those of the DOX_{out} -SWCNT (grey lines) and DOX_{in} -SWCNT (black line), especially at the atoms substituted on the three planar and aromatic hydroxyanthraquinonic rings of DOX. Therefore, the ordering of water accessibility is of $DOX_{free} \gg DOX_{out}$ -SWCNT $> DOX_{in}$ -SWCNT. This is due the curvature effect and the volume constraint in which the inner surface was, as expected, found to play stronger role than that of the outer one.

4. CONCLUSIONS

MD simulations provide insight into the structure and dynamic properties of the anticancer drug, DOX, when carried by (bound to) SWCNT. The pristine SWCNT with hydrated DOX bound inside (DOX_{in}-SWCNT) or outside (DOX_{out}-SWCNT) were studied in comparison to the drug in the free aqueous state (DOX_{free}). During 10 ns simulations, it was found that the collaborative interaction with the surface of the tube caused a lower flexibility of the aminoglycosidic ring and -OCH3 group of DOX inside the tube relative to those of the other two systems, DOX_{out}-SWCNT and DOX_{free}. Additionally, the formation of an aromatic stacking interaction was detected between the three aromatic hydroxyanthraquinonic rings of DOX and the surface of the SWCNT. This interaction is slightly stronger in the DOX_{out}-SWCNT complex than the DOX_{in}-SWCNT complex due to lack of steric hindrance and the curvature effect on the drug structure. DOX was also observed to move from one end of the SWCNT to the other. Interestingly, the movement does not take place at the center of the tube, but at the distance (from the center of mass of the drug) of 4.5 Å and 4.0 Å from the surface of the tube of the DOX $_{\rm in}$ -SWCNT and the DOX $_{\rm out}$ -SWCNT complexes, respectively. In terms of ligand solvation, the ordering of water accessibility is of DOX $_{\rm free}\gg$ DOX $_{\rm out}$ -SWCNT >DOX $_{\rm in}$ -SWCNT.

Acknowledgments: This work was supported by The Thailand Research Fund and the Thai Government Stimulus Package 2 (TKK2555), under the Project for Establishment of Comprehensive Center for Innovative Food, Health Products and Agriculture. Purinchaya Sornmee is grateful for the M.Sc. program from the graduate school Chulalongkorn University. Thanyada Rungrotmongkol thanks the Ratchadaphiseksomphot Endowment Fund from Chulalongkorn University, and the funding for New Research (Grant No. TRG5280035) from TRF. Oraphan Saengsawang thanks the Commission on Higher Education for the Postdoctoral fellowship. The Computational Chemistry Unit Cell at Chulalongkorn University, the Applied Mathematics Research Group (AMRG) at Khon Kaen University, and the HPC service at National Electronics and Computer Technology Center (NECTEC) provided the computing facilities. The Center of Excellence for Petroleum, Petrochemicals and Advanced Materials, Chulalongkorn University, is acknowledged.

References

- 1. K. K. Jain, Tech. in Cancer Res. 4, 311 (2005).
- T. Lebold, C. Jung, J. Michaelis, and C. Bräuchle, Nano Lett. 9, 2877 (2009).
- 3. T. A. Hilder and J. M. Hill, Curr. App. Phys. 8, 258 (2008).
- 4. M. Foldvari and M. Bagonluri, Nanomedicine 4, 183 (2008).
- Z. Lui, K. Chen, C. Davis, S. Sherlock, Q. Cao, X. Chen, and H. Dai, *Cancer Res.* 68, 6652 (2008).
- G. Speelmans, R. W. H. M. Staffhorst, H. G. Steenbergen, and B. de Kruijff, *Biochim. Biophys. Acta.* 1284, 240 (1996).
- K. A. Janes, M. P. Fresneau, A. Marazuela, A. Fabra, and M. J. Alonsao, J. Control Release 73, 255 (2001).
- 8. T. Pirawattana and T. Srinophakun, Int. J. Mol. Sci. 9, 2290 (2008).
- L. Brannon-Peppas and J. O. Blanchette, Adv. Drug Deliv. Rev. 56, 1649 (2004).
- L. Vaccari, D. Canton, N. Zaffaroni, R. Villa, M. Tormen, and E. D. Fabrizio, *Microelec. Eng.* 83, 1598 (2006).
- 11. T. Lebold, C. Jung, J. Michaelis, and C. Bräuchle, *Nano Lett.* 9, 2877 (2009)
- 12. Z. Liu, X. Sun, N. Nakayama-Ratchford, and H. Dai, Am. Chem. Soc. Nano. 1, 50 (2007).
- E. Heistera, V. Neves, C. Tilmaciub, K. Lipert, V. S. Beltrán, H. M. Coley, S. R. P. Silva, and J. McFadden, *Carbon* 47, 2152 (2009).
- JCrystalSoft, Nanotube Modeler [online], Available from: http://www.jcrystal.com/products/wincnt (2010).
- D. S. Wishart, C. Knox, A. C. Guo, D. Cheng, S. Shrivastava, D. Tzur, B. Gautam, and M. Hassanali, *Nucleic Acids Res.* 36, D901 (2008).

- D. S. Wishart, C. Knox, A. C. Guo, S. Shrivastava, M. Hassanali, P. Stothard, Z. Chang, and J. Woolsey, *Nucleic Acids Res.* 34, D668 (2006).
- 17. D. J. Adams, Curr. Med. Chem.—Anti-Cancer Agents 5, 1 (2005).
- L. Kleeberger and E. M. Röttinger, Cancer Chemo. Pharm. 33, 144 (1993).
- J. M. Wang, P. Cieplak, and P. A. Kollman, J. Comp. Chem. 21, 1049 (2000).
- M. J. Frisch, G. W. Trucks, H. B. Schlegel, G. E. Scuseria, M. A. Robb, J. R. Cheeseman, J. A. Montgomery, T. Vreven, K. N. Kudin, J. C. Burant, J. M. Millam, S. S. Iyengar, J. Tomasi, V. Barone, B. Mennucci, M. Cossi, G. Scalmani, N. Rega, G. A. Petersson, H. Nakatsuji, M. Hada, M. Ehara, K. Toyota, R. Fukuda, J. Hasegawa, M. Ishida, T. Nakajima, Y. Honda, O. Kitao, H. Nakai, M. Klene, X. Li, J. E. Knox, H. P. Hratchian, J. B. Cross, V. Bakken, C. Adamo, J. Jaramillo, R. Gomperts, R. E. Stratmann, O. Yazyev, A. J. Austin, R. Cammi, C. Pomelli, J. W. Ochterski, P.Y. Ayala, K. Morokuma, G. A. Voth, P. Salvador, J. J. Dannenberg, V. G. Zakrzewski, S. Dapprich, A. D. Daniels, M. C. Strain, O. Farkas, D. K. Malick, A. D. Rabuck, K. Raghavachari, J. B. Foresman,
- J. V. Ortiz, Q. Cui, A. G. Baboul, S. Clifford, J. Cioslowski, B. B. Stefanov, G. Liu, A. Liashenko, P. Piskorz, I. Komaromi, R. L. Martin, D. J. Fox, T. Keith, M. A. Al-Laham, C. Y. Peng, A. Nanayakkara, M. Challacombe, P. M. W. Gill, B. Johnson, W. Chen, M. W. Wong, C. Gonzalez, and J. A. Pople, Gaussian 03, Revision C.02. Gaussian, Inc., Wallingford CT (2004).
- 21. D. A. Case, T. A. Darden, T. E. Cheatham III, C. L. Simmerling, J. Wang, R. E. Duke, R. Luo, K. M. Merz, D. A. Pearlman, M. Crowley, R. C. Walker, W. Zhang, B. Wang, S. Hayik, A. Roitberg, G. Seabra, K. F. Wong, F. Paesani, X. Wu, S. Brozell, V. Tsui, H. Gohlke, L. Yang, C. Tan, J. Mongan, V. Hornak, G. Cui, P. Beroza, D. H. Mathews, C. Schafmeister, W. S. Ross, and P. A. Kollman, AMBER 10, University of California, San Francisco (2008).
- J. Wang, R. M. Wolf, J. W. Caldwell, P. A. Kollman, and D. A. Case, J. Comp. Chem. 25, 1157 (2004).
- 23. E. L. Pollock and J. GLlosli, Comput. Phys. Commun. 81, 93 (1996).
- J. P. Ryckaert, G. Cicotti, and H. J. C. Berendsen, J. Comput. Phys. 23, 327 (1977).
- E. Heistera, V. Neves, C. Tilmaciub, K. Lipert, V. S. Beltrán, H. M. Coley, S. R. P. Silva, and J. McFadden, *Carbon* 47, 2152 (2009).

Received: 3 July 2010. Accepted: 9 August 2010.

Author's personal copy

Chemical Physics Letters 507 (2011) 134-137



Contents lists available at ScienceDirect

Chemical Physics Letters

journal homepage: www.elsevier.com/locate/cplett



Increased dispersion and solubility of carbon nanotubes noncovalently modified by the polysaccharide biopolymer, chitosan: MD simulations

Thanyada Rungrotmongkol ^{a,g}, Uthumporn Arsawang ^a, Chularat Iamsamai ^b, Arthit Vongachariya ^c, Stephan T. Dubas ^{d,g}, Uracha Ruktanonchai ^e, Apinan Soottitantawat ^f, Supot Hannongbua ^{a,g,*}

- ^a Computational Chemistry Unit Cell, Department of Chemistry, Faculty of Science, Chulalongkorn University, Bangkok 10330, Thailand
- ^b Doctor of Philosophy Program in Nanoscience and Technology, Graduate School, Chulalongkorn University, Bangkok 10330, Thailand
- ^c UBE Technical Center (Asia) Limited, UBE Group (Thailand), Rayong 21000, Thailand
- d Metallurgy and Materials Science Research Institute, Chulalongkorn University, Bangkok 10330, Thailand
- ^e National Nanotechnology Center, National Science and Technology Development Agency, Pathumthani 12120, Thailand
- f Department of Chemical Engineering, Faculty of Engineering, Chulalongkorn University, Bangkok 10330, Thailand
- ^g Center of Innovative Nanotechnology, Chulalongkorn University, Bangkok 10330, Thailand

ARTICLE INFO

Article history: Received 16 November 2010 In final form 21 March 2011

ABSTRACT

In order to explain the solubility of carbon nanotubes (CNT), including single walled CNTs, wrapped with chitosan of a 60% degree of deacetylation, MD simulations were applied to represent three chitosan concentrations, using two pristine CNTs (pCNT-pCNT), and one and two CNTs wrapped (pCNT-cwCNT and cwCNT-cwCNT). The CNT aggregation was observed in pCNT-pCNT and pCNT-cwCNT due to van der Waals interactions between tube-tube aromatic rings, and inter-CNT bridging by chitosan, respectively. At higher chitosan concentrations, such that most to all of CNTs were wrapped with chitosan, charge-charge repulsion was found to separate robustly the cwCNTs and lead to a well dispersed solution.

© 2011 Elsevier B.V. All rights reserved.

1. Introduction

Since the discovery of carbon nanotubes (CNTs) by Iijima in 1991 [1], they have been widely studied, with the different properties of single walled (SWCNT), double walled and multiple walled CNTs being characterized, and gained a great number of applications, such as in electronic circuits (especially SWCNTs), nanocomposites, sensor devices, smart textiles and drug delivery systems. However, CNTs are poorly solvated in any solvent but rather they tend to aggregate due to the van der Waals' interactions between the CNTs. Therefore, surface modification of CNTs is required to overcome this vital problem. Both covalent and noncovalent surface modifications have been shown to be effective approaches and provide a wide variety of functional groups on the surface of CNTs, improving the dispersion efficiency and the stability of modified CNTs in aqueous solution [2,3]. Whilst covalent modifications may be unsuitable for SWCNT due to the creation of 'holes' in the wall, noncovalent surface modification has been found to be an effective way to preserve the integrity of SWCNTs and in particular their electronic properties [4]. However, to accelerate the optimal

E-mail address: supot.h@chula.ac.th (S. Hannongbua).

development and application of CNTs, it is required to understand at the molecular level how polysaccharide biopolymers, such as chitosan, can provide a high dispersion efficiency and stability of CNTs in aqueous solution through wrapping on the outer surface of the CNTs including SWCNTs [5].

Surfactants, as sodium dodecylsulfate or sodium benzoylsulfonate [6,7], polyelectrolytes, such as polystyrene sulfonate, polydiallyldimethyl ammonium chloride and polyethyleneimine [8–10], and even biopolymers, as chitosan [11,12], gelatin [13] and gum arabic [14], have been successfully used as dispersing agents to increase the solubility of CNTs through noncovalent interactions. The wrapping phenomenon of modified CNTs (including SWCNTs) with various polymers has frequently been proposed in both theoretical and experimental works [15,16]. Such wrapping polymers include synthetic polymers, such as poly(*m*-phenylenevinylene-*co*-2,5-dioctyloxy-*p*-phenylenevinylene) (PPV) [15] and poly(*p*-phenylenevinylene) (PPV) [17], as well as natural polymers, such as the polysaccharides amylase [18], alginate [19] and chitosan [20].

Since chitosan presents a good biocompatibility, is readily available and is a relatively cheap and renewable resource, it has been widely used to improve SWCNT dispersion in electrochemical electrodes, the manufacture of biosensors and drug delivery applications [21–23]. Recently, lamsamai et al. reported that chitosan with a 61% degree of deacetylation (DD) is more favorably adsorbed onto the surface of CNTs than that of 93% DD chitosan,

^{*} Corresponding author at: Computational Chemistry Unit Cell, Department of Chemistry, Faculty of Science, Chulalongkorn University, Bangkok 10330, Thailand. Fax: +66 22 187603.

possibly because of their cumulative hydrophobic parts [24]. In addition, CNTs wrapped with 61% DD chitosan (cwCNT) were found to be highly dispersed and remain stable at aqueous concentrations of more than 1 mM. However, no explanation at the molecular level for that behavior in aqueous solutions is currently available.

Molecular dynamics (MD) simulation is a specific tool for providing detailed theoretical information at the molecular level, and is especially relevant and useful for biological systems which are hard to access experimentally. As a testament to the suitability of MD approaches to biological systems, success has already been attained with evaluation of the interaction (loading and release) of anticancer drugs carried by CNT [25], as well as the ligand–enzyme interactions in viral influenza [26], human immunodeficiency virus type 1 (HIV-1) [27], severe acute respiratory syndrome coronavirus (SARS-coV) [28] and chikungunya virus (CHIKV) [29].

In the present report, MD simulation was applied to acquire detailed molecular information so as to try to understand and explain the solubility of the SWCNT wrapped with 60% DD chitosan (cwCNT) as a function of the bound chitosan: SWCNT ratio and concentration. There are three different theoretical chitosan concentrations, using two pristine SWCNTs (pCNT-pCNT), and one and two CNTs wrapped (pCNT-cwCNT) and (cwCNT-cwCNT) as representative model components from a very low to no chitosan concentration, a chitosan to SWCNT ratio and concentration such that \sim 50% of SWCNT molecules exist as cwCNT, and an excess of chitosan such that all SWCNT molecules are cwCNT, respectively. The results were extensively analyzed and discussed in terms of the displacement between two SWCNTs, tube–tube orientation and the solvation properties of chitosan fragments relative to those of pristine SWCNTs (pCNT-pCNT).

2. Materials and methods

The 60% DD chitosan and the (8,8) armchair SWCNTs with a diameter of 11 Å, chiral vectors n = 8 and m = 8, and 12 repeating units were constructed using the Material Studio 4.3 package. The 60%DD chitosan containing 12 p-glucosamine (GLS or G) and 8 N-acetyl-D-glucosamine (NAG or N) with the random symmetric sequence of GGNGNGNGNGNGNGNGNGNGNGNGW was used in this study. The three models, as shown in Figure 1, are (a) two pristine SWCNTs (pCNT-pCNT), (b) a pristine SWCNT - chitosan wrapped SWCNT (pCNT-cwCNT), and (c) two chitosan wrapped SWCNTs (cwCNT-cwCNT). Each model was solvated in an aqueous solution. To neutralize the pCNT-cwCNT and cwCNT-cwCNT systems, the chloride ions were added using the LEaP module of AMBER. The MD simulations were set up and carried out as previously reported [25]. The SWCNTs and chitosan were parameterized by AMBER03 [30] and GLYCAM06 [31] force fields, respectively. The SPC/E water model, with an octagonal box over 12 Å from the surface of the CNTs or chitosan-CNT complexes, was applied. Then the solvated box edges were set to 68.0, 80.4 and 91.6 Å in the pCNT-pCNT, pCNT-cwCNT and cwCNT-cwCNT systems, respectively. The simulations were calculated using the AMBER10 program package [32] with the NPT ensemble (constant number of atoms, pressure and temperature) at 1 atm and a time step of 2 fs. The SHAKE algorithm was applied to all bonds involving hydrogen atoms to constraint their motions. Periodic boundary conditions were applied and the cutoff function was set at 12 Å for nonbonded interactions with the particle mesh Ewald method. The whole system was heated from 10 to 300 K for 200 ps and equilibrated at 300 K for 5 ns. Finally, the production stage was performed until 20 ns and the structural coordinates were saved every 1 ps for analysis.

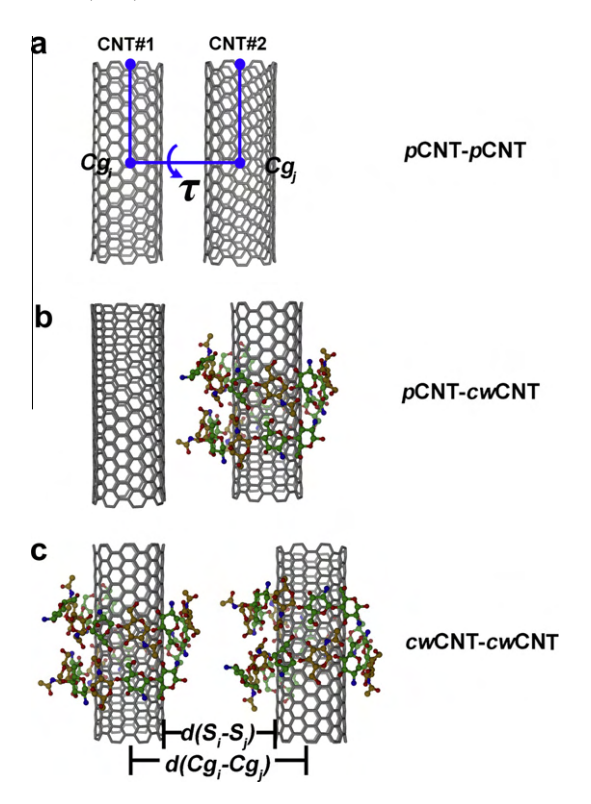


Figure 1. Schematic views of (a) two pristine SWCNTs (pCNT-pCNT), (b) pCNT-cwCNT and (c) cwCNT-cwCNT, where the SWCNT (labeled CNT in the figure) and the polymer used are the (8,8) armchair and 60% DD chitosan, respectively. The distances ($d(Cg_i-Cg_j)$) and ($d(S_i-S_j)$) and the torsion angle (τ) between the two SWCNTs were defined through the center of gravity (Cg) and the surface of each tube in which $\tau=0^\circ$ means the two tubes are parallel.

3. Results and discussion

3.1. Dispersion and solubility of SWCNTs

In order to understand the chitosan-assisted dispersion and separation of the SWCNTs in aqueous solution, the tube–tube displacement and orientation were monitored in terms of the distance from the center of gravity of the ith tube (Cg_i) to that of the jth tube (Cg_j), $d(Cg_i-Cg_j)$, and the torsion angle between the two SWCNTs' axis, τ , respectively, as defined in Figure 1. The calculated results are summarized in Figure 2.

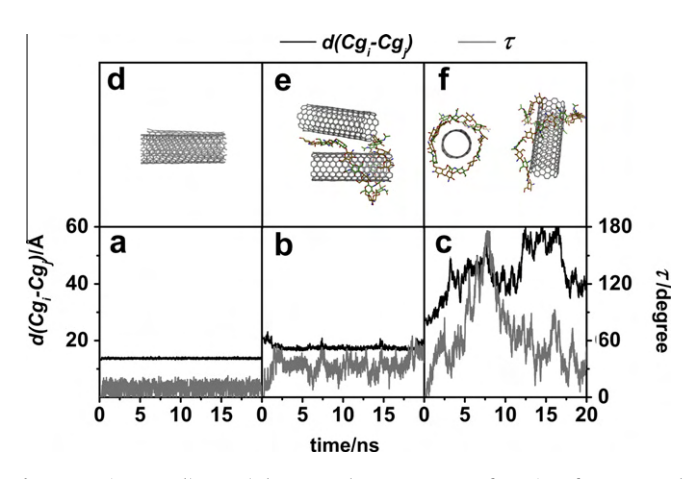


Figure 2. Distance, $d(Cg_i-Cg_j)$, between the two centers of gravity of SWCNT and torsion angle, τ (see Figure 1 for definition), as a function of the simulation time for the three systems, (a) pCNT-pCNT, (b) pCNT-cwCNT and (c) cwCNT-cwCNT, where their corresponding structures taken from the MD simulations are also shown (d–f).

With the no chitosan (or very low chitosan: CNT bound ratio) model system of pCNT-pCNT, the averaged tube–tube displacement represented by the distance between the tube centers of gravity, $d(Cg_i-Cg_j)$, was ~ 14 Å, which is equivalent to a distance between the tube surfaces, $d(S_i-S_j)$, of 3 Å (Figure 2a). In addition, the tilt angle designated by the torsion τ angle is $\sim 11^\circ$. These values are almost constant over the entire simulation period. The τ data indicated that the two pristine SWCNTs were oriented in an almost parallel configuration (Figure 2d), whilst the distance between the surfaces of the two SWCNTs ($d(S_i-S_j)=\sim 3$ Å) implied that the hydrophobic and van der Waals interactions between the aromatic rings of both CNTs played a role. This provides a clear answer as to why the pCNTs (and so by likely extrapolation, pCNTs in general) were found to aggregate experimentally in solution.

With an inadequate concentration of chitosan, such that a bound ratio of chitosan: CNT of \sim 1:2 was attained, represented by the model pCNT-cwCNT system in this MD simulation approach, the $d(Cg_i-Cg_j)$ was increased by \sim 3 Å (from 14 to 17 Å) and the tilt angle was increased from 11 to 33°, relative to the pCNT-pCNT system. Interestingly, one end of the chitosan was found to unwrap from the modified tube (CNT#2 in Figure 1b) and change its configuration to interact with the pCNT (CNT#1 in Figure 1b), *i.e.*, the chitosan rearranges its conformation to locate in between and interact with both SWCNTs (Figure 2e). Although the $d(Cg_i-Cg_j)$ distance of \sim 17 Å, with the corresponding $d(S_i-S_j)$ of \sim 6 Å, is rather long for molecular interactions between the two SWCNTs, the detected CNT#1-chitosan-CNT#2 configuration signifies that chitosan can act as the linker bridging the tubes together.

The situation is dramatically different for the model system where both SWCNTs were wrapped by chitosan (cwCNT-cwCNT), used to represent SWCNTs in a solution with a sufficiently high enough concentration of chitosan that almost all SWCNT molecules are wrapped (cwCNT). In this system the MD simulation revealed that the two cwCNTs were totally separate and freely rotating (Figure 2f), i.e., the noncovalent modified cwCNTs are highly soluble, supported by the $d(Cg_i-Cg_j)$ distance (\sim 35–60 Å) and the τ angle (\sim 60–180°), as seen in Figure 2c. The high dispersion and solubility levels of the two cwCNTs are mainly due to the strong repulsive interactions between the positively charged ammonium groups of the glucosamine units on each cwCNT.

3.2. Role of chitosan fragments

According to a previous study on chitosan-modified CNTs [24], the binding mechanism of chitosan wrapping on the outer surface of CNTs is thought to be due to the hydrophobic interactions between the acetyl groups of chitosan and the aromatic rings of the CNT. In order to provide detailed information at the molecular level so as to understand the mechanism of action, the atom–atom radial distribution function (RDF, $g_{xy}(r)$), that is the probability of finding a particle of type y within a sphere radius r around the particle of type x, were calculated. Here, x represents the nitrogen atoms of chitosan fragments (the N-acetyl-p-glucosamine (NAG), and p-glucosamine (GLS)), and y denotes all the carbon atoms of the wrapped SWCNTs (only the cwCNTs shown in Figure 1, CNT#2 for the pCNT-cwCNT and both CNT#1 and CNT#2 for the cwCNT-cwCNT) or the water oxygen atoms. The results are plotted and compared in Figure 3.

In the *p*CNT-*cw*CNT system (Figure 3a), the RDF plots from the *N* atom on the acetyl group of the NAG unit, N(NAG), and the ammonium group of the GLS unit, N(GLS), to all carbon atoms of the wrapped SWCNT show broad maxima at 5.2 Å (black line) and 5.7 Å (gray line) with high and low intensities, respectively. This means that the hydrophobic acetyl group of NAG can approach closer to and interact with the outer surface of the SWCNTs

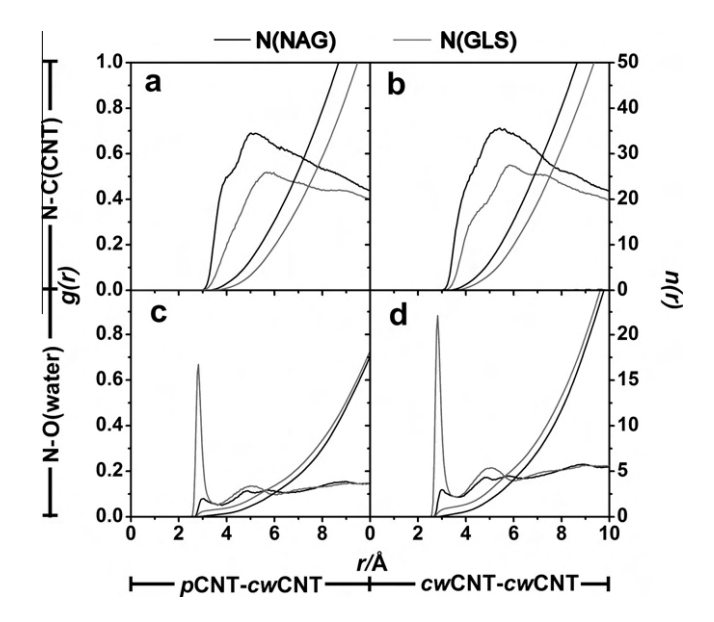


Figure 3. RDFs from the nitrogen atoms on the *N*-acetyl-p-glucosamine (N(NAG), black line) and p-glucosamine (N(GLS), gray line) of chitosan to the carbon atoms of the *cw*CNTs (a) CNT#2 for *p*CNT-*cw*CNT, (b) both CNT#1 and CNT#2 for *cw*CNT-*cw*CNT and the oxygen atoms of water for (c) *p*CNT-*cw*CNT and (d) *cw*CNT-*cw*CNT.

through van der Waals interactions than the hydrophilic ammonium group (GLS). Similarly for the *cw*CNT-*cw*CNT system (Figure 3b), the maximum RDF for the NAG (5.6 Å, black line) takes place at a shorter distance than that of the GLS (6.2 Å, gray line) with a higher density and coordination number. It is interesting that these N(NAG)-C(CNT) and N(GLS)-C(CNT) distances of the *cw*CNT-*cw*CNT system are longer than those of the *p*CNT-*cw*CNT system, respectively. This fact can be explained using the molecular configurations shown in Figure 2e and f, as that the chitosan in the highly soluble *cw*CNT-*cw*CNT system can be accessed by water molecules much more easily than in the aggregated *p*CNT-*cw*CNT system. This solvation effect then pulls the chitosan fragments in the *cw*CNT-*cw*CNT system out to a longer distance from the SWCNT outer surface than that of the *p*CNT-*cw*CNT one.

As expected for the both systems containing chitosan, the RDFs for the N(GLS) are much sharper with much higher density than those of the N(NAG) (gray and black lines, respectively, in Figure 3c and d). The corresponding running integration number, the number of water molecules at the distance r, around the neutral NAG is lower than that of the positively charged GLS at all distances. The corresponding coordination numbers, integrated to the first minima, of the N(NAG) and N(GLS) for both systems are 0.3 and 0.9 water molecules.

4. Conclusions

A MD simulation approach was applied to investigate the increase in dispersion and solubility of SWCNT when wrapped with 60% DD chitosan as the chitosan concentration is increased. The calculated distance between the centers of each SWCNT and the tube–tube orientation for the three modeled systems, pCNT–pCNT, pCNT–cwCNT and cwCNT–cwCNT, indicate the pCNT aggregates due to the hydrophobic and van der Waals interactions between the aromatic rings of the pCNTs. For the pCNT–cwCNT, the chitosan on the cwCNT#2 was found to act as a linker to bridge the pCNT#1 and cwCNT#2 together to aggregate. In contrast, in the high-concentration chitosan model (cwCNT–cwCNT) the two cwCNTs were totally separated, freely rotated and well dispersed in the aqueous solution owing to the charge–charge repulsive force of the ammo-

nium groups of GLS, with a fragment of the 60% DD chitosan wrapped on each tube. Interestingly, the hydrophobic acetyl group of the NAG fragment is likely to interact with the aromatic rings of the carbon nanotube via van der Waals interactions while the positively charged ammonium group of GLS fragment was strongly hydrated by water molecules.

Acknowledgments

This work was supported by the National Research University Project of CHE and Ratchadaphiseksomphot Endowment Fund (HR1155A) and the Thai Government Stimulus Package 2 (TKK2555), under the Project for Establishment of Comprehensive Center for Innovative Food, Health Products and Agriculture. T.R. thanks the postdoctoral fellowship from the Ratchadaphiseksomphot Endowment Fund from Chulalongkorn University, and the TRF Grant for New Research (Grant No. TRG5280035). C.I. thanks Thailand Graduate Institute of Science and Technology (TGIST Grant No. TG-55-09-50-059D), and The 90th Anniversary of Chulalongkorn University Fund (Ratchadaphiseksomphot Endowment Fund). The Center of Excellence for Petroleum, Petrochemicals and Advanced Materials, Chulalongkorn University is acknowledged.

References

- [1] S. Iijima, Nature (London) 354 (1991) 56.
- [2] J.L. Bahr, J.M. Tour, J. Mater. Chem. 12 (2002) 1952.
- [3] M.O. Lisunova, N.I. Lebovka, O.V. Melezhyk, Y.P. Boiko, J. Colloid Interface Sci. 299 (2006) 740.
- [4] Y.-L. Zhao, J.F. Stoddart, Acc. Chem. Res. 42 (2009) 1161.

- [5] Q. Yang, L. Shuai, X. Pan, Biomacromolecules 9 (2008) 3422.
- [6] V.C. Moore, M.S. Strano, E.H. Haroz, R.H. Hauge, R.E. Smalley, J. Schmidt, Y. Talmon, Nano Lett. 3 (2003) 1379.
- [7] J. Yu, N. Grossiord, C.E. Koning, J. Loos, Carbon 45 (2007) 618.
- [8] X. Hu, T. Wang, X. Qu, S. Dong, J. Phys. Chem. B 110 (2006) 853.
- [9] D.-Q. Yang, J.-F. Rochette, E. Sacher, J. Phys. Chem. B 109 (2005) 4481.
- [10] S. Zhan, Y. Li, J. Dispers. Sci. Technol. 29 (2008) 240.
- [11] T. Takahashi, C.R. Luculescu, K. Uchida, T. Ishii, H. Yajima, Chem. Lett. 34 (2005) 1516.
- [12] H. Yang, S.C. Wang, P. Mercier, D.L. Akins, Chem. Commun. (2006) 1425.
- [13] W. Zheng, Y.F. Zheng, Electrochem. Commun. 9 (2007) 1619.
- [14] R. Bandyopadhyaya, E. Nativ-Roth, O. Regev, R. Yerushalmi-Rozen, Nano Lett. 2 (2002) 25. [15] M. Yang, V. Koutsos, M. Zaiser, J. Phys. Chem. B 109 (2005) 10009. [16] S.S. Tallury, M.A. Pasquinelli, J. Phys. Chem. B 114 (2010) 4122.

- [17] W. Liu, C.-L. Yang, Y.-T. Zhu, M.-S. Wang, J. Phys. Chem. C 112 (2008) 1803.
- [18] Y.H. Xie, A.K. Soh, Mater. Lett. 59 (2005) 971. [19] Y. Liu, C. Chipot, X. Shao, W. Cai, J. Phys. Chem. B 114 (2010) 5783.
- [20] F. Peng, F. Pan, H. Sun, L. Lu, Z. Jiang, J. Memb. Sci. 300 (2007) 13.
- [21] J. Chen, G. Yang, M. Chen, W. Li, Russ. J. Electrochem. 45 (2009) 1287.
- [22] X. Zhang, L. Meng, Q. Lu, Z. Fei, P.J. Dyson, Biomaterials 30 (2009) 6041.
 [23] G. Zhao, X. Zhan, Electrochim. Acta 55 (2010) 2466.
- [24] C. Iamsamai, S. Hannongbua, U. Ruktanonchai, A. Soottitantawat, S.T. Dubas, Carbon 48 (2010) 25.
- [25] U. Arsawang, O. Saengsawang, T. Rungrotmongkol, P. Sornmee, T. Remsungnen, S. Hannongbua, J. Mol. Graph. Model. 29 (2011) 591.
- T. Rungrotmongkol et al., Biochem. Biophys. Res. Commun. 385 (2009) 390.
- [27] T. Rungrotmongkol, A.J. Mulholland, S. Hannongbua, J. Mol. Graph. Model. 26 (2007) 1.
- [28] V. Nukoolkarn, V.S. Lee, M. Malaisree, O. Aruksakulwong, S. Hannongbua, J. Theor. Biol. 254 (2008) 861.
- [29] T. Rungrotmongkol, N. Nunthaboot, M. Malaisree, N. Kaiyawet, P. Intharathep, A. Meepraset, S. Hannongbua, J. Mol. Graph. Model. 29 (2010) 347. [30] Y. Duan et al., J. Comput. Chem. 24 (2003) 1999.
- [31] M.B. Tessier, M.L. DeMarco, A.B. Yongye, R.J. Woods, Mol. Simul. 34 (2008) 349.
- [32] D.A. Case et al., AMBER 10, San Francisco, 2008.

Concerns, recent outbreak and molecular insight into H5N1 and pandemic H1N1-2009 influenza A viruses

T. Rungrotmongkol^{1,2}, M. Malaisree¹, P. Intharathep¹, P. Decha¹, N. Nunthaboot³, C. Laohpongspaisan¹, O. Aruksakunwong¹, T. Udommaneethanakit¹, S. Sompornpisut¹ and S. Hannongbua^{1,C}

¹Computational Chemistry Unit Cell, Chulalongkorn University, Bangkok, 10330, Thailand ²Center of Innovative Nanotechnology, Chulalongkorn University, Bangkok, 10330, Thailand ³Department of Chemistry, Faculty of Science, Mahasarakham University, Mahasarakham, Thailand ^CE-mail: supot.h@chula.ac.th; Tel. 02-2187603

ABSTRACT

This study aims at gaining insight into molecular details at Neuraminidase (NA), Hemagglutinin (HA) and M2 protein channel of viral influenza A H5N1 and H1N1-2009. In NA, interest is focused on drug's inhibitory activity against the wild-type and mutated N1 strains. The H1N1-2009 virus was predicted to be susceptible to oseltamivir, with all important interactions being well conserved. Loss of drug-target interaction energies especially in terms of electrostatic contributions and hydrogen-bonds were established in the probable E119V and R292K. For both viruses, the known H274Y mutation conferred the high oseltamivir-resistance with decreased hydrophobicity, pocket size and vdW interactions at the bulky group. Instead, N294S was found to demonstrate medium drugresistant level. In addition, combinatorial chemistry was used to find potent NA inhibitors based on the oseltamivir and pyrrolidine scaffolds. In HA target, the low and high pathogenic forms (HPH5 and LPH5) were carried out using MD simulations, aimed at understanding why HPH5 was experimentally observed to be 5-fold better cleaved by furin. The HPH5's cleavage loop was found to fit well and bind strongly into the catalytic site of human furin, serving as a conformation suitable for acylation process. Then, the HPH5furin complex was used as the starting structure for mechanistic investigation by QM/MM method. The energy profile shows a concerted reaction of the first step of acylation, known as the proton transfer and nucleophilic attack with a formation of tetrahedral intermediate. Investigation was also extended to the M2 proton channel with/without adamantane bound in many protonation states of selective filter residue His37, corresponding to channel conformations. Two mechanisms of drug inhibiting the M2 functions are: (i) drug facilitating the His37's imidazole to lie in close conformation and (ii) acting as blocker at extracellular site. Loss of drug-M2 interactions was found to be a primary source of resistance in the single mutants of H5N1, and H1N1-2009 containing the S31N mutation.

REFERENCES

- 1. Rungrotmongkol, T.; Malaisree, M.; Nunthaboot, N.; Sompornpisut, P.; and Hannongbua, S. *Amino Acids*, 2010, DOI 10.1007/s00726-009-0452-3.
- 2. Rungrotmongkol, T.; Intharathep, P.; Malaisree, M.; Nunthaboot, N.; Kaiyawet, N.; Sompornpisut, P.; Payungporn, S.; Poovorawan, Y.; and Hannongbua, S. *Biochem. Biophys Res. Commun.*, 2009, 385(3), 390-394.
- 3. Rungrotmongkol, T.; Frecer, V.; De-Eknamkul, W.; Hannongbua, S., and Miertus, S. *Antivir. Res.*, 2009, 82(1), 51-8.
- 4. Rungrotmongkol, T., Decha, P., Sompornpisut, P., Malaisree, M., Intharathep, P., Nunthaboot, N., Udommaneethanakit, T., Aruksakunwong, O., and Hannongbua, S., *PROTEINs*, 2009, 76, 62-71.

Computational Enzymology, Drug Discovery and Drug Delivery System: A Case Study of Influenza Virus and Cancer Therapy

Thanyada Rungrotmongkol

Computational Chemistry Unit Cell, Department of Chemistry, Faculty of Science,

Chulalongkorn University, Bangkok, 10330, Thailand

Center of Innovative Nanotechnology, Chulalongkorn University, Bangkok, 10330, Thailand

(t.rungrotmongkol@gmail.com)

This study aims at gaining insight into molecular details at neuraminidase (NA) and M2-protein of viral influenza A H5N1 and H1N1-2009. On NA, interest is focused on drug's inhibitory activity against the wild-type and mutated N1 strains using molecular dynamics (MD) simulation, and design of NA inhibitors through combinatorial chemistry approach. The H1N1-2009 virus was predicted to be susceptible to oseltamivir, with all important interactions being well conserved [1]. For both viruses, the known H274Y mutation conferred the high oseltamivir-resistance with decreased hydrophobicity, pocket size and vdW interactions at the bulky group. Combinatorial chemistry was used to find potent NA inhibitors based on the oseltamivir and pyrrolidine scaffolds [2]. Based on 3D-RISM theory, the distribution of water and hydronium ion in M2 channel was predicted [3]. The results of potential of mean force and distribution showed that the tri-protonated state of protein is likely to be the most active conformation in implication of enzymatic functions on proton-transfer through M2 pore.

References

- [1] T. Rungrotmongkol, M. Malaisree, N. Nunthaboot, P. Sompornpisut and S. Hannongbua, Amino Acids, **39** (2010) 393.
- [2] T. Rungrotmongkol, V. Frecer, W. De-Eknamkul, S. Hannongbua and S. Miertus, Antivir. Res., 82 (2009) 51.
- [3] S. Phongphanphanee, T. Rungrotmongkol, N. Yoshida, S. Hannongbua and F. Hirata, J. Am. Chem. Soc., **132** (2010) 9782.

The Inaugural CU-IMS Joint Symposium, Chulalongkorn University, Bangkok, Thailand, October 19-21, 2010.

Computational Studies on Influenza A Virus Subtypes H5N1 and Pandemic H1N1

Thanyada Rungrotmongkol

Computational Chemistry Unit Cell, Department of Chemistry, Faculty of Science, Chulalongkorn University, Bangkok, 10330, Thailand Center of Innovative Nanotechnology, Chulalongkorn University, Bangkok, 10330, Thailand (t.rungrotmongkol@gmail.com)

Computational approach is a specific tool for providing detailed theoretical information at the molecular level, and is especially relevant and useful for biological systems which are hard to access experimentally. The influenza virus has been a major health problem for humanity since the first pandemic of Spanish flu in 1918. Recently, the outbreak of avian influenza virus subtype H5N1 has caused illness in several animals including human infections, while the subsequent appearance of the novel pandemic in 2009 caused by the new strain of influenza virus subtype H1N1, has become the first pandemic of the 21st century. Here, molecular dynamics (MD) simulation has been used to reveal the ligand-enzyme interactions and source of drug resistance in neuraminidase (NA), hemagglutinin (HA) and M2-channel of the influenza H5N1 and pandemic H1N1 viruses. The combinatorial chemistry was applied to design new potent NA inhibitors against the H5N1 virus using the oseltamivir and pyrrolidine scaffolds. Combined quantum mechanical/molecular mechanical (QM/MM) methods make possible the modelling of chemical reactions in large systems such as enzymes. The mechanistic reaction on highly pathogenic hemagglutinin cleaved by furin, a serine protease in host cell, was investigated by QM/MM. Three-dimensional reference interaction site model (3D-RISM) was performed on the M2-channel at different pH conditions explaining its enzymatic function on proton transports through the M2 pore.

Dr. Thanyada Rungrotmongkol

PERSONAL DETAILS

Current position: Researcher

Current institution & address:

Center of Innovative Nanotechnology, and Computational Chemistry Unit Cell, Department of Chemistry, Faculty of Science,

Chulalongkorn University,

254 Phayathai Rd., Patumwan, Bangkok, 10330, Thailand

Birth: January 14 1979, Ratchaburi, Thailand

Gender: Female
Nationality: Thai
Country: Thailand
Age: 32

Affiliation: Chulalongkorn University

Phone Number: +66-2218-7602 Fax Number: +66-2218-7603

E-mail address: <u>t.rungrotmongkol@gmail.com</u>

EDUCATION

Kasetsart University, Bangkok, Thailand

• Ph.D. in Physical Chemistry

2006

The Royal Golden Jubilee Ph.D. Program, Thailand Research Fund, Thailand

■ B.Sc. in Chemistry (with First Class Honors)

2001

The Development and Promotion of Science and Technology talents project of Thailand (DPST)

ACADEMICAL EXPERIENCE

Researcher (2009-present)

Center of Innovative Nanotechnology, Chulalongkorn University, Bangkok, Thailand

Postdoctoral fellow (2006-present)

Computational Chemistry Unit Cell, Department of Chemistry, Faculty of Sciences, Chulalongkorn University, Bangkok, Thailand

International expert and Consultant (2008-2009)

International Centre for Science and High Technology, United Nations Industrial Development Organization (ICS-UNIDO), Trieste, Italy

COOPERATION ABROAD

Professor Dr. Adrian J. Mulholland

School of Chemistry, University of Bristol, Bristol BS8 1TS, UK

Professor Dr. Stanislav Miertus

Area of Pure and Applied Chemistry, ICS-UNIDO, AREA Science Park, Padriciano 99, Trieste 34012, Italy

Professor Dr. Fumio Hirata

Department of Theoretical and Computational Molecular Science, Division of Theoretical Molecular Science II, Institute of Molecular Science, Okazaki, Japan

Professor Dr. Karl Peter Wolschann

Institute of Theoretical Chemistry, University of Vienna, Wahringer Strasse, 17 A-1090 Vienna, Austria

SCHOLARSHIPS, GRANTS AND FUNDING:

RESEARCH GRANTS

2011	Ratchadaphiseksomphot Endowment Fund, Chulalongkorn University, Thailand
	(Postdoctoral Research Fund, 2 years: January 2011-present)
2010	Ratchadaphiseksomphot Endowment Fund, Chulalongkorn University, Thailand
	(Postdoctoral Research Fund, 1 year: December 2009-November 2010)
2009	TRF Grant for New Researcher, Thailand Research Fund, Thailand
	(2 years: March 2009-present)
2007	Postdoctoral Research Fund, Commission on Higher Education. Thailand
	(Postdoctoral Research Fund, 2 years: January2007-December2008)

SCHOLARSHIPS FOR SHORT TERM VISIT

2011	Institute for Molecular Science (IMS), Okazaki Japan
	(JENESYS fellowship, 1.5 month: May-June 2011)
2011	Institute of Theoretical Chemistry, University of Vienna, Vienna, Austria
	(OEAD and university scholarships, 3 months: January-March 2011)
2010	Institute of Theoretical Chemistry, University of Vienna, Vienna, Austria
	(ASEA-UNINET scholarship, 1 month: August-September 2010)
2010	Institute for Molecular Science (IMS). Okazaki, Japan
	(Research grant, 1.5 month: February-March 2010)
2009	International Centre for Science and High Technology, United Nations Industrial
	Development Organization (ICS-UNIDO), Trieste, Italy
	(6 months: May-October 2009)
2009	Institute for Molecular Science (IMS), Okazaki Japan
	(JENESYS fellowship (JSPS), 2 months: February-March 2009)
2008	International Centre for Science and High Technology, United Nations Industrial
	Development Organization (ICS-UNIDO), Trieste, Italy
	(6 months: May-October 2008)
2007	International Centre for Science and High Technology, United Nations Industrial
	Development Organization (ICS-UNIDO), Trieste, Italy
	(Fellowship, 10 months: March-December 2007)

AWARDS

- 1. Oral presentation award of The Royal Golden Jubilee Ph.D. Congress VI. Thailand (2005)
- 2. Poster presentation award from Development and Promotion of Science and Technology talents project of Thailand (DPST). (2000)

RESEARCH INTERESTS

- The structural information and drug-target interactions in four drug targets of life cycle of avian influenza subtype H5N1: hemaglutinin, neuraminidase, M2 integral membrane protein (M2-ion channel), and polymerases PA and PB1
- Rotational drug designs against influenza A neuraminidase subtype H5N1
- Reaction mechanism of enzymatic reaction: acylation process of hemagglutinin subtype H5 by serine protease
- Chikungunya and venezuelan equine encephalitis viruses
- Dengue serine protease

- Cancer
- Drug delivery and development through carbon nanotube serving as the drug carrier
- Hepatitis C virus (HCV): NS3/4A, NS5A and NS5B targets

INVITED LECTURER

QM/MM (Quantum & Molecular Mechanics)/(P&A)*, BIF 632 การออกแบบและการกันหายาใหม่ (Drug Design & Discovery) 3 credits (3-0-9), Bioinformatics & Systems Biology Program, KMUTT, December 22, **2010**

PUBLICATIONS

- 1. **T. Rungrotmongkol**, S. Hannongbua* and A. J. Mulholland, Mechanistic study of HIV-1 reverse transcriptase at the active site based on QM/MM method, *Journal of Theoretical and Computational Chemistry* **2004**; 3(4): 491-500. (**IF2009** = **0.958**)
- 2. **T. Rungrotmongkol**, A. J. Mulholland and S. Hannongbua*, Active site dynamics and combined quantum mechanics/molecular mechanics (QM/MM) modelling of a HIV-1 reverse transcriptase/DNA/dTTP complex, *Journal of molecular graphics and modelling* **2007**; 26(1): 1-13. (**IF2009** = **2.169**)
- 3. M. Malaisree, **T. Rungrotmongkol**, P. Decha, P. Intharathep, O. Aruksakunwong, and S. Hannongbua*, Understanding of known drug-target interactions in the catalytic pocket of neuraminidase subtype N1, *Proteins: Structure, Function, and Bioinformatics* **2008**; 71(4): 1908-1918. **(IF2009 = 3.085)**
- 4. P. Decha, **T. Rungrotmongkol**, P. Intharathep, M. Malaisree, O. Aruksakunwong, C. Laohpongspaisan, V. Parasuk, P.Sompornpisut, S. Pianwanit, S. Kokpol and S. Hannongbua*, Source of high pathogenicity of an avian influenza virus H5N1: Why H5 is better cleaved by furin, *Biophysical Journal* **2008**; 95(1): 128-134. **(IF2009 = 4.390)**
- 5. P. Intharathep, C. Laohpongspaisan, **T. Rungrotmongkol**, A. Loisruangsin, M. Malaisree, P. Decha, O. Aruksakunwong, K. Chuenpennit, N. Kaiyawet, P. Sompornpisut, S. Pianwanit, and S. Hannongbua*, How amantadine and rimantadine inhibit proton transport in the M2 protein channel, *Journal of molecular graphics and modelling* **2008**; 27(3): 342-348. (**IF2009** = **2.169**)
- 6. V. Nukoolkarn, S. Saen-oon, **T. Rungrotmongkol**, S. Hannongbua, K. Ingkaninan, K. Suwanborirux*, Petrosamine, a potent anticholinesterase pyridoacridine alkaloid from a Thai marine sponge Petrosia n. sp., *Bioorganic & Medicinal Chemistry* **2008**; 16(13): 6560-6567. (**IF2009** = **2.822**)
- 7. **T. Rungrotmongkol**, P. Decha, M. Malaisree, P. Sompornpisut, and S. Hannongbua*, Comment on "Cleavage mechanism of the H5N1 hemagglutinin by trypsin and furin" [Amino Acids 2008, January 31, Doi: 10.1007=s00726-007-0611-3], *Amino Acids* 2008; 35: 511-512. (**IF2009** = 3.877)
- 8. M. Malaisree, **T. Rungrotmongkol**, N. Nunthaboot, O. Aruksakunwong, P. Intharathep, P. Decha, P. Sompornpisut and S. Hannongbua*, Source of Oseltamivir Resistance in Avian Influenza H5N1 Virus with the H274Y Mutation. *Amino Acids* **2009**; 37(4):725–732. **(IF2009 = 3.877)**
- 9. **T. Rungrotmongkol**, P. Decha, P. Sompornpisut, M. Malaisree, P. Intharathep, N. Nunthaboot, T. Udommaneethanakit, O. Aruksakunwong, and S. Hannongbua*, Combined QM/MM mechanistic study of the acylation process in furin complexed with the H5N1 avian influenza virus hemagglutinin's cleavage site. *Proteins: Structure, Function, and Bioinformatics* **2009**; 76(1): 62-71. (**IF2009** = **3.085**)

- 10. C. Laohpongspaisan, **T. Rungrotmongkol**, P. Intharathep, M. Malaisree, P. Decha, O. Aruksakunwong, P. Sompornpisut, S. Hannongbua*, Why amantadine loses its function in influenza M2 mutants: MD simulations. *Journal of Chemical Information and Modeling* **2009**; 49(4):847-52. **(IF2009 = 3.882)**
- 11. **T. Rungrotmongkol**, M. Malaisree, T. Udommaneethanakit and S. Hannongbua*, Comment on "Another look at the molecular mechanism of the resistance of H5N1 influenza A virus neuraminidase (NA) to oseltamivir (OTV)" *Biophysical Chemistry* **2009**; 141: 131-132. **(IF2009 = 2.276)**
- 12. **T. Rungrotmongkol**, V. Frecer, W. De-Eknamkul, S. Hannongbua, and S. Miertus*, Design and in silico screening of combinatorial library of oseltamivir analogs inhibiting neuraminidase of avian influenza virus H5N1. *Antiviral Research* **2009**; 82(1):51-8. (**IF2009** = **3.612**)
- 13. **T. Rungrotmongkol**, P. Intharathep, M. Malaisree, N. Nunthaboot, N. Kaiyawet, P. Sompornpisut, S. Payungporn, Y. Poovorawan, and S. Hannongbua*, Susceptibility of antiviral drugs against 2009 influenza A (H1N1) virus. *Biochemical and Biophysical Research Communications* **2009**; 385(3):390-4. (**IF2009** = **2.548**)
- 14. **T. Rungrotmongkol**, T. Udommaneethanakit, M. Malaisree, N. Nunthaboot, P. Intharathep, P. Sompornpisut and S. Hannongbua*, How does each substituent functional group of oseltamivir lose its activity against virulent H5N1 influenza mutants? *Biophysical Chemistry* **2009**; 145(1):29–36. **(IF2009** = **2.276)**
- 15. T. Udommaneethanakit, **T. Rungrotmongkol**, U. Bren, V. Frecer and S. Miertus*, Dynamic Behavior of Avian Influenza A Virus Neuraminidase Subtype H5N1 in Complex with Oseltamivir, Zanamivir, Peramivir, and their Phosphonate Analogues, *Journal of Chemical Information and Modeling* **2009**; 49:2323–2332. (**IF2009** = **3.882**)
- 16. **T. Rungrotmongkol**, T. Udommaneethanakit, V. Frecer, and S. Miertus, Combinatorial design of avian influenza neuraminidase inhibitors containing pyrrolidine core with a reduced susceptibility to viral drug resistance, *Combinatorial Chemistry & High Throughput Screening* **2010**; 13(3):268-77. **(IF2009 = 2.464)**
- 17. **T. Rungrotmongkol**, M. Malaisree, N. Nunthaboot, P. Sompornpisut, and S. Hannongbua*, Molecular prediction of oseltamivir efficiency against probable influenza A (H1N1-2009) mutants: Molecular modelling approach, *Amino Acids* **2010**; 39(2):393-398. (**IF2009** = **3.877**)
- 18. N. Nunthaboot, **T. Rungrotmongkol**, M. Malaisree, P. Decha, N. Kaiyawet, P. Intharathep, P. Sompornpisut, Y. Poovorawan and S. Hannongbua*, Molecular insights into human receptor binding to 2009 H1N1 influenza A hemagglutinin, *Monatshefte fur Chemie Chemical Monthly* **2010**; 141(7):801-807. (**IF2009 = 1.312**)
- 19. P. Intharathep, **T. Rungrotmongkol**, P. Decha, N. Nunthaboot, N. Kaiyawet, T. Kerdcharoen, P. Sompornpisut, and S. Hannongbua*, Evaluating how rimantadines control the proton gating of the Influenza A M2-proton port via allosteric binding outside of the M2-channel: MD simulations, *Journal of Enzyme Inhibition and Medicinal Chemistry* **2011**; 26(2):162-168. (**IF2009 = 1.496**)

- 20. S. Phongphanphanee, **T. Rungrotmongkol**, N. Yoshida, S. Hannongbua, F. Hirata*, Proton transport through the influenza A M2 channel: 3D-RISM study, *Journal of American Chemical Society* **2010**;132(28):9782-9788. **(IF2009 = 8.580)**
- 21. N. Nunthaboot, **T. Rungrotmongkol**, M. Malaisree, N. Kaiyawet, P. Decha, P. Sompornpisut, and S. Hannongbua*, Evolution of the human-receptor binding affinity of influenza A (H1N1) 2009 pandemic hemagglutinin from 1918- and 1930-H1N1 influenza viruses *Journal of Chemical Information and Modeling* **2010**;50:1410-1417. (**IF2009** = **3.882**)
- 22. **T. Rungrotmongkol***, N. Nunthaboot, M. Malaisree, N. Kaiyawet, P. Intharathep, A. Meepraset and S. Hannongbua, Molecular Insight into the Specific Binding of ADP-ribose to the nsP3 Macro Domains of Chikungunya and Venezuelan Equine Encephalitis Viruses: Molecular Dynamics Simulations and Free Energy Calculations *Journal of molecular graphics and modelling* **2010**;29:347–353. (**IF2009 = 2.169**)
- 23. P. Sornmee, **T. Rungrotmongkol**, O. Saengsawang, U. Arsawang, T. Remsungnen and S. Hannongbua*, Understanding of molecular properties of the doxorubicin anticancer drug filling inside and wrapping outside the single-walled carbon nanotube *Journal of Computational and Theoretical Nanosciencs* **2011**; in press. (**IF2009 = 0.899**)
- 24. U. Arsawang, O. Saengsawang, **T. Rungrotmongkol**, P. Sornmee, T. Remsungnen and S. Hannongbua*, How do carbon nanotubes serve as carriers for gemcitabine transport in drug delivery system? *Journal of molecular graphics and modelling* **2011**;29:591–596. (**IF2009** = **2.169**)
- 25. **T. Rungrotmongkol**, U. Arsawang, C. Iamsamai, A. Vongachariya, S. Dubas, U. Ruktanonchai, A. Soottitantawat and S. Hannongbua*, Increase in dispersion and solubility of carbon nanotubes noncovalently modified by chitosan-polysaccharide biopolymer: MD simulations, *Chemical Physics Letter* **2011**;507:134–137. (**IF =2.291**).
- 26. **T. Rungrotmongkol**, P. Yotmanee, N. Nunthaboot and S. Hannongbua*, Computational studies of influenza A virus at three important targets: hemagglutinin, neuraminidase and M2 protein, *Current Pharmaceutical Design* **2011**;17:1720-1739. (**IF2009** = **4.414**)
- 27. N. Kaiyawet, **T. Rungrotmongkol** and S. Hannongbua*, Identification of the probable novel strains of high pathogenic influenza A H5N1 virus in human, **Submitted**.
- 28. A. Vongachariya, C. Iamsamai, O. Saengsawang, **T. Rungrotmongkol**, S. Dubas, V. Parasuk and S. Hannongbua*, On the effect of surface curvature of carbon nanotube on its cation- π interaction with monovalent cations, **Submitted**.
- 29. P. Kongsune, **T. Rungrotmongkol**, N. Nunthaboot, P. Yotmanee, P. Sompornpisut, Y. Poovorawan, P. Wolschann and S. Hannongbua, Molecular insights into the binding affinity and specificity of high pathogenic H5N1 hemagglutinin cleavage loop toward proprotein convertase furin **Submitted.**
- 30. W. Khuntawee, **T. Rungrotmongkol*** and S. Hannongbua. Molecular dynamic behavior and binding affinity of cyciln dependent kinase 6/Vcyclin and flavonoid analogues **Submitted.**
- 31. P. Yotmanee, T. Rungrotmongkol, K. Wichapong, R. Roslim, H.A. Wahab, P. Sompornpisut, S. Hannongbua, Insight into Polypeptide Substrates of Dengue virus Type 2 Cleaved by its NS2B-NS3(Pro) Serine Protease: Molecular Dynamics Simulations. **In preparation.**

BOOK, PROCEEDING AND MEETING ABSTRACT

- 1. **T. Rungrotmongkol**, M. Malaisree, P. Decha, C. Laohppongspaisan, O. Aruksakunwong, P. Intharathep, S. Pianwanit, P. Sompornpisutl, V. Parasuk, E. Megnassan, V. Frecer, S. Miertus, S. Hannongbua, Understanding of drug-target interactions: a case study in influenza virus A subtype H5N1. AIP Conference Proceedings **2007**, 963 (Computation in Modern Science and Engineering, Volume 2, Part B), 913-916.
- 2. **T. Rungrotmongkol**, M. Malaisree, P. Decha, P. Intharathep, O. Aruksakunwong, S.Pianwanit, V. Parasuk, S. Hannongbua, Susceptibility and drug-resistance of highly pathogenic A H5N1 to the neuraminidase inhibitors: molecular dynamics simulations. FEBS Journal **2007**, 274 (32nd Congress of the Federation-of-European-Biochemical-Societies (FEBS) Vienna, AUSTRIA, July 07-12, 2007), 365-365.
- 3. **T. Rungrotmongkol**, T. Udommaneethanakit, V. Frecer, S. Hannongbua, S. Miertus, Combinatorial drug designs and drug-target interactions in neuraminidase of avian influenza virus subtype H5N1. Book of selected papers of invited experts, ICS-UNIDO International Conference, **2009**, 91-103.
- 4. N. Yoshida, Y. Kiyota, **T. Rungrotmongkol**, S. Phongphanphanee, T. Imai, F. Hirata, Statistical-Mechanics Theory of Molecular Recognition: Water and Other Molecules Recognized by Protein, in Bihan and Fukuyama(Ed.): "Water, the forgotten biological molecule.", Chapter 4, (Pan Stanford Publishing, **2010**)

INTERNATIONAL CONFERENCES AND PRESENTATIONS:

ORAL PRESENTATIONS:

- 1. T. Rungrotmongkol, A. J. Mulholland and S. Hannongbua. Modelling the enzymatic reaction of HIV-1 RT based on combined QM/MM approach. Workshop on Modeling Interactions in Biomolecules II, Czech University of Agriculture, Prague, Czech, September 5-9 **2005**.
- 2. T. Rungrotmongkol, P. Decha, M. Malaisree, C. Laohpongspaisan, O. Aruksakunwong, P. Intharathep, S. Pianwanit, P. Sompornpisut, V. Parasuk, E. Megnassan, V. Frecer, S. Miertus and S. Hannongbua. Influenza Virus A Subtype H5N1: Structural basis, Drug-Target Interactions and Molecular properties. Pure and Applied Chemistry International Conference (PACCON), Bangkok, Thailand, January 31-Febuary 1 2008.
- 3. T. Rungrotmongkol, M. Malaisree, P. Intharathep, P. Decha, N. Nunthaboot, C. Laohpongspaisan, O. Aruksakunwong, T. Udommaneethanakit, S. Sompornpisut and S. Hannongbua. Concerns, recent outbreak and molecular insight into H5N1 and pandemic H1N1-2009 influenza A viruses. 14th International Annual Symposium on Computational Science and Engineering, Mae Fah Luang University, Chiang Rai, Thailand, March 23-26, **2010**. (*Invited speaker*)
- 4. T. Rungrotmongkol, N. Nunthaboot, P. Intharathep, M. Malaisree, N. Kaiyawet, P. Sompornpisut and S. Hannongbua, Computational studies on H5N1 and pandemic H1N1 influenza A viruses, The 3rd National Seminar on Computer-Aided Drug Design: Virtual Screening, Gurney Hotel, Penang, Malaysia, December 2-3, **2010**. (*Invited speaker*)

POSTER PRESENTATIONS:

1. T. Rungrotmongkol and S. Hannongbua. Structural Calculations of Dihydrofolate Reductase Inhibitor, Cycloguanil. The International Conference on Bioinformatics 2002: North-South Networking (INCOB 2002), Le Royal Meridien, Bangkok, Thailand, February 6-8 **2002**.

- 2. T. Rungrotmongkol, A. J. Mulholland and S. Hannongbua. Modelling the structure and mechanism of HIV-1 reverse transcriptase. MGMS Young Modellers' Forum in Conjunction with the RSC MMG, London, U.K., December 1 2003.
- 3. T. Rungrotmongkol, A. J. Mulholland and S. Hannongbua. Mechanistic study of HIV-1 Reverse Transcriptase at the active site based on QM/MM method. 1st Asian Pacific Conference on Theoretical and Computational Chemistry (APCTCC1), Institute for Molecular Science (IMS), Okazaki, Japan, May 12-15 **2004**.
- 4. T. Rungrotmongkol, A. J. Mulholland and S. Hannongbua. Molecular mechanics and combined quantum mechanical and molecular mechanical (QM/MM) simulations on enzymatic reaction of HIV-1 RT active. 2nd Asian Pacific Conference on Theoretical and Computational Chemistry (APCTCC2), Chulalongkorn University, Bangkok, Thailand, May 2-6 **2005**.
- 5. T. Rungrotmongkol, M. Malaisree, P. Decha, C. Laohpongspaisan, O. Aruksakunwong, P. Intharathep, S. Pianwanit, P. Sompornpisut, V. Parasuk, E. Megnassan, V. Frecer, S. Miertus and S. Hannongbua. Structural Information and Drug-Target Interaction of Influenza Virus A Subtype H5N1. Bangkok International Conference on Avian Influenza 2008: Integration from Knowledge to Control. Bangkok, Thailand, January 23-25 **2008**.
- 6. T. Udommaneethanakit, T. Rungrotmongkol, U. Bren, V. Frecer and M. Stanislav. Binding free energy calculations of inhibitors bound to neuraminidase subtype N1 of avian influenza A virus. Drug Design and Discovery for Developing Countries, Trieste, Italy, July 3-5 **2008**.
- 7. T. Rungrotmongkol, P. Decha, P. Sompornpisut, M. Malaisree, P. Intharathep, N. Nunthaboot, T. Udommaneethanakit, O. Aruksakunwong, and S. Hannongbua. Molecular modelling on the acylation process in furin complexed with the cleavage site of hemagglutinin H5. Drug Design and Discovery for Developing Countries, Trieste, Italy, July 3-5 **2008**.
- 8. T. Rungrotmongkol, T. Udommaneethanakit, M. Malaisree, N. Nunthaboot, P. Intharathep, and S. Hannongbua. How does oseltamivir lose its activity against virulent H5N1 mutants? Sokendai Asian Winter School, Okazaki, Japan, December 9-12, **2008**.
- 9. T. Rungrotmongkol, M. Malaisree, S. Hannongbua, S. Phongphanphanee, N. Yoshida, F. Hirata, Neuraminidase and M2-channel of influenza A viruses H5N1 and pandemic H1N1: molecular modelling and 3D-RISM, The Inaugural CU-IMS Joint Symposium, Chulalongkorn University, Bangkok, Thailand, October 19-21, **2010**.
- 10. T. Rungrotmongkol, Computational Studies on Influenza A Virus Subtypes H5N1 and Pandemic H1N1, EXODASS General Meeting & Mini-Symposium, Institute for Molecular Science, Okazaki, Japan, May 26, **2011**